HELMHOLTZ ZENTRUM
DRESDEN ROSSENDORF

# ANNUAL REPORT 2018

## Institute of Ion Beam Physics and Materials Research

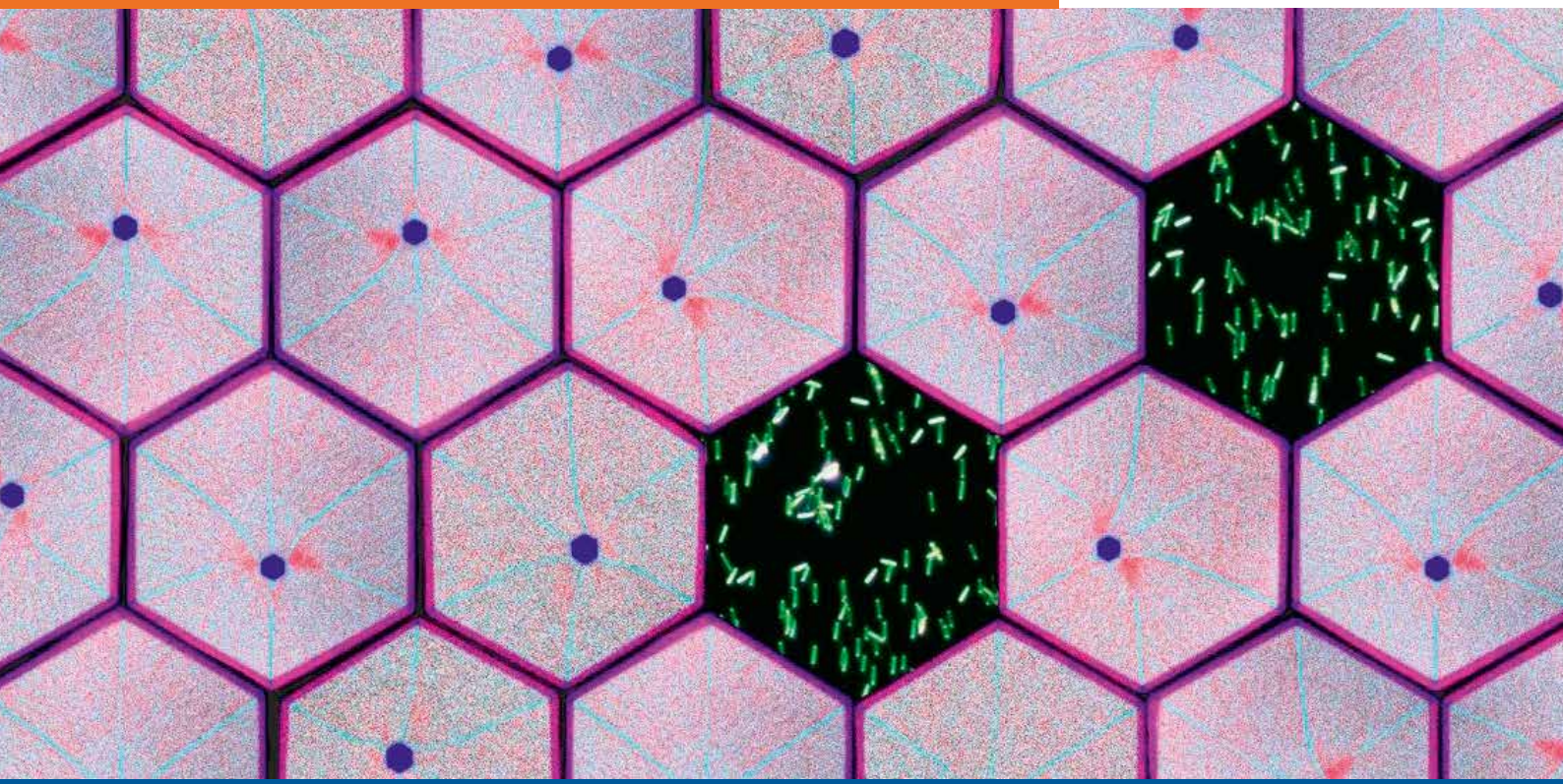

HZDR-097

Wissenschaftlich-Technische Berichte
HZDR–097

# Annual Report 2018

## Institute of Ion Beam Physics and Materials Research

Editors

J. Fassbender, M. Helm,
P. Zahn

HELMHOLTZ ZENTRUM
DRESDEN ROSSENDORF

## Cover Picture

The cover picture illustrates an artistic arrangement of two-dimensional compositional maps (hexagons) from GaAs / InAlAs / InGaAs core / shell / shell nanowire cross-sections. The different colors correspond to different group-III elements (blue for gallium, red for indium, and cyan for aluminum) as measured by energy-dispersive X-ray spectroscopy in scanning transmission electron microscopy mode. The pattern of hexagons is a repetitive reproduction of three different compositional maps. The large lattice-mismatch between the thin core (approximately 25 nm in diameter) and the shells causes the development of tensile hydrostatic strain up to 7 % in the core. In that way, we can tune the bandgap of the GaAs core in a very wide range, rendering these nanowires suitable for photonic devices across the near-infrared range, including telecom photonics at 1.3 and 1.55 µm. The fact that the nanowires grow epitaxially on Si substrates could enable in the future the monolithic integration of GaAs-based devices in Si-CMOS circuits. Two dark-field optical microscopy images of randomly dispersed nanowires (removed from their substrate) are also illustrated. The nanowire length is approximately 2 µm.

Image: © HZDR / L. Balaghi, R. Hübner, E. Dimakis

For further information see:
Balaghi, L. et al., **Widely tunable GaAs bandgap via strain engineering in core/shell nanowires with large lattice mismatch**, Nature Communications **10**, 2793 (2019)

Many thanks for providing material and for technical assistance to: S. Gebel, S. Kirch, J. v. Borany, S. Facsko, P. Michel, and L. Balaghi.

Print edition: ISSN 2191-8708
Electronic edition: ISSN 2191-8716

urn:nbn:de:bsz:d120-qucosa2-340789
www.hzdr.de/publications/Publ-29482
Published by Helmholtz-Zentrum Dresden - Rossendorf e.V.

This report is also available at https://www.hzdr.de/FWI.

Helmholtz-Zentrum Dresden - Rossendorf e.V.
Institute of Ion Beam Physics and Materials Research
Bautzner Landstraße 400
01328 Dresden
Germany

| | | |
|---|---|---|
| Directors | Prof. Dr. M. Helm | Prof. Dr. J. Fassbender |
| Phone | +49 351 260 2260 | +49 351 260 3096 |
| Fax | +49 351 260 3285 | +49 351 260 3285 |
| Email | m.helm@hzdr.de | j.fassbender@hzdr.de |

www.hzdr.de/FWI

# Preface by the directors

The Institute of Ion Beam Physics and Materials Research conducts materials research for future applications in, e.g., information technology. To this end, we make use of the various possibilities offered by our Ion Beam Center (IBC) for synthesis, modification, and analysis of thin films and nanostructures, as well as of the free-electron laser FELBE at HZDR for THz spectroscopy. The analyzed materials range from semiconductors and oxides to metals and magnetic materials. They are investigated with the goal to optimize their electronic, magnetic, optical as well as structural functionality. This research is embedded in the Helmholtz Association's programme "From Matter to Materials and Life". Six publications from last year are highlighted in this Annual Report to illustrate the wide scientific spectrum of our institute.

The early highlight of the year 2018 was an evaluation in the framework of the Helmholtz Programme-Oriented Funding (POF). This was in fact an evaluation looking at the achievements of the individual "Research Units" (in our case: Institutes) in the present POF period. Our institute received the grade "outstanding", the highest out of 7 possible grades. We would like to take this opportunity to thank all members of the institute for their tremendous efforts that have led to this fantastic outcome! However, this is not the end – presently we are preparing the so-called "strategic evaluation" of the Helmholtz Programmes, which will take place in January 2020.

Our third-party funding remains on a high level: we are coordinating two large I3 projects from the EU – one related to the European synchrotrons and free-electron lasers (CALIPSOplus) and one related to European ion beam facilities (RADIATE). In particular remarkable are 10 DFG grants successfully acquired by our scientists during the 12-months period from 4/2018 to 3/2019. We think this is a quite extraordinary achievement within the Helmholtz Association considering the eligibility restrictions we are bound to.

Our scientists demonstrated their excellence through a number of recognitions and awards. Dr. Nico Klingner and Dr. René Heller received the HZDR Innovation Award for the development of a retrofitable time-of-flight secondary ion mass spectrometer for the Helium ion microscope. The 2$^{nd}$ prize went to Dr. Slawomir Prucnal and Max Stöber (jointly with Dr. Charaf Cherkouk from TUBAF) for their work on novel electrodes for secondary batteries. Toni Hache was honored with the Georg-Simon-Ohm Award 2018 of the German Physical Society (DPG) for his Master Thesis on the "Fabrication and Characterization of Spin-Hall-Effect based Nano-Microwave Oscillators". We sincerely congratulate all prize winners! A large part of our research is actually being done by our PhD students – seven of them successfully finished their PhD in 2018, remarkable three of them even with the highest honor "summa cum laude". The education of the PhD students was supported by topical courses on "How to manage your PhD project" and "Scientific Presentation".

Several conferences and workshops were organized by scientists from our institute: the "2$^{nd}$ international HeFIB conference on Helium and emerging Focused Ion Beams" was organized by Dr. Gregor Hlawacek and attracted around 80 participants. It covered a wide range of emerging FIB technologies and had strong support by several companies. Dr. Mahdi Ghorbani-Asl co-organized the conference "Flatlands Beyond Graphene" in Leipzig and Prof. Sibylle Gemming a summer school on "Deep materials: Perspectives on data-driven materials research" at TU Dresden.

In the framework of the HZDR "High-Potential Programme", PD Dr. Georgy Astakhov from University of Würzburg joined our institute and established a new group on "Quantum Materials and Technology" within the Semiconductor Materials department.

Finally, we would like to cordially thank all partners, friends, and organizations who supported our progress in 2018. Special thanks are due to the Executive Board of the Helmholtz-Zentrum Dresden-Rossendorf, the Minister of Science and Arts of the Free State of Saxony, and the Ministers of Education and Research, and of Economic Affairs and Energy of the Federal Government of Germany. Numerous partners from universities, industry and research institutes all around the world contributed essentially, and play a crucial role for the further development of the institute. Last but not least, the directors would like to thank again all members of our institute for their efforts and excellent contributions in 2018.

Prof. Manfred Helm

Prof. Jürgen Fassbender

# Contents

## Selected Publications



## Statistics

# Selected Publications

Image: HZDR / N. Klingner

# Copyright remarks

The following journal articles are reprinted with kind permission from:

**DNA-Mold Templated Assembly of Conductive Gold Nanowires**
Bayrak, T.; Helmi, S.; Ye, J.; Kauert, D.; Kelling, J.; Schönherr, T.; Weichelt, R.; Erbe, A.; Seidel, R.
Nano Letters Vol. 18, pp. 2116 – 2123

DOI: 10.1021/acs.nanolett.8b00344

**Electronic-skin compasses for geomagnetic field-driven artificial magnetoreception and interactive electronics**
Cañón Bermúdez, G. S.; Fuchs, H.; Bischoff, L.; Fassbender, J.; Makarov, D.
Nature Electronics Vol. 1(11), pp. 589 – 595

DOI: 10.1038/s41928-018-0161-6

**Laser-Rewriteable Ferromagnetism at Thin-Film Surfaces**
Ehrler, J.; He, M.; Shugaev, M. V.; Polushkin, N. I.; Wintz, S.; Liersch, V.; Cornelius, S.; Hübner, R.; Potzger, K.; Lindner, J.; Fassbender, J.; Ünal, A. A.; Valencia, S.; Kronast, F.; Zhigilei, L. V.; Bali, R.
ACS Applied Materials and Interfaces Vol. 10(17), pp. 15232 – 15239

DOI: 10.1021/acsami.8b01190

**Supported Two-Dimensional Materials under Ion Irradiation: The Substrate Governs Defect Production**
Kretschmer, S.; Maslov, M.; Ghaderzadeh, S.; Ghorbani-Asl, M.; Hlawacek, G.; Krasheninnikov, A. V.
ACS Applied Materials and Interfaces Vol. 10(36), 30827 – 30836

DOI: 10.1021/acsami.8b08471

**Gapless Broadband Terahertz Emission from a Germanium Photoconductive Emitter**
Singh, A.; Pashkin, A.; Winnerl, S.; Helm, M.; Schneider, H.
ACS Photonics Vol. 5, pp. 2718 – 2723

DOI: 10.1021/acsphotonics.8b00460

**Extended Infrared Photoresponse in Te-Hyperdoped Si at Room Temperature**
Wang, M.; Berencén, Y.; García-Hemme, E.; Prucnal, S.; Hübner, R.; Yuan, Y.; Xu, C.; Rebohle, L.; Böttger, R.; Heller, R.; Schneider, H.; Skorupa, W.; Helm, M.; Zhou, S.
Physical Review Applied Vol. 10(2), 024054

DOI: 10.1103/PhysRevApplied.10.024054

NANO LETTERS
Letter
Cite This: Nano Lett. 2018, 18, 2116−2123
pubs.acs.org/NanoLett

# DNA-Mold Templated Assembly of Conductive Gold Nanowires

Türkan Bayrak,[†,§,▽] Seham Helmi,[⊥,#,▽] Jingjing Ye,[§,⊥,▽] Dominik Kauert,[⊥] Jeffrey Kelling,[‡] Tommy Schönherr,[†] Richard Weichelt,[∥,§] Artur Erbe,[*,†,§] and Ralf Seidel[*,§,⊥]

[†]Institute of Ion Beam Physics and Materials Research and [‡]Department of Information Services and Computing, Helmholtz-Zentrum Dresden-Rossendorf, 01328 Dresden, Germany

[§]Cluster of Excellence Center for Advancing Electronics Dresden (cfaed) and [∥]Institute of Physical Chemistry, TU Dresden, 01062 Dresden, Germany

[⊥]Molecular Biophysics Group, Peter Debye Institute for Soft Matter Physics, Universität Leipzig, 04103 Leipzig, Germany

Supporting Information

**ABSTRACT:** We introduce a new concept for the solution-based fabrication of conductive gold nanowires using DNA templates. To this end, we employ DNA nanomolds, inside which electroless gold deposition is initiated by site-specific attached seeds. Using programmable interfaces, individual molds self-assemble into micrometer-long mold superstructures. During subsequent internal gold deposition, the mold walls constrain the metal growth, such that highly homogeneous nanowires with 20−30 nm diameters are obtained. Wire contacting using electron-beam lithography and electrical conductance characterization at temperatures between 4.2 K and room temperature demonstrate that metallic conducting wires were produced, although for part of the wires, the conductance is limited by boundaries between gold grains. Using different mold designs, our synthesis scheme will, in the future, allow the fabrication of complex metal structures with programmable shapes.

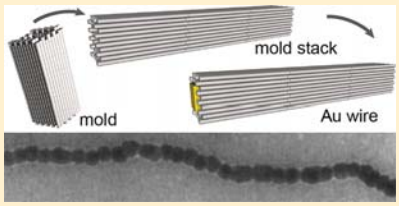


**KEYWORDS:** *Metal nanowires, seeded growth, DNA metallization, DNA nanostructures, DNA template, nanoelectronics*

The past decade has seen a boost in the field of DNA nanotechnology. A number of pioneering techniques[1−6] were developed that allow the self-assembly of large two- and three-dimensional DNA structures with complex shapes. The basis of these techniques are specific interactions between complementary DNA strands. By appropriate sequence design of the involved DNA molecules, a desired structure can thus be obtained in a fully programmable, sequence-encoded manner. The beauty, the complexity[1−6] and the increased rigidity[7] of the down-to-the-atomic-level defined objects instantaneously motivated the usage of DNA nanostructures to assemble non-DNA materials in defined patterns. Examples include the arrangements of proteins,[8] chemical[9] and photoactive groups,[10,11] the assembly of metal nanoparticles into plasmonic nanostructures,[12−14] and the sculpting of lipid membranes.[15,16]

DNA nanotechnology is particularly successful in generating soft nanostructures. However, many applications in "hard-matter nanotechnology", particularly in nano-optics and nanoelectronics, require structures made from inorganic, e.g., metallic and semiconducting, rather than biological materials. In particular, the low electrical conductance found in contacts to single DNA duplexes is detrimental for applications in nanoelectronics.[17] Therefore, it would be highly desirable if one could "replace" the DNA structure atom by atom site-specifically with a material of choice to enable a programmable synthesis of inorganic nanostructures. Though a direct replacement will be practically impossible, the outlined idea inspired the usage of DNA as a template for inorganic material growth. Hereby, the biomolecule would donate its shape to the growing material film. In first approaches, linear DNA molecules were metallized by so-called electroless deposition, in which metal seeds are first deposited on the molecule that are subsequently grown to more-continuous structures. This way, elongated metal particle assemblies could be fabricated.[18−20] Later, this concept could be extended to many different materials, including gold, silver, platinum, palladium, copper, and cobalt.[21] With the advances in DNA nanotechnology, rigid DNA template structures with more-complex shapes became available enabling the growth of elongated wires,[22] metal rings,[23] junctions,[24] and spheres[25] as well as structures consisting of two types of metals.[26] The deposited metal films were, however, not homogeneous and typically contained many distinct grains. This made the resulting structures either discontinuous[20] or inhomogeneous,[27] depending on the amount of deposited material.

Nonetheless, wires produced this way were often found to conduct electric current when contacted either by electron-beam-lithography-fabricated electrodes[19,28−32] or by conductive AFM tips.[33,34] Reported resistance values spanned several orders of magnitude. Typically, the observed resistivities were significantly larger than expected for the respective metal forming the wire, indicating that grain boundaries can act as significant barriers. This was supported by recent temperature-dependent (4.2 to 293 K) conductance measurements on

**Received:** January 24, 2018
**Revised:** February 26, 2018
**Published:** February 27, 2018






DOI: 10.1021/acs.nanolett.8b00344
Nano Lett. 2018, 18, 2116−2123

DNA-origami-based Au nanowires from our laboratory showing that tunneling, thermionic, and hopping conduction mechanisms govern the conductance at low, intermediate, and high temperatures, respectively.[22] In addition, a recent study of 500 nm nanopillars, realized as a multilayer heterostructure of DNA origami tiles and Au nanoparticles, suggested a tunneling or hopping conduction mechanism at room temperature.[28] To limit the number of grain boundaries, recently elongated Au nanorods were deposited in an aligned manner on DNA origami templates and connected using limited electroless Au-plating.[35] This provided resistance values for wires of 12 to 30 nm widths in the range of 440 Ω to 37 MΩ with resistivities close to bulk gold for the wires with the highest conductances. This further supports the idea that grain boundaries due to inhomogeneous growth conditions appear to be one of the challenges in DNA-templated fabrication of metallic wires.

A key problem for the traditional external deposition on DNA templates is the lack of size control for the particles that grow at the different positions along the DNA chain. This makes the methodology prone to inhomogeneities. Inspired by internal metal deposition schemes inside protein shells,[36,37] we and others recently developed a DNA mold-based nanoparticle fabrication scheme.[38,39] Here, the metal deposition occurs on a nucleation seed inside the cavity of a DNA origami mold, such that the mold wall influences the shape of the resulting particle. This way, it was possible to synthesize gold and silver cuboids of different dimensions and shapes.

Here, we extend the mold-based nanostructure fabrication scheme by coupling mold monomers into large linear mold superstructures (Figure 1). This enables the growth of highly homogeneous, micrometer-long nanowires with ~30 nm width that in part exhibit metallic conductance. To this end, we assembled DNA molds using the DNA origami method[1,2] from an 8064 nucleotide long single-stranded DNA scaffold and corresponding DNA staple oligomers (see the Methods section). The mold monomers had a 40 nm long tube-like shape with a quadratic cross-section.[39] Each side wall of the mold was composed of two layers of 10 parallel DNA helices of equal length (Figure 1) providing a total of 64 helices for the whole mold structure. Fabricated mold monomers were preloaded with 5 nm DNA-functionalized gold nanoparticles[40,41] serving as seeds for the subsequent gold growth. They were attached within the molds via four complementary DNA capture strands extruding from the four cavity faces at the given binding position (Figure 1a).[39]

To allow the formation of long linear mold superstructures via sequential docking of mold monomers, we extended or shortened the staples at the DNA helix ends (further called end staples) by two nucleotides, such that the 2-nt extensions of one mold could invade into the other mold and hybridize with its scaffold (Figure 1a,b).

The mold geometry with helices of identical length is asymmetric with respect to its ends. If we call one mold end the head and the other end the tail side, then a particular DNA helix that is recessed at the head side is extended at the tail side (and vice versa), which results in a symmetry break. Thus, when mold ends bind in a head-to-tail fashion, docking can be obtained at all 64 helix ends, leaving no gap at the interface. However, for head-to-head or tail-to-tail binding, a significantly lower number of docking helices is obtained (44 or 36, respectively). To obtain "neat-less", i.e., gap-free, mold superstructures we therefore designed end staples to support head-to-tail binding. We prepared two different types of

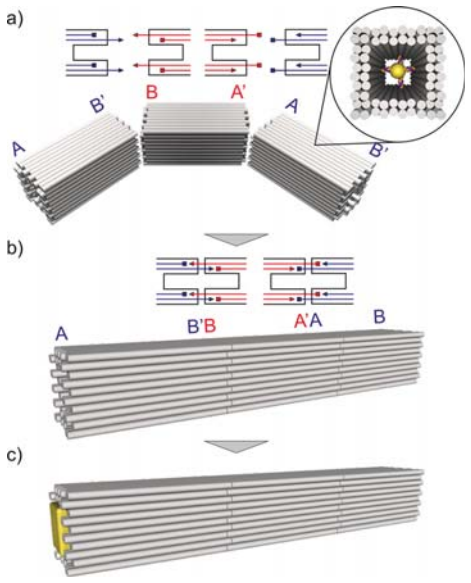


**Figure 1.** Scheme illustrating the mold-based gold nanowire. (a) Design scheme of the mold bricks with specifically interacting ends containing an internally attached 5 nm gold seed (see the inset in the upper right corner). Adhesion of mold ends is obtained by either protruding 5′-staple ends together with correspondingly recessed 3′-staple ends at the mold ends (A−A′ interface; see the sketches in the top row) or protruding 3′-staple ends together with recessed 5′-staple ends (B−B′ interface). (b) Self-assembly of a long mold superstructure using two mold types, each carrying an A or a B interface, being complementary to the A′ or the B′ interface of the other mold type, respectively. (c) Gold nanowire formation by metal deposition at the seeds inside the mold chain.

interfaces: interface A−A′, for which end staples were extended by 2 nt at the 5′-ends and correspondingly recessed at the 3′-ends, as well as interface B−B′ with recessed 5′-ends and extended 3′-ends (Figure 1a). Here, A and B denote the head side of the mold and A′ and B′ the complementary side on a mold tail side, respectively.

For the assembly of linear mold chains a single interface, e.g., monomers with A−A′ ends would suffice. In this case mold chains would already form during origami hybridization, which would, however, inhibit the loading of the molds with gold seeds at internal sites. We therefore designed two different mold monomers: one with AB′ ends and the other with BA′ ends. While each mold type would be monomeric alone, their mixing should result in the desired chain formation (Figures 1 and 2).

Following the outlined approach, we assembled AB′ and BA′ molds, loaded them with gold nanoparticle seeds, and subjected them to TEM imaging (Figures 2a and S1). In contrast to our expectations, both monomers alone formed extended linear, partially staggered, chains, which, in turn, led to poor decoration with seeds. We hypothesized that, due to the large number of "attractive" ends (all 64 helix ends contained 2 nt recessions and extensions), mold monomers could bind to themselves, forming nondesired head-to-head and tail-to-tail interactions. Apparently, the presence of mismatches between staple extension and scaffold did not lower the affinity between single helix ends sufficiently to prevent unspecific binding.

To suppress unspecific interactions, the number of attractive helix ends was reduced by omitting end staples at some of the helix ends, which are in the following called nonattractive ends.



DOI: 10.1021/acs.nanolett.8b00344
Nano Lett. 2018, 18, 2116−2123

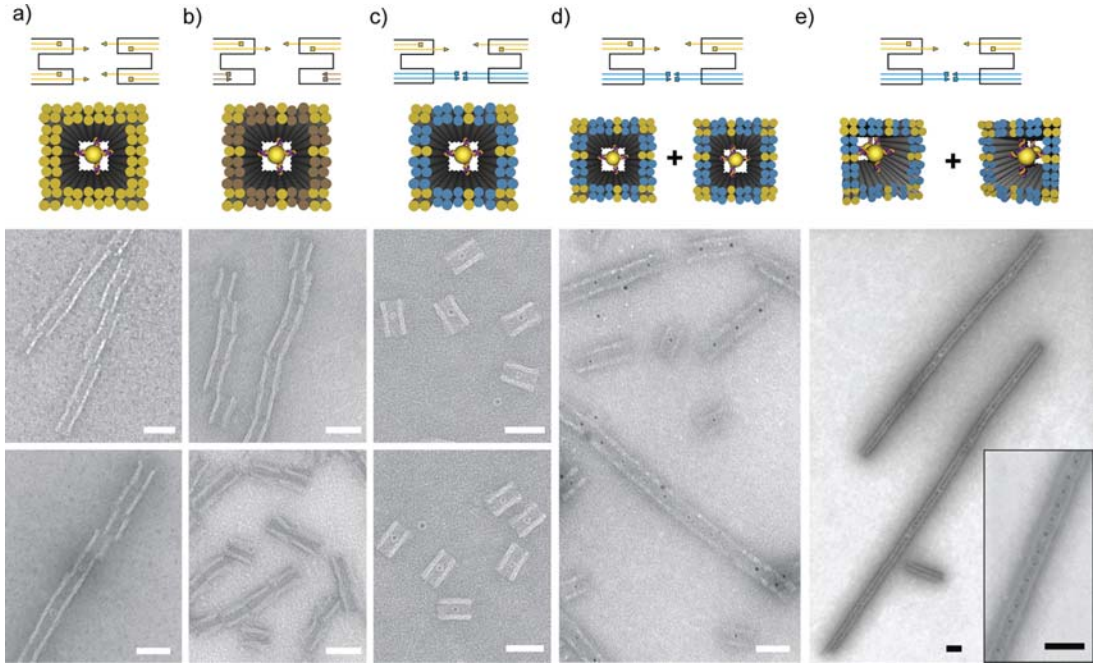


**Figure 2.** Fine-tuning the specificity of adhesive mold ends. (a–c) Type of staple ends used and their positions on the 3D model (upper row) as well as corresponding TEM images of the AB′ and BA′ mold monomers. Tested were (a) attractive ends only (in yellow), (b) attractive ends together with nonattractive ends (in gray, obtained by omitting ends staples), and (c) attractive and repulsive ends (blue, obtained by 6 nt non-complementary 5′-staple overhangs). (d) Mixing AB′ and BA′ mold monomers comprising attractive and repulsive end staples (as in panel c) results in mold oligomer formation. (e) By using optimized multimerization conditions, long linear mold chains are obtained. Preloading of the monomers with two seeds at high decoration efficiency results in a homogeneous loading of seeds inside the mold superstructure (see the inset). The scale bars correspond to 50 nm.

Here, the scaffold forms a dangling loop. For 16 to 24 attractive ends with the remaining ends being nonattractive, considerable unspecific interactions between mold monomers were observed nonetheless (Figures 2b and S1). To further reduce unspecific binding, repulsive interactions between helix ends were incorporated. To this end, the previously nonattractive ends were made repulsive by extending the end staples at these positions by 6 nt for both 5′ and 3′ ends (see the sketch in Figure 2c). The steric clash between these dangling ends should introduce an energetic penalty compared to the nonattractive end configuration. In agreement with this expectation, TEM imaging revealed the monomeric nature of molds containing up to 24 attractive helix ends (Figures 2c and S1). These monomers exhibited a high seed decoration efficiency because gold nanoparticles could freely enter the mold ends.

We next tested whether the optimized molds with attractive and repulsive ends could form specific interactions by mixing seed decorated AB′ and BA′ monomers. While molds with 16 and 20 attractive helix ends remained mostly monomeric (Figure S1), molds with 24 attractive ends supported the formation of linear oligomeric mold assemblies already after 10 min of incubation (Figure 2d). To prepare long mold chains for subsequent metallization, we carried out the following optimizations: (i) addition of 2 seeds per mold monomer to avoid interruption of gold wire in case of missing seeds, (ii) chain formation overnight to obtain long assemblies, and (iii) polyethylene glycol (PEG) precipitation[42] after chain formation to remove unbound gold seeds. All together, these optimizations yielded $\mu$m-long linear mold chains containing evenly 20 nm spaced gold seeds with 96 ± 2% decoration efficiency (Figure 2e).

To fabricate gold nanowires, the linear mold superstructures were used in a previously established seeded growth procedure.[39] Mold chains were premixed with the reducing agent hydroxylamine. Subsequently, a solution of the gold precursor H[$AuCl_4$] was quickly injected into the rapidly stirred solution. The reaction self-terminated due to the consumption of H[$AuCl_4$] after ~1 min as judged from color changes of the solution. TEM and SEM imaging revealed a homogeneous gold deposition at all seeds (Figure 3). The lengths of the grown structures were in the micrometer range (Figure S2). At low amounts of precursor, the grown gold particles still remained well-separated (Figure 3a), while at larger amounts of precursor, the grown particles appeared more and more connected to each other (Figures 3b,c and S3). At the largest precursor concentration the particles formed quasi-continuous $\mu$m-long wires that were occasionally interrupted by smaller gaps (Figures 3c,d, and S4). These structures were stable in solution for several days. Only at larger precursor concentrations did aggregation occur. We note that the highly homogeneous particle growth and the stability of the wires was only achieved when the seed-loaded mold chains were subjected to the PEG precipitation before metallization. This was most likely due to residual PEG traces because PEG is also used as a surfactant in nanoparticle synthesis.[43] The resulting nanowires (Figure 3d) had diameters of 32 ± 3 nm. Despite occasional gaps, these wires were of excellent homogeneity compared with other DNA-templated metal structures. Thus, the mold-assisted growth of metal nanoparticles can be successfully transferred to large mold superstructures.

To reveal which role residual gaps are playing and whether the wires can exhibit metal-like conductance, we investigated



DOI: 10.1021/acs.nanolett.8b00344
*Nano Lett.* 2018, 18, 2116–2123

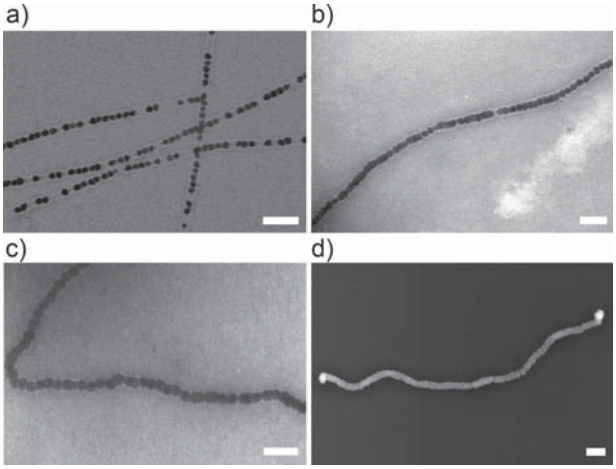


**Figure 3.** Gold nanowires obtained by gold deposition within the seed decorated linear mold superstructures. TEM images of the obtained structures for different relative amounts of gold precursor are shown: (a) 1-fold, (b) 2-fold, and (c) 4-fold $H[AuCl_4]$. (d) SEM image of a gold nanowire on a $SiO_2$ support grown with 4-fold $H[AuCl_4]$. The scale bars correspond to 50 nm.

the electrical transport properties of several fabricated nanowires with 110 to 1000 nm in length. The electrical contacting of individual DNA origami mold-based gold nanowires was performed in three steps. (i) Using electron beam lithography, 45 contact areas (in three parallel arrays) were patterned on top of $SiO_2$ substrates containing the adsorbed gold nanowires. Each contact area had a total of 4 90 $\mu$m × 90 $\mu$m Au contact pads and 144 alignment marks arranged in a square lattice with an 8 $\mu$m distance between neighboring marks (Figure 4a). (ii) Using scanning electron microscopy, the coordinates of the individual wires relative to the alignment marks were recorded (Figure 4b). (iii) The recorded locations of the nanowires were used to obtain corresponding electron-beam exposure positions to place electrical contacts on the nanowires. This procedure allowed to write four electrodes, even on a 600 nm long nanowire (Figure 4c). Overall, the wires adhered well to the substrate, such that they retained their shape during the lithography and the solvent-based ultrasonic lift-off process, as confirmed by SEM imaging.

Two-terminal current−voltage ($I$−$V$) measurements were performed on 22 individual wires. The measured resistance values at room temperature (RT, i.e., 293 K) including the contact resistance between EBL-patterned gold electrodes and nanowires were between 90 Ω and 30 GΩ without showing a clear length dependence (Figure 5).

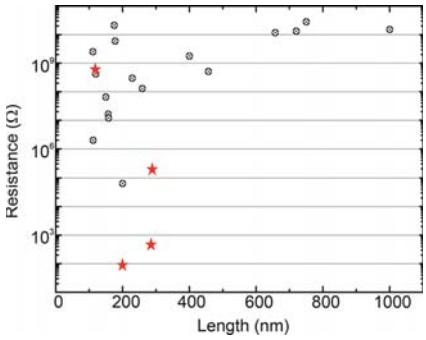


**Figure 5.** Resistance values as a function of length for the characterized gold nanowires. Wires chosen for temperature-dependent measurements are shown by a star-shaped symbol.

The limited resolution of SEM imaging on the $SiO_2$ substrates did not allow to correlate the measured resistance with the wire morphology (Figure S5). Therefore, to understand the large variation in resistance values, we measured the temperature dependence of the charge transport of two highly conductive nanowires (labeled CW-1 and CW-2 with RT resistances of 90 ± 5 Ω and 460 ± 10 Ω) as well as two highly resistive nanowires (labeled RW-1 and RW-2 with RT resistances of 190 ± 5 kΩ and 690 ± 5 MΩ). The inset of Figure 6a depicts a nanowire with a length of 800 nm, which was contacted by four terminal gold contacts. SEM imaging revealed 13−15 nm gaps between the contact points 2 and 3 as well as 3 and 4 leading to insulating behavior in $I$−$V$ measurements (see Figure S6). A high conductance was found for the wire segment between contacts 1 and 2 (CW-1). The $I$−$V$ characteristics of CW-1 (200 nm length and 40 nm width) was linear throughout the considered temperature range between 4.2 K and RT (see Figures 6b and 7a). This indicates an ohmic behavior of the nanowire itself as well as its contacts. The resistance of the wire was weakly decreasing with temperature from 90 Ω at 293 K to 50 Ω at 4.2 K, as expected for a metallic wire. A qualitatively similar behavior was observed for the 285 nm long nanowire CW-2 with a 30 nm average width (see Figures 6b and 7b) for which resistances of 460 and 420 Ω at 293 and 4.2 K were measured, respectively.

Temperature-dependent $I$−$V$ measurements on the more resistive nanowires RW-1 (290 nm length and 36 nm width)

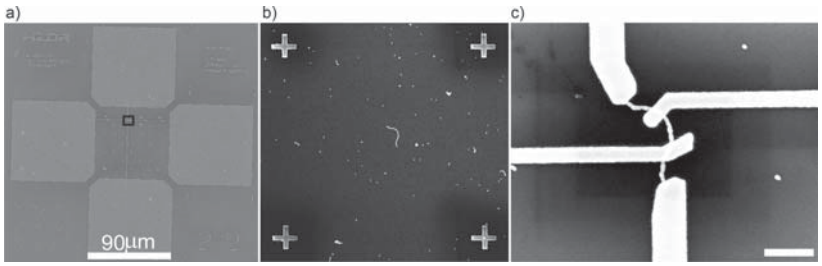


**Figure 4.** Electrical contacting of mold-templated nanowires. (a) SEM images of one out of 45 contact areas comprising four contact pads. Contact pads were fabricated on $SiO_2$ substrates containing the adsorbed gold nanowires. In between the electrodes, 144 alignment markers arranged in a square lattice defined 36 "writing" fields of 8 $\mu$m × 8 $\mu$m size. (b) Enlarged view into a single writing field (corresponding to the black square in panel a) containing a 600 nm long gold nanowire. (c) The gold nanowire shown in panel b after contact writing. Each contact to the wire connects to one of the four contact pads shown in panel a.



DOI: 10.1021/acs.nanolett.8b00344
*Nano Lett.* 2018, 18, 2116−2123

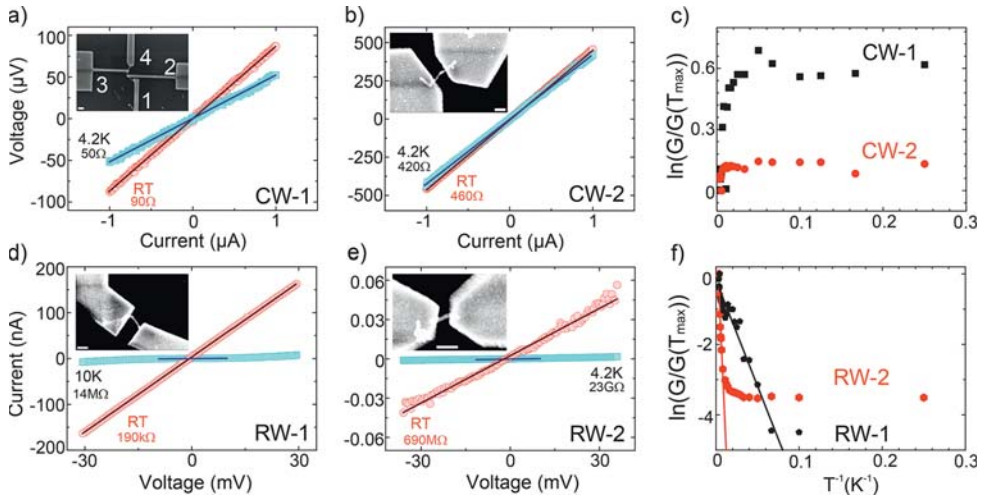


**Figure 6.** $I-V$ characteristics of the different nanowires measured at the temperatures of 4.2 and 293 K. SEM inset images show the nanowires after contacting (scale bars are 200 nm). (a,b) $I-V$ curves for the highly conductive wires CW-1 and CW-2 obtained by sourcing the current and measuring the voltage drop across the wire. Resistance values shown next to the curves were obtained from linear fits (solid lines). (c) Normalized natural logarithm of the conductance values as a function of $T^{-1}$ for CW-1 and CW-2. (d,e) $I-V$ curves for the resistive wires RW-1 and RW-2 obtained by applying a voltage bias and measuring the resulting current. (f) Normalized natural logarithm of the conductance values as a function of $T^{-1}$ for RW-1 and RW-2 (filled circles). Exponential fits to the data in a selected temperature range are shown as solid lines.

and RW-2 (115 nm length and 39 nm width) revealed linear behavior at RT (Figure 6d,e). However, at low temperatures (50 to 4 K), the $I-V$ curves became nonlinear in between −30 and +30 mV (Figure S7). Therefore, resistance values were calculated from the slope of the linear part of the curves (−10 to 10 mV). The resistance was strongly temperature dependent for both wires; it increased for RW-1 from 190 kΩ at RT to 14 MΩ at 10 K and for RW-2 from 700 MΩ at RT to 23 GΩ at 4 K. Thus, both wires did not show metallic conductance behavior.

To better understand the nature of the charge transport in these nanowires, we plotted the normalized natural logarithm of the conductance $\ln[G/G(T_{max})]$ as a function of the reciprocal temperature ($T^{-1}$). The conductance of both CW-1 and CW-2 increased mildly with decreasing temperature, as discussed above (Figure 6c). Saturation of the conductance at low temperatures (4.2 to 20 K) was observed in CW-1 and CW-2. In contrast, the conductance of the resistive nanowires RW-1 and RW-2 decreased strongly, initially in an exponential fashion with the reciprocal temperature (Figure 6f). While RW-1 exhibited an exponential decrease over the whole temperature range, the conductance of RW-2 saturated for temperatures below 30 K.

An exponential conductance decrease indicates a thermally activated hopping mechanism for the charge transport, e.g., due to low conductance barriers in between conductive wire segments. Here, the conductance is governed by the activation energy, $E_a$, necessary to overcome the barrier according to $G \approx \exp(-E_a/k_BT)$, where $k_B$ is the Boltzmann constant.[44−46]

The activation energies of the wires were obtained from the slope of the linear sections in the conductance yielding 5 ± 0.5 meV for RW-1 (temperature range from 10K to RT) and 45 ± 5 meV for the more-resistive wire RW-2 (temperature range from 70 K to RT). While a hopping mechanism seems to dominate the conduction of RW-1 at all temperatures, hopping conductivity is observed for RW-2 only at high temperatures. At low temperatures, between 4 and 30 K, the independence of the conductance of RW-2 on the temperature suggests that direct tunneling of electrons through an energy barrier is the dominant mechanism in this regime. For temperatures in between the tunneling and the hopping regime (30 to 70 K) a thermionic conduction mechanism comes into play[21] due to decreases in the effective barrier height and the excitation of more electrons.

In summary, we successfully demonstrated the fabrication of highly homogeneous and conductive nanowires using DNA molds. An important step was herein the fine-tuning of the specificity of the mold−mold interactions using attractive and repulsive ssDNA overhangs. In only this way did molds of a given type stay monomeric and could thus be efficiently loaded with gold nanoparticle seeds. Mixing two mold types with likewise attractive interfaces resulted in the formation of linear mold superstructures being hundreds of nanometers long and comprising dozens of monomers. The subsequent gold deposition at the seeds produced nanowire structures that consisted of nearly perfectly aligned gold nanoparticles of homogeneous size. This demonstrates that the mold-assisted growth of metal nanoparticles can be applied to large superstructures. Our approach represents thus a new way to DNA-templated nanostructure fabrication.

At elevated amounts of deposited gold, the grown nanoparticles became connected to each other, such that the resulting structures became quasi-continuous. To verify whether actual gold−gold contacts between the particles had been established, we employed temperature-dependent conductance measurements enabled by high-precision contacting of the wires using electron beam lithography. These characterizations provided diverging results. A small part of the wires exhibited high metal-like conductivity, verifying that metallic gold−gold contacts could be successfully formed over 20 to 30 contiguous particle boundaries (being spaced by 20 nm). This is remarkable because only very recently were high conductivities of DNA templated gold structures achieved using long gold nanorods with much fewer interfaces and a surface-based metallization procedure.[35]



DOI: 10.1021/acs.nanolett.8b00344
Nano Lett. 2018, 18, 2116−2123

Establishing metallic contacts at the particle−particle interfaces still remains a critical factor because many of the tested wires exhibited significantly reduced conductance values. Comprehensive temperature-dependent characterization of two more resistive wires revealed that the charge transport was dominated by a single effective energy barrier reflected by the single exponential decrease of the conductivity with reciprocal temperature. This suggests that the charge transport was dominated by a single nonmetallic interparticle interface that needed to be overcome by hopping at higher temperatures. The width of such nonmetallic gaps was presumably in the low nanometer range supported by the observation of tunneling dominating the charge transport at low temperatures for one of the tested wires.

Future work will focus on improving the perfection of the obtained wires by increasing the yield for establishing metallic interparticle contacts. Nonetheless, our results represent a considerable advancement in DNA-templated fabrication of electronic devices regarding the homogeneity and the potentially high conductivity of the obtained structures. Beyond that our approach, based on large DNA mold superstructures, opens a versatile route for self-assembly-based device fabrication. Using molds with different geometries (e.g., different diameters, additional docking sites, and junctions) and specific interfaces as well as different materials should enable the fabrication of whole devices including gate electrodes and even device networks.

**Methods.** *DNA-Origami Design, Assembly, and Analysis.* The DNA origami molds (Figures S8 and S9) were designed using CaDNAno[47] and comprised of parallel helices arranged in a square lattice.[48] Reverse-phase cartridge purified oligonucleotides for the DNA origami objects were purchased from Eurofins MWG Operon. Single-stranded p8064 scaffold DNA was purchased from Tilibit Nanosystems (Garching). The one-pot assembly reaction was performed as follows: the 10 nM scaffold p8064 was mixed in folding buffer containing 5 mM Tris−HCl, 1 mM ethylenediaminetetraacetic acid, and 11 mM $MgCl_2$ (pH 8.0) with unpurified staple strands and capture strands in a molar ratio of 1:10:1 (per individual sequence). The reaction was heated to 80 °C for 5 min and cooled to 25 °C over 15 h using a nonlinear temperature ramp, with the slowest temperature decrease occurring between 55 to 45 °C. The folded objects were investigated with gel-electrophoresis (1% agarose gel, 0.5× TBE, 11 mM $MgCl_2$, and 3.5 V/cm). Subsequently, the molds were purified using precipitation with polyethylene glycol to remove excess staples.[42] For TEM imaging, 2−3 μL of a diluted origami sample solution (1−2 nM) was applied to glow-discharged carbon-coated grids. The sample was subsequently stained using a filtered 2% solution of uranyl formate in 5 mM NaOH for 2 min. TEM imaging was performed in a Zeiss Libra 120 or a Phillips CM200 Ultra Twin transmission electron microscope at 80 or 120 kV, respectively.

*Decoration of DNA Molds with Gold Nanoparticle Seeds.* AuNPs (5 nm; Sigma-Aldrich) were densely coated with 15 nt poly thymidine oligonucleotides carrying a 5′-thiol modification as described before using the method of salt aging.[39,40,49] The particle concentration was estimated from the absorbance at 520 nm. DNA-functionalized gold nanoparticles were mixed with the purified DNA origami molds in the presence of 300 mM NaCl at a molar ratio of 3:1 or 6:1 for molds with one or two seed binding sites, respectively. The mixture was slowly heated to 40 °C and afterward cooled down to 23 °C over a duration of 5 h to allow hybridization of the AuNPs with the complementary capture strands on the mold.

*Formation of Linear-Mold Superstructures.* A pair of types of mold monomers (AB′ and BA′) were designed that only allow specific head-to-tail binding to the other monomer type (see Figures S8 and S9 for the design details of the mold ends). After preloading with seeds, both monomers were mixed in a 1:1 molar ratio and incubated for up to 24 h followed by a precipitation with PEG to remove excess seeds.

*Seeded Growth of Gold within Mold Superstructures.* The concentration of the mold superstructures was adjusted with folding buffer (see above), such that 1 nM mold monomers were present in solution, and hydroxyl amine ($NH_2OH$) was added at a 6-fold molar access over the subsequently added gold precursor. The gold growth was initiated by injecting 1×, 2×, or 4× of 0.9 μL of 25 mM $H[AuCl_4]$ into a 100 μL final volume of the $NH_2OH$-containing mold solution.[39] During growth, the solution was vigorously stirred, and after 1 min, the grown wires were deposited on TEM grids or $SiO_2$ substrates.

**Deposition of the Gold Nanowires on Wafer Substrates.** Grown gold nanowires were deposited on p-doped $Si/SiO_2$ (300 nm oxide layer) wafer substrates diced into 1 cm × 1 cm squares. The surface was treated with an $O_2$ plasma (PICO, Diener Electronic-Plasma Surface Technology) at 7 sccm $O_2$ and a power of 240W for 3 min to make the hydrophobic surface more hydrophilic (see Figure S10). The sample was rinsed with ethanol (20 s) and pure-membrane water (20 s). Subsequently, 20 μL of the nanowire sample were placed on the wafer surface for 1 h. Afterward, the substrate was dipped in a 1:1 mixture of ethanol and deionized water for 30 s. To remove the organic DNA layer around the nanowires, the sample was again subjected to $O_2$ plasma at 7 sccm $O_2$ and 300 W for 30 min.

**Electron-Beam Lithography and Electrical Measurements.** The electrical contact pads and markers were fabricated using electron beam lithography (RAITH e-line Plus). ZEP520 electron beam resist was spin-coated on the samples and baked at 150 °C for 10 min. The resist was exposed at a 35 $\mu C/cm^2$ area dose to define contact pads, markers, and small contacts. The resist was developed in n-Amyl acetate for 90s and subsequently in isopropanol for 30 s. A 5 nm Ti adhesion layer followed by a 100 nm gold layer were deposited at 0.2 and 2 Å/s with electron-beam evaporation (Bestec UHV Evaporation Tool). Lift-off was performed by immersion in ZDMAC (Dimethylacetamide) and subsequent washing with IPA, followed by drying in a $N_2$-stream. Electrical measurements were carried out using a semiconductor parameter analyzer (Agilent 4156-C) in vacuum ($10^{-5}$ mbar) and in the dark using two probes. A helium flow cryostat system was used for temperature-dependent electrical measurements. The samples were cooled to 4.2 K, and measurements were performed while heating up. $I-V$ measurements were performed by sweeping of the voltage (0 to 30 mV and 0 to −30 mV) or the current (0 to 1 μA and 0 to −1 μA) for resistive or conductive wires, respectively. The resistances or conductances of the were determined by least-squares fitting of a linear function to the measured $V-I$ or $I-V$ curves, respectively. For wires that showed nonlinear $I-V$ relations at low temperatures (RW-1 and RW-2), we determined the zero-bias resistance (conductance) as the slope of the curve at the inflection point near zero current (voltage).



DOI: 10.1021/acs.nanolett.8b00344
Nano Lett. 2018, 18, 2116−2123

## ■ ASSOCIATED CONTENT

### Supporting Information

The Supporting Information is available free of charge on the ACS Publications website at DOI: 10.1021/acs.nanolett.8b00344.

Figures showing additional electron microscopy micrographs, conductance measurements, temperature-dependent $I-V$ behavior, design templates for the origami mold construction, and contact angles and surface energies. (PDF)

## ■ AUTHOR INFORMATION


### Corresponding Authors

*E-mail: a.erbe@hzdr.de. Phone: +49-351-260-2366.
*E-mail: ralf.seidel@uni-leipzig.de. Phone: +49-341-97-32501.

### ORCID

Ralf Seidel: 0000-0002-6642-053X

### Present Address

[#]Department of Physics, University of Oxford, Oxford OX13PU, U.K.

### Author Contributions

[▽]T.B., S.H., and J.Y. contributed equally to the presented work.



### Funding

This work was supported by the Deutsche Forschungsgemeinschaft within the Cluster of Excellence Center for Advancing Electronics Dresden (cfaed/TU Dresden) as well as grant no. SE 1646/8-1 to R.S. and by the Helmholtz Association through IHRS for Nanoelectronic Networks NanoNet (VH-KO-606).


### Notes

The authors declare no competing financial interest.

## ■ ACKNOWLEDGMENTS

We gratefully acknowledge Martin Bähler, Oliver Oeckler, Roger Gläser, Marius Grundmann, Jörg Lenzner, Markus Löffler, and the Dresden Center for Nanoanalysis for access, training, and support with respect to TEM and SEM imaging. We furthermore acknowledge Matthias Krause, Angela Schneider, and Claudia Neisser for their help with and access to the drop-shape analysis system and the helium flow for the cryostat. We thank Peter Zahn for useful discussions on the data of the electrical measurements.

## ■ REFERENCES


(1) Rothemund, P. W. K. Folding DNA to create nanoscale shapes and patterns. *Nature* **2006**, *440*, 297−302.
(2) Douglas, S. M.; Dietz, H.; Liedl, T.; Högberg, B.; Graf, F.; Shih, W. M. Self-assembly of DNA into nanoscale three-dimensional shapes. *Nature* **2009**, *459*, 414−418.
(3) Seeman, N. C. Nanomaterials based on DNA. *Annu. Rev. Biochem.* **2010**, *79*, 65−87.
(4) Han, D.; Pal, S.; Nangreave, J.; Deng, Z.; Liu, Y.; Yan, H. DNA origami with complex curvatures in three-dimensional space. *Science* **2011**, *332*, 342−346.
(5) Wei, B.; Dai, M.; Yin, P. Complex shapes self-assembled from single-stranded DNA tiles. *Nature* **2012**, *485*, 623−626.
(6) Benson, E.; Mohammed, A.; Gardell, J.; Masich, S.; Czeizler, E.; Orponen, P.; Högberg, B. DNA rendering of polyhedral meshes at the nanoscale. *Nature* **2015**, *523*, 441−444.
(7) Kauert, D. J.; Kurth, T.; Liedl, T.; Seidel, R. Direct mechanical measurements reveal the material properties of three-dimensional DNA origami. *Nano Lett.* **2011**, *11*, 5558−5563.
(8) Mikkilä, J.; Eskelinen, A.-P.; Niemelä, E. H.; Linko, V.; Frilander, M. J.; Törmä, P.; Kostiainen, M. A. Virus-encapsulated DNA origami nanostructures for cellular delivery. *Nano Lett.* **2014**, *14*, 2196−2200.
(9) Voigt, N. V.; Tørring, T.; Rotaru, A.; Jacobsen, M. F.; Ravnsbaek, J. B.; Subramani, R.; Mamdouh, W.; Kjems, J.; Mokhir, A.; Besenbacher, F.; Gothelf, K. V. Single-molecule chemical reactions on DNA origami. *Nat. Nanotechnol.* **2010**, *5*, 200−203.
(10) Hemmig, E. A.; Creatore, C.; Wünsch, B.; Hecker, L.; Mair, P.; Parker, M. A.; Emmott, S.; Tinnefeld, P.; Keyser, U. F.; Chin, A. W. Programming Light-Harvesting Efficiency Using DNA Origami. *Nano Lett.* **2016**, *16*, 2369−2374.
(11) Steinhauer, C.; Jungmann, R.; Sobey, T. L.; Simmel, F. C.; Tinnefeld, P. DNA origami as a nanoscopic ruler for super-resolution microscopy. *Angew. Chem., Int. Ed.* **2009**, *48*, 8870−8873.
(12) Gür, F. N.; Schwarz, F. W.; Ye, J.; Diez, S.; Schmidt, T. L. Toward Self-Assembled Plasmonic Devices: High-Yield Arrangement of Gold Nanoparticles on DNA Origami Templates. *ACS Nano* **2016**, *10*, 5374−5382.
(13) Thacker, V. V.; Herrmann, L. O.; Sigle, D. O.; Zhang, T.; Liedl, T.; Baumberg, J. J.; Keyser, U. F. DNA origami based assembly of gold nanoparticle dimers for surface-enhanced Raman scattering. *Nat. Commun.* **2014**, *5*, 3448.
(14) Kuzyk, A.; Schreiber, R.; Fan, Z.; Pardatscher, G.; Roller, E.-M.; Högele, A.; Simmel, F. C.; Govorov, A. O.; Liedl, T. DNA-based self-assembly of chiral plasmonic nanostructures with tailored optical response. *Nature* **2012**, *483*, 311−314.
(15) Yang, Y.; Wang, J.; Shigematsu, H.; Xu, W.; Shih, W. M.; Rothman, J. E.; Lin, C. Self-assembly of size-controlled liposomes on DNA nanotemplates. *Nat. Chem.* **2016**, *8*, 476−483.
(16) Czogalla, A.; Kauert, D. J.; Franquelim, H. G.; Uzunova, V.; Zhang, Y.; Seidel, R.; Schwille, P. Amphipathic DNA origami nanoparticles to scaffold and deform lipid membrane vesicles. *Angew. Chem., Int. Ed.* **2015**, *54*, 6501−6505.
(17) Livshits, G. I.; Stern, A.; Rotem, D.; Borovok, N.; Eidelshtein, G.; Migliore, A.; Penzo, E.; Wind, S. J.; Di Felice, R.; Skourtis, S. S.; Cuevas, J. C.; Gurevich, L.; Kotlyar, A. B.; Porath, D. Long-range charge transport in single G-quadruplex DNA molecules. *Nat. Nanotechnol.* **2014**, *9*, 1040−1046.
(18) Seidel, R.; Ciacchi, L. C.; Weigel, M.; Pompe, W.; Mertig, M. Synthesis of platinum cluster chains on DNA templates: Conditions for a template-controlled cluster growth. *J. Phys. Chem. B* **2004**, *108*, 10801−10811.
(19) Braun, E.; Eichen, Y.; Sivan, U.; Ben-Yoseph, G. DNA-templated assembly and electrode attachment of a conducting silver wire. *Nature* **1998**, *391*, 775−778.
(20) Mertig, M.; Ciacchi, L. C.; Seidel, R.; Pompe, W.; De Vita, A. DNA as a selective metallization template. *Nano Lett.* **2002**, *2*, 841−844.
(21) Wirges, C. T.; Timper, J.; Fischler, M.; Sologubenko, A. S.; Mayer, J.; Simon, U.; Carell, T. Controlled nucleation of DNA metallization. *Angew. Chem., Int. Ed.* **2009**, *48*, 219−223.
(22) Teschome, B.; Facsko, S.; Schönherr, T.; Kerbusch, J.; Keller, A.; Erbe, A. Temperature-Dependent Charge Transport through Individually Contacted DNA Origami-Based Au Nanowires. *Langmuir* **2016**, *32*, 10159−10165.
(23) Schreiber, R.; Kempter, S.; Holler, S.; Schüller, V.; Schiffels, D.; Simmel, S. S.; Nickels, P. C.; Liedl, T. DNA origami-templated growth of arbitrarily shaped metal nanoparticles. *Small* **2011**, *7*, 1795−1799.
(24) Liu, J.; Geng, Y.; Pound, E.; Gyawali, S.; Ashton, J. R.; Hickey, J.; Woolley, A. T.; Harb, J. N. Metallization of branched DNA origami for nanoelectronic circuit fabrication. *ACS Nano* **2011**, *5*, 2240−2247.
(25) Schreiber, R.; Do, J.; Roller, E.-M.; Zhang, T.; Schüller, V. J.; Nickels, P. C.; Feldmann, J.; Liedl, T. Hierarchical assembly of metal nanoparticles, quantum dots and organic dyes using DNA origami scaffolds. *Nat. Nanotechnol.* **2014**, *9*, 74−78.
(26) Uprety, B.; Gates, E. P.; Geng, Y.; Woolley, A. T.; Harb, J. N. Site-specific metallization of multiple metals on a single DNA origami template. *Langmuir* **2014**, *30*, 1134−1141.




DOI: 10.1021/acs.nanolett.8b00344
*Nano Lett.* 2018, 18, 2116−2123

(27) Richter, J.; Seidel, R.; Kirsch, R.; Mertig, M.; Pompe, W.; Plaschke, J.; Schackert, H. K. Nanoscale palladium metallization of DNA. *Adv. Mater.* **2000**, *12*, 507−510.
(28) Tian, C.; Cordeiro, M. A. L.; Lhermitte, J.; Xin, H. L.; Shani, L.; Liu, M.; Ma, C.; Yeshurun, Y.; DiMarzio, D.; Gang, O. Supra-Nanoparticle Functional Assemblies through Programmable Stacking. *ACS Nano* **2017**, *11*, 7036.
(29) Richter, J.; Mertig, M.; Pompe, W.; Mönch, I.; Schackert, H. K. Construction of highly conductive nanowires on a DNA template. *Appl. Phys. Lett.* **2001**, *78*, 536−538.
(30) Lund, J.; Dong, J.; Deng, Z.; Mao, C.; Parviz, B. A. Electrical conduction in 7 nm wires constructed on λ-DNA. *Nanotechnology* **2006**, *17*, 2752.
(31) Geng, Y.; Pearson, A. C.; Gates, E. P.; Uprety, B.; Davis, R. C.; Harb, J. N.; Woolley, A. T. Electrically conductive gold- and copper-metallized DNA origami nanostructures. *Langmuir* **2013**, *29*, 3482−3490.
(32) Pearson, A. C.; Liu, J.; Pound, E.; Uprety, B.; Woolley, A. T.; Davis, R. C.; Harb, J. N. DNA origami metallized site specifically to form electrically conductive nanowires. *J. Phys. Chem. B* **2012**, *116*, 10551−10560.
(33) Park, S. H.; Prior, M. W.; LaBean, T. H.; Finkelstein, G. Optimized fabrication and electrical analysis of silver nanowires templated on DNA molecules. *Appl. Phys. Lett.* **2006**, *89*, 033901.
(34) Harnack, O.; Ford, W. E.; Yasuda, A.; Wessels, J. M. Tris(hydroxymethyl)phosphine-capped gold particles templated by DNA as nanowire precursors. *Nano Lett.* **2002**, *2*, 919−923.
(35) Uprety, B.; Westover, T.; Stoddard, M.; Brinkerhoff, K.; Jensen, J.; Davis, R. C.; Woolley, A. T.; Harb, J. N. Anisotropic Electroless Deposition on DNA Origami Templates To Form Small Diameter Conductive Nanowires. *Langmuir* **2017**, *33*, 726−735.
(36) Wong, K. K.; Mann, S. Biomimetic synthesis of cadmium sulfide-ferritin nanocomposites. *Adv. Mater.* **1996**, *8*, 928−932.
(37) Balci, S.; Hahn, K.; Kopold, P.; Kadri, A.; Wege, C.; Kern, K.; Bittner, A. M. Electroless synthesis of 3 nm wide alloy nanowires inside Tobacco mosaic virus. *Nanotechnology* **2012**, *23*, 045603.
(38) Sun, W.; Boulais, E.; Hakobyan, Y.; Wang, W. L.; Guan, A.; Bathe, M.; Yin, P. Casting inorganic structures with DNA molds. *Science* **2014**, *346*, 1258361.
(39) Helmi, S.; Ziegler, C.; Kauert, D. J.; Seidel, R. Shape-controlled synthesis of gold nanostructures using DNA origami molds. *Nano Lett.* **2014**, *14*, 6693−6698.
(40) Ding, B.; Deng, Z.; Yan, H.; Cabrini, S.; Zuckermann, R. N.; Bokor, J. Gold nanoparticle self-similar chain structure organized by DNA origami. *J. Am. Chem. Soc.* **2010**, *132*, 3248−3249.
(41) Zhao, Z.; Jacovetty, E. L.; Liu, Y.; Yan, H. Encapsulation of gold nanoparticles in a DNA origami cage. *Angew. Chem., Int. Ed.* **2011**, *50*, 2041−2044.
(42) Stahl, E.; Martin, T. G.; Praetorius, F.; Dietz, H. Facile and scalable preparation of pure and dense DNA origami solutions. *Angew. Chem., Int. Ed.* **2014**, *53*, 12735−12740.
(43) Seol, S. K.; Kim, D.; Jung, S.; Chang, W. S.; Kim, J. T. One-step synthesis of PEG-coated gold nanoparticles by rapid microwave heating. *J. Nanomater.* **2013**, *2013*.110.1155/2013/531760
(44) Morris, J.; Coutts, T. Electrical conduction in discontinuous metal films: A discussion. *Thin Solid Films* **1977**, *47*, 3−65.
(45) Barwinski, B. Temperature dependence of electrical conduction in discontinuous gold films on sapphire substrates. *Thin Solid Films* **1985**, *128*, 1−9.
(46) Brust, M.; Bethell, D.; Kiely, C. J.; Schiffrin, D. J. Self-Assembled Gold Nanoparticle Thin Films with Nonmetallic Optical and Electronic Properties. *Langmuir* **1998**, *14*, 5425−5429.
(47) Douglas, S. M.; Marblestone, A. H.; Teerapittayanon, S.; Vazquez, A.; Church, G. M.; Shih, W. M. Rapid prototyping of 3D DNA-origami shapes with caDNAno. *Nucleic Acids Res.* **2009**, *37*, 5001−5006.
(48) Ke, Y.; Douglas, S. M.; Liu, M.; Sharma, J.; Cheng, A.; Leung, A.; Liu, Y.; Shih, W. M.; Yan, H. Multilayer DNA origami packed on a square lattice. *J. Am. Chem. Soc.* **2009**, *131*, 15903−15908.
(49) Hill, H. D.; Mirkin, C. A. The bio-barcode assay for the detection of protein and nucleic acid targets using DTT-induced ligand exchange. *Nat. Protoc.* **2006**, *1*, 324−336.



DOI: 10.1021/acs.nanolett.8b00344
*Nano Lett.* 2018, 18, 2116−2123

nature electronics

ARTICLES

https://doi.org/10.1038/s41928-018-0161-6

# Electronic-skin compasses for geomagnetic field-driven artificial magnetoreception and interactive electronics

Gilbert Santiago Cañón Bermúdez*, Hagen Fuchs, Lothar Bischoff, Jürgen Fassbender and Denys Makarov*

**Magnetoreception is the ability to detect and respond to magnetic fields that allows certain organisms to orientate themselves with respect to the Earth's magnetic field for navigation purposes. The development of an artificial magnetoreception, which is based solely on an interaction with geomagnetic fields and can be used by humans, has, however, proved challenging. Here we report a compliant and mechanically robust electronic-skin compass system that allows a person to orient with respect to Earth's magnetic field. The compass is fabricated on 6-μm-thick polymeric foils and accommodates magnetic field sensors based on the anisotropic magnetoresistance effect. The response of the sensor is tailored to be linear and, by arranging the sensors in a Wheatstone bridge configuration, a maximum sensitivity around the Earth's magnetic field is achieved. Our approach can also be used to create interactive devices for virtual and augmented-reality applications, and we illustrate the potential of this by using our electronic-skin compass in the touchless control of virtual units in a game engine.**

The continuing expansion of electronic devices into daily life has led to an increased interest in electronics with seamless integration schemes. Electronic skins (e-skins)[1–3], which combine sensors[4,5] and actuators[6–10] in a compliant and mechanically imperceptible[11–18] format, eliminate the need for rigid interfaces, and could simplify and enhance the interaction experience between the user and the device.

Magnetic sensors have been proposed as a way to interact with objects in a touchless manner and move beyond conventional tactile interactions. Such sensors have been applied to virtual reality systems[19–21] or to create artificial magnetoreception[22–24]. However, these approaches require the use of either cumbersome implanted rigid magnets[24] or bulky non-ergonomic equipment[19–21,23]. Flexible magnetosensitive skins[25–29], enabled by shapeable magnetoelectronics[30], could offer artificial magnetoreception in a seamless and comfortable on-skin platform, which also avoids the need for complex implantations.

A range of flexible magnetic sensors have previously been created, based on giant magnetoresistance (GMR)[25,29,31–35], spin valves[26,32], tunnelling magentoresistance (TMR)[36,37], anisotropic magnetoresistance (AMR)[38,39], magnetoimpedance (GMI)[28,40] and the Hall effect[27,41–43]. Moreover, stretchable sensors based on GMR[25,31,44] and spin valves[45,46] have also been developed. (The advantages and disadvantages of different fabrication technologies for flexible magnetic field sensors have recently been reviewed[30,47,48].) The basic building blocks of magnetosensitive e-skin technology—the emulation of pressing (proximity sensing)[25,27–29] and turning (direction sensing)[26]—have already been established. However, these magnetosensitive e-skins are still limited by the need to operate at magnetic fields in the range of millitesla, which requires the use of permanent magnets[26,30,47,48].

The ability to operate without any external magnetic biasing, and thus relying only on the geomagnetic field, would simplify the implementation of artificial magnetoreception devices on human skin. Such devices would not require any modification of the magnetic field landscape via the installation of permanent magnets to appropriately modify the magnetic field of the Earth[28,40], and could allow detection of the azimuthal rotation of the body or parts of the body. However, realizing these devices requires harnessing the geomagnetic field of about 50 μT for spatial orientation, which is out of reach for current state-of-the-art approaches in shapeable magnetoelectronics.

In this Article, we report a highly compliant e-skin compass based on geometrically conditioned anisotropic magnetoresistive (AMR) sensors, which enables the detection of geomagnetic fields. Our design results in a two orders of magnitude improvement in field detection range compared with previous magnetoresistive sensors for angle detection. High mechanical compliancy is achieved by fabricating the device on ultrathin 6-μm-thick Mylar foils, which results in a 25 times better bendability than previously reported values for flexible AMR sensors, without sacrificing sensor performance. The fabricated device exhibits high durability, withstanding two thousand bending cycles while retaining its functionality. The combination of an improved magnetic field detection range and mechanical endurance enables epidermal electronics with artificial magnetoreception, in an approach that does not require any permanent magnets and is driven by the geomagnetic field. To illustrate the capabilities of our device, we use it for human orientation in an outdoor setting and the manipulation of objects in virtual reality.

## E-skin compass fabrication and mechanical performance

To fabricate the e-skin compass we began with 6-μm-thick Mylar foils laminated to a rigid support based on polydimethylsiloxane (PDMS) coated glass slides. On the foils we deposited a sensing layer based on 50-nm-thick ferromagnetic stripes of Permalloy (Py, $Fe_{81}Ni_{19}$ alloy), capped by a 100-nm-thick gold (Au) contact and conditioning layer (Fig. 1a and Supplementary Figure 1). The

Helmholtz-Zentrum Dresden-Rossendorf e.V., Institute of Ion Beam Physics and Materials Research, Dresden, Germany. *e-mail: g.canon-bermudez@hzdr.de; d.makarov@hzdr.de

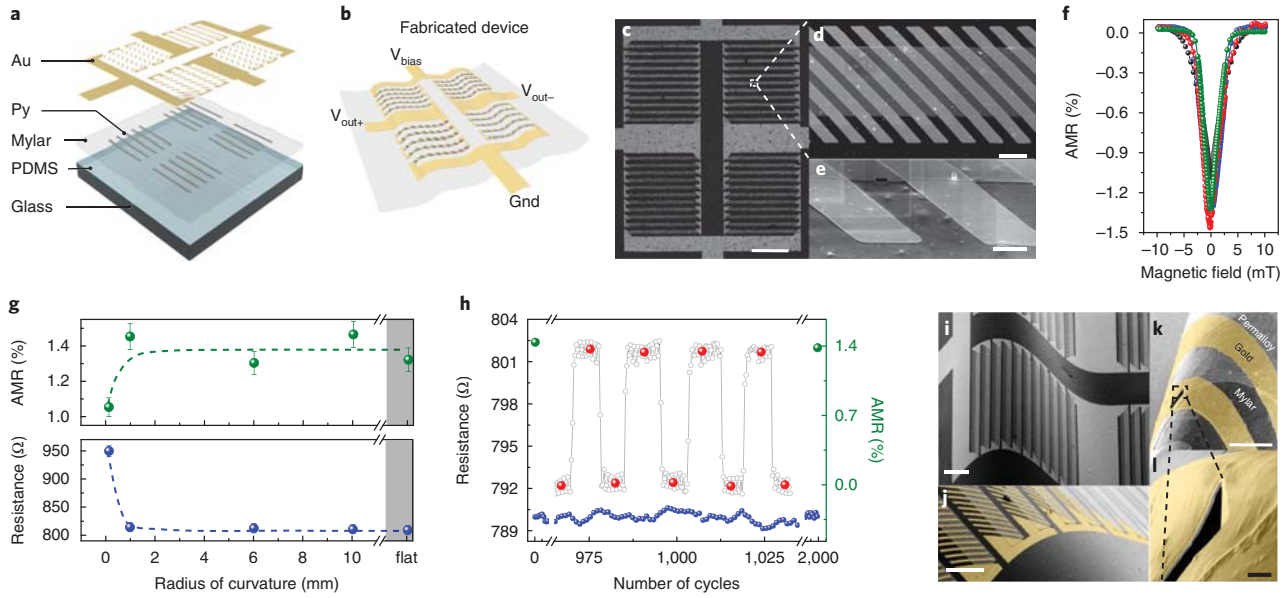


**Fig. 1 | Fabrication and mechanical performance of the e-skin compass. a**, Fabrication process of the e-skin compass. **b**, Schematic of the device after fabrication and connection layout. **c**, Optical micrography of the fabricated device. Scale bar, 500 µm. **d**,**e**, Close-up SEM images of the upper-right meander of the device. Scale bars, 20 and 5 µm, respectively. **f**, AMR response of a single meander bent to different radii of curvature (150 µm in black, 6 mm in blue, 10 mm in red and flat state in green). **g**, AMR effect and nominal resistance for a single meander as a function of the radius of curvature. The dots represent the experimental data with its respective error bars and the dashed lines are a guide to the eye. The error bars represent the RMS noise level. **h**, AMR performance and resistance change of a single meander as a function of the number of bending cycles. The blue dots represent the resistance variation upon mechanical cycling without a magnetic field. The inset with black open circles depicts the resistance change when an external magnetic field is applied (plateaus) during mechanical cycling. The red dots are introduced to highlight the average values at the baseline (no magnetic field) and the plateaus (with a magnetic field). **i**,**j**, SEM close-up images of the e-skin compass under a bending radius of 200 µm. Scale bars, 100 µm for both images. **k**,**l**, SEM images and FIB cross sectional cut of the e-skin compass under a bending radius of 10 µm. Scale bars, 10 and 1 µm, respectively.

layout of the compass was designed as a full Wheatstone bridge where each of the four elements is a geometrically conditioned AMR sensor based on Py meander stripes (Fig. 1b–e).

To evaluate the performance of the Py sensing layer on ultrathin foils, we measured the AMR response of single meanders under different radii of curvature down to 150 µm (Fig. 1f). The AMR effect remains unchanged at about 1.4% until 150 µm bending radius, when it decreases slightly to about 1.1% (Fig. 1g, upper panel). This change was accompanied by an increase in the electrical resistance, which suggests there might be some cracking involved as the Py film approaches its fracture strain (Fig. 1g, lower panel). This is at least one order of magnitude boost in bendability compared to AMR sensors prepared on thicker substrates[38,39]. To examine the effects of dynamic bending, we carried out cyclic bending tests, where a single meander sensor is repeatedly bent from its flat state up to a radius of curvature 1 mm for 2,000 cycles. The AMR response remains stable at about 1.4% even after 2,000 bending cycles. At the same time the change of the electrical resistance of the sensor due to mechanical deformations does not exceed 0.2% (Fig. 1h).

To assess the impact of mechanical deformations on the functional layer stack of the e-skin compass, we studied the morphology and integrity of its functional layers using scanning electron microscopy (SEM) imaging of the top surface of the devices but also of the cross-sectional cuts realized via focused ion beam (FIB) etching. The e-skin compass does not experience any film damage even for radii of curvature as low as 200 µm (Fig. 1i,j). This is about an order of magnitude smaller compared to previous reports on flexible AMR sensors prepared on 100-µm-thick foils[39]. This superior bendability of e-skin compasses is enabled by using ultrathin foils, which reduce the effective strain in the functional layers of the device[12,18,25,49]. The analytical calculations (described in Methods) allow us to estimate a minimum bending radius of 100 µm before reaching the critical strain in the layer stack. This prediction agrees with the experimental data, as occasional fracturing is observed when the sample is bent to a radius of below 100 µm (Fig. 1k, Supplementary Fig. 2), also correlated with an increase of the sample resistance. Investigating the cross-section within the crack region reveals that even in these extremely bent areas of the device, the integrity of the functional layers is preserved, and no delamination can be perceived (Fig. 1l). Another advantage of the reduced thickness of the sensor on ultrathin films is the diminished stress (1.25% at 150 µm bending radius) on the metal layer. This is caused by the rather close positioning of the neutral mechanical plane to the magnetic film (1.8 µm below). With thicker foils of about 100 µm in thickness, the distance to the neutral mechanical plane is up to 30 times larger, which would also mean a 30-fold increase in the strain at the functional sensing layer (further details are in the Methods section). Furthermore, if an encapsulation layer of about 6 µm were to be included, the strain at the layer could be nulled by placing the sensing layer exactly at the neutral mechanical plane.

## Conditioning and magnetoelectric characterization

The AMR sensors can detect magnetic fields with strengths in the region of 1 mT, which is much greater than Earth's magnetic field (50 µT). However, after geometric conditioning with slabs of gold oriented at 45° or 135° with respect to the long axis of the sensor stripes, the sensor response becomes linearized around zero field and the geomagnetic field can be detected (Fig. 2a). This type

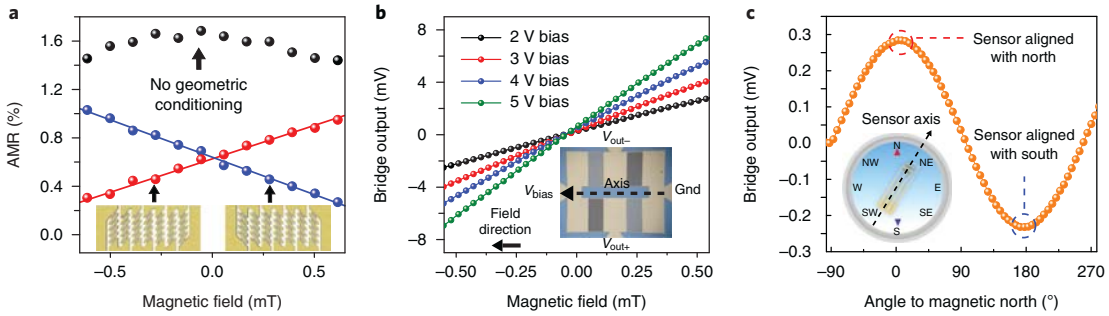


**Fig. 2 | Magnetoelectric characterization of the e-skin compass. a**, Comparison of the AMR response of meander sensors with (red and blue) and without (black) geometric conditioning. **b**, Bridge output voltage as a function of the magnetic field applied along the sensor axis. **c**, Bridge output voltage as a function of the angle of the sensor axis to the magnetic north.

of conditioning is known as the barber pole method, which is the industry standard approach for AMR sensor conditioning[50–52]. Furthermore, by controlling the orientation angle of the slabs, the sensor response can have a positive (for slabs oriented at 45°) or negative (for slabs oriented at 135°) slope (Fig. 2a).

We combine both slab orientations within the same branch of a Wheatstone bridge to maximize the thermal stability and signal output range of the bridge. Optimizing the response of the bridge requires tailoring its geometrical parameters (slab separation, stripe length and stripe width) (Supplementary Fig. 3a) and tuning its bias voltage (Fig. 2b). From our experiments, we determined an optimal stripe width of 50 µm, a slab separation of 10 µm and a bias voltage of 1 V to ensure a compromise between sensitivity, linear range and output stability. With these parameters we achieved a single sensor sensitivity of 0.54% $mT^{-1}$ in the geometrically conditioned case (Fig. 2a). On arranging the sensors in a Wheatstone bridge configuration, the device operates as a compass and allows the detection of the Earth's magnetic field.

To evaluate the capabilities of the e-skin compass to detect Earth's magnetic field, we designed an experiment where the compass was rotated and isolated from all non-geomagnetic sources (Fig. 2c and Supplementary Fig. 4c,d). Then we monitored the compass output voltage as a function of the angle between its sensing axis and magnetic north. As can be seen in Fig. 2c, the output voltage follows a sinusoidal wave pattern with a maximum when the sensor directly aligns with north (verified by a reference compass) and a minimum when it points south. This behaviour indicates that the signal detected corresponded to the geomagnetic field. However, we performed additional experiments to further discriminate the signal due to the Earth's magnetic field from possible spurious signals. We studied the effect of rotational offsets (Supplementary Fig. 5) and external biasing fields (Supplementary Fig. 6). In all cases we could successfully reconstruct the magnitude and orientation of the geomagnetic field, thereby confirming the veracity of our measurements. From all detection events, a peak-to-peak voltage of 496 µV can be determined, which defines the available voltage range for encoding 180° and yields an angular sensitivity of 2.5 µV °$^{-1}$. The effective resolution of the device is ultimately limited by the noise, which was measured to be 0.9 $\mu V_{RMS}$. Assuming a detection margin of twice the noise (that is, 1.8 µV), the resolution of the e-skin compass is about 0.7°, which is of the same order of magnitude as commercial rigid compasses[52]. In addition, thermal drift effects were found not to hinder the performance of the sensor, as the effective field detection limit was found to be less than 50 nT (further information is given in Methods). Overall, these results represent a two orders of magnitude improvement in the field detection range over previous e-skin angle sensors[26]. Furthermore, in contrast to magnetoimpedance (MI) based flexible sensors[40], the e-skin compass does not require any external biasing magnetic field and operates at 1 mA direct current.

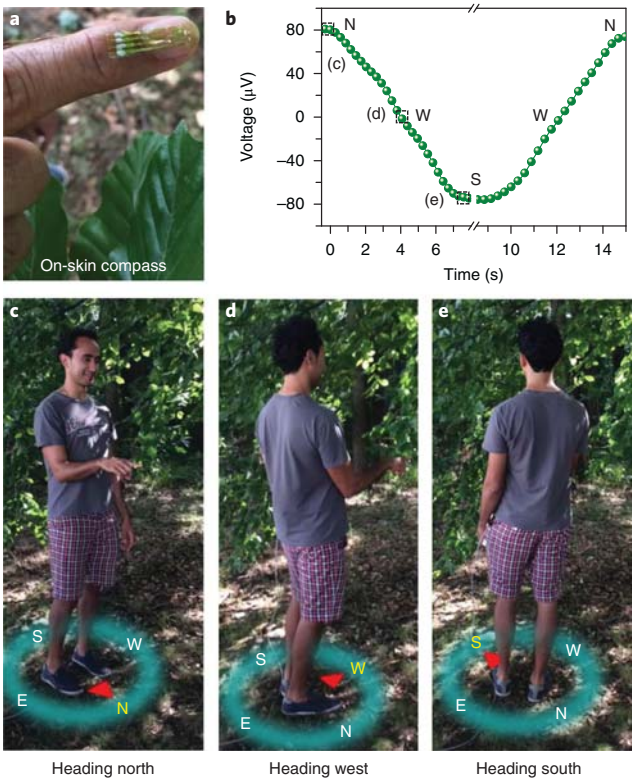


**Fig. 3 | Outdoor geomagnetic detection. a**, E-skin compass attached to the finger of a person. **b**, Time evolution of the output voltage of the e-skin compass when the person rotates back and forth from the magnetic north (N) to magnetic south (S) via west (W). **c**–**e**, Snapshots of Supplementary Video 4 showing the instants when the person points to N, W and S. A compass rose dial with the cardinal points is overlaid on the snapshots to signal the corresponding orientations.

## E-skin compass rose

To demonstrate artificial magnetoreception with the e-skin compass, it is important to investigate its ubiquitous navigation capabilities. Therefore, we devised an open-air experiment where the

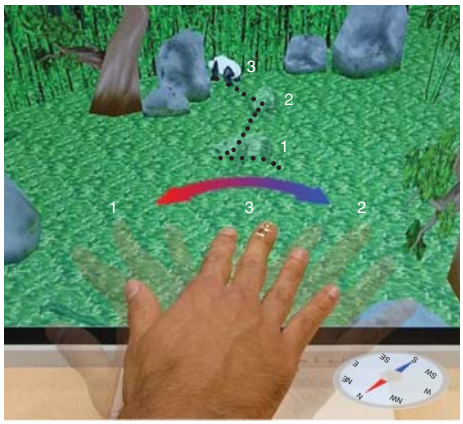


**Fig. 4 | Geomagnetic interaction with a virtual reality environment.** Control of the trajectory of a virtual character (panda) by hand motion in the geomagnetic field. Moving the hand closer to magnetic north (to the left) commands the panda to face left (1). An opposite movement to the right directs the panda towards the screen (2). A hand motion to the centre steers the panda slightly to the left at an angle in between the first two orientations (3).

compass was attached to a person's index finger to indicate his current orientation (Fig. 3a and Supplementary Fig. 7).

Then, the person rotated his body within the geomagnetic field and the compass output voltage was read out by a data acquisition box connected to a laptop computer for visualization. Throughout the experiment, the finger was kept parallel to the ground to read only the in-plane component of the field. The rotation was performed back and forth between magnetic north (N) and south (S) via west (W), with all the orientations being verified by a reference compass and recorded in a video (Fig. 3b and Supplementary Video 4). From the video we selected several representative frames (N, S and W), which are shown in Fig. 3c–e together with a superimposed dial indicating the current heading of the person. These results show an on-skin device that can replicate the functionality of a compass and enable artificial magnetoreception for humans.

## Geomagnetic virtual reality control

Another application area where we envisage the potential of the e-skin compass is augmented or virtual reality (VR). In this case, the e-skin compass will act as a mechanically compliant interactive input device capable of directly translating the real world magnetoreception into the virtual realm. To evaluate the functionality of the e-skin compass within a virtual reality environment, we set up an experiment where we used the output voltage of the compass to control the orientation of a virtual panda inside Panda3D, a Python-based game engine[53]. First, the compass was placed on a person's middle finger to define an axis of directionality. Next, the panda was commanded to move forward at a constant speed within a program, while its rotation angle was given by the movement of the person's hand in the geomagnetic field (Supplementary Fig. 8). By moving the axis of directionality, the person could control at will the trajectory of the panda in the virtual environment without the aid of any permanent magnet or optical sensory system, as typically used in VR applications. The entire experiment was recorded in a video (Supplementary Video 5) from which we selected and superimposed three representative frames, as shown in Fig. 4. On the lower right, a compass drawing is included to indicate the physical location of north during the experiment.

Here, the trajectory of the panda is highlighted as a dotted line and the frames of interest are correspondingly labelled from 1 to 3. In the first frame (1), the person moved his hand to the left, moving closer to magnetic north and thereby orientating the panda to the left of the screen. In the following frames, the hand swung back to the right, towards magnetic south (2), and then came back to the centre at a neutral position (3). In each case the virtual panda correspondingly rotated within its local reference axis, going into the screen and then diagonally towards the left to reach its final position. These results showcase an on-skin, entirely compliant gadget able to manipulate a virtual object in a geomagnetic field.

## Conclusions

We have developed a highly compliant e-skin compass capable of detecting geomagnetic fields (40–60 μT) with no loss of functionality even under bending to a radius of 150 μm. The sensitivity to geomagnetic fields was attained by geometrically conditioning AMR sensors and arranging them in a Wheatstone bridge configuration. High compliancy and mechanical performance were accomplished by using ultrathin foils as a carrier substrate, thereby reducing the effective strain on the functional layers. By combining the device with a game engine, we created a virtual reality environment driven by the motion of a hand in the geomagnetic field. Furthermore, we demonstrated the use of the e-skin compass as an on-skin tag that allows a person to orient outdoors using the geomagnetic field. We envisage that this e-skin compass could enable humans to electronically emulate the magnetoceptive sense, which some mammals possess naturally[54], allowing us to orientate with respect to Earth's magnetic field in any location.

Our e-skin compass is based on the AMR effect. However, the proposed technology can be readily extended to other magnetic field sensors, and flexible sensor concepts such as giant magnetoimpedance[40] or the Hall effect[41]. These approaches can boost the performance of an e-skin compass system by further increasing its sensitivity (giant magnetoimpedance) and allowing out-of-plane magnetic field detection (Hall effect).

## Methods

**E-skin compass fabrication.** Glass slides of 22 × 22 mm² (VWR International) were spin coated with Polydimethylsiloxane (PDMS, Sylgard 184, ratio 1:10) at 4,000 r.p.m. for 30 s and cured at 100 °C for 45 min. Separately, a 3D printed polylactic acid (PLA) frame covering an area of 80 × 50 mm² was used to prestretch 6-μm-thick Mylar (Chemoplex) foils by means of adhesive stripes on the frame edges. After prestretching, the PDMS-coated glasses were flipped over, carefully pressed over the prestretched foil and cut by the edges with a scalpel for release. The resulting Mylar-covered glasses were used as substrates for preparing the e-skin compass devices (Supplementary Fig. 1a).

Photolithography was performed over the Mylar foils using S1813 (Shipley, UK) photoresist spun at 4,000 r.p.m. for 30 s and cured at 110 °C for 2 min. After curing, the photoresist films were exposed using a direct laser writer (DWL66, Heidelberg Instruments) and developed for 30 s in MF319 (Microposit) developer. Following the development process, 50-nm-thick films of Permalloy (Py) were deposited on the samples by e-beam evaporation (pressure: $1 \times 10^{-8}$ mbar, rate: 0.3 Å $s^{-1}$). The unwanted parts were lifted-off in a remover 1165 (Microposit) solution to define stripe patterns of Py with a width of 50 μm on the Mylar foils. Next, a second lithographic step with the same parameters was performed to define the electrical contacts and barber pole slabs of the compass. During this step, a 5-nm-thick adhesion layer of titanium (Ti) was evaporated (pressure: $3.1 \times 10^{-8}$ mbar, rate: 0.3 Å $s^{-1}$) followed by a 100-nm-thick layer of gold (Au) (pressure: $4 \times 10^{-8}$ mbar, rate: 3 Å $s^{-1}$).

**Compass design and geometric conditioning optimization.** The compass was devised as a combination of single AMR sensors made of ferromagnetic thin films of Permalloy (Py). Each of these sensors was designed as a meander structure to achieve, within the most compact footprint possible, the highest aspect ratio between the total length of the meander and its width. This methodology improves the immunity to noise of the sensor by increasing its initial resistance and can extend its linear range by introducing a shape anisotropy, which is observed when the stripe width decreases below 50 μm. For AMR sensors to be useful for compass applications, they have to be geometrically conditioned using the barber pole method[50,52,55]. In this method, the stripes of ferromagnetic material are covered with slabs of a conductive material (Au in our case), which are oriented at 45° with respect to the easy axis of the Py stripes. By performing this modification, the current is forced to flow at 45° within the stripe, which effectively linearizes the

AMR response of the sensor around zero magnetic field. This linearization has the effect of noticeably increasing the sensitivity of the sensor for small fields (less than 1 mT) while also giving it the ability to identify the sign of the field applied. These characteristics are ideal to reliably detect the Earth's magnetic field.

To find the most suitable barber pole geometry for our purposes, we studied the effect of certain geometrical parameters on the overall sensor response. First, we checked how the separation between the slabs influences the sensor output. It was found that the linearization effect arose only at separations of 10 µm (for the case of 50-µm-wide Py stripes). Larger separations between slabs showed very little or no linearization effect. This can be attributed to the fact that at larger separations, the portion of the current, which effectively flows skewed, is greatly reduced (Supplementary Fig. 3b).

Next, we explored how the width of the ferromagnetic stripes changed the overall sensor response. For this purpose, we prepared meanders with stripe widths of 20, 30, 40 and 50 µm and monitored their AMR characteristics. It was observed that as the width of the Py stripes decreased, the linear range increased from ±1 mT at 50 µm up to ±2 mT at 20 µm. However, as the linear range increased, the sensitivity decreased from 0.54 % mT$^{-1}$ at 50 µm down to 0.26% mT$^{-1}$ at 20 µm. As the sensitivity is a more relevant parameter for the compass, we chose a stripe width of 50 µm for the main set of experiments.

Following this optimization, we combined four single meanders into a full Wheatstone bridge to compensate for any thermal effects intrinsic to the metallic nature of Py. In addition, this configuration provided a way to control the bridge output sensitivity by tuning the bias voltage $V_{bias}$ of the bridge ($S_{WB} = V_{bias}S_S$, where $S_{WB}$ is the sensitivity of the bridge and $S_S$ is the sensitivity of a single sensor). In the case of a bridge with 20-µm-wide stripes with a single sensor sensitivity of 0.26% mT$^{-1}$, the output sensitivity can be tuned from 5 µV µT$^{-1}$ at a bias of 2 V, up to 13 µV µT$^{-1}$ at a bias of 5 V (Fig. 2b). Bias voltages below 2 V improve the device performance by avoiding thermal drift in the output due to the increased current density.

To quantify this drift, we calculated the intrinsic thermal (Johnson) noise for the bridge with an output resistance of 1 kΩ at a temperature of 300 K:

$$\frac{V_n}{\sqrt{\Delta f}} = \sqrt{(4k_B TR)} = 4.06\frac{\text{nV}}{\sqrt{\text{Hz}}}.$$

However, the effective thermal noise of our measurements is given by that of the read-out electronics, since it is significantly larger than that of the sensor (55 nV/$\sqrt{\text{Hz}}$). Next, we measured the output voltage noise over 50,000 samples and converted it to the frequency domain via fast Fourier transform (FFT). From the frequency plot we determined the corner frequency of the measurement to be about 20 Hz (Supplementary Fig. 9). Using this frequency, the previously determined output sensitivity of 5 V T$^{-1}$ @ 2 V and the Johnson noise value for the electronics, the detection limit was found to be 49 nT. Introducing low-noise electronics (about 15 nV/$\sqrt{\text{Hz}}$) would further enhance the limit of detection of our device to 13 nT.

**Characterization set-up (linear regime).** The magnetic response of the compass was characterized using a pair of Helmholtz coils (LBL Lehrmittel) with a spacing of 5.5 cm to ensure uniformity of the magnetic field. The coil was powered by a bipolar power supply (Kepco). A Keysight 34461 A (Keysight Technologies) tabletop multimeter was used for collecting the resistance and output voltage of the samples, respectively. A magnetic field sweep was carried out to determine the linear operation range of single sensors by setting the field at an angle of 90° with respect to their magnetic easy axis. Then, the same set-up and methodology were employed to characterize the response of the full Wheatstone bridge within its linear regime under different bias voltages from 1 to 5 V provided by a B2902A Source Measure Unit (Keysight Technologies). Prior to all measurements, the magnetic field inside the coils was measured with a HG09 gaussmeter (Goudsmith Magnetic Systems) for different bias currents to derive a calibration curve. The calibration curve was used during the measurements to determine the strength of the applied magnetic field.

**Validation of geomagnetic field sensing.** Three distinct tests were carried out to verify that the e-skin compass detects the geomagnetic field. Test 1 (Rotation within Earth's magnetic field): As an initial detection test, the e-skin compass was placed on a cylindrical sample holder (radius 35 mm, height 30 mm) which was attached to a ruler and manually rotated in the presence of the geomagnetic field only. During the rotation process, the voltage output of the compass was recorded to determine the orientations at which the maxima and minima arise. These angular positions are assigned to the north and south poles of the geomagnetic field, respectively, as they arise with a phase shift of exactly 180°. Furthermore, the angular positions coincided with magnetic north as shown by a smartphone compass app (Compass, Gabenative, Sony Xperia Z5) used as a reference (Supplementary Fig. 4d and Supplementary Video 1). To precisely determine the angular response and the resolution of the e-skin compass, we replaced the mechanical pivot with a rotating stage driven using a stepper motor (Eckstein). The set-up was applied to continuously rotate the samples in the geomagnetic field for up to two complete turns. The control of the set-up was realized using LabVIEW 2015 software (National Instruments). The samples were positioned 3 cm above the end of the stepper motor's shaft to ensure that there were no disturbances stemming from the in-plane component of the magnetic field generated by the motor during the measurements. The collected curves were further analysed to determine the angular resolution of the compass (Fig. 2 and Supplementary Fig. 4c).

Test 2 (Initial offsetting): To determine if the peak response detected by the e-skin compass always arises at the same geographical location (angular position), the initial orientation of the sensor axis was shifted 90° and −90° with respect to the starting configuration (−108° to magnetic north), as shown in Supplementary Fig. 5 and Supplementary Video 2. For each case (0°, 90° and −90°), the sample was rotated for two complete turns and the output voltage was recorded. The acquired data was used to evaluate the phase shift of the signals. The summary of the data is shown in Supplementary Fig. 5. The extrema at the measured three curves are phase shifted accordingly to the offset angle.

Test 3 (Geomagnetic field reconstruction via vector subtraction): To determine if the detected output voltage peaks univocally correspond to the geomagnetic field, we introduced an external biasing magnetic field $H_{coil}$ of 43 µT using a Helmholtz coil and measured the resulting output voltage $V_{meas}$ (Supplementary Fig. 6 and Supplementary Video 3). From this voltage, we calculated the detected magnetic field from the bridge sensitivity given by: $S_{WB} = V_{bias}S_S$, in our case, with $V_{bias} = 1$ V and $S_S = 0.54\%$ mT$^{-1}$, $S_{WB} = 5.4$ mV mT$^{-1}$. Using this sensitivity and the linear relationship between voltage $V$ and field $H$ in the sensor ($V = SH$), we calculated the measured field $H_{meas}$ from the peak voltage of $V_{meas}$ (68.91 µV), which yields 12.76 µT. Then, by subtracting the coil's magnetic field vector $H_{coil}$ from the measured vector $H_{meas}$, we determined a reconstructed field $H_{rec}$ as (Supplementary Figure 6b):

$$|H_{rec}| = \sqrt{H_{meas}^2 + H_{coil}^2} = 44.85\mu\text{T},\ H_{rec}\angle = \tan^{-1}\left(\frac{H_{coil}}{H_{meas}}\right) = 73.47^\circ,$$

where $|H_{rec}|$ is the magnitude of the reconstructed vector and $H_{rec}\angle$ its angle with respect to the sensor axis. These two values quantitatively correspond to those measured by the nearby reference compass.

As a further confirmation step, we repeated the measurement in the absence of an external biasing magnetic field. In this case, the measured peak voltage $V_{meas}$ was 242.78 µV, which, using the same sensitivity as above, translated into a measured field $H_{meas}$ of 44.95 µT (Supplementary Fig. 6c). This value closely agrees with the reconstructed value obtained before. Furthermore, by using the temporal shift between $V_{meas}$ with the coil on and $V_{meas}$ with the coil off, we estimated the angle between both vectors. This was realized by determining the time needed for a 180° turn to be completed (13.35 s) and comparing this time with the temporal shift between the detection peaks in the on and off cases (5.283 s). The ratio of these two quantities multiplied by 180 gives an estimate of the angle between detection events (71.21°); in close agreement with the previously reconstructed angle $H_{rec}\angle$.

**Mechanical characterization.** Static: Py meander sensors with a stripe width of 150 µm were used as test structures to probe the stability of the AMR sensing layer under static bending. The meanders were placed between the pole shoes of an electromagnet and mounted on differently curved sample holders with radii of curvature ranging from 150 µm to 10 mm. To ensure a uniform field in the sensing plane, the sensors were mounted with their curvature axes perpendicular to the pole shoe axes. The magnetic field of the electromagnet was swept between −10 and 10 mT and the AMR response of the sensors was simultaneously recorded.

Dynamic: The mechanical characterization of the functional AMR layer of the e-skin compass was performed using a motorized stage (controlled via a LabVIEW software) driven with a stepper motor (Eckstein). For the bending trials, the sample was laminated on a 5-µm-thick PDMS film (10 mm × 50 mm) and fixed to the frame of the motorized stage using a pair of clamps. One bending cycle was defined as bending the sample from its initial flat state to a bent state with a radius of 1 mm and back to its initial position (Supplementary Fig. 10a). Using these settings, two types of experiment were performed: one with an external magnetic field and the second one without. For the experiment without an external magnetic field, the sample was repeatedly bent for 2,000 cycles and its resistance was monitored using a multimeter (model Keysight 34461 A; Keysight Technologies). The acquired resistance was used to determine the mechanical stability of the electrical resistance under cyclic deformations. For the experiment with an applied external magnetic field, all conditions were the same as indicated above, but a neodymium magnet was periodically brought near the sensor with an in-plane configuration during the cycling procedure (Supplementary Video 6). The collected resistance data in this experiment allowed us to compare the resistance change under mechanical deformations with that caused by the presence of the magnetic field (Supplementary Fig. 10b).

Theoretical insight: The bending experiments on AMR layers were validated with a theoretical model for strain in curved thin film electronics:[49]

$$\varepsilon_{top} = \frac{(t_f + t_s)}{2R}\frac{(1 + 2\eta + \chi\eta^2)}{(1+\eta)(1+\chi\eta)},$$

where $\varepsilon_{top}$ is the strain of a rigid film (Young's modulus: $E_f$, thickness $t_f$) on a softer substrate (Young's modulus: $E_s$, thickness $t_s$) when bent down to a radius $R$. The

factors $\eta = t_f/t_s$ and $\chi = E_f/E_s$ define the geometric and mechanical ratios between film and substrate. For the Mylar foil in this work, the corresponding parameters are $E_s = 5$ GPa and $t_s = 6$ µm and for the compass sensing layer $E_f = 119$ GPa and $t_f = 150$ nm.

Applying this model and considering the minimum experimentally measured bending radius of 150 µm, we calculated a maximum strain at the compass layer of 1.33%. This estimate is near the fracture strain (2%) for thin films of Py[56]. This threshold defines a minimum theoretical bending radius of 100 µm.

For comparison purposes, if we increase the thickness of the Mylar foil to that of a commercially available polyethylene terephthalate (PET) foil (100 µm) keeping $R = 150$ µm, the resulting strain increases to 32%, a value that would certainly induce cracking in the metallic film. These calculations further emphasize the importance of reducing the substrate thickness to improve the overall mechanical performance of flexible sensors.

Additional mechanical calculations were performed according the model given by Jeong et al.[57] to determine the position of the neutral mechanical plane of the AMR sensors:

$$b = \frac{\sum_{i=1}^{n} E_i t_i \left( \sum_{j=1}^{i} t_j - \frac{t_i}{2} \right)}{\sum_{i=1}^{n} E_i t_i}$$

$$\bar{E}_i = \frac{E_i}{1 - \nu_i^2}$$

where $E_i$, $t_i$ and $\nu_i$ are the Young's modulus, thickness and Poisson's ratio of the layer $i$ in the stack of layers comprising the sensor. $b$ is the height from the bottom of the stack (Mylar foil) at which the mechanical neutral plane is found in the multilayer system. The system was considered to have two layers: the Mylar foil ($E_1 = 5$ GPa, $\nu_{1=}0.38$) and the compass layer (Py + Au, $E_2 = 119$ GPa, $\nu_{2=}0.33$). With these parameters, the mechanical neutral plane is located 4.2 µm above the bottom of the stack, 1.8 µm below the compass layer. The calculated strain in this situation with a distance $\delta = 1.8$ µm from the neutral plane to the metallic layer is defined by $\varepsilon = \frac{\delta}{r} = 1.25\%$, with a radius of curvature of $r = 150$ µm.

**On-skin geomagnetic orientation in the outdoors.** A demonstrator was devised, where the e-skin compass was mounted on a person's index finger while walking outdoors. The device is used to orient the person in the geomagnetic field. During the experiment, the e-skin compass was connected to and powered by a NI-USB 6211 data acquisition box (National Instruments) interfaced with a laptop running a LabVIEW program. The software is used for visualizing the collected output voltage both as a trace and as an on-screen virtual compass indicator. The measurements were performed at the coordinates 51.061851° N, 13.950389° E with the set-up shown in Supplementary Fig. 7 and the computer screen facing northeast (Supplementary Video 4). Two cameras were used to film the experiment: the first one recorded the laptop screen and a close-up of the person's motion, while the second one recorded the full body motion of the person.

**Virtual reality based on the geomagnetic field.** As a demonstrator for this concept, we designed an experimental set-up where the e-skin compass was conformably attached to a person's hand and interfaced to a computer using a NI-USB 6211 data acquisition box. On the computer side, the acquired data was processed in LabVIEW and then read by a Python script. The script calls the Panda3D (Disney/ Carnegie Mellon) game engine for Python and C++, which used the incoming compass data to correspondingly control the orientation of an animated panda on-screen. A Python script commanded the virtual panda to move forward at a constant speed and the angular rotation was determined by the angle of the hand relative to magnetic north. This angle was attained by encoding the output voltage of the e-skin compass between 0 and 180°, with magnetic north (0°) corresponding to a hand rotation towards the left of the screen. Sequential movement of the hand was used to move the panda within a defined trajectory in the virtual environment (Supplementary Fig. 8 and Supplementary Video 5).

## Data availability

The data that support the plots within this paper and other findings of this study are available from the corresponding author upon reasonable request.

Received: 11 August 2018; Accepted: 9 October 2018;
Published online: 12 November 2018

## References

1. Someya, T. et al. A large-area, flexible pressure sensor matrix with organic field-effect transistors for artificial skin applications. *Proc. Natl Acad. Sci. USA* **101**, 9966–9970 (2004).
2. Kim, D.-H. et al. Epidermal electronics. *Science* **333**, 838–843 (2011).
3. Bauer, S. et al. 25th Anniversary Article: A soft future: From robots and sensor skin to energy harvesters. *Adv. Mater.* **26**, 149–162 (2014).
4. Lee, S. et al. A transparent bending-insensitive pressure sensor. *Nat. Nanotech.* **11**, 472–478 (2016).
5. Ren, X. et al. A low-operating-power and flexible active-matrix organic-transistor temperature-sensor array. *Adv. Mater.* **28**, 4832–4838 (2016).
6. Hines, L., Petersen, K., Lum, G. Z. & Sitti, M. Soft actuators for small-scale robotics. *Adv. Mater.* **29**, 1603483 (2017).
7. Carpi, F. et al. Standards for dielectric elastomer transducers. *Smart Mater. Struct.* **24**, 105025 (2015).
8. Gisby, T. A., O'Brien, B. M. & Anderson, I. A. Self sensing feedback for dielectric elastomer actuators. *Appl. Phys. Lett.* **102**, 193703 (2013).
9. Anderson, I. A., Gisby, T. A., McKay, T. G., O'Brien, B. M. & Calius, E. P. Multi-functional dielectric elastomer artificial muscles for soft and smart machines. *J. Appl. Phys.* **112**, 041101 (2012).
10. Miriyev, A., Stack, K. & Lipson, H. Soft material for soft actuators. *Nat. Commun.* **8**, 596 (2017).
11. Choi, M. K. et al. Extremely vivid, highly transparent, and ultrathin quantum dot light-emitting diodes. *Adv. Mater.* **30**, 1703279 (2018).
12. Someya, T., Bauer, S. & Kaltenbrunner, M. Imperceptible organic electronics. *MRS Bull.* **42**, 124–130 (2017).
13. Kim, J. et al. Ultrathin quantum dot display integrated with wearable electronics. *Adv. Mater.* **29**, 1700217 (2017).
14. Miyamoto, A. et al. Inflammation-free, gas-permeable, lightweight, stretchable on-skin electronics with nanomeshes. *Nat. Nanotech.* **12**, 907–913 (2017).
15. Lei, T. et al. Biocompatible and totally disintegrable semiconducting polymer for ultrathin and ultralightweight transient electronics. *Proc. Natl Acad. Sci. USA* **114**, 5107–5112 (2017).
16. Nawrocki, R. A., Matsuhisa, N., Yokota, T. & Someya, T. 300-nm imperceptible, ultraflexible, and biocompatible e-skin fit with tactile sensors and organic transistors. *Adv. Electron. Mater.* **2**, 1500452 (2016).
17. Kaltenbrunner, M. et al. Flexible high power-per-weight perovskite solar cells with chromium oxide–metal contacts for improved stability in air. *Nat. Mater.* **14**, 1032–1039 (2015).
18. Kaltenbrunner, M. et al. An ultra-lightweight design for imperceptible plastic electronics. *Nature* **499**, 458–463 (2013).
19. Electromagnetic tracking systems. *Polhemus* https://polhemus.com/applications/electromagnetics/ (accessed 11 June 2018).
20. 3DCoilCube – Electromagnetic VR motion tracking sensors. *Premo* https://3dcoil.grupopremo.com/ (accessed 11 June 2018).
21. OMMO. *OMMO* https://www.ommo.co/ (accessed 11 June 2018).
22. Monks, K. Forget wearable tech, embeddable implants are already here. *CNN* (9 April 2014); https://go.nature.com/2AnXjlf
23. North Paw. *Sensebridge* https://sensebridge.net/projects/northpaw/ (accessed 11 June 2018).
24. Biomagnets. *Dangerous Things* https://dangerousthings.com/biomagnets/ (accessed 11 June 2018).
25. Meltzer, M. et al. Imperceptible magnetoelectronics. *Nat. Commun.* **6**, 6080 (2015).
26. Cañón Bermúdez, G. S. et al. Magnetosensitive e-skins with directional perception for augmented reality. *Sci. Adv.* **4**, eaao2623 (2018).
27. Melzer, M. et al. Wearable magnetic field sensors for flexible electronics. *Adv. Mater.* **27**, 1274–1280 (2015).
28. Alfadhel, A. & Kosel, J. Magnetic nanocomposite cilia tactile sensor. *Adv. Mater.* **27**, 7888–7892 (2015).
29. Münzenrieder, N. et al. Entirely flexible on-site conditioned magnetic sensorics. *Adv. Electron. Mater.* **2**, 1600188 (2016).
30. Makarov, D., Melzer, M., Karnaushenko, D. & Schmidt, O. G. Shapeable magnetoelectronics. *Appl. Phys. Rev.* **3**, 011101 (2016).
31. Melzer, M. et al. Stretchable magnetoelectronics. *Nano. Lett.* **11**, 2522–2526 (2011).
32. Parkin, S. S. P. Flexible giant magnetoresistance sensors. *Appl. Phys. Lett.* **69**, 3092–3094 (1996).
33. Uhrmann, T. et al. Magnetostrictive GMR sensor on flexible polyimide substrates. *J. Magn. Magn. Mater.* **307**, 209–211 (2006).
34. Chen, Y. et al. Towards flexible magnetoelectronics: Buffer-enhanced and mechanically tunable GMR of Co/Cu multilayers on plastic substrates. *Adv. Mater.* **20**, 3224–3228 (2008).
35. Pérez, N. et al. High-performance giant magnetoresistive sensorics on flexible Si membranes. *Appl. Phys. Lett.* **106**, 153501 (2015).
36. Barraud, C. et al. Magnetoresistance in magnetic tunnel junctions grown on flexible organic substrates. *Appl. Phys. Lett.* **96**, 072502 (2010).
37. Bedoya-Pinto, A., Donolato, M., Gobbi, M., Hueso, L. E. & Vavassori, P. Flexible spintronic devices on Kapton. *Appl. Phys. Lett.* **104**, 062412 (2014).
38. Griesbach, T., Wurz, M. C. & Rissing, L. Design, fabrication, and testing of a modular magnetic field microsensor on a flexible polymer foil. *IEEE Trans. Magn.* **48**, 3843–3846 (2012).
39. Wang, Z. et al. Highly sensitive flexible magnetic sensor based on anisotropic magnetoresistance effect. *Adv. Mater.* **28**, 9370–9377 (2016).
40. Li, B., Kavaldzhiev, M. N. & Kosel, J. Flexible magnetoimpedance sensor. *J. Magn. Magn. Mater.* **378**, 499–505 (2015).
41. Wang, Z., Shaygan, M., Otto, M., Schall, D. & Neumaier, D. Flexible Hall sensors based on graphene. *Nanoscale* **8**, 7683–7687 (2016).

42. Heidari, H., Bonizzoni, E., Gatti, U., Maloberti, F. & Dahiya, R. CMOS vertical Hall magnetic sensors on flexible substrate. *IEEE Sens. J.* **16**, 8736–8743 (2016).
43. Monch, I. J. et al. Flexible Hall sensorics for flux-based control of magnetic levitation. *IEEE Trans. Magn.* **51**, 4004004 (2015).
44. Melzer, M. et al. Direct transfer of magnetic sensor devices to elastomeric supports for stretchable electronics. *Adv. Mater.* **27**, 1333–1338 (2015).
45. Melzer, M., Lin, G., Makarov, D. & Schmidt, O. G. Stretchable spin valves on elastomer membranes by predetermined periodic fracture and random wrinkling. *Adv. Mater.* **24**, 6468–6472 (2012).
46. Li, H. et al. Stretchable spin valve with stable magnetic field sensitivity by ribbon-patterned periodic wrinkles. *ACS Nano* **10**, 4403–4409 (2016).
47. Liu, Y.-W., Zhan, Q.-F. & Li, R.-W. Fabrication, properties, and applications of flexible magnetic films. *Chin. Phys. B* **22**, 127502 (2013).
48. Jogschies, L. et al. Recent developments of magnetoresistive sensors for industrial applications. *Sensors* **15**, 28665–28689 (2015).
49. Suo, Z., Ma, E. Y., Gleskova, H. & Wagner, S. Mechanics of rollable and foldable film-on-foil electronics. *Appl. Phys. Lett.* **74**, 1177–1179 (1999).
50. Rottmann, F. & Dettmann, F. New magnetoresistive sensors: Engineering and applications. *Sens. Actuators A: Phys.* **27**, 763–766 (1991).
51. Caruso, M. J., Bratland, T., Smith, C. H. & Schneider, R. *A New Perspective on Magnetic Field Sensing* (Honeywell, 1998).
52. *1- and 2-Axis Magnetic Sensors HMC1001/1002/1021/1022* (Honeywell, 2008); https://go.nature.com/2Jawa8l
53. Panda3D. *Carnegie Mellon University* https://www.panda3d.org/ (accessed 26 May 2018).
54. Wiltschko, W. & Wiltschko, R. Magnetic orientation and magnetoreception in birds and other animals. *J. Comp. Physiol. A* **191**, 675–693 (2005).
55. Mohamadabadi, K. *Anisotropic Magnetoresistance Magnetometer for Inertial Navigation Systems*. PhD thesis, Ecole Polytechnique X (2013).
56. Li, X., Ding, G., Ando, T., Shikida, M. & Sato, K. Micromechanical characterization of electroplated permalloy films for MEMS. *Microsyst. Technol.* **14**, 131–134 (2007).
57. Jeong, C. K. et al. Self-powered fully-flexible light-emitting system enabled by flexible energy harvester. *Energy Environ. Sci.* **7**, 4035–4043 (2014).


## Acknowledgements

We acknowledge insightful discussions with T. Kosub and J. Ge (both of HZDR). We thank B. Scheumann, R. Kaltofen and J.I. Mönch (all of HZDR) for the deposition of metal layer stacks. Support by the Structural Characterization Facilities Rossendorf at the Ion Beam Center (IBC) at the HZDR is greatly appreciated. This work is financed in part via the European Research Council within the European Union´s Seventh Framework Programme (FP7/2007–2013)/ERC grant agreement no. 306277 and German Research Foundation (DFG) Grant MA 5144/9-1.

## Author contributions

G.S.C.B. designed and fabricated the sensors and conducted the experiments. G.S.C.B and D.M. analysed the data and prepared figures with contributions from all authors. H.F. wrote the scripts to interface the game engine with the acquired data. L.B. carried out structural characterization of the samples. G.S.C.B. and D.M. wrote the manuscript with comments from all authors. All co-authors edited the manuscript. D.M. and J.F. conceived the project.

## Competing interests

The authors declare no competing interests.

## Additional information

**Supplementary information** is available for this paper at https://doi.org/10.1038/s41928-018-0161-6.

**Reprints and permissions information** is available at www.nature.com/reprints.

**Correspondence and requests for materials** should be addressed to G.S.C. or D.M.

**Publisher's note:** Springer Nature remains neutral with regard to jurisdictional claims in published maps and institutional affiliations.

ACS APPLIED MATERIALS & INTERFACES

Research Article

Cite This: ACS Appl. Mater. Interfaces 2018, 10, 15232−15239

www.acsami.org

# Laser-Rewriteable Ferromagnetism at Thin-Film Surfaces

Jonathan Ehrler,[†,‡] Miao He,[§] Maxim V. Shugaev,[§] Nikolay I. Polushkin,[∥,⊥] Sebastian Wintz,[†,#] Vico Liersch,[†] Steffen Cornelius,[†] René Hübner,[†] Kay Potzger,[†] Jürgen Lindner,[†] Jürgen Fassbender,[†,‡] Ahmet A. Ünal,[¶] Sergio Valencia,[¶] Florian Kronast,[¶] Leonid V. Zhigilei,[§,▽] and Rantej Bali*[,†]

[†]Helmholtz-Zentrum Dresden-Rossendorf, Institut für Ionenstrahlphysik und Materialforschung, Bautzner Landstrasse 400, D-01328 Dresden, Germany

[‡]Technische Universität Dresden, Helmholtzstrasse 10, 01069 Dresden, Germany

[§]Department of Materials Science and Engineering, University of Virginia, 395 McCormick Road, Charlottesville, Virginia 22904-4745, United States

[∥]Instituto Superior Techico (IST/UTL), ICEMS, Av. Rovisco Pais 1, 1049-100 Lisboa, Portugal

[⊥]Institute for Physics of Microstructures of RAS, GSP 105, 603950 Nizhny Novgorod, Russia

[#]Paul Scherrer Institute, 5232 Villigen PSI, Switzerland

[¶]Helmholtz-Zentrum Berlin für Materialien und Energie, Albert-Einstein-Strasse 15, D-12489 Berlin, Germany

[▽]Department of Modern Functional Materials, ITMO University, 49 Kronverksky pr., St. Petersburg 197101, Russia

Supporting Information

**ABSTRACT:** Manipulation of magnetism using laser light is considered as a key to the advancement of data storage technologies. Until now, most approaches seek to optically switch the direction of magnetization rather than to reversibly manipulate the ferromagnetism itself. Here, we use ∼100 fs laser pulses to reversibly switch ferromagnetic ordering on and off by exploiting a chemical order−disorder phase transition in $Fe_{60}Al_{40}$, from the B2 to the A2 structure and vice versa. A single laser pulse above a threshold fluence causes nonferromagnetic B2 $Fe_{60}Al_{40}$ to disorder and form the ferromagnetic A2 structure. Subsequent laser pulsing below the threshold reverses the surface to B2 $Fe_{60}Al_{40}$, erasing the laser-induced ferromagnetism. Simulations reveal that the order−disorder transition is regulated by the extent of surface supercooling; above the threshold for complete melting throughout the film thickness, the liquid phase can be deeply undercooled before solidification. As a result, the vacancy diffusion in the resolidified region is limited and the region is trapped in the metastable chemically disordered state. Laser pulsing below the threshold forms a limited supercooled surface region that solidifies at sufficiently high temperatures, enabling diffusion-assisted reordering. This demonstrates that ultrafast lasers can achieve subtle atomic rearrangements in bimetallic alloys in a reversible and nonvolatile fashion.

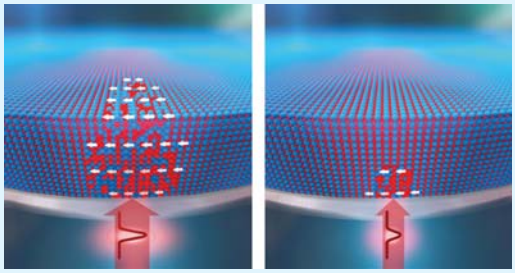

**KEYWORDS:** *magneto-optical devices, data storage, phase transitions, fs laser modifications, supercooling, order−disorder transitions*

## INTRODUCTION

The reversible manipulation of material properties by laser pulses is central to technologies employed on an everyday basis, such as in rewriteable (rw) optical data storage devices. In recent years, there is a thrust toward integrating optical and magnetic data storage, attempting to simultaneously exploit the ultrafast timescales of laser pulsing and the density of magnetic recording. This challenge is currently being approached via optical magnetization reversal[1−4] and heat-assisted magnetic recording.[5−8] The above phenomena do not involve changes to the intrinsic magnetic properties, that is, the saturation magnetization ($M_s$) of the material remains unchanged during the switching process. From a practical point of view, the detection of rw magnets within nonmagnetic matrices will show much stronger demarcations in comparison to the status quo where data bits are recorded in terms of the magnetic stray field direction. Furthermore, laser-assisted on/off switching of ferromagnets has the potential to enable the incorporation of an optical lever to spin-transport devices.

Here, we show strong laser-induced reversible variations of $M_s$ in a B2 $Fe_{60}Al_{40}$ alloy. This alloy is a member of a wider class of alloys of the form $Fe_{1-x}A_x$, where A = Al, V, and Rh, which are nonferromagnetic in the B2 structure but transform to strong ferromagnets via disordering to the A2 structure.[9−13] Disordering implies the exchange of site occupancies between a small fraction of the Fe and A atoms. In B2 $Fe_{60}Al_{40}$, the (001)

Received: January 22, 2018
Accepted: March 26, 2018
Published: April 17, 2018






DOI: 10.1021/acsami.8b01190
ACS Appl. Mater. Interfaces 2018, 10, 15232−15239

planes consist purely of Fe atoms, whereas the (002) planes consist primarily of Al and the remaining Fe atoms. This structure possesses the lowest Fe−Fe coordination and is known to be paramagnetic. Disordering of the B2 structure by randomly exchanging Fe and Al site occupancies, forming antisite defects, increases the average number of Fe−Fe nearest neighbors from 2.7 in the B2 structure to 4.8 in A2. Associated with the B2 → A2 transition is a slight increase in the lattice parameter, which along with the increased number of Fe−Fe nearest neighbors, may play a role in inducing ferromagnetism. Disordering can be generated locally, for example, by using a highly focused noble gas ion beam,[14] to selectively magnetize nanoscale regions of desired geometries.[15]

Although ion-induced reordering is possible in certain disordered alloys,[16] the viability of reversible order−disorder switching has not been demonstrated. Laser pulses are currently used to induce amorphous−crystalline transitions via rapid quenching, to reversibly control surface reflectivity of chalcogenide systems.[17] We demonstrate here a laser-assisted order−disorder transition via supercooling that switches on and off an intrinsic material property, while preserving the crystallinity of the system.

## EXPERIMENT

To study the influence of laser pulses on the magnetization of B2 $Fe_{60}Al_{40}$, thin films were prepared on transparent MgO substrates. Thin films were prepared using magnetron sputtering of a target of the same composition in Ar atmosphere, while holding the substrate at room temperature. The as-deposited $Fe_{60}Al_{40}$ films are of the disordered A2 structure and are ordered to B2 via annealing at 773 K in vacuum. Details of the thin-film growth and characterization of the ordered structure have been published elsewhere.[18] Laser irradiation experiments were performed at the spin-resolved photoemission electron microscope (SPEEM) at the BESSY II storage ring in Berlin.[19] This setup provides high-resolution magnetic imaging in combination with a titanium−sapphire laser for local laser excitation. The SPEEM was used for imaging magnetization at the $Fe_{60}Al_{40}$/vacuum surface, whereas underneath the sample, a microlens was used to focus a laser of 800 nm wavelength and ∼100 fs pulse duration to a 2 $\mu$m spot. Note that, in this geometry, the laser is incident on the MgO/$Fe_{60}Al_{40}$ interface (Figure 1). The SPEEM setup and, in particular, the geometric arrangement of laser incidence and surface probing have been described in ref 20. Laser pulse irradiation was performed on B2 $Fe_{60}Al_{40}$ films of 20, 40, and 80 nm thicknesses. The laser repetition rate was 2.5 MHz, and a pulse picker was used to select single pulses or trains of defined number of pulses. Magnetic images of the laser exposed area were recorded at the $L_3$ resonance of Fe (707 eV), exploiting the element-specific X-ray magnetic circular dichroism.

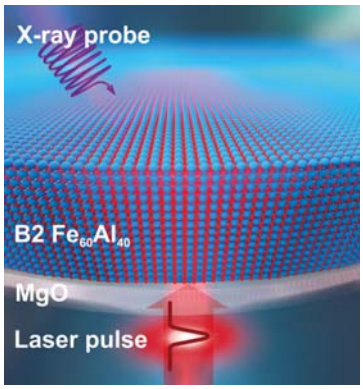


**Figure 1.** Experimental scheme. The interface between $Fe_{60}Al_{40}$ and MgO is irradiated by high-intensity ∼100 fs laser pulses. The magnetic properties of the $Fe_{60}Al_{40}$ surface are probed by an X-ray beam.

Irradiation of a 40 nm thick B2 $Fe_{60}Al_{40}$ film by a single laser pulse at a fluence of 500 mJ $cm^{-2}$ induces strong surface magnetic contrast (Figure 2a). The magnetic contrast is displayed as the difference of the two images recorded with circular polarization and opposite helicity, divided by their sum. The contrast sensitivity lies along the X-ray beam, with the magnetization parallel to the probe beam shown in red and antiparallel as blue. The magnetized region shows multiple domains, with some domains with lateral dimensions of 800 nm. Magnetic domains of similar sizes have been previously observed in A2 $Fe_{60}Al_{40}$.[21]

To observe the effect of low-fluence pulses, the magnetized region was irradiated with a pulse train of $10^5$ pulses at 200 mJ $cm^{-2}$. The pulse train erases the surface magnetization induced by the first, high-fluence laser pulse. As seen in Figure 2b, the magnetization of this region is severely suppressed, and the multidomain state is erased. The 500 mJ $cm^{-2}$ single-pulse irradiation was repeated on the same spot as above, but in the presence of a small field of +5 mT. Figure 2c shows that the field forces the formation of a single magnetic domain. The area with the single domain was irradiated with $10^4$ pulses at 200 mJ $cm^{-2}$, again leading to the suppression of the magnetization (Figure 2d).

The process was repeated under varying conditions for optimization. Figure 2e shows B2 $Fe_{60}Al_{40}$ magnetized by a single 400 mJ $cm^{-2}$ pulse irradiation under a magnetic field of −15 mT, which induces a single domain of strong magnetization. Finally, in Figure 2f, instead of a pulse train, the spot was irradiated with a single pulse at 200 mJ $cm^{-2}$. The single low-fluence pulse significantly suppresses the surface magnetization, by 40% on average in the case of 40 nm thick $Fe_{60}Al_{40}$.

To reveal the dependence of the magnetic contrast on the fluence in the single-pulse regime, the initial B2 $Fe_{60}Al_{40}$ film was irradiated at fluences increased in steps and the induced magnetic contrast was measured after each pulse. A magnetic field of +15 mT was applied to always confine the magnetization in the single-domain state. Figure 3a shows the increase of the induced magnetization with laser fluence for 20, 40, and 80 nm thick B2 $Fe_{60}Al_{40}$ films. The SPEEM contrast, which is proportional to $M_s$, increases in a sigmoidal fashion with increasing fluence. Half-maximum $M_s$ is achieved at 300, 390, and 650 mJ $cm^{-2}$ for 20, 40, and 80 nm film thicknesses, respectively (crosses in Figure 3a) and can be considered as the effective critical thresholds for magnetic writing, as measured by surface magnetic probing.

The magnetization suppression by trains of low-fluence laser pulses is illustrated in Figure 3b. A single "write" pulse was applied at fluences of 400 mJ $cm^{-2}$ for the 20 and 40 nm thick films and 700 mJ $cm^{-2}$ for the 80 nm film, followed by the application of 200 mJ $cm^{-2}$ pulses for studying erasure. The "erase" pulses were applied in logarithmic steps, that is, $10^0$, $10^1$...$10^4$, $5 \times 10^4$, and $5 \times 10^6$ pulses, and after each pulse train, the surface magnetic contrast was measured. Figure 3b illustrates the variation of the magnetic contrast signal, normalized to the contrast induced by the write pulse. For the 40 and 80 nm $Fe_{60}Al_{40}$ films, this normalized magnetization,



DOI: 10.1021/acsami.8b01190
ACS Appl. Mater. Interfaces 2018, 10, 15232−15239

ACS Applied Materials & Interfaces Research Article

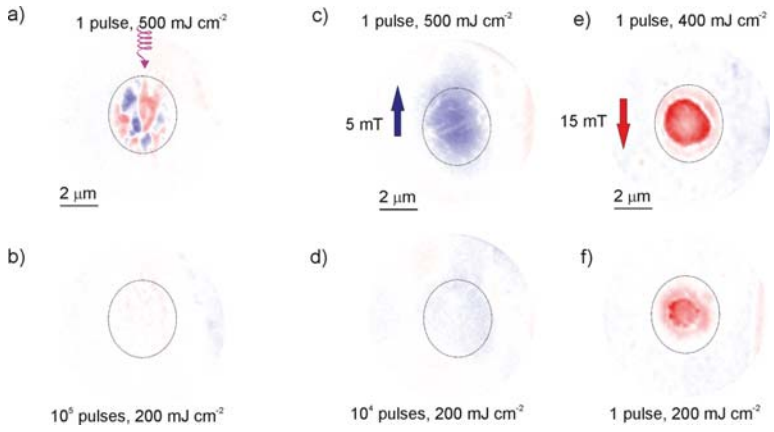


**Figure 2.** Laser-assisted magnetic writing and erasing at surfaces. (a) Single pulse at 500 mJ $cm^{-2}$ incident on a 40 nm thick B2 $Fe_{60}Al_{40}$ film generates a magnetic multidomain state. (b) Sample is irradiated with $10^5$ pulses of the same laser, but at 200 mJ $cm^{-2}$ per pulse, thereby erasing the multidomain state. (c) Single pulse of 500 mJ $cm^{-2}$ is incident while a magnetic field of +5 mT is applied, generating a single domain magnet. (d) Train of $10^4$ pulses at 200 mJ $cm^{-2}$ per pulse, while retaining the magnetic field, erases the magnet. (e) Single pulse of 400 mJ $cm^{-2}$ incident on the sample, while applying a magnetic field of −15 mT, generates a single domain magnet. (f) Significant reduction of magnetic contrast is obtained by applying a single pulse at 200 mJ $cm^{-2}$. The dotted ellipses outline the approximate laser-affected zone. The direction of X-ray incidence is indicated by the spiral arrow in (a). Red and blue indicate parallel and antiparallel magnetization components, respectively, with respect to the X-ray incidence.

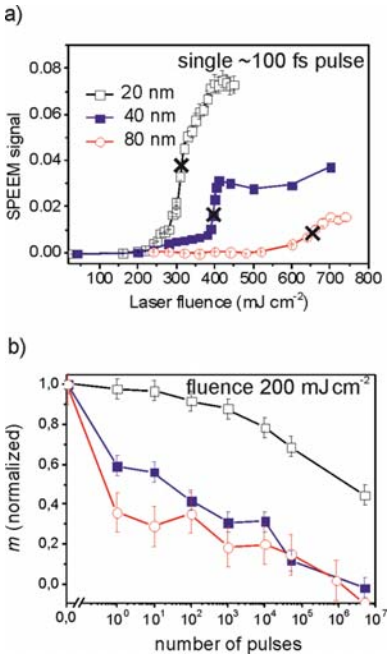


**Figure 3.** Magnetic response of B2 $Fe_{60}Al_{40}$ films to femtosecond laser irradiation. (a) Induced magnetization in terms of SPEEM contrast for single-shot irradiation of 20, 40, and 80 nm films and (b) effect of laser pulse trains of 200 mJ $cm^{-2}$ per pulse on the normalized magnetization. The crosses in (a) indicate the fluence of the single-shot irradiation, prior to the irradiation by pulse trains in (b).

*m*, is suppressed strongly by the erase pulses, with 40 and 60% reductions with a single erase pulse for the 40 and 80 nm films, respectively. In comparison, for the 20 nm film, *m* is suppressed by 50%, but only after the application of $5 \times 10^6$ pulses.

To confirm that chemical ordering (B2 → A2 phase transition) is responsible for the laser-induced magnetic writing, an ex situ experiment was performed. The surface of a 40 nm thick B2 $Fe_{60}Al_{40}$ film was irradiated in air using a Q-switched Nd:YAG laser of 355 nm wavelength. The pulse width was 5 ns, and $10^5$ pulses at 500 mJ $cm^{-2}$ fluence were applied. A large laser-affected zone of ~300 $\mu$m diameter is obtained, with an ablated region at the center. A magneto-optic Kerr effect was used to detect induced magnetization. A large induced magnetization is observed in the annular region surrounding the ablated spot. For structure analysis, a cross-sectional transmission electron microscopy (TEM) lamella was extracted from the magnetized region, away from the ablated zone, by in situ lift-out using a focused ion beam tool. The bright-field image (see Supporting Information) shows that the film possesses a flat topography, and intermixing at the film−substrate interface is negligible. Selected-area electron diffraction confirms the absence of any superstructure reflections, viz., 100, 111, and 210 associated with the B2 $Fe_{60}Al_{40}$ structure, thereby proving that the laser-irradiated region is fully disordered. Furthermore, no secondary phases are detected. Because the disordered structure is known to be ferromagnetic,[9−11,14,15] it is clear that the observed laser-induced magnetization occurs purely due to the formation of A2 $Fe_{60}Al_{40}$. The laser-assisted B2 → A2 transition is consistent with the decreasing surface magnetization with increasing film thicknesses seen in Figure 3a, with the degree of disorder decaying with the distance from the point of laser incidence.

Despite the differences in laser parameters and experimental geometry, the magnetized state is achieved in both the ex situ and in situ experiments, showing that laser pulses over a broad parameter range are effective in disordering B2 $Fe_{60}Al_{40}$ thin films. The reverse effect, however, has only been observed in the in situ experiment, where the laser is incident at the film−substrate interface and the magnetization is probed at the surface.

## ■ SIMULATION RESULTS AND DISCUSSION

To provide a clear understanding of the conditions that control the structural disordering and reordering responsible for the rw magnetization of thin films, a series of simulations of laser-induced phase transformations in $Fe_{60}Al_{40}$ films deposited on MgO substrates were performed. The simulations were done with a continuum level model accounting for the laser



DOI: 10.1021/acsami.8b01190
ACS Appl. Mater. Interfaces 2018, 10, 15232−15239

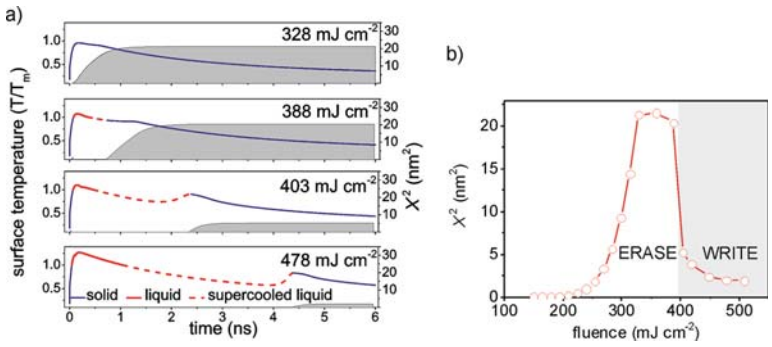


**Figure 4.** Computational predictions of the continuum level model of laser-induced phase transformations. (a) Temporal evolution of the surface temperature and the mean square displacement of vacancies ($X^2$) in the center of irradiated spot. The simulations were performed for 40 nm thick $Fe_{60}Al_{40}$ films irradiated by 100 fs laser pulses at different fluences. The evolution of surface temperature is illustrated by the lines, where the solid blue, solid red, and dashed red lines represent the phase states of solid, liquid, and supercooled liquid, respectively. The cumulative mean square displacement of vacancies in the solidified surface region, $X^2$, is indicated by the gray zone. (b) Dependence of the saturation level of $X^2$ on laser fluence. Fluence ranges suitable for magnetic writing and erasing, as suggested by the vacancy diffusion length, are marked.

excitation of the conduction band electrons, electron−phonon equilibration, heat transfer, and the kinetics of melting and solidification (see Methods). The model accounts for the temperature dependencies of the material properties, and the irradiation conditions similar to those used in the experiments and illustrated in Figure 1 are reproduced in the simulations. The laser pulse is focused on a 2 $\mu$m spot at the film−substrate interface and is assumed to have a Gaussian intensity distribution. Although the calculations were performed for all three film thicknesses, in the discussion below, we focus on the 40 nm thick $Fe_{60}Al_{40}$ films for which the laser-induced magnetic write/erase has been found to be most pronounced.

As the first step, we performed a series of simulations for a broad range of laser fluences and identified incident fluence thresholds for the onset of melting at the $Fe_{60}Al_{40}$/MgO interface (173 mJ cm$^{-2}$), the emergence of the second melting region on the top surface of the film (357 mJ cm$^{-2}$), and the complete melting throughout the thickness of the film when the two melting fronts propagating from the film−substrate interface and the top surface merge together (394 mJ cm$^{-2}$). It can be expected that rapid solidification of the temporally molten part of the film produces a disordered metastable A2 phase. The metastable phase can then undergo the A2 → B2 ordering phase transition upon further cooling of the solidified material. Because the atomic rearrangements responsible for the ordering phase transition proceed through the vacancy diffusion mechanism and SPEEM measurements are sensitive to magnetization in a thin surface layer of the irradiated films, we evaluate the mean square displacement of vacancies, $X^2$, in the surface region located at the center of the laser spot from the time of complete solidification of this region until the cooling brings the vacancy diffusion to a halt. Although the temperature dependence of the thermodynamic driving force for the ordering phase transition does not allow us to quantitatively link the magnitude of $X^2$ to the kinetics of the phase transition, it still provides an instructive measure of the extent of atomic rearrangements involved in the transformation to the chemically ordered state.

The temporal evolution of the surface temperature at the center of the laser spot is illustrated in Figure 4a for four representative simulations. The color of the curves represents the phase of the material, with blue and red colors corresponding to solid and liquid phases, respectively. The supercooling of the molten alloy below $T_m$ is depicted by the dashed red curves (a single value of $T_m$ = 1660 K taken between the solidus and liquidus of the alloy, 1630 and 1680 K,[22] is used here to simplify the discussion and the calculations), and the cumulative mean square displacements of vacancies, $X^2$, are shown by gray zones. At 328 mJ cm$^{-2}$, below the onset of surface melting, a rapid heating of the surface region almost to $T_m$ results in a sharp increase of $X^2$. The following cooling, however, slows down the vacancy diffusion until it becomes negligible as the surface temperature drops below ~0.7$T_m$ (1160 K), as reflected by the saturation of $X^2$. When the laser fluence is increased to 388 mJ cm$^{-2}$, the surface temperature exceeds $T_m$, leading to a transient melting of a thin surface layer of the film. The two melting fronts, propagating from the surface and film−substrate interface, do not merge in this simulation, and a rapid regrowth of the crystalline part of the film results in solidification of the surface region at a very mild supercooling of the melt (the dashed segment of the red curve in Figure 4a is short). The relatively high surface temperature at the time of the surface resolidification ensures that active vacancy diffusion can take place during further cooling of the surface, yielding the saturation level of $X^2$ similar to that observed at 328 mJ cm$^{-2}$.

Above the threshold for complete melting throughout the thickness of the film, the possibility for rapid regrowth of the crystalline part of the thin film is excluded and the solidification of the molten region can only proceed via lateral propagation of the solidification front from the periphery of the molten region to the center of the laser spot. Given the relatively large lateral size of the molten region (controlled by the size of the laser spot) and the limited velocity of the solidification front (≲130 m/s, see Methods), the solidification process takes longer time and allows for much stronger supercooling of the molten material in the central part of the laser spot. In particular, a sharp increase of the solidification time from 740 ps at 388 mJ cm$^{-2}$ to 2.4 ns at 403 mJ cm$^{-2}$ leads to the decrease of the surface temperature at the time of complete solidification from 0.93 to 0.91$T_m$. Moreover, the value 0.91$T_m$ corresponds to a maximum produced by a temperature spike appearing because of a local release of the latent heat of solidification, which quickly dissipates due to the large local temperature gradient near the freshly solidified surface. The low temperature in the resolidified region severely constrains the vacancy diffusion, as



DOI: 10.1021/acsami.8b01190
ACS Appl. Mater. Interfaces 2018, 10, 15232−15239

ACS Applied Materials & Interfaces Research Article

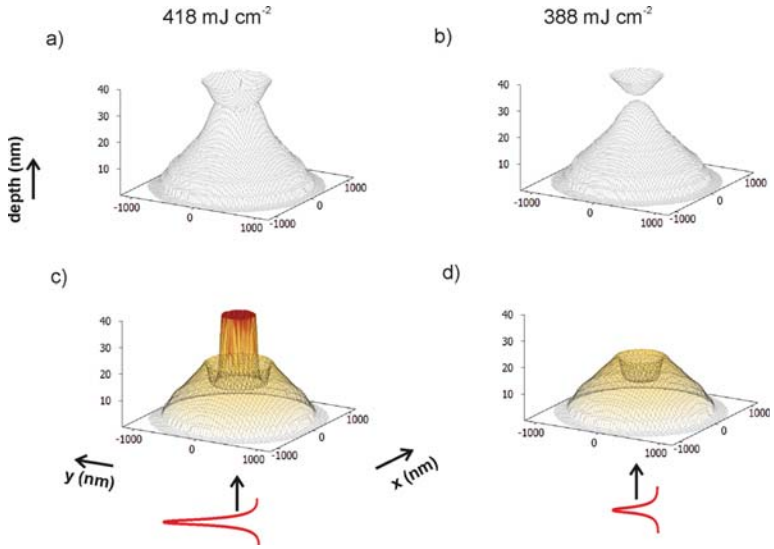


**Figure 5.** Rendering of the furthest extent of the melting front and corresponding effect on the magnetization. The $Fe_{40}Al_{40}$ film is irradiated at laser fluences of 418 mJ $cm^{-2}$ in (a,c) and 388 mJ $cm^{-2}$ in (b,d). (a,b) The maximum extent of the melting fronts during single-pulse laser irradiation of given fluences. (c,d) Spatial distribution of the induced magnetization, by considering a threshold value of the cumulative vacancy mean square displacement in the solidified material, $X^2 = 11$ $nm^2$. The color scale in (c,d) indicates the depth under the film−vacuum surface of the 40 nm thick film, with darker shades used closer to the surface.

indicated by the $X^2$ profile calculated for 403 mJ $cm^{-2}$, and leads to the saturation value of $X^2$ that is about four times smaller than that predicted for 388 mJ $cm^{-2}$. Further increase of the laser fluence results in longer times for solidification of the central part of the laser spots and further suppression of the vacancy diffusion. In particular, when the fluence is increased from 403 to 478 mJ $cm^{-2}$, the surface temperature at the time of solidification drops from $0.91T_m$ to $0.83T_m$ and the saturation level of $X^2$ decreases down to the values that preclude possibility of any significant atomic rearrangements after the surface resolidification, as illustrated in the bottom panel of Figure 4a.

To further illustrate the effect of the laser fluence on vacancy diffusion, we plot in Figure 4b the $X^2$ as a function of fluence. Below the threshold for inducing the second melting front from the surface of the film, the vacancy diffusion length increases exponentially with the laser fluence. After the onset of surface melting, $X^2$ saturates at an almost constant level, with only a slight decrease with the increase of laser fluence due to stronger supercooling at the point of surface resolidification. Above the threshold for complete melting, the time needed for the resolidification of the central part of the laser spot rises sharply and, as a result, a much stronger supercooling is produced prior to the resolidification. The strong supercooling, in turn, limits the vacancy diffusion during the cooling of the resolidified surface and reduces the likelihood of A2 → B2 reordering that requires atomic rearrangements. The chemically disordered state and magnetization, thus, are expected to remain in the central part of the laser spot after rapid quenching down to the room temperature.

Below the threshold for the complete melting of the film, the vacancy diffusion can be sufficiently active to allow for the ordering transition. Indeed, the maximum $X^2 \approx 21.5$ $nm^2$ in Figure 4b corresponds to ∼320 vacancy jumps. Taking into account that a typical concentration of vacancies generated in rapid nonequilibrium solidification of metals is on the order of $10^{-3}$ of lattice sites,[23] we can estimate that approximately 32% of atoms change their positions because of the vacancy diffusion. Although it is not possible to quantitatively relate the total number of vacancy jumps during the cooling process to the relative fractions of the equilibrium B2 and metastable A2 phases generated by the laser irradiation, the above estimation does suggest that a substantial reordering may take place even in a single laser pulse irradiation. This conclusion is in agreement with experimental results shown in Figures 2f and 3b, which demonstrate a substantial magnetization decrease after irradiation of 40 and 80 nm films with a single laser pulse. Experimental observations of vacancies in $Fe_{60}Al_{40}$ films have been reported in ref 24.

The generation of ferromagnetic domains formed by laser irradiation performed in the absence of magnetic fields (Figure 2a) is in line with the predicted melting and resolidification scheme. Resolidification is expected to proceed via regrowth of the solid parts of the film, heterogeneous nucleation of new crystallites at the film−substrate interface, and in the case of sufficiently deep supercooling, for instance, $\sim 0.6T_m$ for a 478 mJ $cm^{-2}$ single pulse (Figure 4a), via the homogeneous nucleation of crystallites within the melt. As resolidification proceeds, latent heat of melting is released at grain growth sites, resulting in a laterally inhomogeneous temperature distribution over the laser-affected zone. The temperature inhomogeneity may persist as the system cools to the Curie temperature ($T_c$), causing a spatially inhomogeneous re-entry of ferromagnetism. Regions at a local temperature of $T_c - \Delta T$ are magnetized, and their stray fields drive the local orientations of magnetic moments in their vicinity that are still at $T_c + \Delta T$, thereby inducing magnetic domains as seen in Figure 2a. The formation of magnetic domains is avoided by applying a small magnetic field during irradiation that is sufficient to override inhomogeneous stray fields and generate the single magnetic domains shown in Figure 2c,e.

To obtain an estimate of the spatial distribution of the induced magnetization, it is necessary to quantitatively relate the simulated $X^2$ distribution to the experimentally observed $m$.



DOI: 10.1021/acsami.8b01190
ACS Appl. Mater. Interfaces 2018, 10, 15232−15239

The first step is to relate $X^2$ to the degree of the B2 ↔ A2 transition, and the next step is to relate the degree of chemical disordering to $m$. In the second step, the correlation between the degree of disordering and the induced $m$ is known to be in the form of an s-shaped curve,[18] which is not dissimilar to the observed laser fluence-$m$ relationship seen in Figure 3a. However, the relationship between $X^2$ and the degree of chemical disordering in $Fe_{60}Al_{40}$ is not unique and depends on the thermal history of the alloy. Moreover, the time−temperature−transformation (TTT) diagram for the B2 ↔ A2 transition, needed for making a quantitative connection between the temperature evolution and the degree of the phase transformation, is not available.

In the absence of TTT curves, we consider our observations: first, as seen in Figure 4b, just below the threshold fluence of ∼400 mJ $cm^{-2}$, $X^2$ exhibits a sharp drop from ∼20 to ∼5 $nm^2$, which we assume is coincident with a sharply increased $m$. Second, it is seen that above the threshold, a postmelting $X^2 \approx 2$ $nm^2$ does not suppress $m$. In the first approximation, we assume that for $X^2 = 20$ $nm^2$, the material is fully ordered ($m = 0$) and at $X^2 = 2$ $nm^2$, it remains fully disordered ($m = 1$). We fix the $m$-spatial distribution to the halfway point of the above limiting values, that is, $X^2 = 11$ $nm^2$. This implies that the induced $m$ is confined to a region within a surface defined by $X^2 = 11$ $nm^2$.

As a cautionary note, because the link between $X^2$ and disorder is dependent on the thermal history, the above limiting values can vary significantly depending on experimental conditions. Nonetheless, for any given case, a comparison of the $X^2$ distributions above and below the threshold fluence sheds light on the single-pulse $m$ writing and erasing. In particular, the shape of the region undergoing transient melting and rapid resolidification and the concomitant $X^2$ distribution provide a qualitative picture of the spatial confinement of the disordering and reordering processes at the film surface. Figure 5a,b shows the spatial extent of the melting process at laser fluences of 388 and 418 mJ $cm^{-2}$, respectively. The corresponding $X^2 = 11$ $nm^2$ surfaces for the two fluences are shown in Figure 5c,d, respectively.

As seen in Figure 5a, at a fluence of 418 mJ $cm^{-2}$, the melting fronts emergent from the film surface and the interface coalesce, leading to the appearance of a melt-through region. The solidification of this region proceeds through the propagation of the solidification front and, as explained above, takes several nanoseconds. The temperature of the molten region continues to decrease and by the time of complete solidification becomes too low for atomic rearrangements needed for full chemical reordering. Figure 5c shows the corresponding limiting $m$ surface, as obtained by plotting $X^2 = 11$ $nm^2$. A magnetized region of approximately 500 nm in diameter is predicted at the surface. At the MgO/film interface, the predicted magnetized region is approximately the size of the laser spot. The size of the surface magnetized region increases with increasing laser fluence.

At a fluence of 388 mJ $cm^{-2}$, which is just below the threshold fluence, the two melting fronts propagating from the MgO/film interface and the film top surface remain separated (Figure 5b). After the temperature drops below the melting point, the melting fronts propagate vertically and the film rapidly resolidifies. The temperature at the end of solidification remains high, which enables active vacancy diffusion. The diffusional atomic rearrangements result in the transformation of the metastable disordered A2 structure formed in the transiently melted and resolidified parts of the film into the equilibrium B2 structure, thus erasing the surface magnetization, as can be seen from Figure 5d.

As seen in the visualizations in Figure 5, a residual magnetization can occur in the bottom 20 nm of the film, even for low-fluence laser pulses. The onset of interfacial melting is ∼180 mJ $cm^{-2}$ for all film thicknesses, and a 200 mJ $cm^{-2}$ pulse leads to transient melting and formation of residual disorder at the MgO/film interface. This is consistent with the observations in Figure 3b, where single-pulse erasure is not observed in 20 nm thick $Fe_{60}Al_{40}$. Laser irradiation by up to $\sim 10^6$ pulses tends to reorder the upper layers of the film, nevertheless the residual magnetization persists. Because the depth of SPEEM probing is limited to a depth of ∼10 nm, the presence of this magnetized layer is detectable only in the case of 20 nm film. Rewritable magnetization, therefore, is observed for film thicknesses above 20 nm.

## CONCLUSIONS

The proof of principle for laser-induced on/off switching of ferromagnetism driven by a disorder−order transition has been demonstrated on B2 alloy thin films. Simulations reveal the crucial role played by supercooling of the transiently melted region in manifesting the disorder−order transition. The process is repeatable-laser pulses of fluences above the writing threshold have been applied up to 10 times at the same spot without the appearance of damage to the film. Repeatability can be limited by ablation of the material or by contamination during the laser irradiation process; factors that can be avoided by an appropriate protective top layer, such as MgO. Engineering the substrate heat conductivity and the inclusion of a buffer and cap layers should be explored for increasing the maximum level of supercooling before the resolidification to control diffusion and reordering, and to achieve optimized laser-assisted reversible property changes. The concept of laser-induced rw magnetization may be applicable to other materials that exhibit order−disorder transitions. Further studies on these materials may improve our understanding of femtosecond laser-induced rapid heating and cooling processes in alloys, in particular, the mechanisms and kinetics of the order−disorder transition that are still largely unexplored. The results of this study may initiate a wider search for new alloys exhibiting laser-induced reversible changes of intrinsic magnetic properties.

## METHODS

**Experiments.** Details on the thin-film preparation can be found in ref 18. The PEEM experiment combined with laser irradiation is described in ref 20.

**Simulations.** The initial response of a $Fe_{60}Al_{40}$ film deposited on a magnesia (MgO) substrate to a short-pulse laser irradiation has been simulated with a conventional one-dimensional (1D) two-temperature model (TTM)[25] that provides a continuum level description of the laser excitation and subsequent relaxation of the conduction band electrons. The description of kinetics of melting and resolidification processes is incorporated into the model as described in ref 26. The temperature profiles and the positions of the solid−liquid interface at 750 ps, predicted in series of 1D simulations, are used as input for the two-dimensional (2D) simulations applied to investigate the lateral propagation of melting front and long-term evolution of the temperature profile affected by the lateral heat transport. Simulations are performed for computational systems consisting of 20, 40, and 80 nm $Fe_{60}Al_{40}$ films on a 1 $\mu$m thick MgO substrate. The choice of the thickness of the substrate ensures a negligible temperature change at the bottom of the substrate on the simulation timescale.



DOI: 10.1021/acsami.8b01190
ACS Appl. Mater. Interfaces 2018, 10, 15232−15239

The irradiation of the target by a 100 fs laser pulse directed from the magnesia−metal interface is represented through a source term added to the TTM equation for the electron temperature. The source term accounts for the excitation of the conduction band electrons by a laser pulse with a Gaussian temporal profile and reproduces the exponential attenuation of laser intensity with depth under the surface (Beer−Lambert law), with the optical absorption depth of 15 nm of Fe at the laser wavelength of 800 nm.[27] Because of the uncertainty in the reflectivity of the $Fe_{60}Al_{40}$ alloy, the absorbed laser fluence is converted into the incident one by matching the threshold of complete melting of a 40 nm film in the experiment and modeling, which gives the value of reflectivity of 0.928. In the 2D simulations, the lateral distribution of laser fluence is described by a Gaussian profile $F(r) = F_0 \exp(-r^2/2\sigma_r^2)$, where $\sigma_r^2$ is the standard deviation related to the laser spot diameter (full width at half-maximum) as $D = \sigma_r 8\ln 2$. The spot diameter is assumed to be 2 $\mu$m, and the results of 1D simulations performed at different laser fluencies are linearly interpolated to account for the radial dependence of the laser fluence when the initial temperature distribution is built.

Because the available temperature dependencies of electron heat capacity and electron−phonon coupling accounting for the contribution from the thermal excitation from the electron states below the Fermi level are mostly limited by pure metals,[28] we use parameters for pure Fe instead of $Fe_{60}Al_{40}$ alloy.[29] Similar to ref 26, the temperature dependence of the electron thermal conductivity is approximated by the Drude model relationship, $K_e(T_e,T_l) = v^2 C_e(T_e)\tau_e(T_e,T_l)/3$, where $C_e(T_e)$ is the electron heat capacity, $v^2$ is the mean square velocity of the electrons contributing to the electron heat conductivity, approximated in this work as the Fermi velocity squared, $v_F^2$, and $\tau_e(T_e,T_l)$ is the total electron scattering time defined by the electron−electron scattering rate, $1/\tau_{e-e} = AT_e^2$, and the electron−phonon scattering rate, $1/\tau_{e-ph} = BT_l$, so that $1/\tau_e = AT_e^2 + BT_l$. The value of the coefficient $A$ ($8.9 \times 10^5$ K$^{-2}$ s$^{-1}$) is estimated within the free electron model.[30] The coefficient $B$ is described as a function of the lattice temperature, so that the experimental temperature dependences of thermal conductivity of the $Fe_{60}Al_{40}$ alloy under conditions of electron−phonon equilibrium[22,31] are reproduced in the simulations. Because in 2D simulations we do not explicitly consider the electron subsystem, the heat capacity used in the model is equal to the sum of electron and phonon heat capacities and the heat conductivity follows the experimental temperature dependence.[22,31]

According to the Fe−Al phase diagram,[22] the temperature of solid−liquid coexistence lies in the range 1630−1680 K and the single value of "melting temperature," $T_m$ = 1660 K, is used to simplify the description of the melting and resolidification processes. The temperature dependence of the velocity of the liquid−crystal interface is described by the Wilson−Frenkel expression,[32] with parameters taken for the Fe(100) interface from ref 33. Because pure Fe has different melting temperatures than the $Fe_{60}Al_{40}$ alloy, the activation energy for diffusion and the heat of fusion are renormalized based on the $T_m$ of the alloy to ensure the same velocity of the interface at the same values of relative undercooling $T/T_m$:

$$V_l = V_0 \cdot \exp(-\tilde{Q} \cdot T_m/T)[1 - \exp(-\tilde{H}_f \cdot (T_m/T - 1))]$$

where $V_0$ is a prefactor equal to 2200 m/s, $\tilde{Q} = Q^{Fe}/k_B T_m^{Fe} = 1.23$ is the reduced activation energy for diffusion, and $\tilde{H}_f = H_f^{Fe}/k_B T_m^{Fe} = 0.884$ is the reduced heat of fusion. To account for the fast homogeneous melting of the superheated solid, the regions of the target where the lattice temperature exceeds $1.3T_m$ (ref 34) are set to undergo instantaneous melting. The lattice heat capacity of the alloy is assumed to be equal to $3R$ and is calculated based on the lattice parameter 2.898 Å (ref 35) of B2 $Fe_{60}Al_{40}$, which gives $3.4 \times 10^6$ J m$^{-3}$ K$^{-1}$. The heat of fusion is estimated as a weighted average of values for Al and Fe based on the concentration in the alloy, which gives $1.7 \times 10^9$ J m$^{-3}$.

The heat capacity of magnesia is assumed to be $3.3 \times 10^6$ J m$^{-3}$ K$^{-1}$ (ref 36), and the thermal conductivity is fitted as $K(T) = 10\,700/(T - 46.0)$ [W K$^{-1}$ m$^{-1}$] based on values provided in ref 37. Because the value of interfacial thermal conductance depends not only on the materials in the contact but also on the method of the film deposition and cannot be evaluated without direct measurement, we assumed it to be $10^8$ W m$^{-2}$ K$^{-1}$, a typical value from the experimentally measured range of $10^7$ to $10^9$ W m$^{-2}$ K$^{-1}$ (refs 38−41).

## ■ ASSOCIATED CONTENT

### Supporting Information

The Supporting Information is available free of charge on the ACS Publications website at DOI: 10.1021/acsami.8b01190.

Results of structural analysis using TEM, as well as additional simulation results included (PDF)

## ■ AUTHOR INFORMATION


### Corresponding Author

*E-mail: r.bali@hzdr.de.

### ORCID

Jonathan Ehrler: 0000-0002-5187-2808
Sergio Valencia: 0000-0002-3912-5797
Rantej Bali: 0000-0002-5325-4018


### Author Contributions

R.B. conceived the project in discussions with N.I.P. and F.K. J.E., S.W., and V.L. performed SPEEM measurements. M.H. and M.V.S. performed simulations. A.A.Ü., S.V., and F.K. provided beamline support. J.E., V.L., and S.C. prepared thin-film samples. N.I.P. performed ex situ tests. R.H. performed TEM analysis. K.P., J.L., and J.F. supervised the experimental work. L.V.Z. supervised the simulations. All co-authors contributed to writing the manuscript. R.B. coordinated the overall project.

### Notes

The authors declare no competing financial interest.

## ■ ACKNOWLEDGMENTS

We thank HZB for the allocation of synchrotron radiation beamtime. The computational part of this study was supported by the National Science Foundation (NSF) through grants CMMI-1436775 & DMR-1610936. L.V.Z. thanks ITMO Fellowship Program. The experimental part benefited from funding from the Deutsche Forschungsgemeinschaft (DFG) grant BA 5656/1-1.

## ■ REFERENCES


(1) Guyader, L. L.; Savoini, M.; El Moussaoui, S.; Buzzi, M.; Tsukamoto, A.; Itoh, A.; Kirilyuk, A.; Rasing, T.; Kimel, A. V.; Nolting, F. Nanoscale sub-100 picosecond all-optical magnetization switching in GdFeCo microstructures. *Nat. Commun.* **2015**, *6*, 5839.

(2) Kimel, A. V.; Kirilyuk, A.; Usachev, P. A.; Pisarev, R. V.; Balbashov, A. M.; Rasing, T. Ultrafast non-thermal control of magnetization by instantaneous photomagnetic pulses. *Nature* **2005**, *435*, 655−657.

(3) Lambert, C.-H.; Mangin, S.; Varaprasad, B. S. D. C. S.; Takahashi, Y. K.; Hehn, M.; Cinchetti, M.; Malinowski, G.; Hono, K.; Fainman, Y.; Aeschlimann, M.; Fullerton, E. E. All-optical control of ferromagnetic thin films and nanostructures. *Science* **2014**, *345*, 1337−1340.

(4) Stupakiewicz, A.; Szerenos, K.; Afanasiev, D.; Kirilyuk, A.; Kimel, A. V. Ultrafast nonthermal photo-magnetic recording in a transparent medium. *Nature* **2017**, *542*, 71−74.

(5) Stipe, B. C.; Strand, T. C.; Poon, C. C.; Balamane, H.; Boone, T. D.; Katine, J. A.; Li, J.-L.; Rawat, V.; Nemoto, H.; Hirotsune, A.; Hellwig, O.; Ruiz, R.; Dobisz, E.; Kercher, D. S.; Robertson, N.; Albrecht, T. R.; Terris, B. D. Magnetic recording at 1.5 Pb m$^{-2}$ using an integrated plasmonic antenna. *Nat. Photonics* **2010**, *4*, 484−488.




DOI: 10.1021/acsami.8b01190
ACS Appl. Mater. Interfaces 2018, 10, 15232−15239

(6) Saga, H.; Nemoto, H.; Sukeda, H.; Takahashi, M. New recording method combining thermo-magnetic writing and flux detection. *Jpn. J. Appl. Phys.* **1999**, *38*, 1839−1840.
(7) McDaniel, T. W. Ultimate limits to thermally assisted magnetic recording. *J. Phys.: Condens. Matter* **2005**, *17*, R315−R332.
(8) Kryder, M. H.; Gage, E. C.; McDaniel, T. W.; Challener, W. A.; Rottmayer, R. E.; Ju, G.; Hsia, Y.-T.; Erden, M. F. Heat assisted magnetic recording. *Proc. IEEE* **2008**, *96*, 1810−1835.
(9) Menéndez, E.; Liedke, M. O.; Fassbender, J.; Gemming, T.; Weber, A.; Heyderman, L. J.; Rao, K. V.; Deevi, S. C.; Suriñach, S.; Baró, M. D.; Sort, J.; Nogués, J. Nanostructures Direct Magnetic Patterning due to the Generation of Ferromagnetism by Selective Ion Irradiation of Paramagnetic FeAl Alloys. *Small* **2009**, *5*, 229−234.
(10) Beck, P. A. Some recent results on magnetism in alloys. *Metall. Mater. Trans. B* **1971**, *2*, 2015−2024.
(11) Huffman, G. P.; Fisher, R. M. Mössbauer Studies of Ordered and Cold-Worked Fe−Al Alloys Containing 30 to 50 at. % Aluminum. *J. Appl. Phys.* **1967**, *38*, 735−742.
(12) Krause, J. C.; Schaf, J.; da Costa, M. I., Jr.; Paduani, C. Effect of composition and short-range order on the magnetic moments of Fe in $Fe_{1-x}V_x$ alloys. *Phys. Rev. B: Condens. Matter Mater. Phys.* **2000**, *61*, 6196−6204.
(13) Heidarian, A.; Bali, R.; Grenzer, J.; Wilhelm, R. A.; Heller, R.; Yildirim, O.; Lindner, J.; Potzger, K. Tuning the antiferromagnetic to ferromagnetic phase transition in FeRh thin films by means of low-energy/low fluence ion irradiation. *Nucl. Instrum. Methods Phys. Res., Sect. B* **2015**, *358*, 251−254.
(14) Cybart, S. A.; Bali, R.; Hlawacek, G.; Röder, F.; Fassbender, J. Focused Helium and Neon Ion Beam Modification of High-TC Superconductors and Magnetic Materials, in Helium Ion Microscopy. In *Helium Ion Microscopy*; Hlawacek, G., Gölzhäuser, A., Eds.; Springer International Publishing, 2016.
(15) Röder, F.; Hlawacek, G.; Wintz, S.; Hübner, R.; Bischoff, L.; Lichte, H.; Potzger, K.; Lindner, J.; Fassbender, J.; Bali, R. Direct Depth- and Lateral- Imaging of Nanoscale Magnets Generated by Ion Impact. *Sci. Rep.* **2015**, *5*, 16786.
(16) Bernas, H.; Attané, J.-P.; Heinig, K.-H.; Halley, D.; Ravelosona, D.; Marty, A.; Auric, P.; Chappert, C.; Samson, Y. Ordering Intermetallic Alloys by Ion Irradiation: A Way to Tailor Magnetic Media. *Phys. Rev. Lett.* **2003**, *91*, 077203.
(17) Wuttig, M.; Yamada, N. Phase change materials for rewriteable data storage. *Nat. Mater.* **2007**, *6*, 824−832.
(18) Bali, R.; Wintz, S.; Meutzner, F.; Hübner, R.; Boucher, R.; Ünal, A. A.; Valencia, S.; Neudert, A.; Potzger, K.; Bauch, J.; Kronast, F.; Facsko, S.; Lindner, J.; Fassbender, J. Printing Nearly-Discrete Magnetic Patterns Using Chemical Disorder Induced Ferromagnetism. *Nano Lett.* **2014**, *14*, 435−441.
(19) Kronast, F.; Molina, S. V. SPEEM: The photoemission microscope at the dedicated microfocus PGM beamline UE49-PGMa at BESSY II. *J. Large Scale Res. Facil.* **2016**, *2*, A90.
(20) Gierster, L.; Pape, L.; Ünal, A. A.; Kronast, F. A sample holder with integrated laser optics for an ELMITEC photoemission electron microscope. *Rev. Sci. Instrum.* **2015**, *86*, 023702.
(21) Fassbender, J.; Liedke, M. O.; Strache, T.; Möller, W.; Menéndez, E.; Sort, J.; Rao, K. V.; Deevi, S. C.; Nogués, J. Ion mass dependence of irradiation-induced local creation of ferromagnetism in $Fe_{60}Al_{40}$ alloys. *Phys. Rev. B: Condens. Matter Mater. Phys.* **2008**, *77*, 174430.
(22) Ruan, Y.; Yan, N.; Zhu, H. Z.; Zhou, K.; Wei, B. Thermal performance determination of binary Fe-Al alloys at elevated temperatures. *J. Alloys Compd.* **2017**, *701*, 676−681.
(23) Lin, Z.; Johnson, R. A.; Zhigilei, L. V. Computational Study of the Generation of Crystal Defects in A BCC Metal Target Irradiated by Short Laser Pulses. *Phys. Rev. B: Condens. Matter Mater. Phys.* **2008**, *77*, 214108.
(24) Liedke, M. O.; Anwand, W.; Bali, R.; Cornelius, S.; Butterling, M.; Trinh, T. T.; Wagner, A.; Salamon, S.; Walecki, D.; Smekhova, A.; Wende, H.; Potzger, K. Open volume defects and magnetic phase transition in $Fe_{60}Al_{40}$ transition metal aluminide. *J. Appl. Phys.* **2015**, *117*, 163908.
(25) Anisimov, S. I.; Kapeliovich, B. L.; Perel'man, T. L. Electron emission from metal surfaces exposed to ultrashort laser pulses. *J. Exp. Theor. Phys.* **1974**, *39*, 375−377.
(26) Sedao, X.; Shugaev, M. V.; Wu, C.; Douillard, T.; Esnouf, C.; Maurice, C.; Reynaud, S.; Pigeon, F.; Garrelie, F.; Zhigilei, L. V.; Colombier, J.-P. Growth Twinning and Generation of High-Frequency Surface Nanostructures in Ultrafast Laser-Induced Transient Melting and Resolidification. *ACS Nano* **2016**, *10*, 6995−7007.
(27) Palik, E. D. *Handbook of Optical Constants of Solids*; Academic Press: New York, 1998.
(28) Lin, Z.; Zhigilei, L. V.; Celli, V. Electron-phonon coupling and electron heat capacity of metals under conditions of strong electron-phonon nonequilibrium. *Phys. Rev. B: Condens. Matter Mater. Phys.* **2008**, *77*, 075133.
(29) http://www.faculty.virginia.edu/CompMat/electron-phonon-coupling/Ce_Fe_BCC.dat.
(30) Groeneveld, R. H. M.; Sprik, R.; Lagendijk, A. Femtosecond spectroscopy of electron-electron and electron-phonon energy relaxation in Ag and Au. *Phys. Rev. B: Condens. Matter Mater. Phys.* **1995**, *51*, 11433−11445.
(31) Rudajevová, A.; Buriánek, J. Determination of Thermal Diffusivity and Thermal Conductivity of Fe-Al Alloys in the Concentration Range 22 to 50 at. % Al. *J. Phase Equilib.* **2001**, *22*, 560−563.
(32) Jackson, K. A. The Interface Kinetics of Crystal Growth Processes. *Interface Sci.* **2002**, *10*, 159−169.
(33) Ashkenazy, Y.; Averback, R. S. Kinetic stages in the crystallization of deeply undercooled body-centered-cubic and face-centered-cubic metals. *Acta Mater.* **2010**, *58*, 524−530.
(34) Luo, S.-N.; Ahrens, T. J.; Çağın, T.; Strachan, A.; Goddard, W. A.; Swift, D. C. Maximum superheating and undercooling: Systematics, molecular dynamics simulations, and dynamic experiments. *Phys. Rev. B: Condens. Matter Mater. Phys.* **2003**, *68*, 134206.
(35) Nogués, J.; Apiñaniz, E.; Sort, J.; Amboage, M.; d'Astuto, M.; Mathon, O.; Puzniak, R.; Fita, I.; Garitaonandia, J. S.; Suriñach, S.; Muñoz, J. S.; Baró, M. D.; Plazaola, F.; Baudelet, F. Volume expansion contribution to the magnetism of atomically disordered intermetallic alloys. *Phys. Rev. B: Condens. Matter Mater. Phys.* **2006**, *74*, 024407.
(36) Slifka, A. J.; Filla, B. J.; Phelps, J. M. Thermal Conductivity of Magnesium Oxide From Absolute, Steady-State Measurements. *J. Res. Natl. Inst. Stand. Technol.* **1998**, *103*, 357.
(37) Chase, M. W. *NIST-JANAF Thermochemical Tables*, 4th ed.; Journal of Physical and Chemical Reference Data; National Institute of Standards and Technology (NIST): Gaithersburg, MA, 1998.
(38) Hopkins, P. E.; Salaway, R. N.; Stevens, R. J.; Norris, P. M. Temperature-Dependent Thermal Boundary Conductance at Al/$Al_2O_3$ and Pt/$Al_2O_3$ interfaces. *Int. J. Thermophys.* **2007**, *28*, 947−957.
(39) Hopkins, P. E.; Phinney, L. M.; Serrano, J. R.; Beechem, T. E. Effects of surface roughness and oxide layer on the thermal boundary conductance at aluminum/silicon interfaces. *Phys. Rev. B: Condens. Matter Mater. Phys.* **2010**, *82*, 085307.
(40) Giri, A.; Foley, B. M.; Hopkins, P. E. Influence of Hot Electron Scattering and Electron−Phonon Interactions on Thermal Boundary Conductance at Metal/Nonmetal Interfaces. *J. Heat Transfer* **2014**, *136*, 092401.
(41) Cheaito, R.; Gaskins, J. T.; Caplan, M. E.; Donovan, B. F.; Foley, B. M.; Giri, A.; Duda, J. C.; Szwejkowski, C. J.; Constantin, C.; Brown-Shaklee, H. J.; Ihlefeld, J. F.; Hopkins, P. E. Thermal boundary conductance accumulation and interfacial phonon transmission: Measurements and theory. *Phys. Rev. B: Condens. Matter Mater. Phys.* **2015**, *91*, 035432.



DOI: 10.1021/acsami.8b01190
*ACS Appl. Mater. Interfaces* 2018, 10, 15232−15239

ACS APPLIED MATERIALS & INTERFACES

Research Article

Cite This: ACS Appl. Mater. Interfaces 2018, 10, 30827−30836

www.acsami.org

# Supported Two-Dimensional Materials under Ion Irradiation: The Substrate Governs Defect Production

Silvan Kretschmer,*[,†] Mikhail Maslov,[†,‡] Sadegh Ghaderzadeh,[†] Mahdi Ghorbani-Asl,[†] Gregor Hlawacek,[†] and Arkady V. Krasheninnikov*[,†,§]

[†]Institute of Ion Beam Physics and Materials Research, Helmholtz-Zentrum Dresden-Rossendorf, 01328 Dresden, Germany

[‡]Moscow Institute of Physics and Technology, 141700 Dolgoprudny, Russia

[§]Department of Applied Physics, Aalto University, 00076 Aalto, Finland

Supporting Information

**ABSTRACT:** Focused ion beams perfectly suit for patterning two-dimensional (2D) materials, but the optimization of irradiation parameters requires full microscopic understanding of defect production mechanisms. In contrast to freestanding 2D systems, the details of damage creation in supported 2D materials are not fully understood, whereas the majority of experiments have been carried out for 2D targets deposited on substrates. Here, we suggest a universal and computationally efficient scheme to model the irradiation of supported 2D materials, which combines analytical potential molecular dynamics with Monte Carlo simulations and makes it possible to independently assess the contributions to the damage from backscattered ions and atoms sputtered from the substrate. Using the scheme, we study the defect production in graphene and $MoS_2$ sheets, which are the two most important and wide-spread 2D materials, deposited on a $SiO_2$ substrate. For helium and neon ions with a wide range of initial ion energies including those used in a commercial helium ion microscope (HIM), we demonstrate that depending on the ion energy and mass, the defect production in 2D systems can be dominated by backscattered ions and sputtered substrate atoms rather than by the direct ion impacts and that the amount of damage in 2D materials heavily depends on whether a substrate is present or not. We also study the factors which limit the spatial resolution of the patterning process. Our results, which agree well with the available experimental data, provide not only insights into defect production but also quantitative information, which can be used for the minimization of damage during imaging in HIM or optimization of the patterning process.

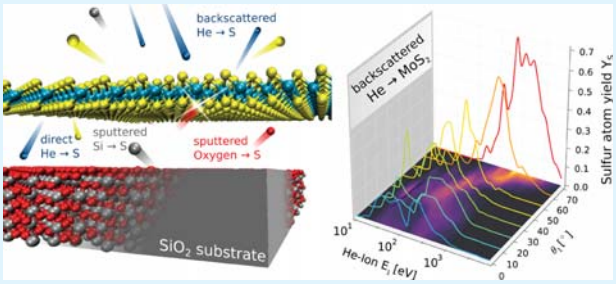


**KEYWORDS:** *two-dimensional materials, ion irradiation, atomistic simulations, defects, sputtering, He ion microscopy*

## INTRODUCTION

Ion irradiation[1,2] is one of the most powerful tools to change the atomic structure and properties of the materials through controllable introduction of impurities and defects. The technique suits particularly well for the processing of two-dimensional (2D) materials because of the small thickness of the system achieving a uniform distribution of dopants and defects with regard to their depth is not an issue, as evident from numerous examples for graphene[3−9] or transition-metal dichalcogenides (TMDs).[10−16] Moreover, exposure to energetic ions can be combined with in situ or postirradiation chemical treatment of these atomically thin targets[11,17−21] to incorporate foreign atoms into the atomic network due to chemically reactive vacancies.

Focused ion beams can be used to produce defects with high spatial resolution. They can also be employed for cutting and patterning 2D materials.[22] In this context, the He ion microscope (HIM),[23] where He or Ne ion beams have subnanometer diameters, has been demonstrated to be a perfect tool for not only getting insights into sample morphology but also altering its structure and geometry at the nanoscale. Specifically, structural defects were controllably introduced in a few-layer $MoS_2$ sample[15] so that its stoichiometry and electronic transport properties could be tuned. Nanoribbons with widths as small as 1 nm were reproducibly fabricated in graphene[4,6,9,24] and $MoS_2$ sheets,[15] and subnanometer nanopores were produced in $MoS_2$ monolayers,[25] which were used to study ionic transport through the sheets. An increase in Young's modulus of $MoSe_2$ samples irradiated in HIM was reported, along with the possibility to tune optical properties of TMDs.[26] Structural changes in freestanding graphene and that encapsulated between the sheets of hexagonal boron nitride under focused helium ion beam irradiation have been studied[27] in the HIM and showed the benefits of graphene encapsulation for postsynthesis doping and self-healing of the beam-induced lattice damage.

Received: May 23, 2018
Accepted: August 17, 2018
Published: August 17, 2018






DOI: 10.1021/acsami.8b08471
ACS Appl. Mater. Interfaces 2018, 10, 30827−30836

In the typical experimental setup used for ion bombardment, the 2D target is placed on a substrate, normally a $Si/SiO_2$ slab. However, the experimental data are frequently rationalized using atomistic computer simulations carried out for free-standing systems.[28−31] It is tacitly assumed that most of the defects are produced from direct interaction of the primary beam with the target, which, as we show below, is not generally true, especially for the case of light ion irradiation in the HIM. Indeed, the experiments carried out for supported and freestanding 2D $MoS_2$[32] and graphene[33] clearly indicate that there are substantial differences in the amount of beam-induced damage and the properties of irradiated samples.

In contrast to freestanding targets [e.g., graphene[34] or $MoS_2$ suspended on a transmission electron microscopy (TEM) grid[15,32]], where all the defects are created by the impinging ions, the substrate can affect defect production in several ways. Putting aside the case of highly charged ions[35] and swift heavy ions which literally "blow-up" the substrate so that the 2D material on top is torn apart by the atoms coming from the substrate,[36] defects in the 2D system can be produced at moderate ion energies by two other mechanisms, in addition to (i) direct ion impacts, (ii) backscattered ions,[a] and (iii) atoms sputtered from the substrate, as schematically illustrated in Figure 1. The latter two mechanisms are indirect defect

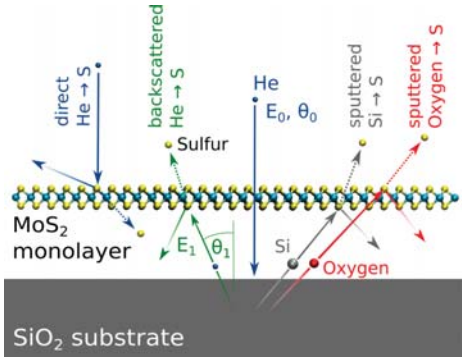


**Figure 1.** Schematic presentation of the channels for defect production in a supported 2D material under ion irradiation by the example of He ion impacts on a $MoS_2$ sheet on a $SiO_2$ substrate. Defects, for example, S vacancies, can be produced by direct ion impacts, by backscattered ions and atoms sputtered from the substrate.

production channels. Moreover, experimental investigations[9,33,37−39] using state-of-the-art focused ion beam technology indicate that the substrate hinders higher patterning resolutions, so that a detailed microscopic understanding of the role of the substrate and its effects on defect production under ion irradiation is required. The substrate also plays the key role in the evolution and annealing of defects.[40] Several attempts to account for the effects of the substrate have been carried out for high-energy (MeV) heavy ion[41] and 30 keV He[33] ion irradiation of supported graphene, but the trends and physical processes involved were not systematically analyzed. Computationally, this is a very challenging task, as first-principles approaches cannot be used because of the high computational costs required to collect representative statistics for systems composed from a few thousand atoms. Furthermore, analytical potentials developed for multiatomic systems are either of limited accuracy or are still computationally too expensive for adequate modeling of the system.

In this work, we suggest an efficient scheme to model the irradiation of supported 2D materials, which combines analytical potential molecular dynamics (MD) simulations for the 2D material, augmented with a universal repulsive potential to account for the effects of the substrate on sputtered atoms and a Monte Carlo (MC) method. This allows to independently assess the contributions to the damage from backscattered ions and atoms sputtered from the substrate and hitting the supported 2D system. Using the scheme, we study defect production in graphene and $MoS_2$ sheets, which are the two most widely used 2D materials, deposited on a $Si/SiO_2$ substrate. We pay particular attention to helium and neon ions because they are used in HIMs for material modification, nanopatterning, and imaging purposes.[23] Although for the patterning processes the controllable production of defects in a narrow region is desirable, minimal defect production should be aimed at for nondestructive imaging. Using our approach, we access the defect production rates of He, Ne, and Ar ions for a wide range of initial ion energies including the HIM typical energy interval from 1 to 30 keV. Our results indicate that in this energy range, defect production in graphene and $MoS_2$ is dominated by backscattered ions and sputtered substrate atoms rather than by the direct ion impacts. Consequently, the area in which defects are introduced is dramatically enlarged as compared to that in the freestanding irradiated material, and in the case of HIM-based irradiation, to the beam diameter (typically 0.5 and 1.8 nm for He and Ne, respectively).

## COMPUTATIONAL METHODS

**MD Simulations.** MD simulations were carried out using the LAMMPS[42] package to extract the statistics of defects produced by the impacts of the projectiles (He, Ne, and Ar ions, and Si and O atoms) onto the 2D materials (graphene and $MoS_2$ monolayers). The MD calculations of ion impacts onto targets were performed as described previously.[28] At least 320 impact points per energy and angle configuration were chosen. A modified Stillinger−Weber potential[43] with a smooth transition to the Ziegler−Biersack−Littmark (ZBL) potential[44] for small distances was used. For collisions of ions with the target atoms, the ZBL part dominates at high energies, so that the ZBL potentials were also used to describe the impacts of atoms sputtered from the substrate. This approximation is further validated by a rather weak interaction of O and Si adatoms with pristine graphene and $MoS_2$: the adatoms are mobile on graphene[45] and $MoS_2$[46] surfaces, so that they should form compounds and desorb from the system. The MD calculations for ion bombardment of graphene were carried out using the combined Tersoff and ZBL potential.

The simulation setup is presented in Figure 2. As we are aiming at assessing the effects of low-dose irradiation, we assumed that the ions always impinge into pristine material. To collect representative statistics for different impact points, an irreducible area was chosen as depicted in Figure 2c. The average number of defects produced by impinging and backscattered particles, along with those produced by sputtered substrate atoms, was obtained from MD simulations as functions of ion energy and angle.

The effects of the $SiO_2$ substrate were modeled as an external repulsive potential acting on the target atoms (Mo, S, or C) in the corresponding region (see Figure 2). The choice of the potential was motivated by the confining effect of the underlying substrate, which makes the presence of sputtered target atoms in the substrate region energetically unfavorable. The potential in this approximation can be expressed as

$$U(z) = A(e^{\beta(z-z_0)} - 1) \quad (1)$$



DOI: 10.1021/acsami.8b08471
ACS Appl. Mater. Interfaces 2018, 10, 30827−30836

ACS Applied Materials & Interfaces Research Article

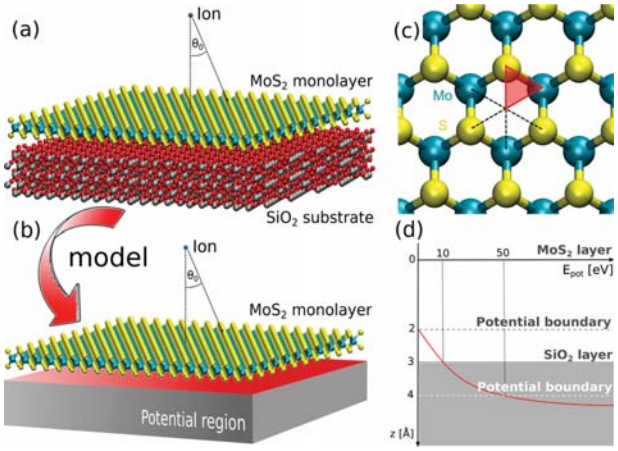


**Figure 2.** Simulation setup. (a) Atomistic model of $MoS_2$ on a $SiO_2$ substrate. (b) Corresponding system where the substrate is modeled using an external potential. (c) Definition of minimal irreducible area used for choosing the ion impact points. (d) External potential acting on the atoms of the 2D target. The $MoS_2$ is positioned at zero $z$ coordinate.

where the coefficients are determined by the boundary of the potential region $z_0$ = 2 Å, the surface approximation energy—the energy required to approach a surface located at $d$ = 3 Å (distance from the monolayer derived from first-principles calculations)[47] from infinity $U(z = d)$ = 10 eV, and a defined kinetic energy loss of the incident particle with $U(z = 4\ Å)$ = 50 eV. This yields the coefficients $A$ = 10/3 eV ≈ 3.33 eV and $\beta$ = 2 ln 2 $Å^{-1}$ ≈ 1.38 $Å^{-1}$. The choice of the parameters is not unique and depends on the target material−substrate pair, but our calculations with slightly different parameters gave qualitatively similar results. As for other simplifications, for sputtered target atoms (e.g., S) with high energies, our approach disregards the fact that the atoms may be captured by the substrate: instead in the current model, it will be reflected and may act as a secondary projectile and create defects, but the probability for this process is very small. Another possible artifact of our approach is that adsorption on the substrate is not taken properly into account. However, in this case, the atoms are trapped between the 2D material and the substrate, and this does not influence defect production.

The potential has no effect on the impinging ions, whereas backscattered ions were treated using a statistical approach with the data collected from the MC simulations. Splitting defect production into two different channels is possible because of a very small probability for the backscattered ions and sputtered atoms to hit the area where defects were already produced by that same ion. Because of the geometry of the system, we independently considered defect production by the ions coming from *above* the 2D target, with ion velocity vectors pointing toward the substrate (direct impacts), and from *below*, with ion velocity vectors pointing away from the substrate (the case for backscattered ions and sputtered substrate atoms).

**MC Simulations.** The MD approach was combined with the MC method implemented in the TRIDYN code[48,49] to account for projectile properties and their statistics (e.g., backscattering

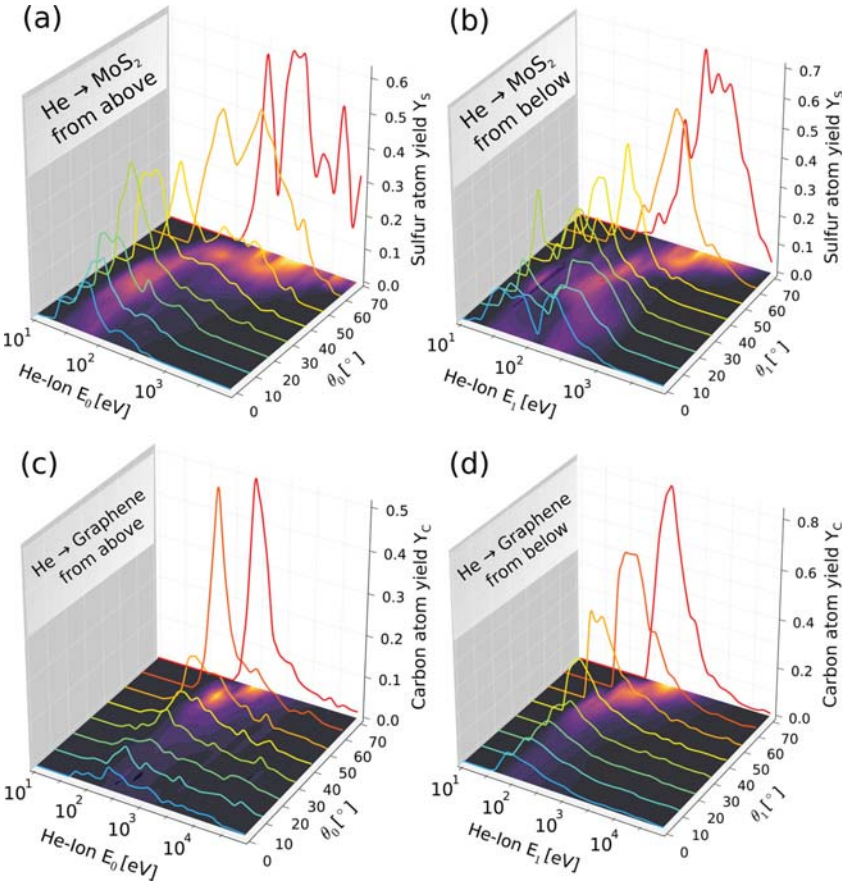


**Figure 3.** Number of atoms sputtered from the supported monolayer $MoS_2$ and graphene by energetic He ions as obtained from MD simulations. Impacts of He atoms onto $MoS_2$ from above (a) and below (b). Impacts of He atoms into graphene from above (c) and below (d). Angles $\theta_0$ and $\theta_1$ are defined in Figure 1.



DOI: 10.1021/acsami.8b08471
ACS Appl. Mater. Interfaces 2018, 10, 30827−30836

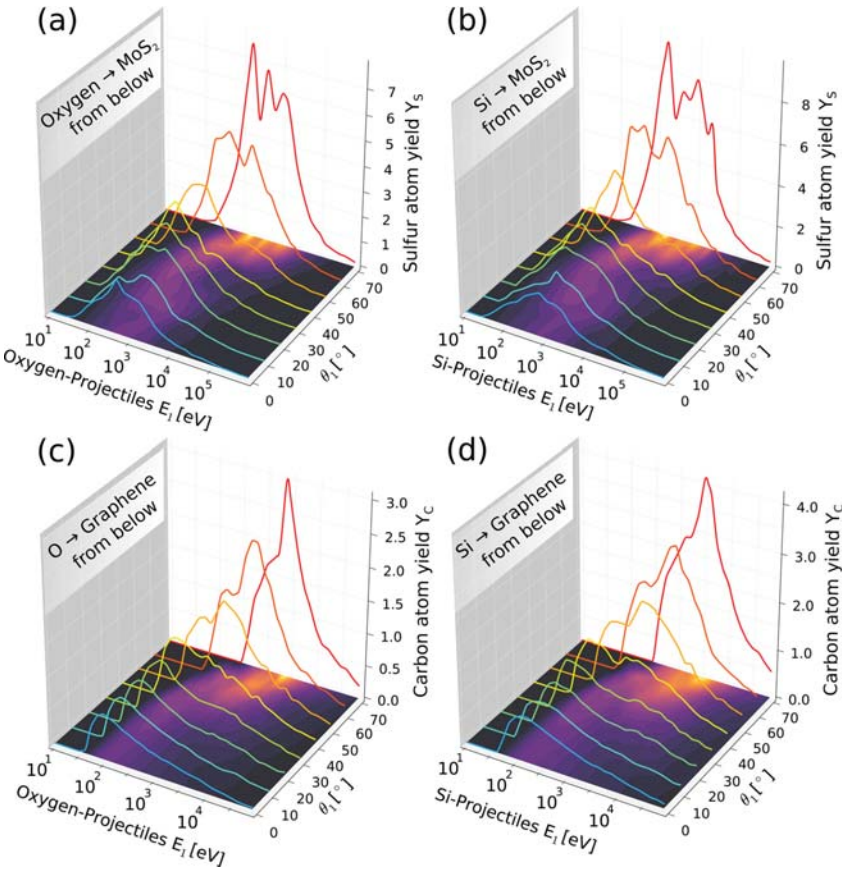


**Figure 4.** Number of atoms sputtered from the supported monolayer $MoS_2$ and graphene by O and Si projectiles hitting the sheets from below as obtained from MD simulations. Impacts of O (a) and Si (b) projectiles onto $MoS_2$. Impacts of O (c) and Si (d) projectiles onto graphene.

probability, energy, and angle distributions). Simulation runs are performed for normal ion incident on a $SiO_2$ layer with a thickness of 1 $\mu$m, and 5 million ions per incident energy. We performed the calculations with the TRIDYN code because it gives more accurate results with respect to the sputtering yield and the angular and energy distribution of the recoils, as compared to the more popular SRIM code.[50] The dependence of the sputtering yield on the surface binding energy was carefully tested, see Figure S2. A value of $E_{surf,oxygen}$ = 2.0 eV is picked, which is the tabulated value for $SiO_2$ in SRIM[50] and known to produce results in accordance with experimental findings. The MD and MC approaches were combined by treating the impacts of the projectiles on the 2D target material in detail with MD (accessing small length scales), whereas the projectile statistics was sampled according to the results of the MC calculations (covering larger length scales).

## RESULTS AND DISCUSSION

**He Ion Irradiation.** The results for He ions are presented in Figure 3. It is evident that the number of sputtered S and C atoms increases with ion energy and then quickly drops because of a decrease in the cross section to displace an atom from the 2D target. This is in agreement with the results of previous calculations.[28,29] The atoms sputtered from the substrate are more abundant than backscattered ions for typical HIM energies. Detailed statistics data of projectile characteristics obtained from the MC data, such as energy and angle probability distributions, can be found in the supplementary material. The number of sputtered atoms also depends on the incidence angle, with the maximum in defect production being shifted toward higher ion energies for off-normal incidence.

We performed similar MD calculations for the impacts of O and Si projectiles onto $MoS_2$ and graphene sheets. Only impacts from "below" were considered. The results are presented in Figure 4. The production of defects shows similar trends as for He ions, but the number of sputtered atoms is considerably higher because of larger atomic masses of O and Si atoms as compared to He.

On the basis of the calculated number of atoms sputtered from $MoS_2$ and graphene sheets per single impact of He, O, and Si projectiles, we evaluated the average number of defects produced in the system by He ion irradiation. To match the usual experimental geometry, normal incidence of He ions was assumed. Using the MC approach, we obtained the number of backscattered He ions as well as sputtered O and Si atoms from the substrate as functions of initial energy of He ions. Using MD simulations, we also assessed the number of ions which have passed through the sheet, which is different from unity at energies below 1 keV. The results for $MoS_2$ sheet are shown in Figure 5.

By combining the MD and MC data, the average number of sputtered target atoms $\langle N_{total} \rangle$ (Mo and S for $MoS_2$ and C for graphene) can now be calculated as

$$\langle N_{total} \rangle = \langle N_{direct}(\mathrm{He}) \rangle + \langle N_{BS}(\mathrm{He}) \rangle + \langle N_{SP}(\mathrm{Si, O}) \rangle \quad (2)$$



DOI: 10.1021/acsami.8b08471
ACS Appl. Mater. Interfaces 2018, 10, 30827−30836

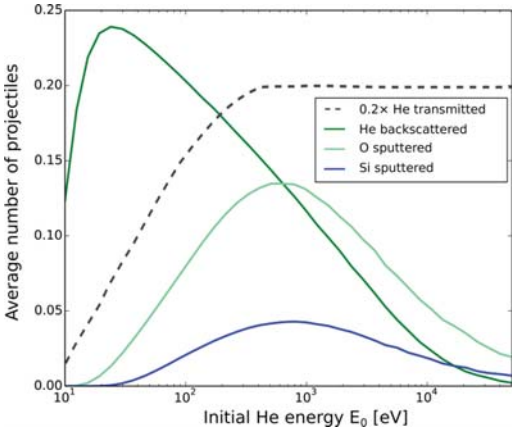


**Figure 5.** Number of He ions which have passed through the $MoS_2$ sheet, the number of ions backscattered by the $SiO_2$ substrate, along with the number of sputtered O and Si atoms as functions of initial He ion energy as obtained from MC calculations. Note that for better visualization, the transmission probability of He ions through monolayer $MoS_2$ is scaled by a factor of 0.2.

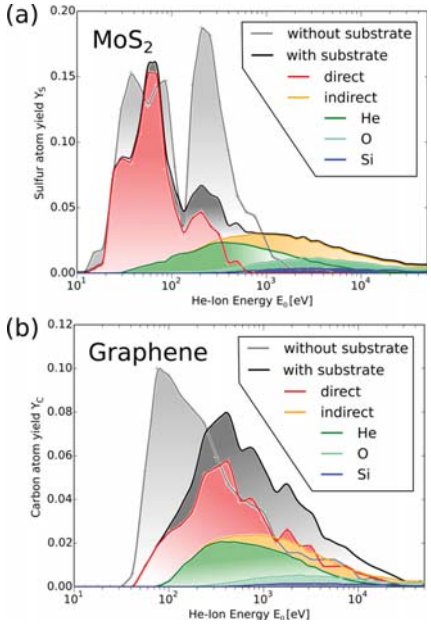


**Figure 6.** Average number of atoms sputtered from $MoS_2$ (a) and graphene (b) per He ion impact. The corresponding numbers for freestanding monolayers (gray) and the direct sputtering (red) are shown for comparison.

where $\langle N_{direct}(He)\rangle$ is the average number of directly sputtered atoms per He ion and $\langle N_{BS}(He)\rangle$ and $\langle N_{SP}(Si,O)\rangle$ are the contributions from the backscattered ions and sputtered substrate atoms, respectively. The average number of created S-vacancies from direct impacts is given by $\langle N_{direct}\rangle = \langle N_{above}(E_0,\theta_0 = 0)\rangle$, where $\langle N_{above}\rangle$ is derived from MD simulations with an impacting ion starting in the upper half plane with the velocity pointing toward the substrate (see the blue trajectory in Figure 1). The average number of S-vacancies created by backscattered ions $\langle N_{BS}(E_0)\rangle$ in turn is estimated by averaging the overall possible trajectories (defined by energies and angles $E_1$, $\theta_1$) of the backscattered ions. This is realized by performing the probability distribution-weighted integration of the average number of defects $\langle N_{below}(E_1,\theta_1)\rangle$ (see green trajectory in Figure 1) over the energies and angles of the backscattered particles. The integral is further multiplied by the probability $P_{BS}(E_0)$ for the ion to be backscattered and hit the 2D target again and the transmission probability $T(E_0)$ to obtain the average number of sputtered S atoms

$$\langle N_{BS}(E_0)\rangle = T(E_0)\cdot P_{BS}(E_0)\cdot \int dE_1 p_{BS}(E_1|E_0)\cdot \int d\theta_1 p_{BS}(\theta_1)\langle N_{below}(E_1,\theta_1)\rangle \quad (3)$$

where $p_{BS}(\theta_1)$ and $p_{BS}(E_1|E_0)$ are the angular and energy probability distributions of the backscattered ions, respectively. The latter depends on the incident ion energy $E_0$, whereas the former is universal.

A similar expression can be used to evaluate the effects of sputtered atoms $\langle N_{SP}(E_0)\rangle$ on vacancy production with the backscattering probability replaced by the average number of sputtered atoms and summing over the contributions from Si and O atoms (gray and red trajectories in Figure 1).

The results obtained with the combined MD and MC approaches are presented in Figure 6. The data for damage production by direct impacts and the data for the freestanding materials are obtained directly from MD simulations carried out for the same setup. The results for freestanding systems agree well with the previously published data.[28,29] As for $MoS_2$, the average number of sputtered S-atoms for He irradiation without the substrate shows two pronounced peaks which can be attributed to sputtering from the top and bottom sulfur layers.[28] The data for direct He ion impacts also show two peaks, but the second one (corresponding to higher energies) is considerably suppressed, meaning that the substrate reduces the forward sputtering for the bottom layer. This is supported by the average number of S vacancies per layer obtained by analyzing the defect density and defect locations after the ion impacts.

As compared to the freestanding system, the direct defect production in supported $MoS_2$ is overall smaller for ion energies below 800 eV. This is a consequence of the reduced sputtering from S-layer facing the substrate. The S recoils generated there (in forward direction) cannot easily leave the sample. Furthermore, for typical HIM energies, see Figure 6a, for almost all energies in the relevant interval (from 1 to 30 keV), direct sputtering is completely absent, whereas defect production is still noticeable in the supported system. In this energy range, indirect sputtering and more specifically sputtering by backscattered ions for lower energies (below 2 keV for $MoS_2$) and sputtered substrate atoms for higher energies can clearly be identified as the dominant damage mechanism. Within the binary collision approximation, the large mass ratio of Mo to He atom $m_{Mo}/m_{He} = 24$ explains the negligible number of sputtered Mo atoms found in the combined MC/MD simulations for both direct and indirect sputtering.

Figure 6b illustrates the defect production in freestanding and supported graphene. It is evident that as in $MoS_2$, the substrate impedes the production of defects at very low energies, but the effect is stronger than that in $MoS_2$, as graphene has only one layer of atoms. At high ion energies, more defects are produced in the supported system with a substantial contribution from backscattered ions. The bird's-



DOI: 10.1021/acsami.8b08471
ACS Appl. Mater. Interfaces 2018, 10, 30827−30836

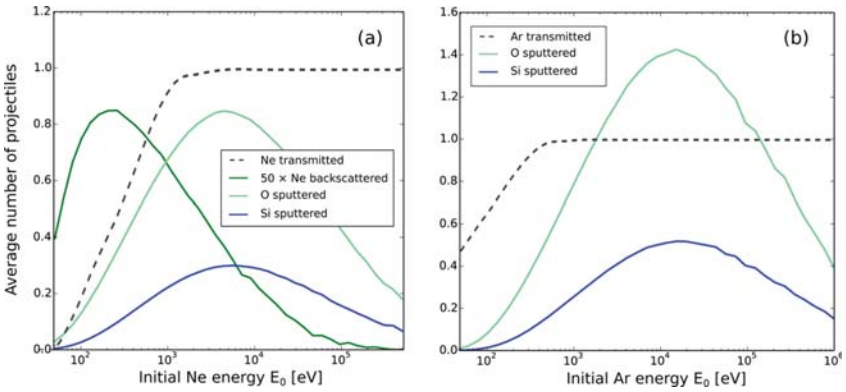


**Figure 7.** Transmitted and backscattered ions along with the sputtered substrate atoms as functions of ion energies for Ne (a) and Ar (b). Note that the average number of backscattered ions for Ne is scaled by a factor of 50.

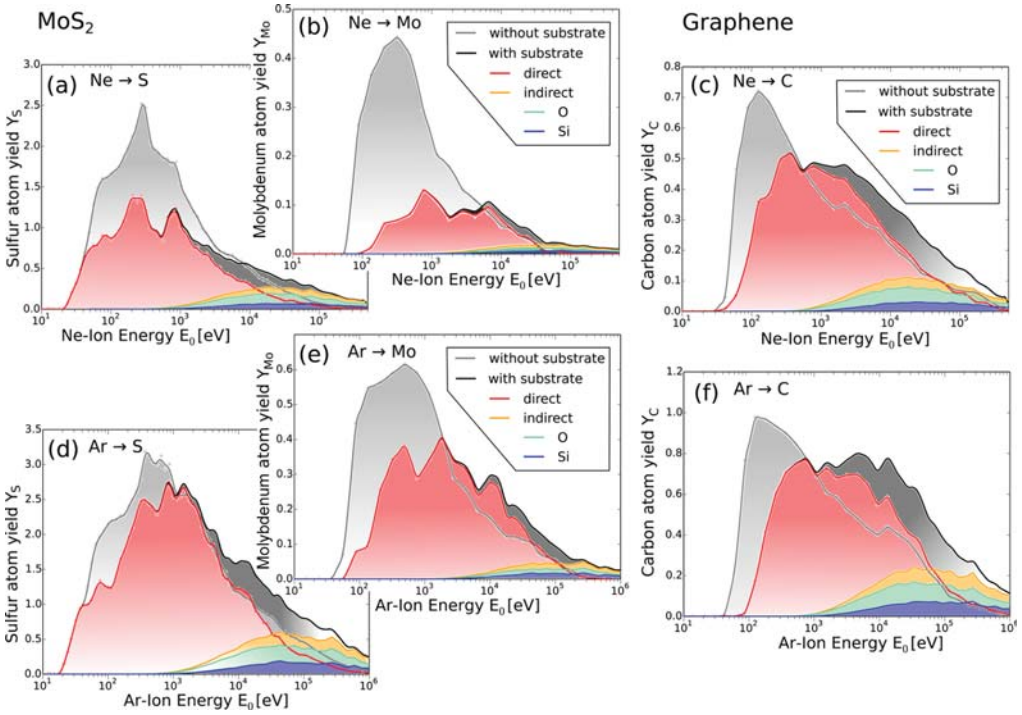


**Figure 8.** Average number of sputtered atoms from $MoS_2$ (left) and graphene (right panels) for Ne (a–c) and Ar (d–f) impacts. The corresponding numbers for freestanding monolayers (grey) are shown for comparison.

eye view on the defect production mechanisms of He-irradiated $MoS_2$ reveals that the substrate has a dramatic influence on the atom-sputtering rate. For $MoS_2$, the sputtering rate is approximately 5 times larger than without the substrate in the HIM energy interval. A similar behavior is observed for graphene. Such an increase in the damage rate was also found experimentally for He ion bombardment of graphene supported by a $Si/SiO_2$ substrate.[33]

**Ne Ion and Ar Ion Irradiation.** Similar to the modeling of He ion irradiation, we carried out simulations of the impacts of heavier Ne and Ar ions onto a supported $MoS_2$ sheet. We found that the number of backscattered ions decreases dramatically as compared to helium, whereas the average number of sputtered substrate atoms increases, see Figure 7. In particular, the probability for Ne ions to be backscattered from the $SiO_2$ substrate is less than 1% for all the energies and is zero for Ar. Both observations can be understood within binary collision approximation considering the projectile-to-target mass ratio, as backscattering is more likely for lighter ions, and the momentum transfer to secondary projectiles is more efficient for a mass ratio close to unity ($m_{He}/m_{Si}$ = 0.14, $m_{Ne}/m_{Si}$ = 0.71, and $m_{Ar}/m_{Si}$ = 1.42). As expected, for an increasing ion mass, the maximum of the sputtering yield shifts to higher energies.

Figure 8 illustrates the effects of the substrate on the defect production for $MoS_2$ and graphene. The results for free-standing monolayers are also presented for the sake of comparison. The data for freestanding monolayers, shown as a reference, agree well with previously published results for noble gas ion bombarded $MoS_2$ and graphene.[28,29] Following from the data on the abundance of the available projectiles, Figure 7, the contribution to the damage in the 2D target from



DOI: 10.1021/acsami.8b08471
ACS Appl. Mater. Interfaces 2018, 10, 30827–30836

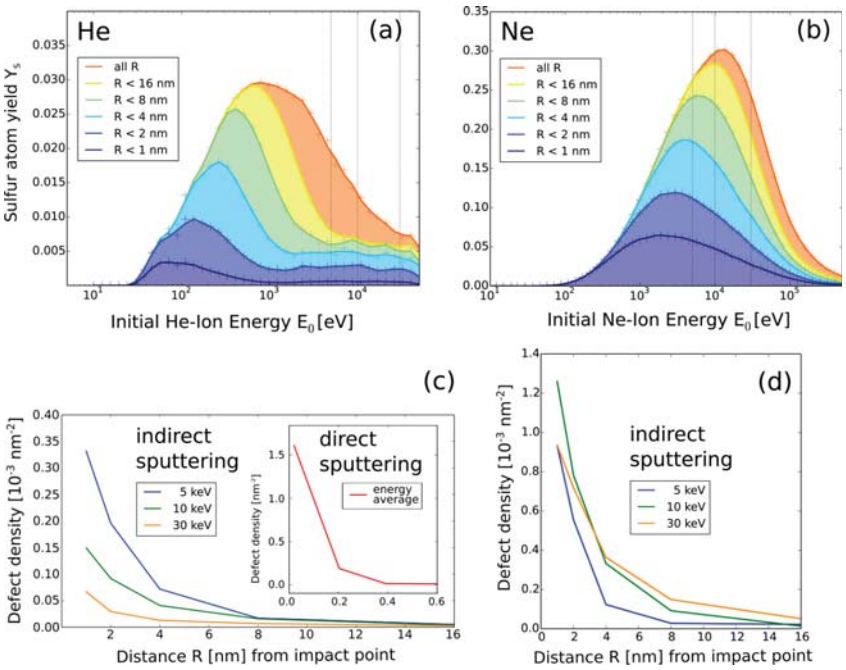


**Figure 9.** Spatial distribution of defects. The average number of S atoms sputtered by backscattered He, Ne ions and Si, O atoms originating from different regions with respect to the impact point. Panels (a,b) show the indirect defect production for different radii from the impact point for He and Ne ions, respectively. Panel (c) depicts the defect density for three selected energies taken as cross sections in panel (a) (dashed vertical lines). Defect density with respect to the impact point is compared to that obtained by direct sputtering (inset), showing increased extension of the defect region for indirect sputtering. Panel (d) shows the indirect defect density for neon ions.

backscattered particles is negligible, and defect production process is governed by direct impacts of ions and by atoms sputtered from the substrate.

A salient feature is the suppression of defect production at low ion energies, as the substrate "stops", the atoms sputtered away from the target and increases the probability for immediate recombination of the vacancy−interstitial pair. It is also evident from Figure 8 that although the total sputtering yield increases because of the higher ion mass, the enhancement in the indirect sputtering of target atoms is less pronounced than the boost in direct sputtering. This means that for heavier ions, the effect of the substrate on defect production is smaller. Nevertheless, as panels (a−c) in Figure 8—illustrating sputtering of S, Mo, and C atoms by Ne—demonstrate, the combined effect of direct and indirect sputtering is twice as large as the sputtering yield without the substrate in the energy range relevant for HIM (from 1 to 30 keV). This indicates that for neon in the HIM, the substrate still plays an important role, whereas the processes which enhance or diminish sputtering compensate each other in the case of argon irradiation, as panels (d−f) in Figure 8 illustrate. For the latter, a substantial increase in the sputtering yield because of the presence of a substrate cannot be observed.

**Spatial Distribution of Defects.** The substrate not only influences the number of defects produced under ion bombardment but also has an important impact on the spatial distribution of defects. From the application point of view, the spatial extension of the defect region in supported 2D materials is of paramount importance, as it determines the resolution of the HIM during patterning of 2D materials. Our combined MC/MD simulations provide direct access to the spatial distribution of defects with respect to the impact point of the ion. Although the impinging ions produce defects only in the immediate vicinity of the impact point (1 nm range; see the inset in panel (c) of Figure 9), the backscattered ions and atoms sputtered from the substrate give rise to the production of defects in a wider region, with the average extension of the region being dependent on initial energy of He (or Ne) ions.

For both He and Ne ions with energies below 1 keV, almost all sulfur vacancies are produced within an 8 nm radius from the impact point. However, for typical HIM energies, the defective region is more extended: up to two-thirds of the defects are produced outside the 8 nm region, as is evident from Figure 9, panels (a) and (b). Although the defect density decays rapidly with an increasing distance $R$ from the impact point, defects can be created at typical HIM energies even outside the 10 nm range. As compared to the freestanding material, where defects are expected only in the close vicinity of the impact point, this result agrees well with the previous experimental observations and indicates that backscattered ions and sputtered substrate atoms are the main reason for resolution limitations in patterning of supported 2D materials.[9,37,39] It is interesting to note that spatial extend of the damage also depends on ion mass. As evident from our results (see Figure 9), higher energies (e.g., 30 keV) would give a better spatial resolution for He, whereas it is the other way around for Ne. For the latter, the lowest energies still attainable in HIM (e.g., 5 keV) are preferable.

**Comparison to Experimental Results.** To validate our approach, we analyzed the available experimental data on the amount of damage produced in the supported graphene and $MoS_2$ under ion irradiation. It should be pointed out that the direct comparison of the theoretical and experimental defect densities is not straightforward. On the one hand, in situ annealing of defects even at room temperature is possible, and on the other hand, at high irradiation doses, more defects can



DOI: 10.1021/acsami.8b08471
ACS Appl. Mater. Interfaces 2018, 10, 30827−30836

be produced, when defects already exist in the area where the ion hits the sample. Neither of these effects can easily be accounted for in simulations, but one can assume that they cancel each other to the first order. The accurate determination of defect concentrations in the experiments from Raman spectra or energy-dispersive X-ray spectroscopy data is also a challenge.

Irradiation of freestanding $MoS_2$ flakes by 30 keV He ions gave rise to the loss of about 50% of the S atoms at a dose of $10^{18}$ $He^+/cm^2$, whereas an order of magnitude smaller dose was required for the sample on a substrate.[15] Our results (Figure 6) indicate that $Y \approx 0.008$ S atoms are on average sputtered away by a 30 keV He ion. A dose of $10^{17}$ $He^+/cm^2$ corresponds to $N_I \approx 90$ ions hitting the primitive cell area. Correspondingly, the relative number of atoms which should still remain in the system is $(2 - Y \cdot N_I)/2 \approx 0.6$, which is in very good agreement with the experimental data.

As for He ion irradiation of graphene in HIM, our simulations indicated that the number of defects should be larger in the supported samples (as compared to freestanding) by a factor of about 3, which qualitatively agrees with the experimental ratio[33] for doses below $10^{15}$ $He^+/cm^2$. Our results for 500 eV Ar irradiation on $MoS_2$ were also in the order-of-magnitude agreement with the dose (about $5 \times 10^{15}$ $Ar^+/cm^2$) required to sputter ca. 25% of the S atoms.[19] The agreement with the published experimental values for higher Ar energies is even more striking: although for bilayer graphene on $SiO_2$ substrate irradiated with 100 keV argon ions a carbon sputtering yield of 0.25 atoms per ion in the top layer (0.13 because of enhanced annealing in the second layer) is determined in the experiment,[40] our results—not accounting for annealing effects—yield 0.28 carbon atoms per Ar ion. For freestanding system, the model suggests only half of this value. Furthermore, our predictions for graphene are consistent with the data extracted by Li et al.[41] from the Raman spectra of irradiated graphene samples: the sputtering yield in graphene bombarded with 35 keV carbon ions is estimated as 0.15 C atoms per incident ion,[51] which is slightly smaller than our predicted value of 0.22 C atoms per (slightly heavier) Ne ion. A similar observation can be made for graphene irradiated with 30 keV N ions (0.186 atoms/ion),[52] which is in line with our simulation results for 30 keV Ne ions (0.25 atoms/ion). In both cases, the calculated sputtering yield of C atoms for freestanding graphene samples is much smaller than the experimental value.

## CONCLUSIONS

We suggested a computationally efficient scheme which combines analytical potential MD and MC simulations to model the irradiation of supported 2D materials. The scheme makes it possible to independently assess the contributions to the damage from backscattered ions and atoms sputtered from the substrate. The approach can in principle be applied to any 2D material−substrate combination, provided that the potential for the 2D target exists. The method does not require to account explicitly for the interaction of the substrate material with the target, as the substrate is replaced by an effective repulsive potential. Using this scheme, we studied defect production in graphene and $MoS_2$ sheets on a $SiO_2$ substrate. Our results, which agree well with the available experimental data, demonstrate that, depending on the ion mass and energy, the number of defects produced in the target by the impinging ions can be smaller or larger than in the freestanding material, which is deposited on top of a trench in the substrate or on a TEM grid. For helium and neon ions with a wide range of initial ion energies including those used in HIM, we showed that the energy defect production in 2D systems can be dominated by backscattered ions and sputtered substrate atoms rather than by the direct ion impacts. The last statement is especially true for light ions. In particular, this is the case for 30 keV He ions, most widely used for imaging and patterning of 2D targets using HIM. We also studied the factors which limit the spatial resolution of the patterning process. Our results provide microscopic insights into defect production mechanism, along with the quantitative information, which can be used for the minimization of damage during imaging or optimization of the patterning process.

## ASSOCIATED CONTENT

### Supporting Information

The Supporting Information is available free of charge on the ACS Publications website at DOI: 10.1021/acsami.8b08471.

Energy and angular distribution from MC (TRIDYN) simulations, influence of surface binding energy on the sputtering yield, and influence of substrate thickness on the sputtering yield (PDF)

## AUTHOR INFORMATION


### Corresponding Authors

*E-mail: s.kretschmer@hzdr.de (S.K.).
*E-mail: a.krasheninnikov@hzdr.de (A.V.K.).

### ORCID

Silvan Kretschmer: 0000-0002-5098-5763
Mahdi Ghorbani-Asl: 0000-0003-3060-4369
Gregor Hlawacek: 0000-0001-7192-716X
Arkady V. Krasheninnikov: 0000-0003-0074-7588


### Notes

The authors declare no competing financial interest.

## ACKNOWLEDGMENTS

The authors thank Dr. S. Facsko and Prof. W. Möller for discussions. They acknowledge funding from the German Research Foundation (DFG), project KR 4866, and the European Commission H-2020 programme under the grant agreement no. 720964. A.V.K. further thanks the Academy of Finland for the support under project no. 286279. The computational support from the HZDR computing cluster is gratefully appreciated.

## ADDITIONAL NOTE

[a]The charge state of the projectile cannot be accounted for in the classical MD simulations, and its value at each moment of time is generally unknown. Therefore, just to differentiate between the target/substrate atoms and primary projectiles, we refer to the former as "atoms" and the latter as "ions".

## REFERENCES

(1) Nastasi, M.; Mayer, J.; Hirvonen, J. *Ion−Solid Interactions—Fundamentals and Applications*; Cambridge University Press, 1996.
(2) *Materials Science with Ion Beams*; Bernas, H., Ed.; Springer, 2010.
(3) Archanjo, B. S.; Barboza, A. P. M.; Neves, B. R. A.; Malard, L. M.; Ferreira, E. H. M.; Brant, J. C.; Alves, E. S.; Plentz, F.; Carozo, V.; Fragneaud, B.; Maciel, I. O.; Almeida, C. M.; Jorio, A.; Achete, C. A. The use of a $Ga^+$ focused ion beam to modify graphene for device applications. *Nanotechnology* **2012**, *23*, 255305.



DOI: 10.1021/acsami.8b08471
*ACS Appl. Mater. Interfaces* 2018, 10, 30827−30836

(4) Lemme, M. C.; Bell, D. C.; Williams, J. R.; Stern, L. A.; Baugher, B. W. H.; Jarillo-Herrero, P.; Marcus, C. M. Etching of Graphene Devices with a Helium Ion Beam. *ACS Nano* **2009**, *3*, 2674−2676.
(5) Kalhor, N.; Boden, S. A.; Mizuta, H. Sub-10nm patterning by focused He-ion beam milling for fabrication of downscaled graphene nano devices. *Microelectron. Eng.* **2014**, *114*, 70−77.
(6) Bell, D. C.; Lemme, M. C.; Stern, L. A.; Williams, J. R.; Marcus, C. M. Precision Cutting and Patterning of Graphene with Helium Ions. *Nanotechnology* **2009**, *20*, 455301.
(7) Standop, S.; Lehtinen, O.; Herbig, C.; Lewes-Malandrakis, G.; Craes, F.; Kotakoski, J.; Michely, T.; Krasheninnikov, A. V.; Busse, C. Ion Impacts on Graphene/Ir(111): Interface Channeling, Vacancy Funnels, and a Nanomesh. *Nano Lett.* **2013**, *13*, 1948−1955.
(8) Madauss, L.; Ochedowski, O.; Lebius, H.; Ban-d'Etat, B.; Naylor, C. H.; Johnson, A. T. C.; Kotakoski, J.; Schleberger, M. Defect Engineering of Single- and Few-Layer MoS2 by Swift Heavy Ion Irradiation. *2D Materials* **2017**, *4*, 015034.
(9) Nanda, G.; Hlawacek, G.; Goswami, S.; Watanabe, K.; Taniguchi, T.; Alkemade, P. F. A. Electronic Transport in Helium-Ion-Beam Etched Encapsulated Graphene Nanoribbons. *Carbon* **2017**, *119*, 419−425.
(10) Wang, D.; Wang, Y.; Chen, X.; Zhu, Y.; Zhan, K.; Cheng, H.; Wang, X. Layer-by-layer Thinning of Two-Dimensional Mos2 Films by Using a Focused Ion Beam. *Nanoscale* **2016**, *8*, 4107−4112.
(11) Stanford, M. G.; Pudasaini, P. R.; Cross, N.; Mahady, K.; Hoffman, A. N.; Mandrus, D. G.; Duscher, G.; Chisholm, M. F.; Rack, P. D. Tungsten Diselenide Patterning and Nanoribbon Formation by Gas-Assisted Focused-Helium-Ion-Beam-Induced Etching. *Small Methods* **2017**, *1*, 1600060.
(12) Bertolazzi, S.; Bonacchi, S.; Nan, G.; Pershin, A.; Beljonne, D.; Samorì, P. Engineering Chemically Active Defects in Monolayer MoS2 Transistors via Ion-Beam Irradiation and Their Healing via Vapor Deposition of Alkanethiols. *Adv. Mater.* **2017**, *29*, 1606760.
(13) Chow, P. K.; Jacobs-Gedrim, R. B.; Gao, J.; Lu, T.-M.; Yu, B.; Terrones, H.; Koratkar, N. Defect-Induced Photoluminescence in Monolayer Semiconducting Transition Metal Dichalcogenides. *ACS Nano* **2015**, *9*, 1520−1527.
(14) Lin, Z.; Carvalho, B. R.; Kahn, E.; Lv, R.; Rao, R.; Terrones, H.; Pimenta, M. A.; Terrones, M. Defect Engineering of Two-Dimensional Transition Metal Dichalcogenides. *2D Materials* **2016**, *3*, 022002.
(15) Fox, D. S.; Zhou, Y.; Maguire, P.; O'Neill, A.; Ó'Coileáin, C.; Gatensby, R.; Glushenkov, A. M.; Tao, T.; Duesberg, G. S.; Shvets, I. V.; Abid, M.; Abid, M.; Wu, H.-C.; Chen, Y.; Coleman, J. N.; Donegan, J. F.; Zhang, H. Nanopatterning and Electrical Tuning of MoS2 Layers with a Subnanometer Helium Ion Beam. *Nano Lett.* **2015**, *15*, 5307−5313.
(16) Ma, L.; Tan, Y.; Ghorbani-Asl, M.; Boettger, R.; Kretschmer, S.; Zhou, S.; Huang, Z.; Krasheninnikov, A. V.; Chen, F. Tailoring the optical properties of atomically-thin WS2via ion irradiation. *Nanoscale* **2017**, *9*, 11027−11034.
(17) Wei, X.; Wang, M.-S.; Bando, Y.; Golberg, D. Electron-Beam-Induced Substitutional Carbon Doping of Boron Nitride Nanosheets, Nanoribbons, and Nanotubes. *ACS Nano* **2011**, *5*, 2916−2922.
(18) Wang, H.; Wang, Q.; Cheng, Y.; Li, K.; Yao, Y.; Zhang, Q.; Dong, C.; Wang, P.; Schwingenschlögl, U.; Yang, W.; Zhang, X. X. Doping Monolayer Graphene with Single Atom Substitutions. *Nano Lett.* **2012**, *12*, 141−144.
(19) Ma, Q.; Odenthal, P. M.; Mann, J.; Le, D.; Wang, C. S.; Zhu, Y.; Chen, T.; Sun, D.; Yamaguchi, K.; Tran, T.; Wurch, M.; McKinley, J. L.; Wyrick, J.; Magnone, K.; Heinz, T. F.; Rahman, T. S.; Kawakami, R.; Bartels, L. Controlled Argon Beam-Induced Desulfurization of Monolayer Molybdenum Disulfide. *J. Phys.: Condens. Matter* **2013**, *25*, 252201.
(20) Ma, Q.; Isarraraz, M.; Wang, C. S.; Preciado, E.; Klee, V.; Bobek, S.; Yamaguchi, K.; Li, E.; Odenthal, P. M.; Nguyen, A.; Barroso, D.; Sun, D.; von Son Palacio, G.; Gomez, M.; Nguyen, A.; Le, D.; Pawin, G.; Mann, J.; Heinz, T. F.; Rahman, T. S.; Bartels, L. Postgrowth Tuning of the Bandgap of Single-Layer Molybdenum Disulfide Films by Sulfur/Selenium Exchange. *ACS Nano* **2014**, *8*, 4672−4677.
(21) Li, H.; Daukiya, L.; Haldar, S.; Lindblad, A.; Sanyal, B.; Eriksson, O.; Aubel, D.; Hajjar-Garreau, S.; Simon, L.; Leifer, K. Site-selective Local Fluorination of Graphene Induced by Focused Ion Beam Irradiation. *Sci. Rep.* **2016**, *6*, 19719.
(22) Krasheninnikov, A. V.; Nordlund, K. Ion and Electron Irradiation-Induced Effects in Nanostructured Materials. *J. Appl. Phys.* **2010**, *107*, 071301.
(23) Hlawacek, G.; Veligura, V.; Gastel, R. V.; Poelsema, B.; Hlawacek, G.; Veligura, V.; Gastel, R. V.; Poelsema, B. Helium Ion Microscopy. *J. Vac. Sci. Technol., B: Microelectron. Nanometer Struct.–Process., Meas., Phenom.* **2014**, *32*, 020801.
(24) Schmidt, M. E.; Iwasaki, T.; Muruganathan, M.; Haque, M.; Van Ngoc, H.; Ogawa, S.; Mizuta, H. Structurally Controlled Large-Area 10 nm Pitch Graphene Nanomesh by Focused Helium Ion Beam Milling. *ACS Appl. Mater. Interfaces* **2018**, *10*, 10362−10368.
(25) Thiruraman, J. P.; Fujisawa, K.; Danda, G.; Das, P. M.; Zhang, T.; Bolotsky, A.; Perea-López, N.; Nicolaï, A.; Senet, P.; Terrones, M.; Drndić, M. Angstrom-Size Defect Creation and Ionic Transport through Pores in Single-Layer MoS2. *Nano Lett.* **2018**, *18*, 1651−1659.
(26) Iberi, V.; Liang, L.; Ievlev, A. V.; Stanford, M. G.; Lin, M.-W.; Li, X.; Mahjouri-Samani, M.; Jesse, S.; Sumpter, B. G.; Kalinin, S. V.; Joy, D. C.; Xiao, K.; Belianinov, A.; Ovchinnikova, O. S. Nanoforging Single Layer MoSe2 Through Defect Engineering with Focused Helium Ion Beams. *Sci. Rep.* **2016**, *6*, 30481.
(27) Nanda, G.; Goswami, S.; Watanabe, K.; Taniguchi, T.; Alkemade, P. F. A. Defect Control and n-Doping of Encapsulated Graphene by Helium-Ion-Beam Irradiation. *Nano Lett.* **2015**, *15*, 4006−4012.
(28) Ghorbani-Asl, M.; Kretschmer, S.; Spearot, D. E.; Krasheninnikov, A. V. Two-dimensional MoS2under ion irradiation: from controlled defect production to electronic structure engineering. *2D Materials* **2017**, *4*, 025078.
(29) Lehtinen, O.; Kotakoski, J.; Krasheninnikov, A. V.; Tolvanen, A.; Nordlund, K.; Keinonen, J. Effects of Ion Bombardment on a Two-Dimensional Target: Atomistic Simulations of Graphene Irradiation. *Phys. Rev. B: Condens. Matter Mater. Phys.* **2010**, *81*, 153401.
(30) Yoon, K.; Rahnamoun, A.; Swett, J. L.; Iberi, V.; Cullen, D. A.; Vlassiouk, I. V.; Belianinov, A.; Jesse, S.; Sang, X.; Ovchinnikova, O. S.; Rondinone, A. J.; Unocic, R. R.; van Duin, A. C. T. Atomistic-Scale Simulations of Defect Formation in Graphene under Noble Gas Ion Irradiation. *ACS Nano* **2016**, *10*, 8376−8384.
(31) Bellido, E. P.; Seminario, J. M. Molecular Dynamics Simulations of Ion-Bombarded Graphene. *J. Phys. Chem. C* **2012**, *116*, 4044−4049.
(32) Wang, D.; Li, X.-B.; Han, D.; Tian, W. Q.; Sun, H.-B. Engineering Two-Dimensional Electronics by Semiconductor Defects. *Nano Today* **2017**, *16*, 30−45.
(33) Fox, D.; Zhou, Y. B.; O'Neill, A.; Kumar, S.; Wang, J. J.; Coleman, J. N.; Duesberg, G. S.; Donegan, J. F.; Zhang, H. Z. Helium Ion Microscopy Of Graphene: Beam Damage, Image Quality and Edge Contrast. *Nanotechnology* **2013**, *24*, 335702.
(34) Bangert, U.; Pierce, W.; Kepaptsoglou, D. M.; Ramasse, Q.; Zan, R.; Gass, M. H.; Van den Berg, J. A.; Boothroyd, C. B.; Amani, J.; Hofsäss, H. Ion Implantation of Graphene-Toward IC Compatible Technologies. *Nano Lett.* **2013**, *13*, 4902−4907.
(35) Wilhelm, R. A.; Gruber, E.; Schwestka, J.; Kozubek, R.; Madeira, T. I.; Marques, J. P.; Kobus, J.; Krasheninnikov, A. V.; Schleberger, M.; Aumayr, F. Interatomic Coulombic Decay: The Mechanism for Rapid Deexcitation of Hollow Atoms. *Phys. Rev. Lett.* **2017**, *119*, 103401.
(36) Akcöltekin, S.; Bukowska, H.; Peters, T.; Osmani, O.; Monnet, I.; Alzaher, I.; d'Etat, B. B.; Lebius, H.; Schleberger, M. Unzipping and Folding of Graphene by Swift Heavy Ions. *Appl. Phys. Lett.* **2011**, *98*, 103103.



DOI: 10.1021/acsami.8b08471
*ACS Appl. Mater. Interfaces* 2018, 10, 30827−30836

(37) Naitou, Y.; Iijima, T.; Ogawa, S.; Naitou, Y.; Iijima, T.; Ogawa, S. Direct Nano-Patterning of Graphene with Helium Ion Beams. *Appl. Phys. Lett.* **2015**, *106*, 033103.
(38) Wang, B.; Yang, S.; Chen, J.; Mann, C.; Bushmaker, A.; Cronin, S. B. Radiation-induced Direct Bandgap Transition in Few-Layer MoS2. *Appl. Phys. Lett.* **2017**, *111*, 131101.
(39) Maguire, P.; Fox, D. S.; Zhou, Y.; Wang, Q.; O'Brien, M.; Jadwiszczak, J.; Cullen, C. P.; McManus, J.; McEvoy, N.; Duesberg, G. S.; Zhang, H. Defect Sizing, Separation and Substrate Effects in Ion-Irradiated Monolayer 2D Materials. **2017**, ArXiv:1707.08893.
(40) Kalbac, M.; Lehtinen, O.; Krasheninnikov, A. V.; Keinonen, J. Ion-Irradiation-Induced Defects in Isotopically-Labeled Two Layered Graphene: Enhanced In Situ Annealing of the Damage. *Adv. Mater.* **2013**, *25*, 1004−1009.
(41) Li, W.; Wang, X.; Zhang, X.; Zhao, S.; Duan, H.; Xue, J. Mechanism of the Defect Formation in Supported Graphene by Energetic Heavy Ion Irradiation: the Substrate Effect. *Sci. Rep.* **2015**, *5*, 9935.
(42) Plimpton, S. Fast Parallel Algorithms for Short-Range Molecular Dynamics. *J. Comput. Phys.* **1995**, *117*, 1−19.
(43) Jiang, J.-w.; Park, H. S.; Rabczuk, T. Molecular Dynamics Simulations of Single-layer Molybdenum Disulphide and Thermal Conductivity. *J. Appl. Phys.* **2013**, *114*, 064307.
(44) Ziegler, J. F.; Biersack, J. P.; Ziegler, M. D. *SRIM—The Stopping and Range of Ions in Matter*; Springer: MA, 1985; pp 93−129.
(45) Wehling, T. O.; Katsnelson, M. I.; Lichtenstein, A. I. Impurities on Graphene: Midgap States and Migration Barriers. *Phys. Rev. B: Condens. Matter Mater. Phys.* **2009**, *80*, 085428.
(46) Lin, Y.-C.; Dumcenco, D. O.; Komsa, H.-P.; Niimi, Y.; Krasheninnikov, A. V.; Huang, Y.-S.; Suenaga, K. Properties of Individual Dopant Atoms in Single-Layer MoS2: Atomic Structure, Migration, and Enhanced Reactivity. *Adv. Mater.* **2014**, *26*, 2857−2861.
(47) Dolui, K.; Rungger, I.; Sanvito, S. Origin of the n-type and p-type Conductivity of MoS2 Monolayers on a SiO2 Substrate. *Phys. Rev. B: Condens. Matter Mater. Phys.* **2013**, *87*, 165402.
(48) Möller, W.; Eckstein, W. Tridyn - a Trim Simulation Code Including Dynamic Composition Changes. *Nucl. Instrum. Methods Phys. Res., Sect. B* **1984**, *2*, 814−818.
(49) Möller, W.; Eckstein, W.; Biersack, J. P. Tridyn-binary collision simulation of atomic collisions and dynamic composition changes in solids. *Comput. Phys. Conunun.* **1988**, *51*, 355−368.
(50) Ziegler, J. F.; Ziegler, M. D.; Biersack, J. P. SRIM - The stopping and range of ions in matter (2010). *Nucl. Instrum. Methods Phys. Res., Sect. B* **2010**, *268*, 1818−1823.
(51) Guo, B.; Liu, Q.; Chen, E.; Zhu, H.; Fang, L.; Gong, J. R. Controllable N-doping of Graphene. *Nano Lett.* **2010**, *10*, 4975−4980.
(52) Buchowicz, G.; Stone, P. R.; Robinson, J. T.; Cress, C. D.; Beeman, J. W.; Dubon, O. D. Correlation Between Structure and Electrical Transport in Ion-Irradiated Graphene Grown on Cu Foils. *Appl. Phys. Lett.* **2011**, *98*, 032102.



DOI: 10.1021/acsami.8b08471
*ACS Appl. Mater. Interfaces* 2018, 10, 30827−30836

ACS Photonics

Letter

Cite This: ACS Photonics 2018, 5, 2718−2723

# Gapless Broadband Terahertz Emission from a Germanium Photoconductive Emitter

A. Singh,[†] A. Pashkin,[†] S. Winnerl,[†] M. Helm,[†,‡] and H. Schneider*[,†]

[†]Helmholtz-Zentrum Dresden-Rossendorf, 01328 Dresden, Germany

[‡]Cfaed and Institute of Applied Physics, TU Dresden, 01062 Dresden, Germany

**ABSTRACT:** Photoconductive terahertz (THz) emitters have been fulfilling many demands required for table-top THz time-domain spectroscopy up to 3−4 THz. In contrast to the widely used photoconductive materials such as GaAs and InGaAs, Ge is a nonpolar semiconductor characterized by a gapless transmission in the THz region due to absence of one-phonon absorption. We present here the realization of a Ge-based photoconductive THz emitter with a smooth broadband spectrum extending up to 13 THz and compare its performance with a GaAs-based analogue. We show that the spectral bandwidth of the Ge emitter is limited mainly by the laser pulse width (65 fs) and, thus, can be potentially extended to even much higher THz frequencies.

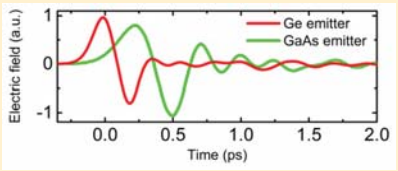


**KEYWORDS:** *Ge photoconductive terahertz emitter, germanium transmission, GaAs transmission, terahertz time-domain spectroscopy, gapless broadband spectrum, broadband terahertz detection*



Generating THz pulses using biased photoconductive (PC) switches is one of the most studied and commonly utilized techniques due to the compact size of THz emitters and their operation flexibility. Major applications of pulsed THz radiation include the study of physical phenomena in materials, nondestructive testing, and chemical identification using time-domain spectroscopic techniques.[1−4] The multioctave spectral bandwidth of THz pulses makes them useful for a broad range of spectroscopic applications. Most common and efficient emitters are fabricated on GaAs which require near-infrared pulse pumping around 800 nm wavelength. This makes them compatible with Ti:sapphire lasers operating at 800 nm wavelength. To bring down the pump laser cost, below band gap excitation in GaAs and low-bandgap semiconductor InGaAs compatible with fiber lasers have been used.[5,6] Current PC emitters are reasonably efficient for time domain spectroscopy in the 0.1−3 THz spectral band, but for higher frequencies, the performance drops drastically.[7−9] The drop in THz signal at higher frequencies is mainly due to THz absorption and screening by optical phonons in GaAs and InGaAs which are polar semiconductors. The polar character of the bonding in these crystals makes their optical phonon infrared active enabling them to absorb THz radiation at the transverse optical (TO) phonon resonance frequency and results in a strong reflectivity within the Reststrahlen band between the TO and longitudinal optical (LO) phonon frequencies. Therefore, the emission spectrum of GaAs-based PC emitters is typically limited to ∼7 THz.[8] Optical rectification techniques using thin crystals have shown some advantage over PC emitters for frequencies above 3 THz. However, all nonlinear crystals used for optical rectification like GaP, ZnTe, and so on are also polar, and therefore, THz absorption by optical phonons affects their spectrum too and their gapless spectrum is limited up to 7 THz.[10,11] There have been continuous efforts to increase the THz bandwidth by exploring new emission techniques, too.[12−17]

The first successful approach for the generation of a gapless THz spectra utilized four-wave mixing process in air plasma induced by mJ femtosecond pulses.[12] Further extension of this technique for a broadband field-resolved detection has enabled a gapless coverage of frequencies up to 10−20 THz for linear and nonlinear spectroscopic measurements.[13] The disadvantage of the air plasma technology is the necessity to use amplified Ti:Sa laser systems with pulse energies above 100 $\mu$J and correspondingly with low repetition rates. A major breakthrough to overcome the frequency limitation problem using conventional femtosecond oscillators with nJ pulse energies came in recent years by the new concept of converting ultrafast photoinjected spin current into THz charge current emitting THz radiation.[14,15] The extremely small thickness of such spintronic emitters (just few nanometers) makes any absorption or screening effects negligible and enables the generation of gapless broadband THz spectra. However, PC emitters offer a number of advantages such as tailoring of THz fields using appropriate electrode designs as well as a fast electrical modulation of the emitted signal for sensitive lock-in detection that avoids the necessity to modulate the incoming optical beam using mechanical choppers or acousto/electro-optical modulators.[18]

Under usual operating conditions a photoconducting substrate is pumped on one side and THz radiation propagates through the substrate and leaves it from the other side. Such simple transmission scheme offers convenient alignment and high collection efficiency of the emitted THz radiation. Therefore, a PC emitter in this geometry should not only be

**Received:** April 10, 2018
**Published:** May 22, 2018

  

DOI: 10.1021/acsphotonics.8b00460
ACS Photonics 2018, 5, 2718−2723

able to radiate THz efficiently but also transmit it without high losses. In the case of GaAs emitters, strong TO phonon absorption around 8 THz limits the gapless spectrum bandwidth to frequencies below 8 THz. There have been attempts to avoid this problem by operating the emitter in a reflection mode, that is, when THz radiated out from the front surface is collected. But it does not solve the problem completely, as even in reflection mode, the TO phonon absorption and an efficient screening at the LO phonon frequency produce anomalies in the THz spectrum.[19−21] The THz emission by the LO phonon in polar semiconductors becomes especially pronounced in case of very high bias fields inherent to p-i-n diode structures resulting in a sharp peak in the emitted broadband THz spectrum.[22] A true gapless broadband PC emitter covering frequencies up to more than 8 THz has still not been realized.

A PC emitter based on a nonpolar semiconductor such as Si or Ge can potentially produce a gapless broadband THz spectrum spanning beyond the limit of 7−8 THz. Although Si-on-Sapphire PC switches were historically among the first THz emitters,[23] most of the modern devices are based on III−V semiconductors (GaAs and InGaAs) due to their higher carrier mobility as compared to Si. In contrast to Si, Ge exhibits much higher carrier mobility that is almost comparable to GaAs (see Table 1) and is capable of supporting high photocurrents.

**Table 1. Carrier Mobility and Bandgap Comparison of GaAs and Ge[34,35]**

| | bandgap (eV) | electron mobility $\mu_e$ ($cm^2\ V^{-1}\ s^{-1}$) | hole mobility $\mu_h$ ($cm^2\ V^{-1}\ s^{-1}$) | $\mu_e + \mu_h$ ($cm^2\ V^{-1}\ s^{-1}$) |
|---|---|---|---|---|
| GaAs | 1.424 | ≤8500 | ≤400 | ≤8900 |
| Ge | 0.661 (0.8 at $E_{\Gamma 1}$ direct bandgap) | ≤3900 | ≤1900 | ≤5800 |

Moreover, due to its small bandgap Ge can be excited using fiber lasers similar to InGaAs emitters. However, due to the indirect bandgap of Ge, its recombination time is of the order of $\mu$s. Probably, this has prevented Ge from getting attention as a PC material for THz emission since for an efficient operation the carrier lifetime should be much shorter than the time period between two pulses used to pump the emitter. There were few reports on THz emission from Ge using different techniques, but these emitters were not efficient and the reported spectral bandwidth was below 3 THz.[24,25] Although for pulsed THz emission, picosecond recombination and trapping times are not mandatory, they can be attractive to improve the performance of a THz emitter.[26] It was demonstrated that ultrashort carrier lifetimes in Ge thin films can be achieved by ion implantation.[25] Moreover, recently thermally evaporated Ge films featuring subps trapping times have been reported.[27]

Here we present broadband THz emission from Ge PC emitter with a gapless spectrum. We demonstrate that the efficiency of the Ge emitter is comparable to an identical semi-insulating GaAs-based PC device and its bandwidth surpasses GaAs by more than factor of 2. Considering the progress in germanium-on-silicon for integrated silicon photonics, Ge is a material with better compatibility to the existing Si electronics as compared to any other THz material for integrating like GaAs, InGaAs, InAs, InSb, GaP, ZnTe, GaSe, and so on. Strain engineered direct and indirect bandgap in Ge gives it further advantage to diversify its compatibility with different fiber lasers.[28−30]

## RESULTS AND DISCUSSION

THz PC emitters are fabricated on nominally undoped Ge and semi-insulating GaAs substrates with the thickness of 500 and 625 $\mu$m, respectively. Figure 1 shows transmission spectra of

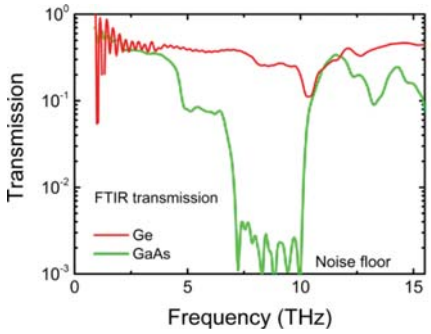


**Figure 1.** Infrared transmission spectra of 625 $\mu$m GaAs and 500 $\mu$m Ge substrates.

these substrates. The spectrum of the GaAs substrate is dominated by the strong absorption band between 7 and 10 THz where the transmission drops below the noise level (~0.2%) of the spectrometer. Obviously, it corresponds to the Reststrahlen band of GaAs defined by the TO and LO phonons. In addition, there are two weaker absorption bands centered around 5 and 13 THz due to two-phonon absorption processes.[31] These features clearly limits the bandwidth of GaAs-based THz emitters. The Ge substrate shows high and almost flat transmittance, apart from a dip around 10 THz due to two-phonon absorption in Ge which is present even in nonpolar semiconductors.[32] However, this high-order absorption processes in Ge are much weaker compared to the TO phonon absorption in GaAs and they should become almost negligible by thinning down the substrate to 100−200 $\mu$m.

To test the THz emission characteristics, the emitters are pumped with 800 nm NIR pulses of width ~65 fs, energy of 12 nJ at the repetition rate of 250 kHz. The pump pulse photogenerates electron−hole pairs in Ge (and GaAs) and these new charge carriers give rise to a current surge in biased emitter electrodes. This current surge causes the THz radiation. The next pump pulse comes after 4 $\mu$s, which gives enough time for carrier recombination and hence reduction in the photocurrent current before the arrival of next pump pulse. With the oscillator laser with repetition rates of a few tens of MHz similar time interval between two consecutive pulses can be achieved with pulse-picker. The carrier recombination time in Ge can also be reduced to make it compatible with oscillator laser with few tens of MHz repetition rate.[25,27] The current−voltage characteristics of both emitters are plotted in Figure 2a. The current through the Ge emitter is obviously larger than that of the GaAs emitter due to its low bandgap and longer carrier lifetime, but still it is just a few mA, hence the device operates without a heating problem.

THz pulses emitted from GaAs and Ge, and recorded using 300 $\mu$m thick GaP are shown in Figure 2b together with their Fourier transforms in the inset. The emitted THz field ratio is close to the carrier mobility sum ($\mu_e + \mu_h$) ratio of Ge and GaAs shown in Table 1. The cutoff frequency for GaAs emitter (~6.5



DOI: 10.1021/acsphotonics.8b00460
ACS Photonics 2018, 5, 2718−2723

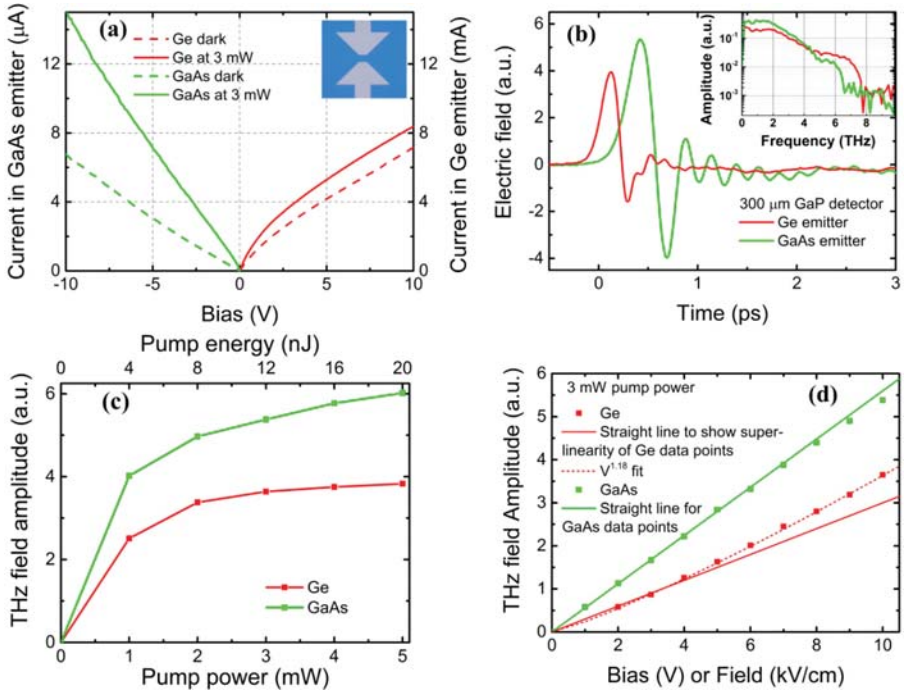


**Figure 2.** (a) *I*–*V* characteristics of the emitters. An optical microscope image of the bowtie electrode structure is shown in the inset. The gap between the two electrodes is 10 $\mu$m. (b) THz pulses recorded from 300 $\mu$m thick GaP electro-optic detector. Fourier spectra of the THz pulses are shown in the inset. (c) Variation of peak electric field of THz pulse with pump power. (d) Variation of the peak electric field with applied electric field on the emitters.

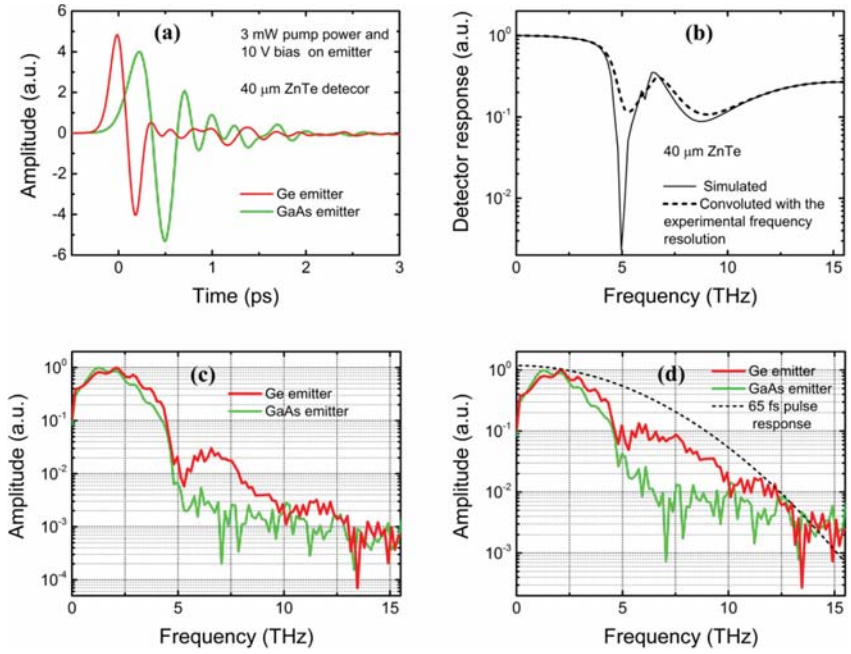


**Figure 3.** (a) Electric field of the THz pulse from Ge and GaAs emitters recorded using 40 $\mu$m thick ZnTe. The THz pulse from Ge is sharper than that of GaAs. (b) Calculated electro-optic detection response function for 40 $\mu$m thick ZnTe. The calculated curve without taking into account any frequency resolution effect is shown as a black solid line. The calculated detector response function is convoluted with the experimental frequency resolution and the convoluted curve is plotted with dashed line. (c) FFTs of the THz pulses shown in (a). (d) FFT spectrum after correcting for the detector response function convoluted with the experimental frequency resolution. The dashed line represents an idealized spectrum limited only by the 65 fs duration of the laser pulses.

THz) is due to low transmission through GaAs in the 5–10 THz band, as shown in FTIR data in Figure 1, but for the Ge emitter, the cutoff frequency around 7.5 THz is due to the limitation of GaP detector response.



DOI: 10.1021/acsphotonics.8b00460
*ACS Photonics* 2018, 5, 2718–2723

Emitter performances are compared at different pump powers and different applied bias. Results are shown in Figure 2c,d. Both emitters show saturation with the pump power at around 2 mW (i.e., 8 nJ) due to screening of the bias field after the electron−hole charge separation. The THz field dependence on the applied bias field is linear for the GaAs emitter as expected. For Ge emitters this dependence is slightly superlinear. This contrasts the sublinear character of the I−V curves for the Ge emitter shown in Figure 2a. Thus, the transient photocurrent emitting the THz pulse scales differently with the applied bias as compared to the average long-lived current flowing through this device. We speculate that this fact can be related to non-Ohmic contact of the Au/Ti metal electrodes with the Ge substrate. A Schottky barrier at one of two contacts is biased in reverse direction and limits the average current flowing through the whole structure leading to the sublinear I−V characteristic. On the other hand, the bias field concentrated in the depletion region at the Schottky barrier can facilitate THz emission by efficient acceleration of the photoinjected carriers. In general, these deviations from the linearity are minor and do not represent a fundamental property of the Ge-based emitter.

To test the emitter performance at higher THz frequencies, THz pulses are recorded using a 40 $\mu$m thick ZnTe ⟨110⟩ crystal and results are shown in Figure 3a. The detector response is calculated by the same method as in ref 33 and it is plotted in Figure 3b with a solid black line. The sharp dip around 5 THz is due to a phonon resonance occurring in ZnTe. At the same applied bias of 10 V and pump power of 3 mW, the peak-to-peak electric field of the Ge pulse is very close to that of GaAs. Total carrier mobility ($\mu_e + \mu_h$) is higher in GaAs than Ge, but as discussed above, the GaAs substrate absorbs most of the THz intensity in the 7−10 THz band, making the THz electric field profile broader with reduced peak electric field. 40 $\mu$m ZnTe is thin enough to detect ultrafast electric field variations corresponding to frequencies in the 7−10 THz band, which was not possible that efficiently when using 300 $\mu$m thick GaP. Therefore, the THz signal from the Ge emitter is improved as compared to the THz signal from the GaAs emitter.

Fourier transforms of the THz pulses recorded with 40 $\mu$m ZnTe are shown in Figure 3c. There is a strong dip at ∼5 THz in both spectra which is due to the dip in the detector response function, as shown in Figure 3b. As expected from the FTIR data there is almost no signal beyond 5 THz for the GaAs emitter, whereas the spectrum of the Ge emitter extends up to 13 THz. The data in Figure 3c also includes the detector response variation with frequency. To obtain the actual spectrum of the emitted THz pulses, the detector response needs to be eliminated by dividing the measured spectrum amplitude by the detector response function. The detector response function is theoretically calculated and it has a very sharp dip around 5 THz. But this dip will not appear that sharp in the experimentally measured spectrum due to limited frequency resolution imposed by the extension of the measured trace in the time domain. To account for the frequency resolution, the calculated detector response function is convoluted with the frequency resolution function of our THz setup defined by the temporal interval used for electro-optic sampling (dash line curve in Figure 3b). Measured spectra are divided by the convoluted detector response of Figure 3b and the corrected FFT spectra are plotted in Figure 3d. For the Ge emitter the THz signal extends up to 13 THz, so the corresponding THz spectrum has been corrected up to 15 THz. The noise floor beyond 15 THz is divided by the value of the response function at 15 THz (∼0.27) to preserve the continuity of the FFT curve. For the GaAs emitter, a clear signal is visible only up to 5 THz and the signal disappears completely beyond 7 THz. The FTIR measurement also shows almost no transmission across the GaAs substrate in the 7−10 THz band, so it is reasonable enough to consider the FFT amplitude at 7 THz to be the noise level for the GaAs emitter. Therefore, the FFT spectrum is corrected only up to 7.5 THz, and the noise floor beyond 7.5 THz is divided by the detector response at 7.5 THz (∼0.19).

In Figure 3d we see a gapless exponentially decaying spectrum reaching up to 13 THz from the Ge emitter, which is far better than that of the GaAs emitter at frequencies above 5 THz. The residual nonuniformity in the spectrum around 5 THz is due to incomplete compensation of the sharp dip in the detector response. The detector response is smooth around 10 THz; therefore the dip in the spectrum at 10 THz is considered real and attributed to the two-phonon absorption dip of Ge as also observed in the FTIR spectrum (see Figure 1). The observation of this absorption feature in the THz spectrum demonstrates that its intensity is well above the noise level at these frequencies. Finally, we compare the measured THz spectrum with a THz spectrum for an idealized infinitely broadband emitter and a hypothetic detector which is limited only by the duration of our laser pulses (65 fs) used for photoexcitation and electro-optic detection. This idealized spectrum is shown in Figure 3d by the black dashed line. Since the transformation due to the focusing optics is not taken into account, the spectral intensity remains finite down to zero frequency. The comparison with the experimental spectra shows good agreement and demonstrates that the high-frequency cutoff limit of the Ge emitter is mainly defined by the pulse duration of the laser amplifier system used in our experiment. Thus, the utilization of much shorter laser pulses from Ti:sapphire oscillators can potentially extend the bandwidth of Ge PC emitters above 20−30 THz or even higher.

## ■ CONCLUSION

In conclusion, we successfully demonstrated the operation of a Ge photoconductive emitter as a THz emitter which is capable of radiating a true gapless spectrum up to 13 THz when pumped with 65 fs laser pulses. The emitted spectrum approaches a nearly ideal THz emitter and it is limited only by the laser pulse duration. In particular, provides broadband THz emission in the frequency range between 5 and 10 THz which is hardly accessible by common methods. Our results demonstrate the superior potential of Ge as a THz photoconductive material, with additional Si CMOS compatibility and longer cutoff wavelengths for the pump laser, and opens a new door for further investigations.

## ■ EXPERIMENTAL METHODS

**Emitter Fabrication.** An electron beam lithography technique is used to fabricate the electrode structures on Ge and GaAs. We fabricate standard bowtie like electrode structures to apply the bias in the semiconductor. The electrode gap is 10 $\mu$m. Both emitters have identical electrode structure. The 45 nm thick Au on top of 5 nm Ti is deposited



DOI: 10.1021/acsphotonics.8b00460
ACS Photonics 2018, 5, 2718−2723

by electron beam evaporation on the substrate to fabricate the electrodes.

**FTIR Measurements.** Transmission spectra of GaAs and Ge substrates are measured using a Fourier-transform infrared (FTIR) spectrometer (Bruker Vertex80v).

**THz TDS Measurement.** A standard THz time domain spectroscopy setup using off-axis parabolic mirrors is used to record the THz pulses. A Ti-Sapphire amplifier laser with wavelength centered around 800 nm, pulse width ~65 fs, and 250 kHz repetition rate is used to pump the emitters, and part of the same laser pulse is used for electro optic sampling of the emitted THz pulse field. Emitters are tested in transmission mode. The frequency resolution of the FFT spectrum depends on the THz pulse span used to take the Fourier transform, which is 6.66 ps for plots in Figure 2 and 6.30 ps for plots in Figure 3.

## AUTHOR INFORMATION


### Corresponding Author

*E-mail: h.schneider@hzdr.de.

### ORCID

A. Singh: 0000-0002-2394-6777


### Author Contributions

A.S. and A.P. designed and performed the experiments. All the authors contributed in data analysis and manuscript writing.

### Notes

The authors declare no competing financial interest.

## ACKNOWLEDGMENTS

Support by the Nanofabrication Facilities Rossendorf at IBC is gratefully acknowledged.

## REFERENCES


(1) Basov, D. M.; Averitt, R. D.; van der Marel, D.; Dressel, M.; Haule, K. Electrodynamics of correlated electron materials. *Rev. Mod. Phys.* **2011**, *83*, 471−541.

(2) Ulbricht, R.; Hendry, E.; Shan, J.; Heinz, T. F.; Bonn, M. Carrier dynamics in semiconductors studied with time-resolved terahertz spectroscopy. *Rev. Mod. Phys.* **2011**, *83*, 543−586.

(3) Tonouchi, M. Cutting-edge terahertz technology. *Nat. Photonics* **2007**, *1* (2), 97−105.

(4) Siegel, P. Terahertz technology in biology and medicine. *IEEE Trans. Microwave Theory Tech.* **2004**, *52* (10), 2438−2447.

(5) Fesharaki, F.; Jooshesh, A.; Bahrami-Yekta, V.; Mahtab, M.; Tiedje, T.; Darcie, T. E.; Gordon, R. Plasmonic Antireflection Coating for Photoconductive Terahertz Generation. *ACS Photonics* **2017**, *4*, 1350−1354.

(6) Jooshesh, A.; Bahrami-Yekta, V.; Zhang, J.; Tiedje, T.; Darcie, T. E.; Gordon, R. Plasmon-Enhanced below Bandgap Photoconductive Terahertz Generation and Detection. *Nano Lett.* **2015**, *15* (12), 8306−8310.

(7) Globisch, B.; Dietz, R. J. B.; Kohlhaas, R. B.; Göbel, T.; Schell, M.; Alcer, D.; Semtsiv, M.; Masselink, W. T. Iron doped InGaAs: Competitive THz emitters and detectors fabricated from the same photoconductor. *J. Appl. Phys.* **2017**, *121*, 053102.

(8) Klatt, G.; Gebs, R.; Janke, C.; Dekorsy, T.; Bartels, A. Rapid-scanning terahertz precision spectrometer with more than 6 THz spectral coverage. *Opt. Express* **2009**, *17* (25), 22847−22854.

(9) Dreyhaupt, A.; Winnerl, S.; Dekorsy, T.; Helm, M. High-intensity terahertz radiation from a microstructured large-area photoconductor. *Appl. Phys. Lett.* **2005**, *86* (12), 121114.

(10) Huber, R.; Brodschelm, A.; Tauser, F.; Leitenstorfer, A. Generation and field-resolved detection of femtosecond electromagnetic pulses tunable up to 41 THz. *Appl. Phys. Lett.* **2000**, *76*, 3191−3193.

(11) Aoki, K.; Savolainen, J.; Havenith, M. Broadband terahertz pulse generation by optical rectification in GaP crystals. *Appl. Phys. Lett.* **2017**, *110*, 201103.

(12) Cook, D. J.; Hochstrasser, R. M. Intense terahertz pulses by four-wave rectification in air. *Opt. Lett.* **2000**, *25*, 1210−1212.

(13) Clough, B.; Dai, J.; Zhang, X.-C. Laser air photonics: beyond the terahertz gap. *Mater. Today* **2012**, *15*, 50−58.

(14) Seifert, T.; Jaiswal, S.; Martens, U.; Hannegan, J.; Braun, L.; Maldonado, P.; Freimuth, F.; Kronenberg, A.; Henrizi, J.; Radu, I.; Beaurepaire, E.; Mokrousov, Y.; Oppeneer, P. M.; Jourdan, M.; Jakob, G.; Turchinovich, D.; Hayden, L. M.; Wolf, M.; Münzenberg, M.; Kläui, M.; Kampfrath, T. Efficient metallic spintronic emitters of ultrabroadband terahertz radiation. *Nat. Photonics* **2016**, *10*, 483−488.

(15) Kampfrath, T.; Battiato, M.; Maldonado, P.; Eilers, G.; Nötzold, J.; Mährlein, S.; Zbarsky, V.; Freimuth, F.; Mokrousov, Y.; Blügel, S.; Wolf, M.; Radu, I.; Oppeneer, P. M.; Münzenberg, M. Terahertz spin current pulses controlled by magnetic heterostructures. *Nat. Nanotechnol.* **2013**, *8*, 256−260.

(16) Luo, L.; Chatzakis, I.; Wang, J.; Niesler, F. B. P.; Wegener, M.; Koschny, T.; Soukoulis; M, C. Broadband terahertz generation from metamaterials. *Nat. Commun.* **2014**, *5*, 3055.

(17) Zhang, Y.; Zhang, X.; Li, S.; Gu, J.; Li, Y.; Tian, Z.; Ouyang, C.; He, M.; Han, J.; Zhang, W. Broadband THz-TDS System Based on DSTMS Emitter and LTG InGaAs/InAlAs Photoconductive Antenna Detector. *Sci. Rep.* **2016**, *6*, 26949.

(18) Winnerl, S.; Zimmermann, B.; Peter, F.; Schneider, H.; Helm, M. Terahertz Bessel-Gauss beams of radial and azimuthal polarization from microstructured photoconductive antennas. *Opt. Express* **2009**, *17*, 1571−1576.

(19) Shen, Y. C.; Upadhya, P. C.; Linfield, E. H.; Beere, H. E.; Davies, A. G. Ultrabroadband terahertz radiation from low-temperature-grown GaAs photoconductive emitters. *Appl. Phys. Lett.* **2003**, *83*, 3117−3119.

(20) Shen, Y. C.; Upadhya, P. C.; E, H.; Beere; Linfield, E. H.; Davies, A. G.; Gregory, I. S.; Baker, C.; Tribe, W. R.; Evans, M. J. Generation and detection of ultrabroadband terahertz radiation using photoconductive emitters and receivers. *Appl. Phys. Lett.* **2004**, *85* (2), 164−166.

(21) Hale, P. J.; Madeo, J.; Chin, C.; Dillon, S. S.; Mangeney, J.; Tignon, J.; Dani, K. M. 20 THz broadband generation using semi-insulating GaAs interdigitated photoconductive antennas. *Opt. Express* **2014**, *22*, 26358−26364.

(22) Leitenstorfer, A.; Hunsche, S.; Shah, J.; Nuss, M. C.; Knox, W. H. Femtosecond Charge Transport in Polar Semiconductors. *Phys. Rev. Lett.* **1999**, *82* (25), 5140−5143.

(23) Auston, D. H.; Cheung, K. P.; Smith, P. R. Picosecond photoconducting Hertzian dipoles. *Appl. Phys. Lett.* **1984**, *45*, 284−286.

(24) Kang, C.; Leem, J. W.; Maeng, I.; Kim, T. H.; Lee, J. S.; Yu, J. S.; Kee, C. S. Strong emission of terahertz radiation from nanostructured Ge surfaces. *Appl. Phys. Lett.* **2015**, *106*, 261106.

(25) Sekine, N.; Hirakawa, K.; Sogawa, F.; Arakawa, Y.; Usami, N.; Shiraki, Y.; Katoda, T. Ultrashort lifetime photocarriers in Ge thin films. *Appl. Phys. Lett.* **1996**, *68*, 3419−3421.

(26) Singh, A.; Pal, S.; Surdi, H.; Prabhu, S. S.; Nanal, V.; Pillay, R. G. Highly efficient and electrically robust carbon irradiated semi-insulating GaAs based photoconductive terahertz emitters. *Appl. Phys. Lett.* **2014**, *104*, 063501.

(27) Lim, W. X.; Manjappa, M.; Srivastava, Y. K.; Cong, L.; Kumar, A.; MacDonald, K. F.; Singh, R. Ultrafast All-Optical Switching of Germanium-Based Flexible Metaphotonic Devices. *Adv. Mater.* **2018**, *30*, 1705331.

(28) Michel, J.; Liu, J.; Kimerling, L. C. High-performance Ge-on-Si photodetectors. *Nat. Photonics* **2010**, *4*, 527−534.

(29) Fang, Y. Y.; Tolle, J.; Roucka, R.; Chizmeshya, A. V. G.; Kouvetakis, J. Perfectly tetragonal, tensile-strained Ge on $Ge_{1-y}Sn_y$ buffered Si(100). *Appl. Phys. Lett.* **2007**, *90*, 061915.

(30) Fang, Y. Y.; Tolle, J.; Tice, J.; Chizmeshya, A. V. G.; Kouvetakis, J.; D'Costa, V. R.; Menéndez, J. Epitaxy-driven synthesis of elemental




DOI: 10.1021/acsphotonics.8b00460
*ACS Photonics* 2018, 5, 2718−2723

Ge/Si strain-engineered materials and device structures via designer molecular chemistry. *Chem. Mater.* **2007**, *19*, 5910−5925.
(31) Jamshidi, H.; Parker, T. J.; Patel, C.; Sherman, W. F. Observation and assignment of phonon combination bands in the far infrared dielectric response of GaAs. *J. Mol. Struct.* **1984**, *113*, 277−280.
(32) Deinzer, G.; Strauch, D. Two-phonon infrared absorption spectra of germanium and silicon calculated from first principles. *Phys. Rev. B: Condens. Matter Mater. Phys.* **2004**, *69*, 045205.
(33) Leitenstorfer, A.; Hunsche, S.; Shah, J.; Nuss, M. C.; Knox, W. H. Detectors and sources for ultrabroadband electro-optic sampling: Experiment and theory. *Appl. Phys. Lett.* **1999**, *74*, 1516−1518.
(34) Blakemore, J. S. Semiconducting and other major properties of gallium arsenide. *J. Appl. Phys.* **1982**, *53*, R123−R181.
(35) Jacoboni, C.; Nava, F.; Canali, C.; Ottaviani, G. Electron drift velocity and diffusivity in germanium. *Phys. Rev. B: Condens. Matter Mater. Phys.* **1981**, *24* (2), 1014−1026.



DOI: 10.1021/acsphotonics.8b00460
*ACS Photonics* 2018, 5, 2718−2723

PHYSICAL REVIEW APPLIED **10,** 024054 (2018)

# Extended Infrared Photoresponse in Te-Hyperdoped Si at Room Temperature

Mao Wang,[1,2,*] Y. Berencén,[1] E. García-Hemme,[3] S. Prucnal,[1] R. Hübner,[1] Ye Yuan,[1,2] Chi Xu,[1,2] L. Rebohle,[1] R. Böttger,[1] R. Heller,[1] H. Schneider,[1] W. Skorupa,[1] M. Helm,[1,2] and Shengqiang Zhou[1]

[1]*Helmholtz-Zentrum Dresden-Rossendorf, Institute of Ion Beam Physics and Materials Research, Bautzner Landstr. 400, 01328 Dresden, Germany*

[2]*Technische Universität Dresden, 01062 Dresden, Germany*

[3]*Univ. Complutense de Madrid, Dpto. de Estructura de la Materia, Física Térmica y Electrónica, 28040 Madrid, Spain*

(Received 14 December 2017; revised manuscript received 25 May 2018; published 31 August 2018)

Presently, silicon photonics requires photodetectors that are sensitive in a broad infrared range, can operate at room temperature, and are suitable for integration with the existing Si-technology process. Here, we demonstrate strong room-temperature sub-band-gap photoresponse of photodiodes based on Si hyperdoped with tellurium. The epitaxially recrystallized Te-hyperdoped Si layers are developed by ion implantation combined with pulsed-laser melting and incorporate Te-dopant concentrations several orders of magnitude above the solid solubility limit. With increasing Te concentration, the Te-hyperdoped layer changes from insulating to quasi-metallic behavior with a finite conductivity as the temperature tends to zero. The optical absorptance is found to increase monotonically with increasing Te concentration and extends well into the mid-infrared range. Temperature-dependent optoelectronic photoresponse unambiguously demonstrates that the extended infrared photoresponsivity from Te-hyperdoped Si *p-n* photodiodes is mediated by a Te intermediate band within the upper half of the Si band gap. This work contributes to pave the way toward establishing a Si-based broadband infrared photonic system operating at room temperature.

DOI: 10.1103/PhysRevApplied.10.024054

## I. INTRODUCTION

Presently, there is a need to overcome the bottleneck in the processing of the huge volume of data transmitted over the traditional telecommunication wavelengths around 1.3 and 1.5 $\mu$m [1,2]. Extending the spectral range from the near-infrared (NIR) (from approximately 0.8 to approximately 2 $\mu$m) to the mid-infrared (MIR) (from approximately 2 to 25 $\mu$m) [3] has been proposed as a viable route for solving this setback [4–6]. Si-based photodetectors, compared with III-V (e.g., InSb) or $(Hg_{1-x}Cd_x)Te$ infrared ones, satisfy the demand for cost-effective and environmentally friendly solutions, and enable the development of on-chip complementary-metal-oxide-semiconductor (CMOS)-compatible photonic systems [5,7,8]. However, their photoresponse is fundamentally limited in the visible and NIR spectral regime owing to the relatively large band gap of Si (1.12 eV, $\lambda = 1.1$ $\mu$m). Therefore, the room-temperature broadband infrared detection is of great interest in the realm of silicon photonics. In particular, hyperdoped Si materials are the spotlight of present-day investigations due to their superior optoelectronic properties (e.g., the highest absorption coefficient (approximately $10^4$ $cm^{-1}$) ever obtained for Si in the infrared range, which is comparable to that of intrinsic Ge after incorporating certain concentrations and types of dopants [9]. More recently, hyperdoping has successfully been extended to nanostructured Si such as nanowires and nanocrystals [10,11] where localized surface plasmon resonances [12] and sub-band-gap optoelectronic photoresponse have been demonstrated [13]. This new type of material is also better than Si-Ge [14] and Si-III-V-semiconductor heterostructures [15] from the standpoint of fabrication [16]. However, extrinsic infrared (IR) photodetectors based on Si with dopants of group III (B, Al, and Ga) and V (P, As, and Sb) can only operate at temperatures below 40 K [7,17–19], since the introduced shallow-dopant levels within the Si band gap are thermally ionized at room temperature.

Alternatively, Si photodetectors that make use of deep-level dopants (with a much higher thermal-ionization energy), such as Ti, Ag, Au, S, and Se [20–25], are effective for strong room-temperature photoresponse, extending well in the IR range [23,24,26,27]. The extended photoresponse has been demonstrated to be associated with known-dopant deep-energy levels within the Si band gap. However, less attention has been paid to the optoelectronic photoresponse of Te-hyperdoped Si [28].

*m.wang@hzdr.de

 

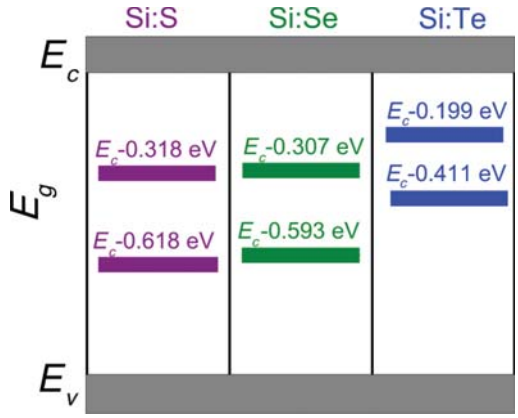


FIG. 1. Energy-level schemes for S-, Se-, and Te-doped Si [29,30,32,33].

In fact, chalcogens are double donors in Si, and Te especially offers important advantages for hyperdoping Si over its chalcogen counterparts, namely S and Se dopants. For instance, Te introduces deep-donor states at $E_c$-0.20 eV and $E_c$-0.41 eV, which are located in the upper half of the Si band gap and in turn are closer to the conduction band (CB) compared with S and Se as schematically shown in Fig. 1 [29,30]. This feature of Te facilitates the further extension of the photoresponse toward the MIR range. However, Te has a larger atomic radius and is much less electronegative than S and Se (S, 2.58; Se, 2.55; Te, 2.10) [31]. The latter results in a larger substitutional formation energy ($E^f$) of Si:Te, e.g., $E^f$ [$Si_{125}$:S] = −0.13 eV, $E^f$ [$Si_{125}$:Se] = +1.29 eV, and $E^f$ [$Si_{125}$:Te] = +1.97 eV [32]. Thus, achieving a hyperdoping level in Si:Te comparable to the one reported for Si:S or Si:Se is more challenging.

In this work, we report on the realization of single-crystalline and epitaxial-hyperdoped Si with Te concentrations as high as $10^{21}$ $cm^{-3}$ by ion implantation combined with pulsed-laser melting (PLM). The observed quasi-metallic behavior is driven by increasing Te concentration. Te-hyperdoped Si *p-n* photodiodes exhibit a remarkably broad spectral range down to 3.1 $\mu$m at room temperature with an enhanced optoelectronic photoresponse compared to the Au-hyperdoped Si-based photodetectors [23]. This work points out the potential of Si hyperdoped with Te for room-temperature infrared detection as the new generation of Si-based photonic systems.

## II. EXPERIMENTAL DETAILS

Double-side-polished Si (100) wafers (*p*-type, boron-doped, $\rho \approx 1$–10 Ω cm) are implanted with Te ions at six different fluences at room temperature (see Table I). The Te depth profile is first calculated using SRIM code [34] and then verified by Rutherford backscattering-spectrometry/channeling (RBS/C) measurements. A combined implantation with energies of 150 and 50 keV with a fluence ratio of 2.5:1 is applied to obtain a uniform distribution of Te in the implanted layer. Subsequently, ion-implanted samples are molten using a pulsed Xe-Cl excimer laser (Coherent COMPexPRO201, wavelength of 308 nm, pulse duration of 28 ns) in ambient air. A single laser pulse of beam size $5 \times 5$ $mm^2$ with a fluence of 1.2 J/$cm^2$ is used to anneal the as-implanted layers. The choice of this pulsed laser melting (PLM) fluence is carried out by inspecting the crystalline quality and the Te depth profile of the layers using Raman and RBS measurements, respectively. During the annealing process, the whole amorphous implanted region is molten and then recrystallized with a solidification speed of the order of 10 m/s while cooling down [35]. This allows for Te concentrations beyond the solid-solubility limit of Te in Si while preserving the epitaxial single-crystal growth.

To analyze the microstructure of the PLM-treated Te-hyperdoped Si layers, high-resolution transmission electron microscopy (HRTEM) is performed on an image $C_s$-corrected Titan 80-300 microscope (FEI) operated at an accelerating voltage of 300 kV. High-angle annular dark-field scanning transmission electron microscopy (HAADF-STEM) imaging and spectrum imaging based on energy-dispersive x-ray spectroscopy (EDXS) are done at 200 kV with a Talos F200X microscope equipped with an X-FEG electron source and a Super-X EDXS detector system (FEI). Prior to STEM analysis, the specimen mounted in a high-visibility low-background holder is placed for 10 s into a Model 1020 Plasma Cleaner (Fischione) to remove contamination. Classical cross-sectional TEM-lamella preparation is done by sawing, grinding, polishing, dimpling, and finally, Ar-ion milling. RBS/C measurements are performed with a collimated 1.7-MeV $He^+$ beam of the Rossendorf van de Graff accelerator with a 10–20 nA beam current at a backscattering angle of 170° to investigate the crystalline quality of the pulsed-laser-annealed Te-hyperdoped Si layers. The channeling spectra are collected by aligning the sample to make the impinging $He^+$ beam parallel to the Si [001] axes.

The conductivity type, carrier concentration, and carrier mobility of the PLM-treated Te-hyperdoped layers are measured by a commercial Lake Shore Hall measurement system in a van der Pauw configuration [38] under a magnetic field perpendicular to the sample plane. The magnetic field is swept from −4 to 4 T. The gold electrodes are sputtered onto the four corners of the square-like samples. The native-$SiO_2$ layer is removed by hydrofluoric acid (HF) etching prior to the sputtering process. Next, a silver-conductive-glue paste is used to contact the wires to the gold electrodes. All contacts are confirmed to be ohmic by measuring the current-voltage curves at different temperatures.

Transmittance ($T$) and reflectance ($R$) measurements are performed at room temperature by means of a

TABLE I. Sample description. The depth distribution of Te (estimated thickness = 120 nm) is calculated using SRIM and verified by RBS measurements (a fit to the RBS random spectrum using the SIMNRA code [36,37] yields the Te concentration). The sample names refer to the peak Te concentration of the as-implanted layer.

| Sample ID | Implantation parameters | Tellurium peak concentration (%) |
|---|---|---|
| Te-0.25% | 150 keV, $7.8 \times 10^{14}$ cm$^{-2}$; 50 keV, $3.1 \times 10^{14}$ cm$^{-2}$ | 0.25 |
| Te-0.50% | 150 keV, $1.6 \times 10^{15}$ cm$^{-2}$; 50 keV, $6.2 \times 10^{14}$ cm$^{-2}$ | 0.50 |
| Te-1.0% | 150 keV, $3.1 \times 10^{15}$ cm$^{-2}$; 50 keV, $1.2 \times 10^{15}$ cm$^{-2}$ | 1.0 |
| Te-1.5% | 150 keV, $4.7 \times 10^{15}$ cm$^{-2}$; 50 keV, $1.9 \times 10^{15}$ cm$^{-2}$ | 1.5 |
| Te-2.0% | 150 keV, $6.2 \times 10^{15}$ cm$^{-2}$; 50 keV, $2.5 \times 10^{15}$ cm$^{-2}$ | 2.0 |
| Te-2.5% | 150 keV, $7.8 \times 10^{15}$ cm$^{-2}$; 50 keV, $3.1 \times 10^{15}$ cm$^{-2}$ | 2.5 |

Fourier-transform infrared (FTIR) spectroscopy using a Bruker Vertex 80v FTIR spectrometer to quantify the sub-band-gap absorptance of the Te-hyperdoped Si layers in the infrared spectral range of 0.05–0.85 eV ($\lambda = 1.4$–$25$ $\mu$m). To this end, the probe beam is focused on the PLM-treated area of the sample ($5 \times 5$ mm$^2$). The absorptance ($A = 1 - T - R$) is then determined by recording the transmittance and reflectance spectra.

The temperature-dependent photoresponsivity from 60 to 300 K is measured in the Te-hyperdoped Si/$p$-Si photodiode devices. A 0.068-cm$^2$ illuminated area is photolithographically processed by defining fingers with a separation of 200 $\mu$m resulting in frame-like Ti/Al top electrodes on top of the Te-hyperdoped Si layer. The bottom-side electrode is made by Ti/Al contact on nearly the entire bottom surface, but avoiding sample edges in order to reduce possible parasitic-electrical conduction through the edges of the sample. Both the top-side and bottom-side electrodes are defined by e-beam evaporation using a 50 nm/100 nm Ti/Al bilayer. The photoresponsivity measurements are conducted by placing the $p$-$n$ photodiodes inside a helium closed-cycle Janis cryostat with a Zn-Se window. A vacuum pump is used to avoid moisture condensation at low temperatures [22]. A Si-C glowbar-infrared source coupled to a TMc300 Bentham monochromator equipped with gratings in Czerny-Turner reflection configuration is used. The incident $1.5 \times 3.0$ cm$^2$ light spot, spatially homogeneous in intensity, is used to study the spectral photoresponse of the device. The system is calibrated with a Bentham pyrometric detector. The short-circuit photocurrent between the top and bottom contacts is measured with a SR830 DSP lock-in amplifier. For all the measurements, the infrared light from the SiC source is mechanically chopped at 87 Hz before entering the monochromator.

## III. EXPERIMENTAL RESULTS

### A. Structural properties

A representative cross-sectional HAADF-STEM micrograph superimposed with the corresponding Te, Si, and O element maps is shown in Fig. 2(a) for the PLM-treated Te-hyperdoped Si layer (Te-1.5%). Apart from the native-oxide layer at the surface, Te is found to be evenly distributed within the top 125 nm of the Si wafer. Neither Te surface segregation nor nano-scale Te agglomerates are detected despite the high-doping concentration of more than $10^{20}$ cm$^{-3}$. Single-crystalline regrowth of the Te-hyperdoped Si layer during the PLM treatment is confirmed by HRTEM imaging and the subsequent fast-Fourier-transform analysis as shown in Fig. 2(b). Moreover, extended defects, secondary phases or cellular breakdowns are not observed.

After the PLM treatment, all the Te-hyperdoped Si samples show a similar crystalline quality and Te depth distribution. Figure 2(c) depicts the representative RBS/C spectra of a PLM-treated Te-hyperdoped Si layer together with the virgin Si and the as-implanted sample. The random spectrum of the as-implanted layer reveals a thickness of about 120 nm for the Te profile, in an approximately Gaussian distribution. No channeling effect is observed in the implanted layer because of the amorphization caused by ion implantation. From the RBS-channeling signal, the PLM-treated layer shows a minimum backscattered yield $\chi_{\min}$ of 4% (defined as the ratio of the aligned to the random yields), which is comparable to that of the virgin-Si substrate. This indicates a full recrystallization and an epitaxial growth of the PLM-treated layer, in agreement with the HRTEM results in Fig. 2(b).

It is evidenced in the Te signal that Te atoms tend to diffuse toward both the surface and the substrate sides during the PLM process, leading to a relatively uniform Te profile with a thickness of 125 nm, as illustrated in Fig. 2(a). Moreover, the inset in Fig. 2(c) shows that the channeling spectrum of the 1.5%-Te-hyperdoped sample exhibits a $\chi_{\min}$ of about 4% for Si and 30% for Te in the Te-implanted region. The substitutional fraction for Te (i.e., the ratio of substitutional-Te dopants at the Si-lattice sites to the total implanted Te atoms) can be estimated as $(1 - 30\%)/(1 - 4\%) = 72\%$ [39]. The substitutional fraction of all the Te-hyperdoped Si samples is around 70%, higher than that of Se in Si [40].

### B. Electrical characterization

Electrical measurements are made to investigate the transport properties of the PLM-treated Te-hyperdoped

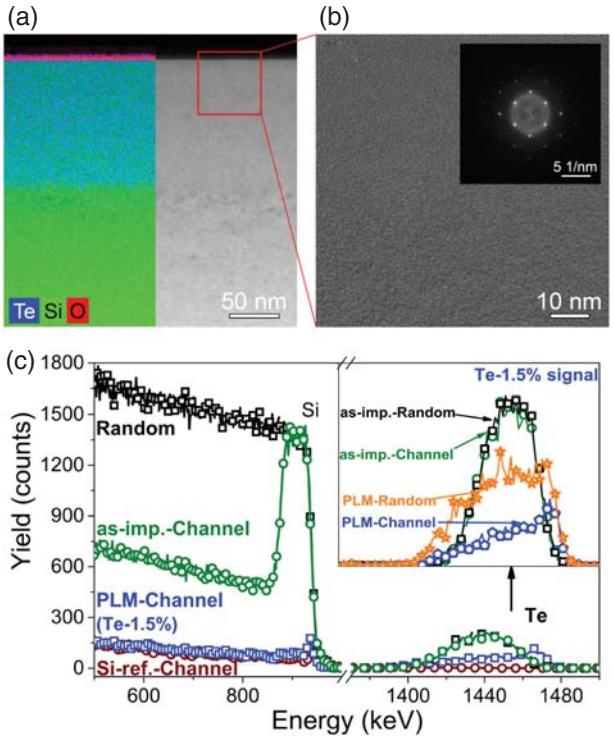


FIG. 2. Microstructure investigation of Te-hyperdoped Si layers (color online). (a) Cross-sectional HAADF-STEM image superimposed with the corresponding EDXS element maps (blue: tellurium, green: silicon, red: oxygen) for the PLM-treated Te-hyperdoped Si layer Te-1.5%; (b) representative HRTEM image with corresponding fast Fourier transform (inset) for a field of view as depicted by the red square in image part (a); (c) a sequence of 1.7 MeV He RBS/C spectra of PLM-treated Te-hyperdoped Si layer. The inset in Fig. 2(c) shows the magnification of random (-R) and channeling (-C) Te signals from as-implanted and PLM-performed Te-hyperdoped Si samples with a concentration of 1.5%.

Si layers. To avoid the influence of the parallel conduction from the $p$-type Si substrate, a set of samples with the same range of Te concentrations are processed on an *intrinsic* Si substrate ($\rho > 10^4$ Ω cm). Figure 3 shows the temperature-dependent resistivity of Te-hyperdoped Si samples with different Te concentrations. At room temperature, the resistivity of the Te-hyperdoped Si layers is less than $10^{-2}$ Ω cm, which is much lower than that of the Si substrate. This confirms that the intrinsic-Si substrate has no influence on the transport properties of the Te-hyperdoped Si layer considering the respective thickness. Figure 3 shows that the resistivity decreases with increasing Te concentration and a remarkable difference in a factor of $10^4$ is reached at 2 K. Samples with 0.25% and 0.50% of Te content behave like insulators with the resistivity sharply increasing at low temperatures. This is because of the electrons' return to their localized ground states from

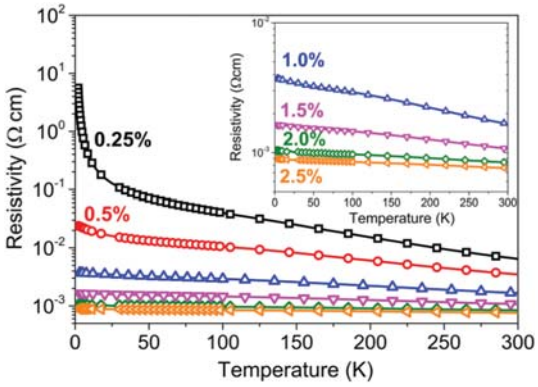


FIG. 3. Temperature-dependent resistivity of the Te-hyperdoped Si layers with different Te concentrations. The inset shows a magnification of the data for samples with higher Te concentration.

the thermally-excited conduction-band states as temperature decreases. However, samples with Te concentrations higher than 1% exhibit a different behavior as shown in the inset of Fig. 3, i.e., their resistivity slightly increases as the temperature decreases. Samples with a higher doping concentration show quasi-metallic behavior, i.e., their conductivity remains finite as the temperature tends to zero due to the delocalization of donor electrons above a critical donor concentration ($n_c$) [41]. This gradual transition from insulating to quasi-metallic behavior driven by the Te concentration involves the formation of a broad intermediate band (IB) in the upper half of the Si band gap [42,43].

### C. Optical absorption

A strong and broad sub-band-gap optical absorptance in Te-hyperdoped Si layers, as compared with a bare Si sample, is shown in Fig. 4. The sharp peaks below 0.15 eV in the absorptance spectra are known to be related with oxygen and carbon impurities [44,45] in the Si substrate. The absorptance extends down to 0.048 eV (the MIR-detection limit of FTIR) while it increases with the Te concentration, which is consistent with the previously reported results about S- and Se-hyperdoped Si [27,46]. The well-defined broad-absorptance band peaking at around 0.36 eV for samples Te-0.25% and Te-0.5% comes from the presence of discrete impurity levels or a narrow intermediate band. The peak position correlates well with the activation energy of the deep Te levels [29] and agrees with previous works [32,47]. On the other hand, samples with Te concentrations in excess of 1% show quasi-metallic behavior and the broad-absorptance band evolves leading to a strong increase of the absorptance down to 0.048 eV. This can be understood in terms of a free-carrier-absorption process because of the high-carrier concentration in the Te-hyperdoped Si layers ($\geq 10^{20}$ cm$^{-3}$). For the sample

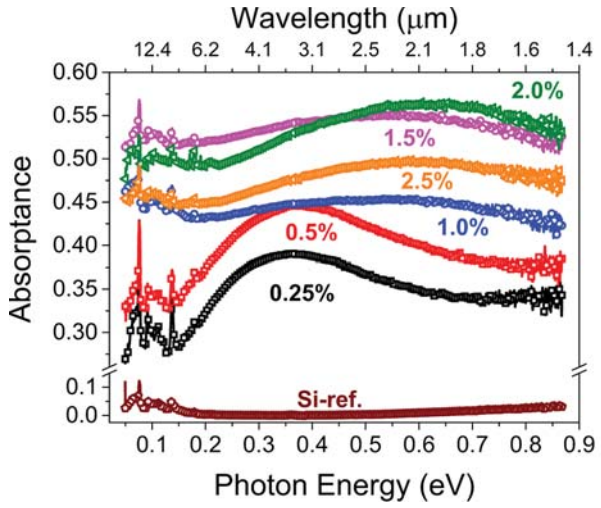


FIG. 4. Room-temperature sub-band-gap optical-absorptance spectra from PLM-treated Te-hyperdoped Si samples with different Te concentrations. A bare Si substrate is shown as a reference.

with the highest Te content, the decrease of the sub-band-gap absorptance is likely due to the formation of inactive Te Vm (vacancy-impurity complexes) with similar complexes as reported in As-hyperdoped Si [48] since the Si host no longer accommodates more Te atoms at such high concentrations ($1 \times 10^{21}$ cm$^{-3}$).

### D. Infrared-optoelectronic response

The sub-band-gap photoresponse in Te-hyperdoped Si layers is further investigated via the spectral responsivity (A·W$^{-1}$) of *p-n* photodiode devices. The top view and cross section of the Te-hyperdoped Si/*p*-Si photodiode are schematically presented in Figs. 5(a) and 5(b), respectively. Figure 5(c) shows an *I-V* curve at room temperature in dark and Fig. 5(d) depicts the infrared responsivity (A·W$^{-1}$), which is estimated at zero bias (i.e., photovoltaic mode), as a function of incident photon energy. Measurements are performed at zero bias in order to prove the pure-photovoltaic effect of the Te-hyperdoped Si/*p*-Si photodiodes. This will rule out any other possible origin of the photoresponse. Measurements under a reverse bias could give a false positive such as a photoconductive effect. The zero-bias room-temperature responsivity of a commercial Si-PIN photodiode (model: BPW34) is also included for comparative purposes in Fig. 5(d). We fabricate the photodiodes on the Te-hyperdoped Si sample with the strongest sub-band-gap absorptance (see Fig. 4, sample Te-2.0%).

Figure 5(c) shows that the fabricated photodiode presents a rectifying behavior. The forward voltage corresponds to positive bias applied to the bottom contact (*p*-Si substrate) and the ratio of direct to reverse current is 36 at ±0.5 V. To further analyze the rectifying behavior, the dark *I-V* curve is fitted to a single-diode model [49] using

$$I = I_0[e^{(q(V-IR_s)/\eta k_B T)} - 1] + \frac{V - IR_s}{R_{shunt}}, \quad (1)$$

where $I_0$ is the saturation current, $q$ is the electron charge, $T$ is the temperature, $\eta$ is the ideality factor, and $k_B$ is the Boltzmann constant. $V$ and $I$ are the total voltage and current whereas $R_s$ and $R_{shunt}$ are the series and parallel resistances, respectively. Hence, $R_s$, $R_{shunt}$, $I_0$, and $\eta$ are found to be 6.4 Ω, 850 Ω, 68 μA, and 2.2, respectively. The deduced series-resistance value is in agreement with the calculated series resistance, $R_s = \rho(t/A)$, assuming a wafer resistivity of $\rho = 1$–$10$ Ω cm, a wafer thickness of $t = 380$ μm, and an electrode area of $A = 0.068$ cm$^2$. This confirms the ohmic character of the contacts. On the other hand, an ideality factor of 2.2 suggests (i) the existence of a *p-n* junction rather than a metal-semiconductor junction, in which the ideality factor is expected to be 1 [50] and (ii) that the main conduction mechanism is ascribed to a recombination/generation process of carriers in the depletion region of the *p-n* photodiode [49]. Therefore, the observed rectifying behavior in Fig. 5(c) is directly related to the *p-n* junction between the *p*-type Si substrate and the *n*-type Te-hyperdoped Si layer.

Figure 5(d) depicts the temperature-dependent responsivity as a function of photon energy. The Te-hyperdoped Si *p-n* photodiode shows a strong sub-band-gap responsivity down to 0.3 eV in the whole temperature range. At room temperature, the Te-hyperdoped Si *p-n* photodiode exhibits a responsivity of around $10^{-4}$ A W$^{-1}$ at the two telecommunication optical wavelengths (1.3 and 1.5 μm), whereas the responsivity at photon energies below 0.9 eV of a commercial Si-PIN photodiode reaches the noise floor as expected. The measured responsivity of $10^{-4}$ A W$^{-1}$ is comparable to those reported for hyperdoped Si-based photodiodes [23] and solar cells [51] at the corresponding wavelengths. Moreover, the external quantum efficiency (EQE) at 1.3 and 1.5 μm is $2 \times 10^{-4}$ and $8 \times 10^{-5}$, respectively, as estimated by

$$\mathrm{EQE}(\lambda) = \frac{R_{ph}}{\lambda} \times \frac{hc}{e} \approx \frac{R_\lambda}{\lambda} \times (1240\ \mathrm{W\ nm/A}), \quad (2)$$

where $R_{ph}$ is the spectral responsivity (i.e., the ratio of the electrical output to the optical input.), λ is the wavelength in nm, $h$ is the Planck constant, $c$ is the speed of light in vacuum, and $e$ is the elementary charge. The estimated EQE values are comparable to other deep-level impurity-hyperdoped-Si photodiodes [23,27].

Regarding the responsivity at different temperatures of the Te-hyperdoped Si *p-n* photodiode, two ranges of temperatures with different behaviors in terms of the line shape and responsivity intensity can be identified. At high-temperature range (300–180 K), the responsivity extends

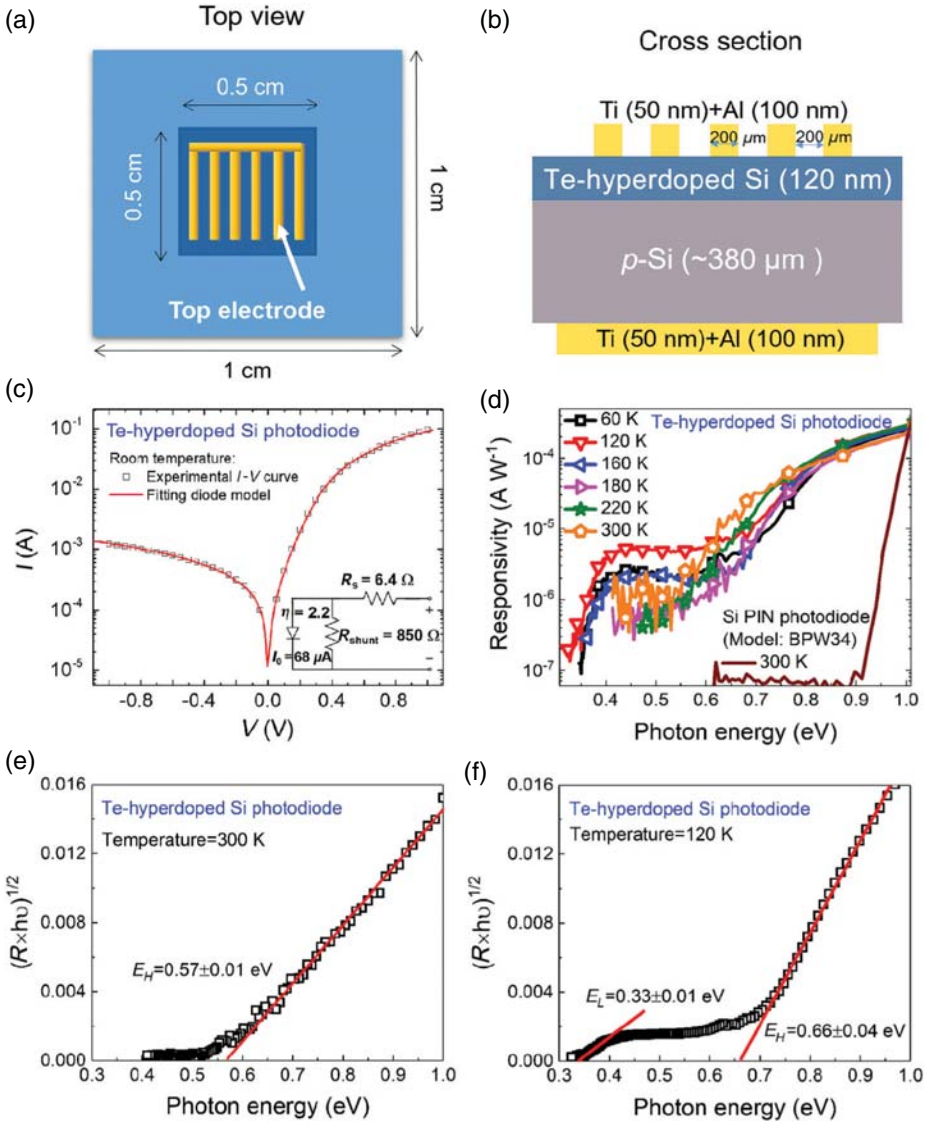


FIG. 5. (a) Top view and (b) cross-sectional scheme of the Te-2.0%-hyperdoped Si/*p*-Si photodiode devices. (c) The dark current as a function of applied bias voltage measured at room temperature. The inset in Fig. 5(c) shows the equivalent electrical circuit of the experimental setup. (d) The spectral responsivity measured at zero bias (i.e. photovoltaic mode) for the Te-hyperdoped Si photodiode and the commercial Si PIN photodiode at different temperatures. (e),(f) show the fitting of the absorption edge using Eq. (3) at different temperature ranges.

down to approximately 0.55 eV, where the noise floor is reached. However, at low-temperature range (160–60 K), an additional broad photoresponse band spanning from 0.60 to 0.33 eV is clearly observed. These features allow us to define a photoresponse band at high photon energies $E_H$, that lies in the range of 0.55–0.65 eV and another one at low photon energies $E_L$, in the range of 0.30–0.40 eV.

To get insight into the optical transitions coming from the Te-related intermediate band, a direct proportionality between the photoresponsivity and the absorption coefficient at energies close to the optical-transition edges is assumed. The sub-band-gap optical transitions can, therefore, be derived by the Tauc method using the following modified expression:

$$R_{\mathrm{ph}} \times h\nu = A(h\nu - E_g)^n, \qquad (3)$$

where $h\nu$ is the photon energy, $A$ is a constant, $E_g$ is the Si band gap, and $n$ would adopt the value of 2 for the indirect optical transitions. A Tauc-type plot for both the high-temperature and the low-temperature ranges at two representative temperatures (viz. 300 and 120 K) is shown in Figs. 5(e) and 5(f), respectively. The energy gap derived from this plot is determined to be $E_H = 0.57 \pm 0.01$ eV at 300 K and $E_H = 0.66 \pm 0.04$ eV at 120 K. Alternatively, a second absorption edge band is found to be $E_L = 0.33 \pm 0.01$ eV at 120 K. The slight differences between the deduced $E_H$ values at 300 and 120 K are thought to be related to the temperature dependence of the Si band gap.

Next, we record the device photocurrent as a function of the input optical power at photon energies of 0.82 and 0.42 eV at 300 and 120 K, respectively (Fig. 6). The

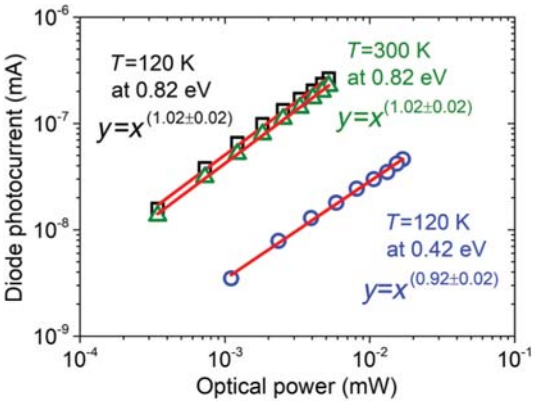


FIG. 6. Diode photocurrent vs input optical power with the corresponding linear fits at the photon energies of 0.82 and 0.42 eV at 120 K and at 0.82 eV at 300 K.

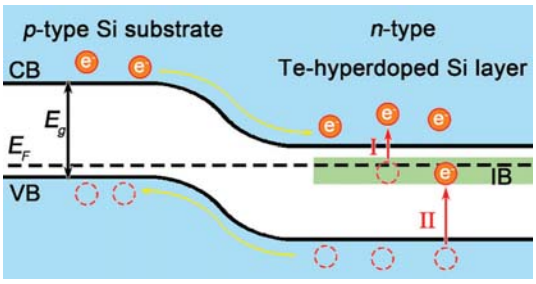


FIG. 7. Band diagram of the Te intermediate-band-based Si *p-n* photodiode. Te dopants introduce electron states (intermediate band) of about 0.33 eV below the conduction band of Si. The Te intermediate band facilitates the generation of charge carriers that participate in the absorption of two or more sub-band-gap-energy photons. The transition of IB to CB (process I) takes place at $E \geq E_L$ while it is only measurable at low temperature because almost no contribution from the thermal generation process occurs. The transition of VB to IB (process II) occurs at $E \geq E_H$.

photocurrent in response to the sub-band-gap illumination at 300 and 120 K is found to scale linearly with the input optical power in a log-log representation with a slope of around 1. This suggests that the sub-band-gap photoresponse mechanism of the Te-hyperdoped Si *p-n* photodiodes is related to a single-photon-absorption process mediated by the intermediate band rather than a two-photon-absorption process. In addition, the possibility of internal photoemission from the top electrode is discarded by the proven ohmic character of the contacts.

## IV. DISCUSSION

We discuss the origin of the sub-band-gap photoresponsivity at room and low temperatures from the Te-hyperdoped Si *p-n* photodiodes. The results derived from the analysis of the material properties in conjunction with the spectral photoresponsivity at different temperatures are consistent with the formation of a Te-related intermediate band in the upper half of the Si band gap. The Te intermediate band facilitates the generation of charge carriers originated by the absorption process of photons with energies lower than the Si band gap. For the sake of clarity, Fig. 7 shows a sketch of the band diagram of the Te intermediate band-based Si *p-n* photodiode with the different involved processes in the sub-band-gap optoelectronic photoresponse:

(i) In the high-temperature range (300–180 K), the transition from the IB to the CB (process I), denoted as $E_L = E_C$-0.33 eV, takes place, but the ratio of thermal-to-optical carrier generation is sufficiently high to screen a measurable photocurrent arising from this transition. In detail, an equilibrium conduction-band-electron concentration coming from the thermal-carrier generation as high as $10^{17}$ $cm^{-3}$ can be estimated by the charge-carrier statistics [49]. This, however, does not impede the occurrence of the transition from the valence band (VB) to the IB (Process II), which is in accordance with the kink in the room-temperature spectral photoresponsivity at $E_H = 0.57 \pm 0.01$ eV as shown in Fig. 5(e).

(ii) In the low-temperature range (160–60 K), the thermal-carrier generation is then suppressed by the freeze-out effect [52]. This leads to a ratio of thermal- to optical-carrier generation low enough that it allows for a measurable photoresponsivity band arising from the IB to the CB (process I) at $E_L = 0.33 \pm 0.01$ eV [Fig. 5(f)]. Likewise, the transition from the IB to the CB (process I) gives rise to available states at the IB which are then populated by electrons from the VB. This results in the photoresponsivity band at $E_H = 0.66 \pm 0.04$ eV [Fig. 5(f)]. The observation of the two sub-band-gap optical transitions (VB→IB and IB→CB) indicates that the IB is not merged with the CB despite the high Te concentration.

While the high-quality hyperdoped-Si material platform is established, further efforts must be made toward an advanced-device design to boost the device efficiency of this prototype of photodiode. This can be achieved by designing a top electrode with narrower fingers and gaps that help to enhance the carrier-collection efficiency. An antireflection-coating layer in conjunction with a passivation layer might also help to improve the efficiency.

## V. CONCLUSION

The possibility of generating photocarriers at room temperature using sub-band-gap radiation in high-quality single-crystal Si films doped with Te concentrations greater than the thermal-solubility limit is established. The

Te-hyperdoped Si films exhibit a broad optical absorptance spanning from 1 to 13 $\mu$m. A clear evolution from the discrete energy levels to the formation of an intermediate band as a function of Te concentration is demonstrated. The extended infrared photoresponse of the Te-hyperdoped Si *p*-*n* photodiodes is proven to be mediated by an intermediate band within the upper half of the Si band gap. The CMOS-compatible approach demonstrated here provides a way to achieve room-temperature sub-band-gap optoelectronic response in single-crystal Si-based intermediate band materials.

## ACKNOWLEDGMENTS

Authors acknowledge the ion implantation group at HZDR for performing the Te implantations. Additionally, support by the Structural Characterization Facilities at Ion Beam Center (IBC) and funding of TEM Talos by the German Federal Ministry of Education of Research (BMBF), Grant No. 03SF0451 in the framework of HEMCP, are gratefully acknowledged. This work is funded by the Helmholtz-Gemeinschaft Deutscher Forschungszentren (Grant No. HGF-VH-NG-713). M.W. acknowledges financial support by Chinese Scholarship Council (File No. 201506240060). Y.B. would like to thank the Alexander-von-Humboldt foundation for providing a postdoctoral fellowship. E.G.H would like to thank the Spanish MINECO (Ministerio de Economía y Competitividad) for the financial support under Grant No. TEC2017-84378-R.

[1] X. Liu, B. Kuyken, G. Roelkens, R. Baets, R. M. Osgood Jr, and W. M. Green, Bridging the mid-infrared-to-telecom gap with silicon nanophotonic spectral translation, Nat. Photonics **6**, 667 (2012).

[2] R. Soref, Group IV photonics: Enabling 2 μm communications, Nat. Photonics **9**, 358 (2015).

[3] E. Theocharous and J. R. Birch, Detectors for mid- and far-infrared spectroscopy: selection and use, in *Handbook of Vibrational Spectroscopy*, vol. 1, edited by J. M. Chalmers and P. R. Griffiths (John Wiley and Sons, Chichester, 2002).

[4] Y. Zhang, T. Liu, B. Meng, X. Li, G. Liang, X. Hu, and Q. J. Wang, Broadband high photoresponse from pure monolayer graphene photodetector, Nat. Commun. **4**, 1811 (2013).

[5] R. Soref, Mid-infrared photonics in silicon and germanium, Nat. Photonics **4**, 495 (2010).

[6] C. B. Simmons, A. J. Akey, J. P. Mailoa, D. Recht, M. J. Aziz, and T. Buonassisi, Enhancing the infrared photoresponse of silicon by controlling the Fermi level location within an impurity band, Adv. Funct. Mater. **24**, 2852 (2014).

[7] A. Rogalski, Infrared detectors: status and trends, Prog. Quantum Electron. **27**, 59 (2003).

[8] M. Casalino, G. Coppola, M. Iodice, I. Rendina, and L. Sirleto, Near-infrared sub-bandgap all-silicon photodetectors: state of the art and perspectives, Sensors **10**, 10571 (2010).

[9] W. Yang, J. Mathews, and J. S. Williams, Hyperdoping of Si by ion implantation and pulsed laser melting, Mater. Sci. Semicond. Process **62**, 103 (2017).

[10] S. Zhou, X. Pi, Z. Ni, Q. Luan, Y. Jiang, C. Jin, T. Nozaki, and D. Yang, Boron-and phosphorus-hyperdoped silicon nanocrystals, Part. Part. Syst. Char. **32**, 213 (2015).

[11] O. Moutanabbir, D. Isheim, H. Blumtritt, S. Senz, E. Pippel, and D. N. Seidman, Colossal injection of catalyst atoms into silicon nanowires, Nature **496**, 78 (2013).

[12] Z. Ni, L. Ma, S. Du, Y. Xu, M. Yuan, H. Fang, Z. Wang, M. Xu, D. Li, J. Yang, and W. Hu, Plasmonic silicon quantum dots enabled high-sensitivity ultrabroadband photodetection of graphene-based hybrid phototransistors, ACS Nano **11**, 9854 (2017).

[13] Y. Berencén, S. Prucnal, W. Möller, R. Hübner, L. Rebohle, R. Böttger, M. Glaser, T. Schönherr, Y. Yuan, M. Wang, Y. M. Georgiev, A. Erbe, A. Lugstein, M. Helm, S. Zhou, and W. Skorupa, CMOS-compatible controlled hyperdoping of silicon nanowires, Adv. Mater. Interfaces **5**, 1800101 (2018).

[14] J. Michel, J. Liu, and L. C. Kimerling, High-performance Ge-on-Si photodetectors, Nat. Photonics **4**, 527 (2010).

[15] H. Park, Y. H. Kuo, A. W. Fang, R. Jones, O. Cohen, M. J. Paniccia, and J. E. Bowers, A hybrid AlGaInAs-silicon evanescent preamplifier and photodetector, Opt. Express **15**, 13539 (2007).

[16] A. Black, A. R. Hawkins, N. M. Margalit, D. I. Babic, A. L. Holmes, Y. L. Chang, P. Abraham, J. E. Bowers, and E. L. Hu, Wafer fusion: materials issues and device results, IEEE J. Sel. Top. Quantum Electron. **3**, 943 (1997).

[17] N. Sclar, Properties of doped silicon and germanium infrared detectors, Prog. Quantum Electron. **9**, 149 (1984).

[18] N. Sclar, Survey of dopants in silicon for 2–2.7 and 3–5 μm infrared detector application, Infrared Phys. **17**, 71 (1977).

[19] A. Rogalski, *Infrared Detectors (Electrocomponent Science Monographs)* (Gordon and Breach, New York, 2000).

[20] A. J. Said, D. Recht, J. T. Sullivan, J. M. Warrender, T. Buonassisi, P. D. Persans, and M. J. Aziz, Extended infrared photoresponse and gain in chalcogen-supersaturated silicon photodiodes, Appl. Phys. Lett. **99**, 073503 (2011).

[21] S. Hu, P. Han, S. Wang, X. Mao, X. Li, and L. Gao, Structural and optoelectronic properties of selenium-doped silicon formed using picosecond pulsed laser mixing, Phys. Status Solidi A **209**, 2521 (2012).

[22] E. García-Hemme, R. García-Hernansanz, J. Olea, D. Pastor, A. del Prado, I. Mártil, and G. Gónzalez-Díaz, Sub-bandgap spectral photo-response analysis of Ti supersaturated Si, Appl. Phys. Lett. **101**, 192101 (2012).

[23] J. P. Mailoa, A. J. Akey, C. B. Simmons, D. Hutchinson, J. Mathews, J. T. Sullivan, D. Recht, M. T. Winkler, J. S. Williams, J. M. Warrender, and P. D. Persans, Room-temperature sub-band gap optoelectronic response of hyperdoped silicon, Nat. Commun. **5**, 3011 (2014).

[24] E. García-Hemme, R. García-Hernansanz, J. Olea, D. Pastor, A. del Prado, I. Mártil, and G. González-Díaz, Room-temperature operation of a titanium supersaturated silicon-based infrared photodetector, Appl. Phys. Lett. **104**, 211105 (2014).

[25] X. Qiu, X. Yu, S. Yuan, Y. Gao, X. Liu, Y. Xu, and D. Yang, Trap assisted bulk silicon photodetector with high photoconductive gain, low noise, and fast response by Ag hyperdoping, Adv. Opt. Mater. **6**, 1700638 (2018).

[26] J. Olea, E. López, E. Antolín, A. Martí, A. Luque, E. García-Hemme, D. Pastor, R. García-Hernansanz, A. del Prado, and G. González-Díaz, Room temperature photoresponse of titanium supersaturated silicon at energies over the bandgap, J. Phys. D: Appl. Phys. **49**, 055103 (2016).

[27] Y. Berencén, S. Prucnal, F. Liu, I. Skorupa, R. Hübner, L. Rebohle, S. Zhou, H. Schneider, M. Helm, and W. Skorupa, Room-temperature short-wavelength infrared Si photodetector, Sci. Rep. **7**, 43688 (2017).

[28] X. Y. Wang, Y.-G. Huang, D.-W. Liu, X.-N. Zhu, and H.-L. Zhu, High response in a tellurium-supersaturated silicon photodiode, Chinese Phys. Lett. **30**, 036101 (2013).

[29] R. Schaub, G. Pensl, M. Schulz, and C. Holm, Donor states in tellurium-doped silicon, Appl. Phys. A **34**, 215 (1984).

[30] E. Janzén, R. Stedman, G. Grossmann, and H. Grimmeiss, High-resolution studies of sulfur-and selenium-related donor centers in silicon, Phys. Rev. B **29**, 1907 (1984).

[31] L. Pauling, The nature of the chemical bond. IV. The energy of single bonds and the relative electronegativity of atoms, J. Am. Chem. Soc. **54**, 3570 (1932).

[32] K. Sánchez, I. Aguilera, P. Palacios, and P. Wahnón, Formation of a reliable intermediate band in Si heavily coimplanted with chalcogens (S, Se, Te) and group III elements (B, Al), Phys. Rev. B **82**, 165201 (2010).

[33] H. G. Grimmeiss, L. Montelius, and K. Larsson, Chalcogens in germanium, Phys. Rev. B **37**, 6916 (1988).

[34] J. F. Ziegler, SRIM-2003, Nucl. Instrum. Methods Phys. Res. B **219**, 1027 (2004).

[35] F. Spaepen, D. Turnbull, J. Poate, and J. Mayer, *Laser Annealing of Semiconductors* (Academic, New York, 1982).

[36] M. Mayer, *SIMNRA user's guide*. Tech. Rep. IPP 9/113 (Max-Planck-Institut für Plasmaphysik, Garching, 1997).

[37] M. Mayer, in *AIP Conference Proceedings*, vol. 475, no. 1, pp. 541–544 (AIP, Denton, 1999).

[38] L. Van der Pauw, A method of measuring the resistivity and Hall coefficient on lamellae of arbitrary shape, Philips Tech. Rev. **20**, 320 (1958).

[39] L. Feldman, *Material Analysis by Ion Channeling* (Academic Press, New York, 1982).

[40] S. Zhou, F. Liu, S. Prucnal, K. Gao, M. Khalid, C. Baehtz, M. Posselt, W. Skorupa, and M. Helm, Hyperdoping silicon with selenium: solid vs. liquid phase epitaxy, Sci. Rep. **5**, 8329 (2015).

[41] N. F. Mott, Metal-insulator transition, Rev. Mod. Phys. **40**, 677 (1968).

[42] E. Ertekin, M. T. Winkler, D. Recht, A. J. Said, M. J. Aziz, T. Buonassisi, and J. C. Grossman, Insulator-to-Metal Transition in Selenium-Hyperdoped Silicon: Observation and Origin, Phys. Rev. Lett. **108**, 026401 (2012).

[43] S. Hu, P. Han, P. Liang, Y. Xing, and S. Lou, Metallic conduction behavior in selenium-hyperdoped silicon, Mater. Sci. Semicond. Process. **17**, 134 (2014).

[44] W. Kaiser, P. H. Keck, and C. Lange, Infrared absorption and oxygen content in silicon and germanium, Phys. Rev. **101**, 1264 (1956).

[45] R. Newman and R. Smith, Vibrational absorption of carbon and carbon-oxygen complexes in silicon, J. Phys. Chem. Solids **30**, 1493 (1969).

[46] J. T. Sullivan, C. B. Simmons, J. J. Krich, A. J. Akey, D. Recht, M. J. Aziz, and T. Buonassisi, Methodology for vetting heavily doped semiconductors for intermediate band photovoltaics: A case study in sulfur-hyperdoped silicon, J. Appl. Phys. **114**, 103701 (2013).

[47] I. Umezu, J. M. Warrender, S. Charnvanichborikarn, A. Kohno, J. S. Williams, M. Tabbal, D. G. Papazoglou, X.-C. Zhang, and M. J. Aziz, Emergence of very broad infrared absorption band by hyperdoping of silicon with chalcogens, J. Appl. Phys. **113**, 213501 (2013).

[48] V. Ranki, K. Saarinen, J. Fage-Pedersen, J. L. Hansen, and A. N. Larsen, Electrical deactivation by vacancy-impurity complexes in highly As-doped Si, Phys. Rev. B **67**, 041201 (2003).

[49] S. M. Sze, and K. K. Ng, *Physics of Semiconductor Devices* (John Willey & Sons, New York, 1981).

[50] B. Boyarbay, H. Çetin, M. Kaya, and E. Ayyildiz, Correlation between barrier heights and ideality factors of H-terminated Sn/p-Si (100) Schottky barrier diodes, Microelectron. Eng. **85**, 721 (2008).

[51] S. Silvestre, A. Boronat, M. Colina, L. Castañer, J. Olea, D. Pastor, A. del Prado, I. Mártil, G. González-Díaz, A. Luque, and E. Antolín, Sub-bandgap external quantum efficiency in Ti implanted Si heterojunction with intrinsic thin layer cells, Jpn. J. Appl. Phys. **52**, 122302 (2013).

[52] M. Grundmann, *The Physics of Semiconductors (An Introduction Including Devices and Nanophysics)* (Springer, Berlin, 2006).

# Statistics

Image: HZDR / D. Janke

# User facilities and services

## Ion Beam Center (IBC)

The Ion Beam Center (IBC) at HZDR combines various machines (electrostatic accelerators, ion implanters, low-energy and focused ion beam systems) into a unique facility used for ion beam modification and ion beam analysis of materials. The available energy range spans from a few eV to 60 MeV with a respective interaction depth in solids between 0.1 nm to 10 µm. In addition to standard broad beams also focused (down to 1 nm) and highly-charged (charge state up to 45+) ion beams are available. In combination with an allocated ion beam experiment, users can also profit from structural analysis (electron microscopy and spectroscopy, X-ray scattering techniques) and sample or device processing under clean-room conditions. At the 6 MV tandem accelerator, the IBC operates the DREAMS (DREsden AMS = accelerator mass spectrometry) facility, which is used for the determination of long-lived radionuclides, like $^{7,10}$Be, $^{26}$Al, $^{35}$Cl, $^{41}$Ca, $^{129}$I, and others. A schematic overview of the IBC including the description of the main beam lines and experimental stations is given on page 65 of this Annual Report. In 2018, about 13.400 beam time hours were delivered for about 340 users from 23 countries worldwide performing experiments at IBC or using the capabilities for ion beam services.


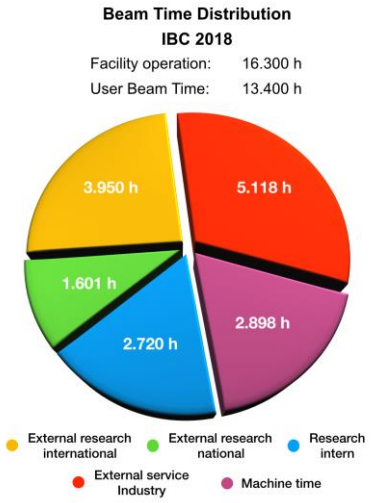


The IBC has provided ion beam technology as a user and competence center for ion beam applications for more than 30 years. With respect to user beam time hours, the IBC is internationally leading and has been supported by numerous national and European grants and by industry.

The research activities cover both ion beam modification and ion beam analysis (IBA).

The operation of IBC is accompanied by a strong in-house research at the affiliated host “Institute of Ion Beam Physics and Materials Research”, both in experiment and theory. Furthermore, the IBC strongly supports the commercial exploitation of ion beam technology of partners from industry, which is essential for materials science applications. For ion beam services, the HZDR Innovation GmbH (spin-off of the HZDR) – www.hzdr-innovation.de – provides a direct and fast access to the IBC facilities based on individual contracts.

Recently, new ion beam tools and end-stations have been commissioned which will attract new users by state-of-the-art experimental instrumentation. The basically upgraded ion microprobe station at the 3 MV machine is now in routine and user-friendly operation mode, delivering the possibility to use – in parallel or sequentially – several IBA techniques with a spatial resolution of about 3 µm. An ion

microscope *ORION NanoFab* (He/Ne ions, 10 – 40 keV) provides unique possibilities for surface imaging, nano-fabrication and, for the first time, elemental analysis based on ion beam analysis techniques. The cluster tool at the 6 MV accelerator allows *in situ* deposition and analysis investigations at temperatures of up to 800 °C. Recently, first instruments for the new low-energy ions nano-engineering laboratory have been commissioned, including the installation of a 100 kV accelerator, a medium-energy ion scattering (MEIS) setup und a new low-energy electron microscope (LEEM) aiming to study low-energy ion interactions at surfaces.

IBC activities are efficiently integrated into various Helmholtz programmes within the research field “Matter”, but also in the Helmholtz cross-programme activities “Mineral Resources”, “Materials Research for Energy Technologies”, and “Helmholtz Energy Materials Foundry”. From 2013, the IBC has been recognized as a large-scale facility within the “BMBF Verbundforschung” promoting long-term collaborations with universities. In addition, from 2019 the IBC is coordinating the EU project RADIATE for providing trans-national access to the largest ion beam centers in Europe (www.ionbeamcenters.eu).

Following the rules of a European and national user facility, access for scientific experiments to IBC is provided on the basis of a proposal procedure (www.hzdr.de/IBC) via the common HZDR user facility portal **HZDR-GATE** (gate.hzdr.de). Due to the availability of multiple machines and versatile instrumentation, IBC proposals can be submitted continuously. The scientific quality of the proposals is evaluated and ranked by an external international User Selection Panel. For successfully evaluated proposals, users get free access to IBC facilities for their experiments. The use of the IBC facilities includes the scientific and technical support during planning, execution and evaluation of the experiments. For AMS samples preparation, two chemical laboratories are available.

For more detailed information, please contact Dr. Johannes von Borany (j.v.borany@hzdr.de) or Dr. Stefan Facsko (s.facsko@hzdr.de) and visit the IBC webpage: www.hzdr.de/IBC.

## Free Electron Laser FELBE

FELBE is an acronym for the free-electron laser (FEL) at the Electron Linear accelerator with high Brilliance and low Emittance (ELBE) located at the Helmholtz-Zentrum Dresden-Rossendorf. The heart of ELBE is a superconducting linear accelerator operating in continuous-wave (cw) mode with a pulse repetition rate of 13 MHz. The electron beam (40 MeV, 1 mA max.) is guided to several laboratories where secondary beams (particle and electromagnetic) are generated. Two free-electron lasers (U37-FEL and U100-FEL) produce intense, coherent electromagnetic radiation in the mid and far infrared, which is tunable over a wide wavelength range (5 – 250 µm) by changing the electron energy or the undulator magnetic field. The previous U27 undulator has been replaced by the U37, in order to provide better coverage of the 20 – 35 µm region. Main parameters of the infrared radiation produced by FELBE are as follows:

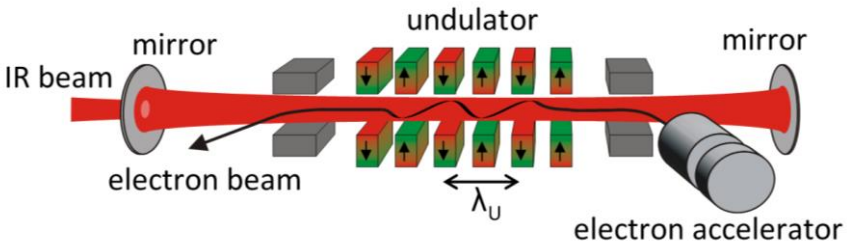


| | | |
|---|---|---|
| Wavelength λ | 5 – 40 µm<br>18 – 250 µm | FEL with undulator U37<br>FEL with undulator U100 |
| Pulse energy | 0.01 – 2 µJ | depends on wavelength |
| Pulse length | 1 – 25 ps | depends on wavelength |
| Repetition rate | 13 MHz | 3 modes: • cw<br>• macropulsed (> 100 µs, < 25 Hz)<br>• single pulsed (Hz … kHz) |

The free electron laser is a user facility. Applications for beam time can be submitted twice a year, typically by April 15 and October 15. Users from EU countries are able to receive support through the HORIZON 2020 Integrated Infrastructure Initiative (I3) CALIPSOplus (**C**onvenient **A**ccess to **Li**ght Sources O**p**en to Innovation, **S**cience and to the W**o**rld) which started in May 2017.

Typical applications are picosecond pump-probe spectroscopy (also in combination with several other femtosecond lasers, which are synchronized to the FEL), near-field microscopy, and nonlinear optics. The FELBE facility also serves as a far-infrared source for experiments at the Dresden High Magnetic Field Laboratory (HLD) involving pulsed magnetic fields up to 70 T.

The statistics shows that the FEL used 1090 hours beam time of the ELBE accelerator. This corresponds to 20 % of total beam time, which is again distributed among internal and external users.

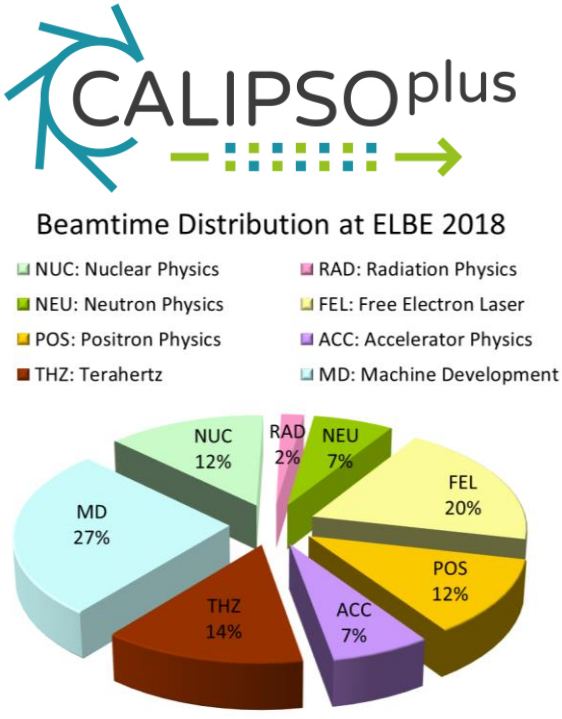


For further information, please contact Prof. Manfred Helm (m.helm@hzdr.de) or visit the FELBE webpage www.hzdr.de/FELBE.

# Experimental equipment

## Accelerators, ion implanters and other ion processing tools

| | | |
|---|---|---|
| Van de Graaff Accelerator (VdG) | 2 MV | *TuR Dresden, DE* |
| Tandetron Accelerator (T1) | 3 MV | *HVEE, NL* |
| Tandetron Accelerator (T2) | 6 MV | *HVEE, NL* |
| Low-Energy Ion Implanter | 0.1 – 40 kV | *Danfysik, DK* |
| High-Current Ion Implanter | 20 – 200 kV | *Danfysik, DK* |
| High-Energy Ion Implanter | 20 – 500 kV | *HVEE, NL* |
| Mass-Separated Focused Ion Beam (FIB)<br>(15 nm, variable ions) | 10 – 30 keV<br>>10 A/cm$^2$ | *Orsay Physics, FR* |
| ORION NanoFab FIB Tool<br>(including GIS and Nanopatterning, RBS, SIMS) | He, Ne ions,<br>10 – 35 kV,<br>Resolution < 2 nm | *Carl Zeiss Microscopy, DE* |
| Highly-Charged Ion Facility | 25 eV – 6 keV × Q<br>Q = 1 … 40 (Xe) | *DREEBIT, DE;*<br>*PREVAC, PL* |
| Ion-Beam Sputtering | 200 – 2000 V | *Home-built* |
| UHV Ion Irradiation (Ar, He, etc.) | 0 – 5 kV<br>Scan 10 × 10 mm$^2$ | *Cremer, DE; VG, USA* |

## Ion beam analysis (IBA)

A wide variety of advanced IBA techniques are available at the MV accelerators (see figure).

| | | | |
|---|---|---|---|
| RBS | Rutherford Backscattering Spectrometry | (A1), (A2), (5), (9), (11), (12) | *VdG, T1, T2, HIM* |
| RBS/C | RBS - Channelling | (1), (11) | *VdG, T1* |
| HR-RBS | High-Resolution RBS | (16) | *T1* |
| ERDA | Elastic Recoil Detection Analysis | (2) | *T2* |
| PIXE | Particle-Induced X-ray Emission | (A2), (4), (5), (12) | *VdG, T1, T2* |
| PIGE | Particle-Induced $\gamma$ Emission | (5), (12) | *T1, T2* |
| NRA | Nuclear Reaction Analysis | (1), (11), (12) | *T1, T2* |
| NRRA | Nuclear Resonance Reaction Analysis | (1), (11), (12) | *T1, T2* |
| NMP | Nuclear Microprobe | (12) | *T1* |
| AMS | Accelerator Mass Spectrometry<br>(focused to long-lived radionuclides: $^{7}$Be, $^{10}$Be, $^{26}$Al, $^{36}$Cl, $^{41}$Ca, $^{129}$I) | (B2) | *T2* |

Some stations are equipped with additional process facilities enabling *in-situ* IBA investigations during ion irradiation, sputtering, deposition, annealing, investigations at solid-liquid interfaces, etc.

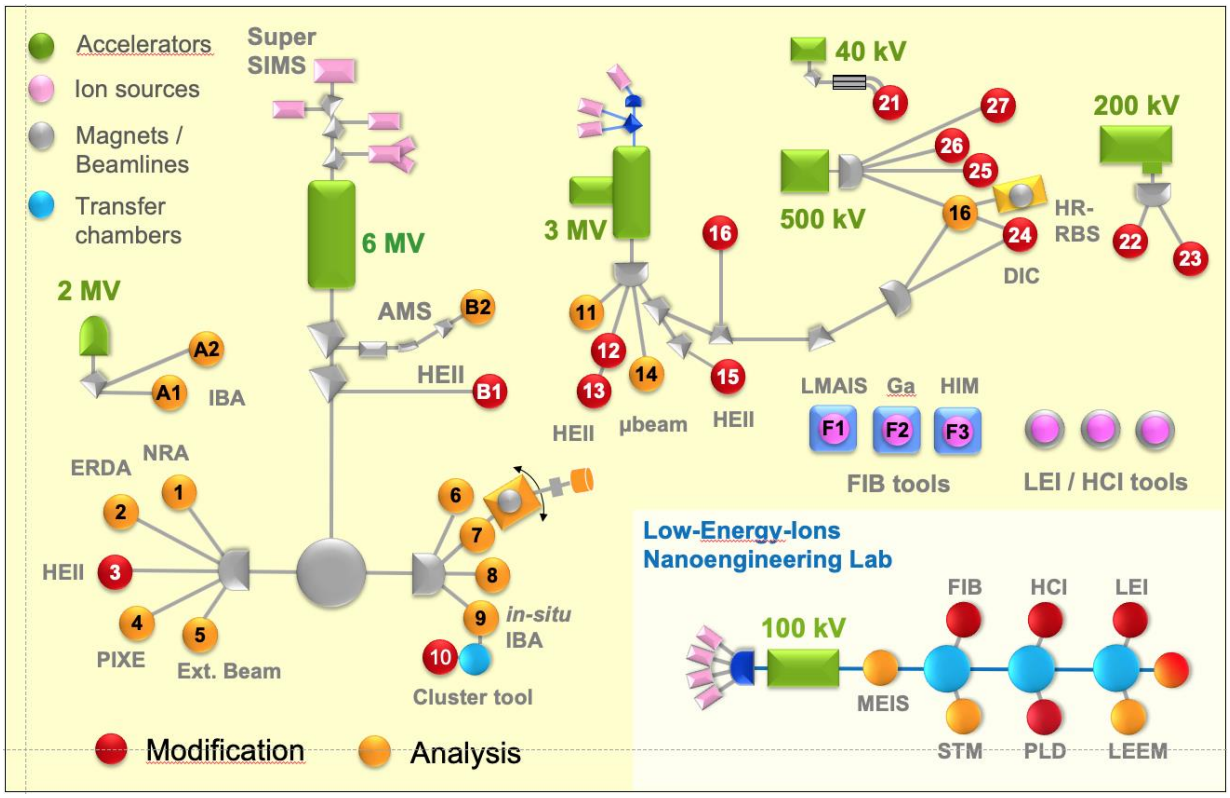


*Schematic overview of the HZDR Ion Beam Center*

## Other particle-based analytical techniques

| | | | |
|---|---|---|---|
| SEM | Scanning Electron Microscope (S4800 II) | 1 – 30 keV<br>+ EDX | *Hitachi, JP* |
| TEM | Transmission Electron Microscope<br>(Titan 80-300 with Image Corrector) | 80 – 300 keV<br>+ EDX, EELS | *FEI, NL* |
| TEM | Transmission Electron Microscope<br>(Talos F200X) | 20 – 200 keV<br>+ SuperX EDX | *FEI, NL* |
| FIB/SEM | Focused Ion/Electron Cross Beam<br>(NVision 40 with Elphy Plus Litho) | 0.5 – 30 keV<br>+ EDX, EBSD | *Carl Zeiss Microscopy, DE* |
| AES | Auger Electron Spectroscopy | + XPS, EDX, CL | *Scienta Omicron, DE* |
| LEEM | Low-Energy Electron Microscope<br>(Spec-LEEM-III) | 0 eV – 4.5 keV<br>Resolution < 6 nm<br>+ AES | *Elmitec, DE* |

## Photon-based analytical techniques

| | | | |
|---|---|---|---|
| XRD/XRR | X-Ray Diffractometers | Cu-Kα | |
| | θ-θ Powder D8 | | *Bruker, DE* |
| | θ-2θ 4-Circle D5005 | | *Siemens, DE* |
| | θ-θ 4-Circle Empyrean | | *PANalytical, NL* |
| | θ-2θ 4+2-Circle SEIFERT XRD3003-HR | | *General Electric, US* |
| SE | Spectroscopic Ellipsometry | 250 – 1700 nm | *Woollam, US* |
| UV-Vis | Solid Spec 3700 DUV | 190 – 3300 nm | *Shimadzu, JP* |
| FTIR | Fourier-Transform Infrared Spectrometer | 50 – 15000 $cm^{-1}$ | *Bruker, DE* |
| | Ti:Sapphire Femtosecond Laser | 78 MHz | *Spectra Physics, US* |
| | Femtosecond Optical Parametric Osci. | | *APE, DE* |
| | Ti:Sapphire Femtosecond Amplifier | 1 kHz, 250 kHz | *Coherent, US* |
| | Femtosecond Optical Parametric Amplifier | | *Light Conversion, LT* |
| THz-TDS | Terahertz Time-Domain Spectroscopy | 0.1 – 4 THz | *Home-built* |
| Raman | Raman Spectroscopy | > 45 $cm^{-1}$ | *Jobin-Yvon-Horiba, FR* |
| | In-situ Raman Spectroscopy | > 100 $cm^{-1}$ | *Jobin-Yvon-Horiba, FR* |
| PL | Photoluminescence (10 – 300 K) | 300 – 1600 nm | *Jobin-Yvon-Horiba, FR* |
| TRPL | Time-Resolved Photoluminescence | τ = 3 ps – 2 ns<br>τ > 5 ns | *Hamamatsu Phot., JP*<br>*Stanford Research, US* |
| EL | Electroluminescence | 300 – 1600 nm | *Jobin-Yvon-Horiba, FR* |
| | Optical Split-Coil Supercond. Magnet | 7 T | *Oxford Instr., UK* |
| PR | Photomodulated Reflectivity | 300 – 1600 nm | *Jobin-Yvon-Horiba, FR* |
| PLE | Photoluminescence Excitation | 300 – 1600 nm | *Jobin-Yvon-Horiba, FR* |
| OES | Optical Emission Spectroscopy | 250 – 800 nm | *Jobin-Yvon-Horiba, FR* |

## Magnetic thin film deposition and analysis

| | | | |
|---|---|---|---|
| PLD | Pulsed Laser Deposition | | *SURFACE, DE* |
| MFM | Magnetic Force Microscope | ~ 50 nm resol. | *VEECO; DI, US* |
| AFM/MFM | Magnetic Force Microscope | ~ 50 nm resol. | *BRUKER ICON tool, US* |
| SQUID MPSM | Supercond. Quantum Interference Device | ± 7 T | *Quantum Design, US* |
| SQUID VSM | Vibrating Sample Magnetometer | ± 7 T | *Quantum Design, US* |
| Vector-VSM | Vibrating Sample Magnetometer | ± 2 T | *Quantum Design, US* |
| MOKE | Magneto-Optic Kerr Effect (in-plane) | ± 0.35 T | *Home-built* |
| MOKE | Magneto-Optic Kerr Effect (perpend.) | ± 2 T | *Home-built* |
| FR-MOKE | Frequency-Resolved Magneto-Optic KE | ± 1.1 T | *Home-built* |
| SKM | Scanning Kerr Microscope | | *Home-built* |
| | Kerr Microscope | | *Evico Magnetics, DE* |
| TR-MOKE | Time-Resolved MOKE (Pump-Probe) | | *Home-built* |
| VNA-FMR | Vector Network Analyzer Ferromagnetic Resonance | 50 GHz | *Agilent, DE; Home-built* |

| | | | |
|---|---|---|---|
| Cryo-FMR | Variable-Temperature Ferromagnetic Resonance | 3 – 300 K | *Attocube, DE; Home-built* |
| ME | Magnetoellipsometer | | *LOT, DE; AMAC, US* |
| µBLS | Brillouin Light Scattering Microscope | ± 0.8 T, 532 nm & 491 nm | *Home-built* |
| SKM | Scanning Kerr Microscope with RF Detection (Spectrum Analyzer) | ± 0.5 T, 40 GHz | *Home-built* |
| MT-50G | High Frequency Magneto-Transport Setup | ± 1.5 T, 50 GHz 250 ps | *Home-built* |

## Other analytical and measuring techniques

| | | | |
|---|---|---|---|
| STM/AFM | UHV Scanning Probe Microscope (variable T) | | *Omicron, DE* |
| AFM | Atomic Force Microscope (Contact, Tapping, Spreading) | | *Bruker, US* |
| AFM | Atomic Force Microscope (with c-AFM, SCM-Module) | | *Bruker, US* |
| | Dektak Surface Profilometer | | *Bruker, US* |
| | Micro Indenter/Scratch Tester | | *Shimatsu, JP* |
| MPMS | Mechanical Properties Measurement System – Stretcher | | *Home-built* |
| MS | Mass Spectrometers (EQP-300, HPR-30) | | *HIDEN, UK* |
| | Wear Tester (pin-on disc) | | *Home-built* |
| LP | Automated Langmuir Probe | | *Impedans, IE* |
| HMS | Hall Measurement System | 2 – 400 K, ≤ 9 T | *LakeShore, US* |
| | Van-der-Pauw HMS Ecopia | 300 K & LNT, 0.5 T | *Bridge Technol., US* |
| MTD | Magneto-Transport Device | 300 K, ≤ 3 T | *Home-built* |
| RS | Sheet-Rho-Scanner | | *AIT, KR* |
| RMAG | Redmag Tensormeter System | 240 – 350 K, 1.5 T | *Home-built* |
| GMAG | Greymag Tensormeter System | 300 K, 0.7 T | *Home-built* |
| DLTS | Deep Level Transient Spectroscopy | + I-U/C-V 10 – 300 K, 1 MHz | *PhysTech, DE* |
| IV / CV | Photocapacitance (+I-V/G-V) | 250 – 2500 nm | *Home-built* |
| IV / CV | I-V and C-V Analyzer | | *Keithley, US* |
| IV / CV | I-V and C-V Semi-Automatic Prober | -60 – 300 °C | *Süss, DE; Keithley, US* |
| IV | I-V Prober | 4.2 – 600 K | *LakeShore, Agilent, US* |
| GC | Gas Chromatography (GC-2010) | | *Shimadzu, JP* |
| ECW | Electrochemical workstation (CHI 760e) | | *CH instruments, US* |
| FDA | Force-displacement analysis machine | | *Sauter, DE* |
| IV / VNA | I-V and VNA Prober for VHF, LCR and frequency analysis measurements | 20-120 MHz | *Süss, DE; Cascade, US; Keysight, US* |
| OSCI | 4-channel real time oscilloscope | 1,5 GHz (BW), 5 GSa/s | *Keysight, US* |
| IR-Cam | TrueIR Thermal Imager | -20 – 350 °C | *Keysight, US* |
| CM | Confocal Microscope (Smartproof 5) | 405 nm LED, z drive res. ~ 1 nm | *Carl Zeiss, DE* |
| FAS | Fluidic Analytic Setup – microscope, high speed camera, and fluidic pumps | 2 GB 120 kfps, 5 modules | *Zeiss, DE; Photron, US; Cetoni, DE* |

## Deposition and processing techniques

| | | |
|---|---|---|
| Physical Deposition | Sputtering DC/RF, Evaporation | *Nordiko, UK* |
| | Electron Beam Evaporation System | *Leybold Optics, DE* |
| | Thermal Evaporation | *Bal-Tec, LI* |
| | DC/RF magnetron sputter system, 4x 3'' + 4x 2'' magnetrons, substrate heating: RT – 950 °C, up to 4" wafers | *BESTEC, DE* |
| | DC/RF magnetron sputter system, 6x 2'' confocal magnetrons, substrate heating: RT – 650 °C, up to 3" wafers | *AJA International, US* |
| | High Power Impulse Magnetron Sputtering | *Melec, DE* |
| Molecular Beam Epitaxy | III-V Semiconductors | *Riber, FR* |
| Chemical Vapour Deposition | Plasma Enhanced CVD: a-Si, a-Ge, $SiO_2$, SiON, $Si_3N_4$ | *Oxford Instr., UK* |
| Atomic Layer Deposition | $Al_2O_3$, $HfO_2$, $SiO_2$ | *Ultratech, US* |
| Dry Etching | ICP-RIE: $CF_4$, $SF_6$, $C_4F_8$ | *Sentech, DE* |
| | RIBE, ∅ 6": Ar, $CF_4$ | *Roth & Rau, DE* |
| | Barrel reactor, ∅ 4": $O_2$, $SF_6$ | *Diener electronic, DE* |
| Etching/Cleaning | incl. Anisotropic Selective KOH Etching | |
| Photolithography | Mask-Aligner MJB3, 2 µm accur.; ∅ 3" | *Süss, DE* |
| | Direct Laser Writer DWL 66FS, 2 µm accuracy, ∅ 8"x8" | *Heidelberg Instr., DE* |
| | Laser Micro Writer ML, 10 µm accuracy | *Durham Magneto Optics, UK* |
| Electron Beam Lithography | Raith 150-TWO: ∅ 6", 10 nm resol. | *Raith, DE* |
| | e-Line Plus: ∅ 4", 10 nm resol. | *Raith, DE* |
| Thermal Treatment | Room Temperature – 2000 °C | |
| Furnace | | *InnoTherm, DE* |
| Rapid Thermal Annealing JETFIRST 100 | | *JIPELEC, FR* |
| Rapid Thermal Annealing AW 610 | | *Allwin21, USA* |
| Flash-Lamp Units (0.5 – 20 ms) | | *Home-built;FHR/DTF, DE* |
| Combined Flash Lamp Sputter Tool (Magnetron sputtering plus flash lamp annealing 0.3 – 3 ms, up to 10 Hz) | | *ROVAK GmbH, DE* |
| RF Heating (Vacuum) | | *JIPELEC, FR* |
| Laser Annealing (CW, 808 nm, 450 W)<br>Laser Annealing (30 ns pulse,10 Hz, 308 nm, 500 mJ) | | *LIMO, DE;*<br>*COHERENT, USA* |
| CVD Tube furnace (RT– 1200 °C, three channel gas) | | *NBD, CN* |
| Vacuum oven (RT – 250 °C, Vacuum < 133 Pa) | | *LAB-KITS, CN* |
| Bonding Techniques | Ultrasonic Wire Bonding | *Kulicke & Soffa, US* |
| | Semi-automatic Wire-bonder: Gold-ball and wedge-wedge bonding Ultrasonic generator: 60 kHz, 140 kHz Wire deformation control software | *F & S Bondtec, AT* |
| Cutting, Grinding, Polishing | | *Bühler, DE* |
| TEM Sample Preparation | Plan View and Cross Section incl. Ion Milling Equipment | *Gatan, US* |
| Disperse and mixer | Mixer for pastes and emulsions | *IKA, DE* |
| Centrifuge | Max. 17850 rpm, -10 – 40 °C | *Thermo Scientific, US* |

# Doctoral training programme

## International Helmholtz Research School NANONET

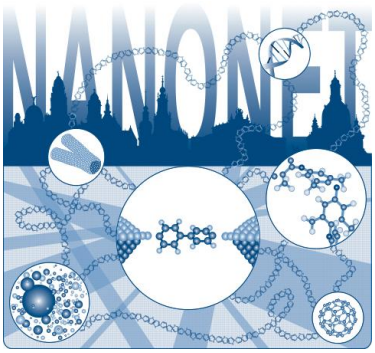


The Institute of Ion Beam Physics and Materials Research is coordinating the International Helmholtz Research School for Nanoelectronic Networks (IHRS NANONET) supported by the Initiative and Networking Fund of the Helmholtz Association. The project started in October 2012. The total funding is 1.2 Mio. € for a period of 8 years.

The IHRS NANONET is an international, interdisciplinary and thematically focused doctoral programme in the field of molecular electronics. The research school aims at attracting and promoting excellence by educating promising doctoral candidates with backgrounds in physics, chemistry, materials science and electrical engineering. During a period of three years, PhD candidates benefit from well-structured, comprehensive training curricula and multiple mentorship, while performing cutting edge research projects within one of the 15 NANONET research groups. The doctoral candidates have the unique opportunity to contribute to the advancement of molecular electronics by developing strategies for the integration of single nano-sized building blocks into large interconnected networks.

The IHRS NANONET fosters not only professional qualification but also personal development by equipping young graduates with competencies for successful careers in a wide variety of positions in academia and industry. The NANONET Annual Workshop 2018 was conducted at the hotel Augustusberg in Bad Gottleuba and was attended by 35 participants of 15 nationalities. Three senior students concluded their PhD degrees in 2018: Congratulations to Dr. Jeffrey Kelling (TU Chemnitz), Dr. Florian Günther and Dr. Eunhye Baek (both TU Dresden).

**The consortium**

- Helmholtz-Zentrum Dresden-Rossendorf (HZDR)
- Technische Universität (TU) Dresden
- Leibniz Institute of Polymer Research (IPF) Dresden
- Fraunhofer Institute for Ceramic Technologies and Systems (IKTS) Dresden
- Nanoelectronic Materials Laboratory (NaMLab) gGmbH Dresden


For further information, please contact the NANONET coordinator, Dr. Peter Zahn (nanonet@hzdr.de), or visit the IHRS NANONET website: www.hzdr.de/nanonet.

# Publications

## Publications in journals


1. Bayrak, T.; Helmi, S.; Ye, J.; Kauert, D.; Kelling, J.; Schönherr, T.; Weichelt, R.; Erbe, A.; Seidel, R.
**DNA-Mold Templated Assembly of Conductive Gold Nanowires**
Nano Letters **18**, 2116 (2018)

2. Cañón Bermúdez, G.S.; Fuchs, H.; Bischoff, L.; Fassbender, J.; Makarov, D.
**Electronic-skin compasses for geomagnetic field driven artificial magnetoreception and interactive electronics**
Nature Electronics **1**, 589 (2018)

3. Ehrler, J.; He, M.; Shugaev, M.V.; Polushkin, N.I.; Wintz, S.; Liersch, V.; Cornelius, S.; Hübner, R.; Potzger, K.; Lindner, J.; Fassbender, J.; Ünal, A.A.; Valencia, S.; Kronast, F.; Zhigilei, L.V.; Bali, R.
**Laser-Rewriteable Ferromagnetism at Thin-Film Surfaces**
ACS Applied Materials and Interfaces **10**, 15232 (2018)

4. Kretschmer, S.; Maslov, M.; Ghaderzadeh, S.; Ghorbani-Asl, M.; Hlawacek, G.; Krasheninnikov, A.V.
**Supported Two-Dimensional Materials under Ion Irradiation: The Substrate Governs Defect Production**
ACS Applied Materials and Interfaces **10**, 30827 (2018)

5. Singh, A.; Pashkin, A.; Winnerl, S.; Helm, M.; Schneider, H.
**Gapless broadband terahertz emission from a germanium photoconductive emitter**
ACS Photonics **5**, 2718 (2018)

6. Wang, M.; Berencén, Y.; García-Hemme, E.; Prucnal, S.; Hübner, R.; Yuan, Y.; Xu, C.; Rebohle, L.; Böttger, R.; Heller, R.; Schneider, H.; Skorupa, W.; Helm, M.; Zhou, S.
**Extended Infrared Photoresponse in Te-Hyperdoped Si at Room Temperature**
Physical Review Applied **10**, 024054 (2018)

7. Al Motasem, A.T.; Posselt, M.; Bergström, J.
**Nanoindentation and nanoscratching of a ferrite/austenite iron bi-crystal: An atomistic study**
Tribology International **127**, 231 (2018)

8. Anisimov, A.N.; Soltamov, V.A.; Breev, I.D.; Babunts, R.A.; Mokhov, E.N.; Astakhov, G.V.; Dyakonov, V.; Yakovlev, D.R.; Suter, D.; Baranov, P.G.
**All-optical quantum thermometry based on spin-level cross-relaxation and multicenter entanglement under ambient conditions in SiC**
AIP Advances **8**, 085304 (2018)

9. Bai, X.; Shuai, Y.; Gong, C.; Wu, C.; Luo, W.; Böttger, R.; Zhou, S.; Zhang, W.
**Surface modifications of crystal-ion-sliced LiNbO3 thin films by low energy ion irradiations**
Applied Surface Science **434**, 669 (2018)

10. Bakaev, A.; Terentyev, D.; Chang, Z.; Posselt, M.; Olsson, P.; Zhurkin, E.E.
**Effect of isotropic stress on dislocation bias factor in bcc iron: an atomistic study**
Philosophical Magazine **98**, 54 (2018)

11. Barthen, R.; Karimzadeh, L.; Gründig, M.; Grenzer, J.; Lippold, H.; Franke, K.; Lippmann-Pipke, J.
**Glutamic acid leaching of synthetic covellite – A model system combining experimental data and geochemical modeling**
Chemosphere **196**, 368 (2018)

12. Bayrak, T.; Jagtap, N.S.; Erbe, A.
**Review of the electrical characterization of metallic nanowires on DNA templates**
International Journal of Molecular Sciences **19**, 3019 (2018)

13. Benad, A.; Jürries, F.; Vetter, B.; Klemmed, B.; Hübner, R.; Leyens, C.; Eychmüller, A.
**Mechanical Properties of Metal Oxide Aerogels**
Chemistry of Materials **30**, 145 (2018)

14. Berencén, Y.; Prucnal, S.; Möller, W.; Hübner, R.; Rebohle, L.; Böttger, R.; Glaser, M.; Schönherr, T.; Yuan, Y.; Wang, M.; Georgiev, Y.M.; Erbe, A.; Lugstein, A.; Helm, M.; Zhou, S.; Skorupa, W.
**CMOS-compatible controlled hyperdoping of silicon nanowires**
Advanced Materials Interfaces, 1800101 (2018)

15. Berencén, Y.; Prucnal, S.; Möller, W.; Hübner, R.; Rebohle, L.; Schönherr, T.; Bilal Khan, M.; Wang, M.; Glaser, M.; Georgiev, Y.M.; Erbe, A.; Lugstein, A.; Helm, M.; Zhou, S.
**Formation of n- and p-type regions in individual Si/SiO2 core/shell nanowires by ion beam doping**
Nanotechnology **29**, 474001 (2018)

16. Bergner, F.; Hlawacek, G.; Heintze, C.
**Helium-ion microscopy, helium-ion irradiation and nanoindentation of Eurofer 97 and ODS Eurofer**
Journal of Nuclear Materials **505**, 267 (2018)

17. Bhowmick, S.; Pal, S.; Das, D.; Singh, V.K.; Khan, S.A.; Hübner, R.; Barman, S.R.; Kanjilal, D.; Kanjilal, A.
**Carbon doping controlled thermoluminescent defect centers in nanoporous alumina for ion beam dosimetry**
Journal of Applied Physics **124**, 134902 (2018)

18. Bonny, G.; Bakaev, A.; Terentyev, D.; Zhurkin, E.; Posselt, M.
**Atomistic study of the hardening of ferritic iron by Ni-Cr decorated dislocation loops**
Journal of Nuclear Materials **498**, 430 (2018)

19. Börner, P.C.; Kinyanjui, M.K.; Björkman, T.; Lehnert, T.; Krasheninnikov, A.V.; Kaiser, U.
**Observation of charge density waves in free-standing 1T-$TaSe_2$ monolayers by transmission electron microscopy**
Applied Physics Letters **113**, 173103 (2018)

20. Braucher, R.; Keddadouche, K.; Aumaître, G.; Bourlès, D.L.; Arnold, M.; Pivot, S.; Baroni, M.; Scharf, A.; Rugel, G.; Bard, E.
**Chlorine measurements at the 5MV French AMS national facility ASTER: Associated external uncertainties and comparability with the 6MV DREAMS facility**
Nuclear Instruments and Methods in Physics Research B **420**, 40 (2018)

21. Braun, J.M.; Schneider, H.; Helm, M.; Mirek, R.; Boatner, L.A.; Marvel, R.E.; Haglund Jr., R.F.; Pashkin, A.
**Ultrafast response of photoexcited carriers in $VO_2$ at high-pressure**
New Journal of Physics **20**, 083003 (2018)

22. Brem, S.; Wendler, F.; Winnerl, S.; Malic, E.
**Electrically pumped graphene-based Landau-level laser**
Physical Review Materials **2**, 034002 (2018)

23. Buchriegler, J.; Klingner, N.; Hanf, D.; Munnik, F.; Nowak, S.H.; Scharf, O.; Ziegenrücker, R.; Renno, A.D.; von Borany, J.
**Enhancements in full-field PIXE imaging - large area elemental mapping with increased lateral resolution devoid of optics artefacts**
X-Ray Spectrometry **47**, 327 (2018)

24. Bueckle, M.; Hauber, V.C.; Cole, G.D.; Gaertner, C.; Zeimer, U.; Grenzer, J.; Weig, E.M.
**Stress control of tensile-strained $In_{1-x}Ga_xP$ nanomechanical string resonators**
Applied Physics Letters **113**, 1 (2018)

25. Cai, B.; Hübner, R.; Sasaki, K.; Zhang, Y.; Su, D.; Ziegler, C.; Vukmirovic, M.B.; Rellinghaus, B.; Adzic, R.R.; Eychmüller, A.
**Core-Shell Structuring of Pure Metallic Aerogels towards Highly Efficient Platinum Utilization for the Oxygen Reduction Reaction - Kern-Schale-Strukturierung rein metallischer Aerogele für eine hocheffiziente Nutzung von Platin für die Sauerstoffreduktion**
Angewandte Chemie - International Edition **57**, 2963 (2018); Angewandte Chemie **130**, 3014 (2018)

26. Cañón Bermúdez, G.S.; Karnaushenko, D.D.; Karnaushenko, D.; Lebanov, A.; Bischoff, L.; Kaltenbrunner, M.; Fassbender, J.; Schmidt, O.G.; Makarov, D.
**Magnetosensitive e-skins with directional perception for augmented reality**
Science Advances **4**, eaao2623 (2018)

27. Cansever, H.; Narkowicz, R.; Lenz, K.; Fowley, C.; Ramasubramanian, L.; Yildirim, O.; Niesen, A.; Huebner, T.; Reiss, G.; Lindner, J.; Fassbender, J.; Deac, A.M.
**Investigating spin-transfer torques induced by thermal gradients in magnetic tunnel junctions by using micro-cavity ferromagnetic resonance**
Journal of Physics D: Applied Physics **51**, 224009 (2018)

28. Castañeda-Uribe, O.A.; Criollo, C.A.; Winnerl, S.; Helm, M.; Avila, A.
**Comparative study of equivalent circuit models for photoconductive antennas**
Optics Express **26**, 29017 (2018)

29. Chen, Z.; Higley, D.J.; Beye, M.; Hantschmann, M.; Mehta, V.; Hellwig, O.; Mitra, A.; Bonetti, S.; Bucher, M.; Carron, S.; Chase, T.; Jal, E.; Kukreja, R.; Liu, T.; Reid, A.H.; Dakovski, G.L.; Föhlisch, A.; Schlotter, W.F.; Dürr, H.A.; Stöhr, J.
**Ultrafast Self-Induced X-Ray Transparency and Loss of Magnetic Diffraction**
Physical Review Letters **121**, 137403 (2018)

30. Chesnel, K.; Westover, A.S.; Cardon, K.H.; Dodson, B.; Healey, M.; Newbold, B.; Hindman, L.; Montealegre, D.; Metzner, J.; Fallarino, L.; Böhm, B.; Schneider, T.; Samad, F.; Hellwig, O.
**Morphological stripe-bubble transition in remanent magnetic domain patterns of Co/Pt multilayer films and its dependence on Co thickness**
Physical Review B **98**, 224404-1 (2018)

31. Coelho, P.M.; Komsa, H.-P.; Diaz, H.C.; Ma, Y.; Krasheninnikov, A.V.; Batzill, M.
**Post-synthesis modifications of two-dimensional MoSe2 or MoTe2 by incorporation of excess metal atoms into the crystal structure**
ACS Nano **12**, 3975 (2018)

32. Coutts, C.; Arora, M.; Hübner, R.; Heinrich, B.; Girt, E.
**Magnetic properties of Co/Ni grain boundaries after annealing**
AIP Advances **8**, 056318 (2018)

33. Dash, S.; Schleicher, B.; Schwabe, S.; Reichel, L.; Heller, R.; Fähler, S.; Neu, V.; Patra, A.K.
**Structural and magnetic properties of epitaxial Mn–Ge films grown on Ir/Cr buffered MgO(0 0 1)**
Journal of Physics D: Applied Physics **51**, 255002 (2018)

34. Dell'Anna, R.; Iacob, E.; Barozzi, M.; Vanzetti, L.; Hübner, R.; Böttger, R.; Giubertoni, D.; Pepponi, G.
**The role of incidence angle in the morphology evolution of Ge surfaces irradiated by medium-energy Au ions**
Journal of Physics: Condensed Matter **30**, 324001 (2018)

35. Dhal, S.; Das, P.; Rajbhar, M.K.; Chatterjee, S.; Möller, W.; Chatterjee, S.; Ramgir, N.
**Superior electrical conduction of a water repelling 3D interconnected nano-network**
Journal of Materials Chemistry C **6**, 1951 (2018)

36. Dimitrakopulos, G.P.; Vasileiadis, I.G.; Bazioti, C.; Smalc-Koziorowska, J.; Kret, S.; Dimakis, E.; Florini, N.; Kehagias, T.; Suski, T.; Karakostas, T.; Moustakas, T.D.; Komninou, P.
**Compositional and strain analysis of In(Ga)N/GaN short period superlattices**
Journal of Applied Physics **123**, 024304 (2018)

37. Domènech, G.; Corominas, J.; Mavrouli, O.; Merchel, S.; Abellán, A.; Pavetich, S.; Rugel, G.
**Calculation of the rockwall recession rate of a limestone cliff, affected by rockfalls, using cosmogenic chlorine-36. Case study of the Montsec Range (Eastern Pyrenees, Spain)**
Geomorphology **306**, 325 (2018)

38. Dong, R.; Han, P.; Arora, H.; Ballabio, M.; Karakus, M.; Zhang, Z.; Shekhar, C.; Adler, P.; St. Petkov, P.; Erbe, A.; Mannsfeld, S.C.B.; Felser, C.; Heine, T.; Bonn, M.; Feng, X.; Canovas, E.
**High-Mobility, Band-Like Charge Transport in a Semiconducting Two-Dimensional Metal-Organic Framework**
Nature Materials **17**, 1027 (2018)

39. Dong, R.; Zhang, Z.; Tranca, D.C.; Zhou, S.; Wang, M.; Adler, P.; Liao, Z.; Liu, F.; Sun, Y.; Shi, W.; Zhang, Z.; Zschech, E.; Mannsfeld, S.; Felser, C.; Feng, X.
**A coronene-based semiconducting two-dimensional metal-organic framework with ferromagnetic behavior**
Nature Communications **9**, 2637 (2018)

40. Döring, J.; Lang, D.; Wehmeier, L.; Kuschewski, F.; Nörenberg, T.; Kehr, S.C.; Eng, L.M.
**Low-temperature nanospectroscopy of the structural ferroelectric phases in single-crystalline barium titanate**
Nanoscale **10**, 18074 (2018)

41. Du, N.; Manjunath, N.; Li, Y.; Menzel, S.; Linn, E.; Waser, R.; You, T.; Burger, D.; Skorupa, I.; Walczyk, D.; Walczyk, C.; Schmidt, O.G.; Schmidt, H.
**Field-Driven Hopping Transport of Oxygen Vacancies in Memristive Oxide Switches with Interface-Mediated Resistive Switching**
Physical Review Applied **10**, 054025 (2018)

42. Duan, B.; Bergner, F.; Heintze, C.; Akhmadaliev, S.; Wang, T.
**Post-irradiation annealing behavior of oxide dispersion strengthened Fe-Cr alloys studied by nanoindentation**
Philosophical Magazine Letters **98**, 536 (2018)

43. Duan, J.; Wang, M.; Vines, L.; Böttger, R.; Helm, M.; Zeng, Y.J.; Zhou, S.; Prucnal, S.
**Formation and characterization of shallow junctions in GaAs made by ion implantation and ms-range flash lamp annealing**
Physica Status Solidi (A) (2019)

44. Escobar-Galindo, R.; Guillén, E.; Heras, I.; Rincón-Llorente, G.; Alcón-Camas, M.; Lungwitz, F.; Munnik, F.; Schumann, E.; Azkona, I.; Krause, M.
**Design of high-temperature solar-selective coatings based on aluminium titanium oxynitrides $Al_yTi_{1-y}(O_xN_{1-x})$. Part 2: Experimental validation and durability tests at high temperature**
Solar Energy Materials and Solar Cells **185**, 183 (2018)

45. Fallarino, L.; Riego, P.; Kirby, B.J.; Miller, C.W.; Berger, A.
**Modulation of magnetic properties at the nanometer scale in continuously graded ferromagnets**
Materials **11**, 251 (2018)

46. Feige, J.; Wallner, A.; Fifield, L.K.; Golser, R.; Merchel, S.; Rugel, G.; Steier, P.; Tims, S.G.; Winkler, S.R.
**Limits on Supernova- Associated Fe-60/Al-26 Nucleosynthesis Ratios from Accelerator Mass Spectrometry Measurements of Deep-Sea Sediments**
Physical Review Letters **121**, 221103 (2018)

47. Ferhati, R.; Amirthapandian, S.; Fritzsche, M.; Bischoff, L.; Bolse, W.
**Swift heavy ion shaping of oxide-structures at (sub)-micrometer scales**
Nuclear Instruments and Methods in Physics Research B **435**, 93 (2018)

48. Finizio, S.; Wintz, S.; Bracher, D.; Kirk, E.; Semisalova, A.S.; Förster, J.; Zeissler, K.; Weßels, T.; Weigand, M.; Lenz, K.; Kleibert, A.; Raabe, J.
**Thick Permalloy films for the imaging of spin texture dynamics in perpendicularly magnetized systems**
Physical Review B **98**, 104415 (2018)

49. Finizio, S.; Wintz, S.; Gliga, S.; Kirk, E.; Suszka, A.K.; Wohlhüter, P.; Zeissler, K.; Raabe, J.
**Unexpected field-induced dynamics in magnetostrictive microstructured elements under isotropic strain**
Journal of Physics: Condensed Matter **30**, 314001 (2018)

50. Finizio, S.; Wintz, S.; Zeissler, K.; Sadovnikov, A.V.; Mayr, S.; Nikitov, S.A.; Marrows, C.H.; Raabe, J.
**Dynamic Imaging of the Delay-and Tilt-Free Motion of Neel Domain Walls in Perpendicularly Magnetized Superlattices**
Nano Letters **19**, 375 (2019)

51. Firkala, T.; Kuschewski, F.; Nörenberg, T.; Klopf, J.M.; Pashkin, A.; Foerstendorf, H.; Rudolph, M.; Kehr, S.C.; Eng, L.M.
**Near-field optical examination of potassium n-butyl xanthate / chalcopyrite flotation products**
Minerals **8**, 118 (2018)

52. Förster, A.; Gemming, S.; Seifert, G.
**Functional thiols as repair and doping agents of defective $MoS_2$ monolayers**
Journal of Physics: Condensed Matter **30**, 235302 (2018)

53. Fowley, C.; Rode, K.; Lau, Y.C.; Thiyagarajah, N.; Betto, D.; Borisov, K.; Atcheson, G.; Kampert, E.; Wang, Z.; Yuan, Y.; Zhou, S.; Lindner, J.; Stamenov, P.; Coey, J.M.D.; Deac, A.M.
**Anomalous Hall effect in fully compensated half-metallic $Mn_2Ru_xGa$ thin films**
Physical Review B **98**, 220406(R) (2018)

54. Fuchs, F.; Gemming, S.; Schuster, J.
**Radially resolved electronic structure and charge carrier transport in silicon nanowires**
Physica E **108**, 181 (2019)

55. Gaididei, Y.; Kravchuk, V.P.; Mertens, F.G.; Pylypovskyi, O.V.; Saxena, A.; Sheka, D.D.; Volkov, O.M.
**Localization of magnon modes in a curved magnetic nanowire**
Low Temperature Physics **44**, 814 (2018)

56. Gallardo, R.A.; Schneider, T.; Roldan-Molina, A.; Langer, M.; Fassbender, J.; Lenz, K.; Lindner, J.; Landeros, P.
**Dipolar interaction induced band gaps and flat modes in surface-modulated magnonic crystals**
Physical Review B **97**, 144405 (2018)

57. Gallardo, R.A.; Schneider, T.; Roldán-Molina, A.; Langer, M.; Núñez, A.S.; Lenz, K.; Lindner, J.; Landeros, P.
**Symmetries and localization properties of defect modes in metamaterial magnonic superlattices**
Physical Review B **97**, 174404 (2018)

58. Gan'shina, E.; Kulatov, E.; Golik, L.; Kun'kova, Z.; Uspenskii, Y.; Zykov, G.; Yuan, Y.; Zhou, S.
**Ab-initio study of electronic and magneto-optical properties of InAs:Mn**
Moscow International Symposium on Magnetism (MISM 2017): EPJ Web of Conferences **185**, 06008 (2018)

59. Gerber, U.; Hübner, R.; Rossberg, A.; Krawczyk-Bärsch, E.; Merroun, M.L.
**Metabolism-dependent bioaccumulation of uranium by Rhodosporidium toruloides isolated from the flooding water of a former uranium mine**
PlosOne **13**, e0201903 (2018)

60. Gierak, J.; Mazarov, P.; Bruchhaus, L.; Jede, R.; Bischoff, L.
**Review of electrohydrodynamical ion sources and their applications to focused ion beam technology**
Journal of Vacuum Science & Technology B **36**, 06J101 (2018)

61. Gupta, A.; Rana, G.; Bhattacharya, A.; Singh, A.; Jain, R.; Bapat, R.D.; Duttagupta, S.P.; Prabhu, S.S.
**Enhanced optical-to-THz conversion efficiency of photoconductive antenna using dielectric nano-layer encapsulation**
APL Photonics **03**, 051706-1 (2018)

62. Haye, E.; Pierron, V.; Barrat, S.; Capon, F.; Munnik, F.; Bruyère, S.
**Nitrogen redistribution in annealed $LaFeO_xN_y$ thin films investigated by FTIR spectroscopy and EELS mapping**
Applied Surface Science **427**, 1041 (2018)

63. Heras, I.; Guillén, E.; Lungwitz, F.; Rincón-Llorente, G.; Munnik, F.; Schumann, E.; Azkona, I.; Krause, M.; Escobar-Galindo, R.
**Design of high-temperature solar-selective coatings based on aluminium titanium oxynitrides $Al_yTi_{1-y}(O_xN_{1-x})$. Part 1: Advanced microstructural characterisation and optical simulation**
Solar Energy Materials and Solar Cells **176**, 81 (2018)

64. Hesse, J.; Klier, D.T.; Sgarzi, M.; Nsubuga, A.; Bauer, C.; Grenzer, J.; Hübner, R.; Wislicenus, M.; Joshi, T.; Kumke, M.U.; Stephan, H.
**Rapid synthesis of sub-10 nm hexagonal NaYF4-based upconverting nanoparticles using Therminol 66**
ChemistryOpen **7**, 159 (2018)

65. Hiller, D.; Göttlicher, J.; Steininger, R.; Huthwelker, T.; Julin, J.; Munnik, F.; Wahl, M.; Bock, W.; Schoenaers, B.; Stesmans, A.; König, D.
**Structural Properties of Al–O Monolayers in $SiO_2$ on Silicon and the Maximization of their Negative Fixed Charge Density**
ACS Applied Materials and Interfaces **10**, 30495 (2018)

66. Holland-Moritz, H.; Graupner, J.; Möller, W.; Pacholski, C.; Ronning, C.
**Dynamics of nanoparticle morphology under low energy ion irradiation**
Nanotechnology **29**, 314002 (2018)

67. Hu, X.; Wang, Y.; Shen, X.; Krasheninnikov, A.V.; Sun, L.; Chen, Z.
**1T phase as an efficient hole injection layer to TMDs transistors: a universal approach to achieve p-type contacts**
2D Materials **5**, 031012 (2018)

68. Huang, J.; Loeffler, M.; Muehle, U.; Moeller, W.; Mulders, J.J.L.; Kwakman, L.F.T.; van Dorp, W.F.; Zschech, E.
**Si amorphization by focused ion beam milling: Point defect model with dynamic BCA simulation and experimental validation**
Ultramicroscopy **184**, 52 (2018)

69. Jäger, N.; Klima, S.; Hruby, H.; Julin, J.; Keckes, J.F.; Mitterer, C.; Daniel, R.
**Evolution of structure and residual stress of a fcc/hex-AlCrN multi-layered system upon thermal loading revealed by cross-sectional X-ray nano-diffraction**
Acta Materialia **162**, 55 (2019)

70. Jia, Q.; Grenzer, J.; He, H.; Anwand, W.; Ji, Y.; Yuan, Y.; Huang, K.; You, T.; Yu, W.; Ren, W.; Chen, X.; Liu, M.; Facsko, S.; Wang, X.; Ou, X.
**3D Local Manipulation of the Metal-Insulator Transition Behavior in $VO_2$ Thin Film by Defect-Induced Lattice Engineering**
Advanced Materials Interfaces **5**, 1 (2018)

71. Jia, Q.; Ou, X.; Langer, M.; Schreiber, B.; Grenzer, J.; Siles, P.F.; Rodriguez, R.D.; Huang, K.; Yuan, Y.; Heidarian, A.; Hübner, R.; You, T.; Yu, W.; Lenz, K.; Lindner, J.; Wang, X.; Facsko, S.
**Ultra-dense planar metallic nanowire arrays with extremely large anisotropic optical and magnetic properties**
Nano Research **11**, 3519 (2018)

72. John, M.; Dalla, A.; Ibrahim, A.M.; Anwand, W.; Wagner, A.; Böttger, R.; Krause-Rehberg, R.
**Improving depth resolutions in positron beam spectroscopy by concurrent ion-beam sputtering**
Nuclear Instruments and Methods in Physics Research B **423**, 62 (2018)

73. Kelling, J.; Odor, G.; Gemming, S.
**Dynamical universality classes of simple growth and lattice gas models**
Journal of Physics A **51**, 035003 (2018)

74. Kirby, B.J.; Fallarino, L.; Riego, P.; Maranville, B.B.; Miller, C.W.; Berger, A.
**Nanoscale Magnetic Localization in Exchange Strength Modulated Ferromagnets**
Physical Review B **98**, 064404 (2018)

75. Kirschbaum, J.; Teuber, T.; Donner, A.; Radek, M.; Bougeard, D.; Lundsgaard Hansen, J.; Nylandsted Larsen, A.; Posselt, M.; Bracht, H.; Böttger, R.
**Self-Diffusion in Amorphous Silicon by Local Bond Rearrangements**
Physical Review Letters **120**, 225902 (2018)

76. Klingner, N.; Heller, R.; Hlawacek, G.; Facsko, S.; von Borany, J.
**Time-of-flight secondary ion mass spectrometry in the helium ion microscope**
Ultramicroscopy **198**, 10 (2019)

77. Kluge, T.; Rödel, M.; Metzkes, J.; Bussmann, M.; Erbe, A.; Galtier, E.; Garcia, A.L.; Garten, M.; Georgiev, Y.M.; Gutt, C.; Hartley, N.; Huebner, U.; Lee, H.J.; Mcbride, E.E.; Nakatsutsumi, M.; Nam, I.; Pelka, A.; Prencipe, I.; Rehwald, M.; Christian, R.; Schönherr, T.; Zacharias, M.; Zeil, K.; Glenzer, S.; Schramm, U.; Cowan, T.E.
**Observation of ultrafast solid-density plasma dynamics using femtosecond X-ray pulses from a free-electron laser**
Physical Review X **8**, 031068 (2018)

78. Kolkovsky, V.; Scholz, S.; Kolkovsky, V.; Schmidt, J.U.; Heller, R.
**Interaction of hydrogen with hafnium dioxide grown on silicon dioxide by the atomic layer deposition technique**
Journal of Vacuum Science & Technology B **36**, 062901 (2018)

79. Komsa, H.-P.; Berseneva, N.; Krasheninnikov, A.V.; Nieminen, R.M.
**Erratum: Charged Point Defects in the Flatland: Accurate Formation Energy Calculations in Two-Dimensional Materials [Phys. Rev. X 4, 031044 (2014)]**
Physical Review X **8**, 039902(E) (2018)

80. Kosmala, T.; Diaz, H.C.; Komsa, H.-P.; Ma, Y.; Krasheninnikov, A.V.; Batzill, M.; Agnoli, S.
**Metallic twin boundaries boost the hydrogen evolution reaction on the basal plane of molybdenum selenotellurides**
Advanced Energy Materials **8**, 1800031 (2018)

81. Kosub, T.; Velez, S.; Gomez-Perez, J.M.; Hueso, L.E.; Fassbender, J.; Casanova, F.; Makarov, D.
**Anomalous Hall-like transverse magnetoresistance in Au thin films on $Y_3Fe_5O_{12}$**
Applied Physics Letters **113**, 222409 (2018)

82. Krasheninnikov, A.V.
**When defects are not defects**
Nature Materials **17**, 757 (2018)

83. Kravchuk, V.P.; Sheka, D.D.; Kákay, A.; Volkov, O.M.; Rößler, U.K.; van den Brink, J.; Makarov, D.; Gaididei, Y.
**Multiplet of skyrmion states on a curvilinear defect: Reconfigurable skyrmion lattices**
Physical Review Letters **120**, 1 (2018)

84. Kretzschmar, J.; Haubitz, T.; Hübner, R.; Weiss, S.; Husar, R.; Brendler, V.; Stumpf, T.
**Network-like arrangement of mixed-valence uranium oxide nanoparticles after glutathione-induced reduction of uranium(VI)**
Chemical Communications **54**, 8697 (2018)

85. Kühne, M.; Börrnert, F.; Fecher, S.; Ghorbani-Asl, M.; Biskupek, J.; Samuelis, D.; Krasheninnikov, A.V.; Kaiser, U.; Smet, J.H.
**Reversible superdense ordering of lithium between two graphene sheets**
Nature **564**, 234 (2018)

86. La Torre, E.; Smekhova, A.; Schmitz-Antoniak, C.; Ollefs, K.; Eggert, B.; Cöster, B.; Walecki, D.; Wilhelm, F.; Rogalev, A.; Lindner, J.; Bali, R.; Banerjee, R.; Sanyal, B.; Wende, H.
**Local probe of irradiation induced structural changes and orbital magnetism in Fe60Al40 thin films via order-disorder phase transition**
Physical Review B **98**, 024101 (2018)

87. Lang, D.; Balaghi, L.; Winnerl, S.; Schneider, H.; Hübner, R.; Kehr, S.C.; Eng, L.M.; Helm, M.; Dimakis, E.; Pashkin, A.
**Nonlinear plasmonic response of doped nanowires observed by infrared nanospectroscopy**
Nanotechnology **30**, 1 (2019)

88. Lang, D.; Döring, J.; Nörenberg, T.; Butykai, Á.; Kézsmárki, I.; Schneider, H.; Winnerl, S.; Kehr, S.C.; Eng, L.M.; Helm, M.
**Infrared nanoscopy down to liquid helium temperatures**
Review of Scientific Instruments **89**, 1 (2018)

89. Li, L.; Bürger, D.; Shalimov, A.; Kovacs, G.J.; Schmidt, H.; Zhou, S.
**Activation of acceptor levels in Mn implanted Si by pulsed laser annealing**
Journal of Physics D: Applied Physics **51**, 165304 (2018)

90. Li, L.; Xu, C.; Yuan, Y.; Zhou, S.
**Large refrigerant capacity induced by table-like magnetocaloric effect in amorphous $Er_{0.2}Gd_{0.2}Ho_{0.2}Co_{0.2}Cu_{0.2}$ ribbons**
Materials Research Letters **6**, 413 (2018)

91. Li, L.; Xu, C.; Yuan, Y.; Zhou, S.
**Glassy formation ability, magnetic properties and magnetocaloric effect in Al27Cu18Er55 amorphous ribbon**
Journal of Magnetism and Magnetic Materials **454**, 121 (2018)

92. Li, R.; Pang, C.; Amekura, H.; Ren, F.; Hübner, R.; Zhou, S.; Ishikawa, N.; Okubo, N.; Chen, F.
**Ag nanoparticles embedded in Nd:YAG crystals irradiated with tilted beam of 200 MeV Xe ions: optical dichroism correlated to particle reshaping**
Nanotechnology **29**, 424001 (2018)

93. Lin, J.; You, T.; Wang, M.; Huang, K.; Zhang, S.; Jia, Q.; Zhou, M.; Yu, W.; Zhou, S.; Wang, X.; Ou, X.
**Efficient ion-slicing of InP thin film for Si-based hetero-integration**
Nanotechnology **29**, 504002 (2018)

94. Lin, Y.-C.; Li, S.; Komsa, H.-P.; Chang, L.-J.; Krasheninnikov, A.V.; Eda, G.; Suenaga, K.
**Revealing the Atomic Defects of $WS_2$ Governing Its Distinct Optical Emissions**
Advanced Functional Materials **28**, 1704210 (2018)

95. Lisauskas, A.; Ikamas, K.; Massabeau, S.; Bauer, M.; Cibiraité, D.; Matukas, J.; Mangeney, J.; Mittendorff, M.; Winnerl, S.; Krozer, V.; Roskos, H.G.
**Field-effect transistors as electrically controllable nonlinear rectifiers for the characterization of terahertz pulses**
APL Photonics **3**, 051705 (2018)

96. Liu, C.; Berencén, Y.; Yang, J.; Wei, Y.; Wang, M.; Yuan, Y.; Xu, C.; Xie, Y.; Li, X.; Zhou, S.
**Irradiation effects on the structural and optical properties of single crystal β-$Ga_2O_3$**
Semiconductor Science and Technology **33**, 095022-1 (2018)

97. Liu, C.; Hübner, R.; Xie, Y.; Wang, M.; Xu, C.; Jiang, Z.; Yuan, Y.; Li, X.; Yang, J.; Li, L.; Weschke, E.; Prucnal, S.; Helm, M.; Zhou, S.
**Ultra-fast annealing manipulated spinodal nano-decomposition in Mn-implanted Ge**
Nanotechnology **30**, 054001 (2019)

98. Liu, F.; Prucnal, S.; Yuan, Y.; Heller, R.; Berencén, Y.; Böttger, R.; Rebohle, L.; Skorupa, W.; Helm, M.; Zhou, S.
**Structural and electrical properties of Se-hyperdoped Si via ion implantation and flash lamp annealing**
Nuclear Instruments and Methods in Physics Research B **424**, 52 (2018)

99. Liu, F.; Wang, M.; Berencén, Y.; Prucnal, S.; Engler, M.; Hübner, R.; Yuan, Y.; Heller, R.; Böttger, R.; Rebohle, L.; Skorupa, W.; Helm, M.; Zhou, S.
**On the insulator-to-metal transition in titanium-implanted silicon**
Scientific Reports **8**, 4164 (2018)

100. Liu, W.; Hiekel, K.; Hübner, R.; Sun, H.; Ferancova, A.; Sillanpää, M.
**Pt and Au bimetallic and monometallic nanostructured amperometric sensors for direct detection of hydrogen peroxide: Influences of bimetallic effect and silica support**
Sensors and Actuators B **255**, 1325 (2018)

101. Lonsky, M.; Teschabai-Oglu, J.; Pierz, K.; Sievers, S.; Schumacher, H.W.; Yuan, Y.; Böttger, B.; Zhou, S.; Müller, J.
**Investigation of a possible electronic phase separation in the magnetic semiconductors $Ga_{1-x}Mn_xAs$ and $Ga_{1-x}Mn_xP$ by means of fluctuation spectroscopy**
Physical Review B **97**, 054413 (2018)

102. Lonsky, M.; Teschabai–Oglu, J.; Pierz, K.; Sievers, S.; Schumacher, H.W.; Yuan, Y.; Böttger, R.; Zhou, S.; Müller, J.
**Charge Carrier Dynamic in $Ga_{1-x}Mn_xAs$ Studied by Resistance Noise Spectroscopy**
Acta Physica Polonica A **133**, 520 (2018)

103. Luna, L.V.; Bookhagen, B.; Niedermann, S.; Rugel, G.; Scharf, A.; Merchel, S.
**Glacial chronology and production rate cross-calibration of five cosmogenic nuclide and mineral systems from the southern Central Andean Plateau**
Earth and Planetary Science Letters **500**, 242 (2018)

104. Macková, A.; Malinský, P.; Jagerová, A.; Mikšová, R.; Nekvindová, P.; Cajzl, J.; Rinkevičiūtė, E.; Akhmadaliev, S.
**Damage formation and Er structural incorporation in m-plane and a-plane ZnO**
Nuclear Instruments and Methods in Physics Research B, in press (2019), https://doi.org/10.1016/j.nimb.2018.10.003

105. Mackova, A.; Malinsky, P.; Jágerova, A.; Sofer, Z.; Klímová, K.; Sedmidubský, D.; Mikulics, M.; Böttger, R.; Akhmadaliev, S.
**Damage accumulation and structural modification in c-plane and a-plane GaN implanted with 400 keV Kr and Gd ions**
Surface & Coatings Technology **355**, 22 (2018)

106. Mackova, A.; Malinsky, P.; Jágerova, A.; Sofer, Z.; Sedmidubský, D.; Klímová, K.; Böttger, R.; Akhmadaliev, S.
**Damage accumulation and structural modification in a- and c-plane GaN implanted with 400-keV and 5-MeV Au+ ions**
Surface and Interface Analysis **50**, 1099 (2018)

107. Maehrlein, S.F.; Radu, I.; Maldonado, P.; Paarmann, A.; Gensch, M.; Kalashnikova, A.M.; Pisarev, R.V.; Wolf, M.; Oppeneer, P.M.; Barker, J.; Kampfrath, T.
**Dissecting spin-phonon equilibration in ferrimagnetic insulators by ultrafast lattice excitation**
Science Advances **4**, eaar5164 (2018)

108. Malinsky, P.; Macková, A.; Florianová, M.; Cutroneo, M.; Hnatowicz, V.; Bohácová, M.; Szokölová, K.; Böttger, R.; Sofer, Z.
**The Structural and Compositional Changes of Graphene Oxide Induced by Irradiation with 500 keV Helium and Gallium Ions**
Physica Status Solidi (B) **256**, 1800409 (2018)

109. Marynowska, A.; Misiuna, P.; Lewińska, S.; Dynowska, E.; Wawro, A.; Ślawska-Waniewska, A.; Böttger, R.; Fassbender, J.; Baczewski, L.T.
**Modification of structural and magnetic properties in Fe/Pt (111)-oriented multilayers with ion beam irradiation**
Nuclear Instruments and Methods in Physics Research B **415**, 136 (2018)

110. Mikhaylov, A.A.; Priamushko, T.S.; Babikhina, M.N.; Kudiiarov, V.N.; Heller, R.; Laptev, R.S.; Lider, A.M.
**Hydrogen calibration of GD-spectrometer using Zr-1Nb alloy**
Applied Surface Science **432**, 85 (2018)

111. Mohanty, B.; Ghorbani-Asl, M.; Kretschmer, S.; Ghosh, A.; U. Guha, P.; Panda, S.K.; Jena, B.; Krasheninnikov, A.V.; Jena, B.K.
**$MoS_2$ quantum dots as an efficient catalyst material for oxygen evolution reaction**
ACS Catalysis **8**, 1683 (2018)

112. Müller-Landau, C.; Malzer, S.; Weber, H.B.; Döhler, G.H.; Winnerl, S.; Burke, P.; Gossard, A.C.; Preu, S.
**Terahertz Generation with Ballistic Photodiodes under Pulsed Operation**
Semiconductor Science and Technology **33**, 114015 (2018)

113. Nasdala, L.; Akhmadaliev, S.; Artac, A.; Chanmuang, N.C.; Habler, G.; Lenz, C.
**Irradiation effects in monazite-(Ce) and zircon: Raman and photoluminescence study of Au-irradiated FIB foils**
Physics and Chemistry of Minerals **45**, 855 (2018)

114. Nebogatikova, N.A.; Antonova, I.V.; Erohin, S.V.; Kvashnin, D.G.; Olejniczak, A.; Volodin, V.A.; Skuratov, A.V.; Krasheninnikov, A.V.; Sorokin, P.B.; Chernozatonskii, L.A.
**Nanostructuring few-layer graphene films with swift heavy ions for electronic application: tuning of electronic and transport properties**
Nanoscale **10**, 14499 (2018)

115. Neumann-Heyme, H.; Shevchenko, N.; Lei, Z.; Eckert, K.; Keplinger, O.; Grenzer, J.; Beckermann, C.; Eckert, S.
**Coarsening evolution of dendritic sidearms: from synchrotron experiments to quantitative modeling**
Acta Materialia **146**, 176 (2018)

116. Nie, W.J.; Zhang, Y.X.; Yu, H.H.; Li, R.; He, R.Y.; Dong, N.N.; Wang, J.; Hübner, R.; Böttger, R.; Zhou, S.Q.; Amekura, H.; Chen, F.
**Plasmonic nanoparticles embedded in single crystals synthesized by gold ion implantation for enhanced optical nonlinearity and efficient Q-switched lasing**
Nanoscale **10**, 4228 (2018)

117. Nsubuga, A.; Sgarzi, M.; Zarschler, K.; Kubeil, M.; Hübner, R.; Steudtner, R.; Graham, B.; Joshi, T.; Stephan, H.
**Facile Preparation of Multifunctionalisable 'Stealth' Upconverting Nanoparticles for Biomedical Applications**
Dalton Transactions **47**, 8595 (2018)

118. Ohshima, T.; Satoh, T.; Kraus, H.; Astakhov, G.V.; Dyakonov, V.; Baranov, P.G.
**Creation of silicon vacancy in silicon carbide by proton beam writing toward quantum sensing applications**
Journal of Physics D: Applied Physics **51**, 333002 (2018)

119. Olbinado, M.P.; Cantelli, V.; Mathon, O.; Pascarelli, O.; Rack, A.; Grenzer, J.; Pelka, A.; Roedel, M.; Prencipe, I.; Garcia, A.L.; Helbig, U.; Kraus, D.; Schramm, U.; Cowan, T.; Scheel, M.; Pradel, P.; de Resseguier, T.
**Ultra-high-speed X-ray imaging of laser-driven shock compression using synchrotron light**
Journal of Physics D: Applied Physics **51**, 055601 (2018)

120. Olbinado, M.P.; Grenzer, J.; Pradel, P.; de Resseguier, T.; Vagovic, P.; Zdora, M.-C.; Guzenko, V.A.; David, C.; Rack, A.
**Advances in indirect detector systems for ultra high-speed hard X-ray imaging with synchrotron light**
Journal of Instrumentation **13**, 1 (2018)

121. Osten, J.; Lenz, K.; Schultheiss, H.; Lindner, J.; McCord, J.; Fassbender, J.
**Interplay between magnetic domain patterning and anisotropic magnetoresistance probed by magnetooptics**
Physical Review B **97**, 014415 (2018)

122. Otalora, J.A.; Kákay, A.; Lindner, J.; Schultheiss, H.; Thomas, A.; Fassbender, J.; Nielsch, K.
**Frequency linewidth and decay length of spin waves in curved magnetic membranes**
Physical Review B **98**, 014403 (2018)

123. Pacheco-Sanchez, A.; Fuchs, F.; Mothes, S.; Zienert, A.; Schuster, J.; Gemming, S.; Claus, M.
**Feasible device architectures for ultra-scaled CNTFETs**
IEEE Transactions on Nanotechnology **17**, 100 (2018)

124. Pan, S.; Hellwig, O.; Barman, A.
**Controlled coexcitation of direct and indirect ultrafast demagnetization in Co/Pd multilayers with large perpendicular magnetic anisotropy**
Physical Review B **98**, 214436 (2018)

125. Pandey, P.; Bitla, Y.; Zschornak, M.; Wang, M.; Xu, C.; Grenzer, J.; Meyer, D.C.; Chin, Y.Y.; Lin, H.J.; Chen, C.T.; Gemming, S.; Helm, M.; Chu, Y.H.; Zhou, S.
**Enhancing the Magnetic Moment of Ferrimagnetic $NiCo_2O_4$ via Ion Irradiation driven Oxygen Vacancies**
APL Materials **6**, 066109 (2018)

126. Pandey, P.; Drovosekov, A.B.; Wang, M.; Xu, C.; Nikolaev, S.N.; Chernoglazov, K.Y.; Savitsky, A.O.; Kreines, N.M.; Maslakov, K.I.; Cherebilo, E.A.; Mikhalevsky, V.A.; Novodvorskii, O.A.; Tugushev, V.V.; Rylkov, V.V.; Helm, M.; Zhou, S.
**Engineering of high-temperature ferromagnetic $Si_{1-x}Mn_x$ (x ≈ 0.5) alloyed films by pulsed laser deposition: Effect of laser fluence**
Journal of Magnetism and Magnetic Materials **459**, 206 (2018)

127. Pang, C.; Li, R.; Li, Z.; Dong, N.; Cheng, C.; Nie, W.; Böttger, R.; Zhou, S.; Wang, J.; Chen, F.
**Lithium Niobate Crystal with Embedded Au Nanoparticles: A New Saturable Absorber for Efficient Mode-Locking of Ultrafast Laser Pulses at 1 μm**
Advanced Optical Materials **16**, 1870065 (2018)

128. Pecko, S.; Heintze, C.; Bergner, F.; Anwand, W.; Slugen, V.
**Fe2+ ion irradiated JRQ steel investigated by nanoindentation and slow-positron Doppler broadening spectroscopy**
Nuclear Instruments and Methods in Physics Research B **415**, 1 (2018)

129. Pedroso, D.D.M.; Schmidt, J.; Passaro, A.; Helm, M.; Schneider, H.
**Fano signatures between intersubband and ponderomotive responses in MQW structures**
Optics Express **26**, 24054 (2018)

130. Pelizzo, M.G.; Corso, A.J.; Tessarolo, E.; Böttger, R.; Hübner, R.; Napolitani, E.; Bazzan, M.; Rancan, M.; Armelao, L.; Jark, W.; Eichert, D.; Martucci, A.
**Morphological and Functional Modifications of Optical Thin Films for Space Applications Irradiated with Low-Energy Helium Ions**
ACS Applied Materials and Interfaces **10**, 34781 (2018)

131. Plank, H.; Pernul, J.; Gebert, S.; Danilov, S.N.; König-Otto, J.; Winnerl, S.; Lanius, M.; Kampmeier, J.; Mussler, G.; Aguilera, I.; Grützmacher, D.; Ganichev, S.D.
**Infrared/Terahertz Spectra of the Photogalvanic Effect in (Bi,Sb)Te based Three Dimensional Topological Insulators**
Physical Review Materials **2**, 024202 (2018)

132. Pollmann, K.; Kutschke, S.; Matys, S.; Raff, J.; Hlawacek, G.; Lederer, F.L.
**Bio-recycling of metals: Recycling of technical products using biological applications**
Biotechnology Advances **36**, 1048 (2018)

133. Popovych, V.D.; Böttger, R.; Heller, R.; Zhou, S.; Bester, M.; Cieniek, B.; Mroczka, R.; Lopucki, R.; Sagan, P.; Kuzma, M.
**Heavy doping of CdTe single crystals by Cr ion implantation**
Nuclear Instruments and Methods in Physics Research B **419**, 26 (2018)

134. Prucnal, S.; Berencén, Y.; Wang, M.; Grenzer, J.; Voelskow, M.; Hübner, R.; Yamamoto, Y.; Scheit, A.; Bärwolf, F.; Zviagin, V.; Schmidt-Grund, R.; Grundmann, M.; Żuk, J.; Turek, M.; Droździel, A.; Pyszniak, K.; Kudrawiec, R.; Polak, M.P.; Rebohle, L.; Skorupa, W.; Helm, M.; Zhou, S.
**Strain and Band-Gap Engineering in Ge-Sn Alloys via P Doping**
Physical Review Applied **10**, 064055 (2018)

135. Prucnal, S.; Berencén, Y.; Wang, M.; Rebohle, L.; Böttger, R.; Fischer, I.A.; Augel, L.; Oehme, M.; Schulze, J.; Voelskow, M.; Helm, M.; Skorupa, W.; Zhou, S.
**Ex situ n+ doping of GeSn alloys via non-equilibrium processing**
Semiconductor Science and Technology **33**, 065008 (2018)

136. Pylypovskyi, O.V.; Makarov, D.; Kravchuk, V.P.; Gaididei, Y.; Saxena, A.; Sheka, D.D.
**Chiral Skyrmion and Skyrmionium States Engineered by the Gradient of Curvature**
Physical Review Applied **10**, 064057 (2018)

137. Rahman, M.; Shahzadeh, M.; Braeuninger-Weimer, P.; Hofmann, S.; Hellwig, O.; Pisana, S.
**Measuring the thermal properties of anisotropic materials using beam-offset frequency domain thermoreflectance**
Journal of Applied Physics **123**, 245110 (2018)

138. Ramasamy, S.; Reuther, H.; Adyanpuram, M.N.M.S.; Enoch, I.V.M.V.; Potzger, K.; Samathanam, B.
**Molecular encapsulator on the surface of magnetic nanoparticles. Controlled drug release from calcium Ferrite/Cyclodextrin–tethered polymer hybrid**
Colloids and Surfaces B: Biointerfaces **16**, 347 (2018)

139. Ratajczak, R.; Guziewicz, E.; Prucnal, S.; Łuka, G.; Böttger, R.; Heller, R.; Mieszczynski, C.; Wozniak, W.; Turos, A.
**Luminescence in the Visible Region from Annealed Thin ALD-ZnO Films Implanted with Different Rare Earth Ions**
Physica Status Solidi (A) **215**, 1700889 (2018)

140. Rayapati, V.R.; Du, N.; Bürger, D.; Patra, R.; Skorupa, I.; Matthes, P.; Stöcker, H.; Schulz, S.E.; Schmidt, H.
**Electroforming-free resistive switching in polycrystalline $YMnO_3$ thin films**
Journal of Applied Physics **124**, 144102 (2018)

141. Rebohle, L.; Neubert, M.; Schumann, T.; Skorupa, W.
**Determination of the thermal cycle during flash lamp annealing without a direct temperature measurement**
International Journal of Heat and Mass Transfer **126 B**, 1 (2018)

142. Regensburger, S.; Mukherjee, A.K.; Schönhuber, S.; Kainz, M.A.; Winnerl, S.; Klopf, J.M.; Lu, H.; Gossard, A.C.; Unterrainer, K.; Preu, S.
**Broadband Terahertz Detection With Zero-Bias Field-Effect Transistors Between 100 GHz and 11.8 THz With a Noise Equivalent Power of 250 pW/√Hz at 0.6 THz**
IEEE Transactions on Terahertz Science and Technology **8**, 465 (2018)

143. Reid, A.H.; Shen, X.; Maldonado, P.; Chase, T.; Jal, E.; Granitzka, P.W.; Carva, K.; Li, R.K.; Li, J.; Wu, L.; Vecchione, T.; Liu, T.; Chen, Z.; Higley, D.J.; Hartmann, N.; Coffee, R.; Wu, J.; Dakovski, G.L.; Schlotter, W.F.; Ohldag, H.; Takahashi, Y.K.; Mehta, V.; Hellwig, O.; Fry, A.; Zhu, Y.; Cao, J.; Fullerton, E.E.; Stöhr, J.; Oppeneer, P.M.; Wang, X.J.; Dürr, H.A.
**Beyond a phenomenological description of magnetostriction**
Nature Communications **9**, 388 (2018)

144. Rincón-Llorente, G.; Heras, I.; Guillén Rodríguez, E.; Schumann, E.; Krause, M.; Escobar-Galindo, R.
**On the Effect of Thin Film Growth Mechanisms on the Specular Reflectance of Aluminium Thin Films Deposited via Filtered Cathodic Vacuum Arc**
Coatings **8**, 321 (2018)

145. Röder, F.; Heintze, C.; Pecko, S.; Akhmadaliev, S.; Bergner, F.; Ulbricht, A.; Altstadt, E.
**Nanoindentation of ion-irradiated reactor pressure vessel steels – model-based interpretation and comparison with neutron irradiation**
Philosophical Magazine **98**, 911 (2018)

146. Schlitz, R.; Kosub, T.; Thomas, A.; Fabretti, S.; Nielsch, K.; Makarov, D.; Goennenwein, S.T.B.
**Evolution of the spin hall magnetoresistance in Cr2O3/Pt bilayers close to the Néel temperature**
Applied Physics Letters **112**, 132401 (2018)

147. Schreiber, B.; Gkogkou, D.; Dedelaite, L.; Kerbusch, J.; Hübner, R.; Sheremet, E.; Zahn, D.R.T.; Ramanavicius, A.; Facsko, S.; Rodriguez, R.D.
**Large-scale self-organized gold nanostructures with bidirectional plasmon resonances for SERS**
RSC Advances **8**, 22569 (2018)

148. Schumann, E.; Hübner, R.; Grenzer, J.; Gemming, S.; Krause, M.
**Percolated Si:$SiO_2$ Nanocomposites: Oven- vs. Millisecond Laser-induced Crystallization of $SiO_x$ Thin Films**
Nanomaterials **8**, 525 (2018)

149. Schwestka, J.; Melinc, D.; Heller, R.; Niggas, A.; Leonhartsberger, L.; Winter, H.; Facsko, S.; Aumayr, F.; Wilhelm, R.A.
**A versatile ion beam spectrometer for studies of ion interaction with 2D materials**
Review of Scientific Instruments **89**, 085101 (2018)

150. Schwestka, J.; Wilhelm, R.A.; Gruber, E.; Heller, R.; Kozubek, R.; Schleberger, M.; Facsko, S.; Aumayr, F.
**The role of radiative de-excitation in the neutralization process of highly charged ions interacting with a single layer of graphene**
Nuclear Instruments and Methods in Physics Research B **422**, 63 (2018)

151. Seidel, S.; Rebohle, L.; Prucnal, S.; Lehninger, D.; Hübner, R.; Klemm, V.; Skorupa, W.; Heitmann, J.
**Microstructure and charge trapping in in $ZrO_2$- and $Si_3N_4$-based superlattice layer systems with Ge nanoparticles**
Thin Solid Films **645**, 124 (2018)

152. Shahzadeh, M.; Rahman, M.; Hellwig, O.; Pisana, S.
**High-frequency measurements of thermophysical properties of thin films using a modified broad-band frequency domain thermoreflectance approach**
Review of Scientific Instruments **89**, 084905 (2018)

153. Shivhare, R.; Erdmann, T.; Hörmann, U.; Collado-Fregoso, E.; Zeiske, S.; Benduhn, J.; Ullbrich, S.; Hübner, R.; Hambsch, M.; Kiriy, A.; Voit, B.; Neher, D.; Vandewal, K.; Mannsfeld, S.C.B.
**Alkyl Branching Position in Diketopyrrolopyrrole Polymers: Interplay between Fibrillar Morphology and Crystallinity and Their Effect on Photogeneration and Recombination in Bulk-Heterojunction Solar Cells**
Chemistry of Materials **30**, 6801 (2018)

154. Shuai, Y.; Gong, C.; Bai, X.; Wu, C.; Luo, W.; Böttger, R.; Zhou, S.; Tian, B.; Zhang, W.
**Fabrication of Y128-and Y36-cut lithium niobate single-crystalline thin films by crystal-ion-slicing technique**
Japanese Journal of Applied Physics **57**, 04FK05 (2018)

155. Sippola, P.; Pyymaki Perros, A.; Ylivaara, O.M.E.; Ronkainen, H.; Julin, J.; Liu, X.; Sajavaara, T.; Etula, J.; Lipsanen, H.; Puurunen, R.L.
**Comparison of mechanical properties and composition of magnetron sputter and plasma enhanced atomic layer deposition aluminum nitride films**
Journal of Vacuum Science & Technology A **36**, 051508 (2018)

156. Skidin, D.; Erdmann, T.; Nikipar, S.; Eisenhut, F.; Krüger, J.; Günther, F.; Gemming, S.; Kiriy, A.; Voit, B.; Ryndyk, D.; Joachim, C.; Moresco, F.; Cuniberti, G.
**Tuning the conductance of a molecular wire by the interplay of donor and acceptor units**
Nanoscale **10**, 17131 (2018)

157. Stöber, M.; Cherkouk, C.; Leisegang, T.; Schelter, M.; Zosel, J.; Walter, J.; Hanzig, J.; Zschornak, M.; Prucnal, S.; Böttger, R.; Meyer, D.C.
**Oxygen Exchange Kinetics of $SrTiO_3$ Single Crystals: A Non-Destructive, Quantitative Method**
Crystal Research and Technology **53**, 1800004 (2018)

158. Stolle, A.; Schwanghart, W.; Andermann, C.; Bernhardt, A.; Wittmann, H.; Merchel, S.; Rugel, G.; Fort, M.; Adhikari, B.R.; Korup, O.
**Protracted river response to medieval earthquakes**
Earth Surface Processes and Landforms **44**, 331 (2019)

159. Sveklo, I.; Mazalski, P.; Jaworowicz, J.; Jamet, J.-P.; Vernier, N.; Mougin, A.; Ferre, J.; Kisielewski, M.; Zablotskii, V.; Bourhis, E.; Gierak, J.; Postava, K.; Fassbender, J.; Kanak, J.; Maziewski, A.
**Modification of magnetic properties of Pt/Co/Pt Films by Ga+ Ion irradiation: Focused versus uniform irradiation**
Acta Physica Polonica A **133**, 1215 (2018)

160. Tauchnitz, T.; Berdnikov, Y.; Dubrovskii, V.G.; Schneider, H.; Helm, M.; Dimakis, E.
**A simple route to synchronized nucleation of self-catalyzed GaAs nanowires on silicon for sub-Poissonian length distributions**
Nanotechnology **29**, 504004 (2018)

161. Teichert, F.; Wagner, C.; Croy, A.; Schuster, J.
**Influence of defect-induced deformations on electron transport in carbon nanotubes**
Journal of Physics Communications **2**, 1 (2018)

162. Tiessen, C.; Bemmerer, D.; Rugel, G.; Querfeld, R.; Scharf, A.; Steinhauser, G.; Merchel, S.
**Accelerator mass spectrometry (AMS) for beryllium-7 measurements in smallest rainwater samples**
Journal of Radioanalytical and Nuclear Chemistry **319**, 965 (2019)

163. Trinh, T.T.; Asano, K.; Heller, R.; Reuther, H.; Grenzer, J.; Schreuders, H.; Dam, B.; Potzger, K.
**Hydrogen storage in $Mg_2FeSi$ alloy thin films depending on the Fe-to-Si ratio measured by conversion electron Mössbauer spectroscopy**
Nuclear Instruments and Methods in Physics Research B **434**, 109 (2018)

164. Tripathi, M.; Markevich, A.; Böttger, R.; Facsko, S.; Besley, E.; Kotakoski, J.; Susi, T.
**Implanting Germanium into Graphene**
ACS Nano **12**, 4641 (2018)

165. Turos, A.; Ratajczak, R.; Mieszczynski, C.; Jozwik, P.; Stonert, A.; Prucnal, S.; Heller, R.; Skorupa, W.; von Borany, J.; Guziewicz, E.
**Ion Beam Modification of ZnO Epilayers: Sequential Processing**
Physica Status Solidi (A) **215**, 1700887 (2018)

166. Ueda, M.; Silva, C.; Marcondes, A.R.; Reuther, H.; de Souza, G.B.
**Recent experiments on plasma immersion ion implantation (and deposition) using discharges inside metal tubes**
Surface & Coatings Technology **355**, 98 (2018)

167. Vogel, M.; Fischer, S.; Maffert, A.; Hübner, R.; Scheinost, A.; Franzen, C.; Steudtner, R.
**Biotransformation and detoxification of selenite by microbial biogenesis of selenium-sulfur nanoparticles**
Journal of Hazardous Materials **344**, 749 (2018)

168. Volkov, O.M.; Sheka, D.D.; Kravchuk, V.P.; Gaididei, Y.; Rößler, U.K.; Faßbender, J.; Makarov, D.
**Mesoscale Dzyaloshinskii-Moriya interaction: geometrical tailoring of the magnetochirality**
Scientific Reports **8**, 866 (2018)

169. von Reppert, A.; Willig, L.; Pudell, J.-E.; Rössle, M.; Leitenberger, W.; Herzog, M.; Ganss, F.; Hellwig, O.; Bargheer, M.
**Ultrafast laser generated strain in granular and continuous FePt thin films**
Applied Physics Letters **113**, 123101 (2018)

170. Vyalikh, A.; Zschornak, M.; Köhler, T.; Nentwich, M.; Weigel, T.; Hanzig, J.; Zaripov, R.; Vavilova, E.; Gemming, S.; Brendler, E.; Meyer, D.C.
**Analysis of the defect clusters in the congruent lithium tantalate**
Physical Review Materials **2**, 013804 (2018)

171. Wagner, K.; Smith, A.; Hache, T.; Chen, J.-R.; Yang, L.; Montoya, E.; Schultheiss, K.; Lindner, J.; Fassbender, J.; Krivorotov, I.; Schultheiss, H.
**Injection locking of multiple auto-oscillation modes in a tapered nanowire spin Hall oscillator**
Scientific Reports **8**, 16040 (2018)

172. Wagner, L.; Akhmadaliev, S.; Anders, M.; Bemmerer, D.; Caciolli, A.; Gohl, S.; Grieger, M.; Junghans, A.; Marta, M.; Munnik, F.; Reinhardt, T.P.; Reinicke, S.; Röder, M.; Schmidt, K.; Schwengner, R.; Serfling, M.; Takács, M.P.; Szücs, T.; Vomiero, A.; Wagner, A.; Zuber, K.
**Astrophysical S-factor of the 14N(p,γ)15O reaction at 0.4 – 1.3MeV**
Physical Review C **97**, 015801 (2018)

173. Wang, C.; Chen, C.; Chang, C.-H.; Tsai, H.-S.; Pandey, P.; Xu, C.; Böttger, R.; Chen, D.; Zeng, Y.-J.; Gao, X.; Helm, M.; Zhou, S.
**Defect-induced exchange bias in a single SrRuO3 layer**
ACS Applied Materials and Interfaces **10**, 27472 (2018)

174. Wang, X.; Baraban, L.; Nguyen, A.; Ge, J.; R. Misko, V.; Tempere, J.; Nori, F.; Formanek, P.; Huang, T.; Cuniberti, G.; Fassbender, J.; Makarov, D.
**High-Motility Visible Light-Driven Ag/AgCl Janus Micromotors**
Small **14**, 1803613 (2018)

175. Wang, X.; Baraban, L.; R. Misko, V.; Nori, F.; Huang, T.; Cuniberti, G.; Fassbender, J.; Makarov, D.
**Visible Light Actuated Efficient Exclusion Between Plasmonic Ag/AgCl Micromotors and Passive Beads**
Small **14**, 1802537 (2018)

176. Wang, X.; Posselt, M.; Faßbender, J.
**Influence of substitutional atoms on the diffusion of oxygen in dilute iron alloys**
Physical Review B **98**, 064103 (2018)

177. Wawro, A.; Kurant, Z.; Jakubowski, M.; Tekielak, M.; Pietruczik, A.; Böttger, R.; Maziewski, A.
**Magnetic Properties of Coupled Co/Mo/Co Structures Tailored by Ion Irradiation**
Physical Review Applied **9**, 014029 (2018)

178. Wenisch, R.; Lungwitz, F.; Hanf, D.; Heller, R.; Zscharschuch, J.; Hübner, R.; von Borany, J.; Abrasonis, G.; Gemming, S.; Escobar Galindo, R.; Krause, M.
**Cluster tool for in situ processing and comprehensive characterization of thin films at high temperatures**
Analytical Chemistry **90**, 7837 (2018)

179. Wilhelm, R.; Gruber, E.; Schwestka, J.; Heller, R.; Facsko, S.; Aumayr, F.
**Neutralization Dynamics of Slow Highly Charged Ions in 2D Materials**
Applied Sciences **8**, 1050 (2018)

180. Wolf, D.; Hübner, R.; Niermann, T.; Sturm, S.; Prete, P.; Lovergine, N.; Büchner, B.; Lubk, A.
**Three-Dimensional Composition and Electric Potential Mapping of III−V Core−Multishell Nanowires by Correlative STEM and Holographic Tomography**
Nano Letters **18**, 4777 (2018)

181. Wolff, A.; Klingner, N.; Thompson, W.; Zhou, Y.; Lin, J.; Peng, Y.Y.; Ramshaw, J.A.M.; Xiao, Y.
**Modelling of focused ion beam induced increases in sample temperature: a case study of heat damage in biological samples**
Journal of Microscopy **272**, 47 (2018)

182. Wüthrich, L.; Garcia Morabito, E.; Zech, J.; Trauerstein, M.; Veit, H.; Gnägi, C.; Merchel, S.; Scharf, A.; Rugel, G.; Christl, M.; Zech, R.
**$^{10}$Be surface exposure dating of the last deglaciation in the Aare Valley, Switzerland**
Swiss Journal of Geosciences **111**, 295 (2018)

183. Xie, Y.; Yuan, Y.; Wang, M.; Xu, C.; Hübner, R.; Grenzer, J.; Zeng, Y.; Helm, M.; Zhou, S.; Prucnal, S.
**Epitaxial $Mn_5Ge_3$(100) layer on Ge(100) substrates obtained by flash lamp annealing**
Applied Physics Letters **113**, 222401 (2018)

184. Xu, C.; Yuan, Y.; Wang, M.; Hentschel, H.; Böttger, R.; Helm, M.; Zhou, S.
**P-type co-doping effect of (Ga,Mn)P: Magnetic and magneto-transport properties**
Journal of Magnetism and Magnetic Materials **459**, 102 (2018)

185. Xu, X.; Prüfer, T.; Wolf, D.; Engelmann, H.-J.; Bischoff, L.; Hübner, R.; Heinig, K.-H.; Möller, W.; Facsko, S.; von Borany, J.; Hlawacek, G.
**Site-controlled formation of single Si nanocrystals in a buried $SiO_2$ matrix using ion beam mixing**
Beilstein Journal of Nanotechnology **9**, 2883 (2018)

186. Yershov, K.V.; Kravchuk, V.P.; Sheka, D.D.; Pylypovskyi, O.V.; Makarov, D.; Gaididei, Y.
**Geometry-induced motion of magnetic domain walls in curved nanostripes**
Physical Review B **98**, 060409 (2018)

187. Yin, G.; Zhu, D.; Lv, D.; Zhang, Z.; Hashemi, A.; Krasheninnikov, A.V.; Komsa, H.-P.; Jin, C.
**Hydrogen-assisted Post-growth Doping of Tellurium into Molybdenum Disulfide Monolayers with Tunable Compositions**
Nanotechnology **29**, 145603 (2018)

188. Yuan, Y.; Amarouche, T.; Xu, C.; Rushforth, A.; Boettger, R.; Edmonds, K.; Campion, R.; Gallagher, B.; Helm, M.; von Bardeleben, H.; Zhou, S.Q.
**Switching the uniaxial magnetic anisotropy by ion irradiation induced compensation**
Journal of Physics D: Applied Physics **51**, 145001 (2018)

189. Yuan, Y.; Hübner, R.; Birowska, M.; Xu, C.; Wang, M.; Prucnal, S.; Jakiela, R.; Potzger, K.; Böttger, R.; Facsko, S.; Majewski, J.A.; Helm, M.; Sawicki, M.; Zhou, S.; Dietl, T.
**Nematicity of correlated systems driven by anisotropic chemical phase separation**
Physical Review Materials **2**, 114601 (2018)

190. Yuan, Y.; Wang, M.; Xu, C.; Hübner, R.; Böttger, R.; Jakiela, R.; Helm, M.; Sawicki, M.; Zhou, S.
**Electronic phase separation in insulating (Ga, Mn) As with low compensation: super-paramagnetism and hopping conduction**
Journal of Physics: Condensed Matter **30**, 095801 (2018)

191. Zhai, Z.-H.; Chen, S.-C.; Du, L.-H.; Zhong, S.-C.; Huang, W.; Li, Z.-R.; Schneider, H.; Shi, Q.; Zhu, L.-G.
**Giant impact of self-photothermal on light-induced ultrafast insulator-to-metal transition in $VO_2$ nanofilms at terahertz frequency**
Optics Express **26**, 28051 (2018)

192. Zhai, Z.-H.; Zhu, H.-F.; Shi, Q.; Chen, S.-C.; Li, J.; Li, Z.-R.; Schneider, H.; Zhu, L.-G.
**Enhanced photoresponses of an optically driven $VO_2$-based terahertz wave modulator near percolation threshold**
Applied Physics Letters **113**, 231104-1 (2018)

193. Zhang, N.; Hübner, R.; Wang, Y.; Zhang, E.; Zhou, Y.; Dong, S.; Wu, C.
**Surface-Functionalized Mesoporous Nanoparticles as Heterogeneous Supports To Transfer Bifunctional Catalysts into Organic Solvents for Tandem Catalysis**
ACS Applied Nano Materials **1**, 6378 (2018)

194. Zhang, X.; Li, Q.; Wang, M.; Zhang, Z.; Akhmadaliev, S.; Zhou, S.; Wu, Y.; Guo, B.
**Defects in hydrogen implanted SiC**
Nuclear Instruments and Methods in Physics Research B **436**, 107 (2018)

195. Zhang, X.; Yuan, Q.; Gao, T.; Ren, Y.; Wu, H.; Huang, Q.; Zhao, J.; Wang, X.; Yuan, Y.; Xu, C.; Hu, Y.; Dynes, J.J.; Zhou, J.; Zhou, S.; Liu, Y.; Song, B.
**Transition from antiferromagnetic ground state to robust ferrimagnetic order with Curie temperatures above 420 K in manganese-based antiperovskite-type structures**
Journal of Materials Chemistry C **6**, 13336 (2018)

196. Zhang, Z.T.; Dmytriieva, D.; Molatta, S.; Wosnitza, J.; Khim, S.; Gass, S.; Wolter, A.U.B.; Wurmehl, S.; Grafe, H.-J.; Kühne, H.
**Increasing stripe-type fluctuations in $AFe_2As_2$ (A = K, Rb, Cs) superconductors probed by $^{75}$As NMR spectroscopy**
Physical Review B **97**, 115110 (2018)

197. Zimmermann, M.; Gerhard-Meier, T.N.; Dirnberger, F.; Kákay, A.; Decker, M.; Wintz, S.; Finizio, S.; Josten, E.; Raabe, J.; Kronseder, M.; Bougeard, D.; Lindner, J.; Back, C.H.
**Origin and Manipulation of Stable Vortex Ground States in Permalloy Nanotubes**
Nano Letters **18**, 2828 (2018)

## Publications in conference proceedings

198. Anisimov, A.; Soltamov, V.; Baranov, P.; Astakhov, G.; Dyakonov, V.
**Spin colour centres in SiC as a material platform for sensing and information processing at ambient conditions**
European Physical Journal Web of Conferences **190**, 04001 (2018)

199. Bhowmick, S.; Das, D.; Asirvatham, J.; Khan, S.A.; Sen, D.; Hübner, R.; Kanjilal, D.; Kanjilal, A.
**Study of thermoluminescence property of $C^+$ ion doped anodized alumina**
in: IUAC Annual Report 2016-2017, New Delhi: Inter University Accelerator Centre, 2018, 148-149

200. Gan'shina, E.A.; Golik, L.L.; Kun'kova, Z.E.; Zykov, G.S.; Bykov, I.V.; Rukovishnikov, A.I.; Yuan, Y.; Böttger, R.; Zhou, S.
**Magneto-optical spectroscopy of diluted magnetic semiconductors GaMnAs prepared by ion implantation and further impulse laser annealing**
Journal of Magnetism and Magnetic Materials **459**, 141 (2018)

201. Schmidt, J.; Winnerl, S.; Dimakis, E.; Helm, M.; Schneider, H.
**Dressing intersubband transitions at terahertz frequencies**
43rd International Conference on Infrared, Millimeter, and Terahertz Waves (IRMMW-THz), DOI: 10.1109/IRMMW-THz.2018.8510160 (2018)

202. Simon, M.; Trommer, J.; Liang, B.; Fischer, D.; Baldauf, T.; Khan, M.B.; Heinzig, A.; Knaut, M.; Georgiev, Y.M.; Erbe, A.; Bartha, J.W.; Mikolajick, T.; Weber, W.M.
**A wired-AND transistor: Polarity controllable FET with multiple inputs**
76th Device Research Conference (DRC), DOI: 10.1109/DRC.2018.8442159 (2018)

203. Singh, A.; Pashkin, A.; Winnerl, S.; Helm, M.; Schneider, H.
**Broadband Spectrum from a Photoconductive Emitter Spanning up to 13 THz**
2018 43rd International Conference on Infrared, Millimeter, and Terahertz Waves (IRMMW-THz), DOI: 10.1109/IRMMW-THz.2018.8510016 (2018)

204. Smekhova, A.; La Torre, E.; Eggert, B.; Cöster, B.; Szyjka, T.; Walecki, D.; Salamon, S.; Ollefs, K.; Bali, R.; Lindner, J.; Rogalev, A.; Weschke, E.; Banerjee, R.; Sanyal, B.; Schmitz-Antoniak, C.; Wende, H.
**Peculiarities of Disorder-Induced Ferromagnetism Phenomena in Fe60Al40-films on a local scale**
2018 IEEE International Magnetic Conference (INTERMAG), DOI: 10.1109/INTMAG.2018.8508108 (2018)

205. Wagner, A.; Butterling, M.; Hirschmann, E.; Krause-Rehberg, R.; Liedke, M.O.; Potzger, K.
**Positron Annihilation Studies using a Superconducting Electron LINAC**
AIP Conference Proceedings **1970**, 040003 (2018)

# Concluded scientific degrees

## PhD theses

1. Günther, F.
   **Theoretical studies of structural and electronic properties of donor-acceptor polymers**
   *TU Dresden, 05.07.2018*
2. Kelling, J.
   **Efficient Parallel Monte-Carlo Simulations for Large-Scale Studies of Surface Growth Processes**
   *TU Chemnitz, 13.04.2018*
3. König-Otto, J.
   **Ladungsträgerdynamik in Graphen unterhalb der optischen Phononenenergie**
   *TU Dresden, 29.03.2018*
4. Kowalska, E.
   **Current-induced dynamics in hybrid geometry MgO-based spin-torque nano-oscillators**
   *TU Dresden, 08.11.2018*
5. Liu, F.
   **Hyperdoping Si with deep-level impurities by ion implantation and sub-second annealing**
   *TU Dresden, 20.06.2018*
6. Trinh, T. T.
   **The microscopic effects of transition metal based hydrogen storing and sensing thin films**
   *TU Dresden, 18.12.2018*
7. Wagner, K.
   **Spin-wave generation and transport in magnetic microstructures**
   *TU Dresden, 19.06.2018*

## Bachelor/Master/Diploma theses

1. Bejarano, M.
   **Construction of a measurement instrument for magneto-optical and magneto-thermoelectric characterization of magnetic spin textures in micro- and nanostructures**
   *KU Leuven/TU Dresden (M.Sc.), 09/2018*
2. Chava, P.
   **Fabrication and characterization of logic devices based on two-dimensional van der Waals heterostructures**
   *TU Dresden (M.Sc.), 23.04.2018*
3. Helbig, M.
   **MEIS Detektorkalibrierung**
   *TU Dresden (B.Sc.),12.09.2018*
4. Jazavandi Ghamsari, S.
   **Fabrication and characterization of phosphorus doped germanium nanowires**
   *Universität Ulm (M.Sc.),18.10.2018*
5. Koch, L.
   **Modification of antiferromagnetically coupled multilayer systems with perpendicular anisotropy by He-ion irradiation**
   *TU Chemnitz (M.Sc.), 22.06.2018*

6. Liersch, V.
**Widerstandsmessungen an ionenbestrahlten FeAl Nanostrukturen**
*TU Dresden (M.Sc.), 31.01.2018*

7. Neumann, M.
**Numerische Simulation von drei magnetischen Janus-Partikeln**
*TU Chemnitz (M.Sc.), 06.08.2018*

8. Oelschlägel, A.
**Morphological modification of the ferromagnetic remanent state in cobalt/platinum multilayer structures investigated by means of magnetic force microscopy**
*TU Dresden (B.Sc.), 21.09.2018*

9. Ramasubramanian, L.
**Vortex dynamics in disks with tailored magnetizations**
*TU Chemnitz (M.Sc.), 29.03.2018*

10. Schultz de, R.
**Ion-induced surface nanostructures of germanium(001)**
*TU Dresden (M.Sc.), 02.10.2018*

11. Shan, S.
**Electronic properties of GaAs/InAlAs core/shell nanowires studied by optical-pump terahertz-probe spectroscopy**
*KIT Karlsruhe (M.Sc.), 01.06.2018*

12. Sheldon, R.
**Optically induced anisotropy in doped graphene**
*University of Surrey, Guildford, UK (M.Sc.), 08.01.2018*

# Awards and honors

1. **Arora, Himani**

   PhD student in the department “Scaling Phenomena” and fellow of the International Research School NanoNet received the **First Prize** of the cfAED Scientific Image Contest by the Cluster of Excellence “Center for Advancing Electronics Dresden”.

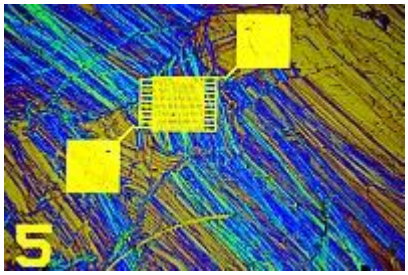

   Additionally, she won the **Third Prize** of the Science Slam at the Dresden Lange Nacht der Wissenschaften with a presentation “2D or not 2D”, June 15, 2018.

2. **Balaghi, Leila**

   PhD student in the group “Molecular Beam Epitaxy” of the department “Spectroscopy” received the **Third Prize** of the cfAED Scientific Image Contest. The picture is shown on the title page of this Annual Report.

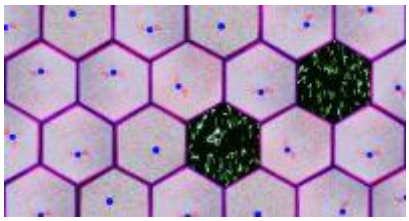

3. **Berencén, Yonder**

   Humboldt Fellow at the department “Semiconductor Materials” got the **1st Award** in the Young Scientist Contest for the Best Oral Presentation at the XIIth International Conference on Ion Implantation and other Applications of Ions and Electrons (ION 2018), Kazimierz Dolny, Poland, June 18 – 21, 2018.

4. **Canon Bermudez, Gilbert Santiago**

   PhD student in the department “Magnetism” received one of the 100 recognition prizes of the national German competition "**Ausgezeichnete Orte im Land der Ideen**".

5. **Deac, Alina**

   Head of the Helmholtz Young Investigator Research Group “Spintronics” of the “Magnetism” department was awarded the **Beller Lectureship** for the 2018 APS March Meeting on "Ultrahigh anisotropy Heusler alloys for THz spin-torque oscillators".

6. **Hache, Toni**

Master student in the department “Magnetism” received the **Georg Simon Ohm Prize 2018** of the Deutsche Physikalische Gesellschaft (DPG) “... for his outstanding Master’s thesis ‘Preparation and Characterization of Spin-Hall Effect-based nano Microwave Oscillators’ within the course Nanotechnology“ at the Westsächsische Hochschule Zwickau. The prize was handed over at the DPG Spring Meeting in Erlangen in March 2018.
In addition, he won a **Poster Prize** at the Summer School of the IEEE Magnetics Society 2018, Universidad San Francisco de Quito, Ecuador, June 3 – 8, 2018 with his presentation “Injection locking of constriction based spin-Hall nano-oscillators”.

7. **Klingner, Nico; Heller, René**

Scientists in the department “Ion Beam Center” won the **HZDR Innovation Award 2018** for their development of a “Time-of-Flight Secondary Ion Mass Spectrometer in a Helium Ion Microscope”.

8. **Krasheninnikov, Arkady**

Head of the “Atomistic Simulations of Irradiation-induced Phenomena” group was announced as **Outstanding Referee 2018** by the American Physical Society (APS) and as **Highly Cited Researcher 2018** by Clarivate Analytics (Web of Science), Philadelphia, PA, USA.

9. **Prucnal, Slawomir; Stöber, Max**

Scientist and PhD student of the department "Semiconductor Materials" received the **2nd Prize** of the **HZDR Innovation Competition 2018** for their project on “Silicon-Metal Electrodes for high Energy-density secondary Batteries”.

10. **Wang, Mao**

PhD student of the department "Semiconductor Materials" received the **Best Poster Prize** at the 21st International Conference on Ion Beam Modifications in Materials (IBMM2018), San Antonio, TX, USA, June 24 – 29, 2018 for her presentation “Extended infrared photoresponse in Te-hyperdoped Si at room-temperature”.
She also got the **3rd prize** of the Young Scientist Contest at the XIIth International Conference on Ion Implantation and other Applications of Ions and Electrons (ION 2018), Kazimierz Dolny, Poland, June 18 – 21, 2018.

11. **Zschornak, Mathias**

Former PhD student and collaborator of the department “Scaling Phenomena”, now at TU Bergakademie Freiberg, won the Ninth **Erwin-Felix-Lewy-Bertaut Prize** of the European Crystallographic Association (ECA) and the European Neutron Scattering Association (ENSA) at the 31st European Crystallographic Meeting in Oviedo, Spain, August 22 – 27, 2018.

# Invited conference contributions

1. Astakhov, G.
**Engineering and coherent control of defects in silicon carbide**
25th Conference on Application of Accelerators in Research and Industry (CAARI-2018), 13.08.2018, Grapevine, USA

2. Astakhov, G.V.
**Coherent control of spin qubit modes associated with defects in silicon carbide**
Theo Murphy international scientific meeting. SiC quantum spintronics: towards quantum devices in a technological material, 05.-06.11.2018, Buckinghamshire, UK

3. Astakhov, G.V.
**Engineering of highly coherent spin centers in silicon carbide**
3rd International Conference on Metamaterials and Nanophotonics METANANO 2018, 16.-21.09.2018, Sochi, Russia

4. Balaghi, L.; Bussone, G.; Grifone, R.; Hübner, R.; Grenzer, J.; Shan, S.; Fotev, I.; Pashkin, A.; Ghorbani-Asl, M.; Krasheninnikov, A.; Schneider, H.; Helm, M.; Dimakis, E.
**Changing the properties of GaAs via strain engineering in core/shell nanowires**
Nanostructures for Photonics, 07.05.2018, Saint Petersburg, Russia

5. Deac, A.M.
**Ultrahigh anisotropy Heusler alloys for THz spin-torque oscillators**
APS March Meeting 2018, 05.03.2018, Los Angeles, USA

6. Erb, D.; Schlage, K.; Röhlsberger, R.; Facsko, S.
**Nanostructure arrays via templated growth**
NAP2018 - 8th International Conference on Nanomaterials: Applications & Properties, 09.-14.09.2018, Zatoka, Ukraine

7. Fowley, C.; Rode, K.; Lau, Y.C.; Thiyagarajah, N.; Betto, D.; Borisov, K.; Atcheson, G.; Kampert, E.; Wang, Z.; Yuan, Y.; Zhou, S.; Lindner, J.; Stamenov, P.; Coey, J.M.D.; Deac, A.M.
**Anomalous Hall effect in fully compensated half-metallic $Mn_2Ru_xGa$ thin films**
Intermag 2018, 23.-27.04.2018, Singapore, Singapore

8. Grenzer, J.; Bähtz, C.; Rack, A.
**Materials science: in-situ, in-operando, time-resolved**
EPDIC16 – The 16th European Powder Diffraction Conference, 01.-04.07.2018, Edinburgh, UK

9. Hache, T.
**Herstellung und Charakterisierung von Spin-Hall Effekt-basierten Nano-Mikrowellenoszillatoren**
DPG-Frühjahrstagung der Sektion Kondensierte Materie (SKM) gemeinsam mit der European Physical Society (EPS-CMD), 11.-16.03.2018, TU Berlin, Deutschland

10. Heller, R.
**Automated Target Model Determination from MEIS Spectra Utilizing an Evolutionary Algorithm**
9th International Workshop on High-Resolution Depth Profiling (HRDP-9), 25.-29.06.2018, Uppsala, Sweden

11. Helm, M.
**Operating three research infrastructures at one site: electrons & photons, ions, magnetic fields**
Conference on International Cooperation of Science Centers, 19.10.2018, Huairou, China

12. Helm, M.; König-Otto, J.; Schmidt, J.; Dimakis, E.; Winnerl, S.; Schneider, H.
**Nonlinear THz Spectroscopy of Two-Dimensional Systems**
Frontiers of photonics, plasmonics and electronics with 2D nanosystems, 14.-20.07.2018, Erice, Italy

13. Helm, M.; König-Otto, J.; Schmidt, J.; Dimakis, E.; Winnerl, S.; Schneider, H.
**Nonlinear THz Spectroscopy of Two-Dimensional Systems**
Advanced Electromagnetics Symposium (AES 2018), 24.06.-01.07.2018, Marseille, France

14. Hlawacek, G.; Facsko, S.; Bischoff, L.; Klingner, N.; Xu, X.; Serralta, E.; Ghaderzadeh, S.
**HeFIB 2018: Helium and emerging focused ion beams**
CAARI 2018 - The Conference on Application of Accelerators in Research and Industry, 13.-17.08.2018, Fort Worth, USA

15. Hlawacek, G.; Klingner, N.; Heller, R.; Veligura, V.; van Gastel, R.; Poelsema, B.; von Borany, J.; Facsko, S.
**Imaging and analytic possibilities in the Helium Ion Microscope**
Imaging 2020 Workshop, 06.04.2018, Sønderborg, Denmark

16. Kelling, J.; Ódor, G.; Weigel, M.; Gemming, S.
**Efficient Correlation-Free Many-States Lattice Monte Carlo on GPUs**
GPU Day 2018, 21.-22.06.2018, Budapest, Hungary

17. Klingner, N.; Heller, R.; Hlawacek, G.; Facsko, S.; von Borany, J.
**High Resolution in 3 dimensions – TOF-SIMS in the Helium Ion Microscope**
9th International Workshop on High-Resolution Depth Profiling (HRDP 9), 25.-29.06.2018, Uppsala, Sweden

18. Klingner, N.; Hlawacek, G.; Heller, R.; von Borany, J.; Facsko, S.
**Time of Flight Backscatter and Secondary Ion Spectrometry in a Helium Ion Microscope**
Microscopy and Microanalysis, 05.-09.08.2018, Baltimore, USA

19. Kosub, T.; Kopte, M.; Appel, P.; Shields, B.; Maletinsky, P.; Hübner, R.; Fassbender, J.; Schmidt, O.G.; Makarov, D.
**Purely Antiferromagnetic Magnetoelectric RAM**
CIMTEC Ceramics Congress, 18.-22.06.2018, Perugia, Italien

20. Kosub, T.; Kopte, M.; Appel, P.; Shields, B.; Maletinsky, P.; Hübner, R.; Fassbender, J.; Schmidt, O.G.; Makarov, D.
**Purely Antiferromagnetic Magnetoelectric RAM**
EMN Meeting, 16.-20.07.2018, Berlin, Deutschland

21. Krause, M.
**Nanocomposite thin film research using ion beams and in situ techniques**
Institutsseminar in der Veranstaltungsreihe - Doctorado en Nanociencia y Tecnologías de Materiales, Facultad de Ciencias, 19.10.2018, Puerto Real, Cadiz, Spain

22. Krause, M.; Heras, I.; Lungwitz, F.; Wenisch, R.; Schumann, E.; Janke, D.; Guillén, E.; Munnik, F.; Azkona, I.; Gemming, S.; Escobar-Galindo, R.
**Design, validation and testing of new receiver coatings for concentrated solar power**
5th European Conference in Nanofilms (ECNF), 20.-22.03.2018, Cranfield, UK

23. Liedke, M.O.; Butterling, M.; Quintana, A.; Menéndez, E.; Ehrler, J.; Bali, R.; Hirschmann, E.; Sireus, V.; Nogués, J.; Sort, J.; Wagner, A.
**Vacancy-mediated magnetic phase-transitions**
18th International Conference on Positron Annihilation (ICPA-18), 19.08.2018, Orlando, USA

24. MacLaren, I.; Nord, M.; Conner, S.; McGrouther, D.; Allen, C.S.; Danaie, M.; Kirkland, A.I.; Bali, R.; Hlawacek, G.; Lindner, J.; Faßbender, J.
**Imaging Structure and Magnetisation in New Ways Using 4D STEM**
Microscopy & Microanalysis 2018 Meeting, 05.-09.08.2018, Baltimore MD, USA

25. Makarov, D.
**Shapeable magnetoelectronics with sensitivities to geomagnetic fields and below**
2018 International Workshop on Nanomembrane Origami Technology, 10.-11.11.2018, Shanghai, China

26. Makarov, D.
**Intelligent materials and devices**
Advancing Science through International Cooperation: Forum of the Ukrainian Research Diaspora, 20.-22.10.2018, Kyiv, Ukraine

27. Makarov, D.
**Spintronics of thin film granular antiferromagnets**
International Workshop on Magneto-Electric Actuation, Magneto-Ionics and Related Phenomena in High-Surface Area Materials, 28.-30.05.2018, Gavà-Barcelona, Spain

28. Makarov, D.
**Magnetic smart skins for augmented reality**
18th International Conference on Experimental Mechanics (ICEM 2018), 01.-05.07.2018, Brussels, Belgium

29. Makarov, D.
**Magnetic Functionalities for Flexible Interactive Electronics**
6th International Conference on Superconductivity and Magnetism, 29.04.-04.05.2018, Antalya, Turkey

30. Makarov, D.
**Spintronics with thin film magnetoelectric antiferromagnets**
2018 Gordon Research Conference on Multiferroic and Magnetoelectric Materials: Effects in Multiferroics Beyond the Coupling of Magnetic and Electric Order, 05.-10.08.2018, Lewiston, Maine, USA

31. Makarov, D.
**Exchange-driven chiral effects in curvilinear magnetism: theoretical abstraction or experimental observable?**
Workshop „Topological Phenomena in Quantum Materials“, 04.-05.12.2018, Dresden, Germany

32. Makarov, D.
**Spintronics with magnetoelectric antiferromagnetic thin films**
2018 International Colloquium on Magnetic Films and Surfaces (ICMFS), 22.-27.07.2018, Santa Cruz, USA

33. Makarov, D.
**From curvilinear magnetism to shapeable magnetoelectronics (plenary)**
XIV International Conference on Applied Physics and Electronics, 24.-26.10.2018, Kyiv, Ukraine

34. Makarov, D.
**Spintronics of thin film granular antiferromagnets**
Joint European Magnetic Symposia (JEMS) 2018, 03.-07.09.2018, Mainz, Germany

35. Rebohle, L.; Skorupa, W.; Prucnal, S.; Berencén, Y.; Zhou, S.; Helm, M.
**Advanced thermal processing of group-IV materials and beyond**
European Materials Research Society Spring Meeting 2018, 18.-22.06.2018, Strasbourg, France

36. Schneider, H.
**Nonlinear THz spectroscopy of graphene and GaAs quantum wells using a free-electron laser**
The 9th International Symposium on Ultrafast Phenomena and Terahertz Waves (ISUPTW 2018), 23.-26.04.2018, Changsha, China

37. Schneider, H.
**Nonlinear THz spectroscopy of graphene and GaAs quantum wells using a free-electron laser**
International Conference on Synchrotron and free electron laser radiation: generation and application (SFR-2018), Budker Institute of Nuclear Physics, 25.-28.06.2018, Novosibirsk, Russia

38. Schultheiss, H.
**Magnon Transport in Spin Textures**
Lüscher Seminar, 08.02.2018, Klosters, Switzerland

39. Schultheiss, H.
**Magnon Transport in Spin Textures**
Spin Mechanics 5 and Nano MRI 6 workshop, 16.02.2018, Chamonix, Switzerland

40. Schultheiss, H.
**Magnon Transport in Spin Textures**
Nano-Magnonics Workshop, 20.02.2018, Kaiserslautern, Germany

41. Schultheiss, H.
**Magnon Transport in Spin Textures**
International Conference on Microwave Magnetics, 25.06.2018, Exeter, UK

42. Schultheiss, H.
**Magnon Transport in Spin Textures**
Workshop on Advances in Brillouin Light Scattering, 13.09.2018, Perugia, Italy

43. Schultheiss, H.
**Magnon Transport in Spin Textures**
International Advanced School on Magnonics, 20.09.2018, Kyiv, Ukraine

44. Schultheiss, K.; Verba, R.; Wehrmann, F.; Wagner, K.; Körber, L.; Hula, T.; Hache, T.; Kákay, A.; Awad, A.A.; Tiberkevich, V.; Slavin, A.N.; Fassbender, J.; Schultheiss, H.
**Excitation of whispering gallery magnons in a magnetic vortex**
International Conference on Magnetism (InterMag), 19.07.2018, San Francisco, USA

45. Semisalova, A.; Stienen, S.; Barton, C.W.; Boettger, R.; Bali, R.; Thomson, T.; Farle, M.; Fassbender, J.; Potzger, K.; Lindner, J.
**Ferromagnetic resonance in FeRh thin films near the antiferromagnetic-ferromagnetic phase transition**
International School-Conference Spinus 2018, 01.-06.04.2018, Saint Petersburg, Russia

46. Skorupa, W.
**Halbleitertechnik im Osten der Republik**
Workshop anlässlich des 60. Jahrestages des Instituts für Halbleitertechnik an der Universität Stuttgart, 01.08.2018, Stuttgart, Germany

47. Wagner, A.; Butterling, M.; Hirschmann, E.; Krause-Rehberg, R.; Liedke, M.O.; Potzger, K.
**Positron Studies with a Superconducting Electron Accelerator**
18th International Conference on Positron Annihilation, 18.-24.08.2018, Orlando, FL, USA

48. Wilhelm, R.A.; Creutzburg, S.; Schwestka, J.; Gruber, E.; Kozubek, R.; Lehnert, T.; Leiter, R.; Heller, R.; Krasheninnikov, A.; Facsko, S.; Kaiser, U.; Kotakoski, J.; Schleberger, M.; Aumayr, F.
**Charge exchange and energy loss of slow highly charged ions transmitted through 2D materials**
IBMM 2018 - International Conference on Ion Beam Modification of Materials, 24.-29.06.2018, San Antonio, TX, USA

49. Wilhelm, R.A.; Gruber, E.; Schwestka, J.; Kozubek, R.; Madeira, T.I.; Marques, J.P.; Kobus, J.; Krasheninnikov, A.V.; Schleberger, M.; Aumayr, F.
**Interatomic coulombic decay - the mechanism for rapid deexcitation of hollow atoms**
19th International Conferences on the Physics of Highly Charged Ions (HCI 2018), 02.-07.09.2018, Lissboa, Portugal

50. Winnerl, S.
**Unusual Coulomb effects in graphene**
Tianjin International Symposium on Epigraphene (TISEG), 22.-27.07.2018, Tianjin, China

51. Winnerl, S.; König-Otto, J.C.; Mittendorff, M.; Pashkin, A.; Venanzi, T.; Schneider, H.; Helm, M.
**Low-energy carrier dynamics in graphene and other 2D materials**
18th International Conference on Laser Optics (ICLO 2018), 04.-08.06.2018, St. Petersburg, Russia

52. Wintz, S.
**Topological spin textures as spin-wave emitters**
DPG-Frühjahrstagung der Sektion Kondensierte Materie, 11.-16.03.2018, Berlin, Germany

53. Wintz, S.
**Topological spin textures as spin-wave emitters**
IEEE Nanomaterials: Applications and Properties, 09.-14.09.2018, Zatoka, Ukraine

54. Zhou, S.
**Ion implantation + sub-second annealing: a route towards hyperdoped semiconductors**
International Conference on Radiation and Emission in Materials, 20.-23.11.2018, Chiang Mai, Thailand

55. Zhou, S.
**Defect induced magnetism in SiC**
International Workshop: Functionality of Oxide Interfaces, 26.02.-02.03.2018, Frauenwörth, Germany

# Conferences, workshops, colloquia and seminars

## Organization of conferences and workshops

1. Bittencourt, C.; Ewels, C.; Facsko, S.; Krasheninnikov, A.
**Conference on Physics of Defects in Solids: Quantum Mechanics Meets Topology**
*09. – 13.07.2018, ICTP, Trieste, Italy*

2. Cuniberti, G.; Gemming, S.; Lehner, W.
**DCMS Materials 4.0 Summer School: Deep Materials – Perspectives on Data-driven Materials Research**
*10. – 14.09.2018, Dresden, Germany*

3. Erbe, A.; Zahn, P.
**NANONET Annual Workshop 2018**
*05. – 07.09.2018, Augustusberg/Bad Gottleuba, Germany*

4. Heine, T.; Kuc, A.; Springer, M.; Kempt, R.; Ghorbani-Asl, M.; Brumme, T.; Zhechkov, L.
**Flatlands beyond Graphene**
*03. – 07.09.2018, Leipzig, Germany*

5. Hlawacek, G.; Wirtz, T.; Ovchinnikova, O.; Ogawa, S.
**2nd International HeFIB Conference on Helium and Emerging Focused Ion Beams**
*11. – 13.06.2018, Dresden, Germany*

6. Inkson, B.; Hlawacek, G.; Pilling, R.
**1st International Meeting of the PicoFIB Network & PicoFIB Workshop Advances in Gas-Ion Microscopy**
*31.01.2018, Dresden, Germany*

## Colloquia

1. Fery, A.
Leibniz-Institut für Polymerforschung, Dresden, Germany
**Colloidal surface assemblies: Nanotechnology meets bioinspiration**
*31.05.2018*

2. Flatau, A. B.
University of Maryland, College Park, USA
**Structural magnetostrictive alloys: From flexible sensors to energy harvesters and magnetically controlled auxetics**
*14.06.2018*

3. Inoue, M.
Toyohashi University of Technology, Japan
**Magnetic phase interference in artificial magnetic lattices - Functions and applications to optical, high-frequency, and spin wave devices**
*09.10.2018*

4. McCord, J.
Institute for Materials Science, Kiel University, Germany
**Thin films magnetism as seen by magneto-optics**
*27.09.2018*

5. Schumacher, H. W.
Physikalisch-Technische Bundesanstalt, Braunschweig, Germany
**Single electron pumps for the redefinition of the SI base unit Ampere**
*29.11.2018*

6. Vyalikh, D.
Donostia International Physics Center (DIPC), San Sebastian, Spain
**Photoemission insight into the strongly-correlated electrons and magnetism in 4f-systems**
*06.09.2018*

7. Zhang, X.
King Abdullah University of Science and Technology, Physical Science and Engineering, Thuwal, Saudi Arabia
**Observation of high temperature magnetic skyrmions**
*20.08.2018*

## Seminars

1. Banyasz, I.
Department of Nuclear Materials Science, Wigner Research Centre for Physics, Budapest, Hungary
**Design, fabrication and characterisation of ion implanted and irradiated optical elements and devices for application in telecommunication and sensors**
*24.08.2018*

2. Bhatnagar, A.
AG Light for high-voltage photovoltaics, ZIK SiLi-nano, Halle/Saale, Germany
**Photoelectronic processes in multiferroic oxides**
*03.05.2018*

3. Bossini, D.
Experimentelle Physik VI, TU Dortmund, Germany
**Femtosecond manipulation of magnets via photoinduced magnons at the edges of the Brillouin Zone**
*05.03.2018*

4. Cosic, M.
Vinča Institute of Nuclear Sciences, Belgrade, Serbia
**Investigation of graphene by proton rainbow scattering**
*10.10.2018*

5. Dam, B.
TU Delft, The Netherlands
**Materials research for a sustainable economy**
*18.12.2018*

6. Fu, R.
Northumbria University, Newcastle upon Tyne, United Kingdom
**Thin film based smart materials and MEMS**
*30.05.2018*

7. Gonçalves, F. J. T.
Osaka Prefecture University and Center for Chiral Science, Hiroshima University, Japan
**Collective excitations in the spin soliton lattice of a chiral helimagnet**
*17.12.2018*

8. Gottschall, T.
Dresden High Magnetic Field Laboratory/HZDR, Dresden, Germany
**On the magnetocaloric properties of Heusler compounds**
*14.02.2018*

9. Gruszecki, P.
Faculty of Physics, Adam Mickiewicz University Poznań, Poland
**Graded index magnonics and magnonic metasurfaces**
*26.02.2018*

10. Herfort, J.
Paul-Drude-Institut Berlin, Germany
**Epitaxial ferromagnetic Heusler alloy/semiconductor hybrid structures for spintronic application**
*13.12.2018*

11. Herklotz, A.
Institute for Physics, Martin-Luther-University Halle-Wittenberg, Halle/Saale, Germany
**Strain doping: A new avenue for understanding and controlling materials**
*19.04.2018*

12. Hiller, D.
Australian National University, Canberra, Australia
**From un-dopable silicon nanocrystals to passivating carrier-selective contacts for silicon solar cells**
*12.09.2018*

13. Iliopoulos, E.
Department of Physics, University of Crete, Greece
**III-Nitride semiconductors' perspectives: from solar cells to nanoelectronics**
*19.09.2018*

14. Jarrahi, M.
Electrical and Computer Engineering, University of California, Los Angeles, USA
**Plasmonic terahertz devices and systems**
*31.08.2018*

15. Kézsmárki, I.
Experimental Physics V, Center for Electronic Correlations and Magnetism, University of Augsburg, Germany
**Skyrmions and antiskyrmions in crystals with axial symmetry**
*11.04.2018*

16. Kirchner, R.
Institut für Halbleiter- und Mikrosystemtechnik, TU Dresden, Germany
**Using material contrast and self-optimizing processes for 3D patterning**
*24.01.2018*

17. Kunze, T.
Fraunhofer-Institut für Werkstoff- und Strahltechnik IWS, Dresden, Germany
**High-speed surface functionalization employing direct laser interference patterning – From small scales to big influences**
*22.03.2018*

18. Kusminskiy, S. V.
Max Planck Institute for the Science of Light, Erlangen, Germany
**Non-linear dynamics and magnetic textures in cavity optomagnonics**
*12.04.2018*

19. Ling, F. C. C.
Department of Physics, The University of Hong Kong
**Defects in the multi-functional material ZnO: Characterization and functionality**
*07.09.2018*

20. Lue, C. S.
Department of Physics, National Cheng Kung University, Tainan, Taiwan
**Recent progress in the growth of single crystalline intermetallic compounds in National Cheng Kung University**
*23.07.2018*

21. Meinert, M.
Zentrum für spinelektronische Materialien und Bauelemente, Fakultät für Physik der Universität Bielefeld, Germany
**Key role of thermal activation in the electrical switching of antiferromagnetic $Mn_2Au$ and CuMnAs**
*08.08.2018*

22. Nadarajan, R.
Department of Physics, Pondicherry University, Puducherry, India
**High temperature stability of $BaZrO_3$: An ab initio thermodynamic study**
*06.03.2018*

23. Neek-Amal, M.
University of Antwerp, Belgium, and Shahid Rajaee Teacher Training University, Tehran, Iran
**Transport of hydrogen isotopes through interlayer spacing in van der Waals crystals**
*23.08.2018*

24. Ney, A.
Abteilung für Festkörperphysik, JKU Linz, Austria
**Time-resolved X-ray detected ferromagnetic resonance with spatial resolution using scanning X-ray transmission microscopy**
*22.06.2018*

25. Ohshima, T.
National Institutes for Quantum and Radiological Science and Technology (QST), Chiba, Japan
**Particle irradiation for creation of spin qubits in wide bandgap semiconductors**
*16.07.2018*

26. Pan, A.
College of Physics and Microelectronics Science, Hunan University, China
**Band-gap engineering and photonics in low dimensional semiconductor structures**
*15.08.2018*

27. Pelekanos, N. T.
Materials Science and Technology Department, University of Crete, and IESL/FORTH, Heraklion, Greece
**Highly uniform GaAs nanowires for photovoltaic applications**
*23.01.2018*

28. Popok, V.
The Faculty of Engineering and Science, Department of Materials and Production, Physics and Mechanics, Aalborg University, Denmark
**2-DEG formation at AlGaN-GaN interfaces**
*10.09.2018*

29. Sadovnikov, A. V.
Department of Electronics, Oscillations and Waves, Saratov State University, Russia
**Brillouin light scattering of spin-wave transport in magnonic structures based on microsized YIG films**
*23.10.2018*

30. Salikhov, R.
University of Duisburg-Essen, Faculty of Physics and Center for Nanointegration (CENIDE), Duisburg, Germany
**A new class of inherently nanolaminated magnetic materials: magnetic MAX phases**
*11.09.2018*

31. Silvani, R.
Dipartimento di Fisica, University of Perugia, Italy
**Micromagnetic simulation of magnonic crystals consisting of L-shaped iron/permalloy nanowires and thin Fe-N magnetic films with stripe domains**
*20.06.2018*

32. Som, T.
Institute of Physics, Sachivalaya Marg, Bhubaneswar, India
**Self-organized nanostructure formation by ion beams**
*28.05.2018*

33. Sun, Y.
Max Planck Institute for Chemical Physics of Solids, Dresden, Germany
**Surface Fermi arc states and bulk transport in Weyl semimetals**
*25.04.2018*

34. Yamazaki Y.
National Institutes for Quantum and Radiological Science and Technology (QST), Chiba, Japan
**Electrical control of color centers introduced in SiC diodes by proton beam writing**
*16.07.2018*

35. Yang, C.
Felix-Bloch-Institut für Festkörperphysik, Universität Leipzig, Germany
**Copper iodide, a high-performance p-type wide bandgap semiconductor**
*01.06.2018*

# Exchange of researchers

## Guests at our institute

1. Arias, R.
   *Universidad de Chile, Santiago, Chile; 01.07. - 14.07.2018*
2. Bezghuba, V.
   *Kyiv University, Ukraine; 22.01. - 28.01.2018*
3. Boamah, D.
   *Kwame Nkrumah University of Science and Technology, Kumasi, Ghana; 01.06. - 31.08.2018*
4. Bohovicova, J.
   *Bratislava University of Technology, Slovakia; 01.09. - 30.11.2018*
5. Chepkasov, I.
   *Khakas State University, Abakan, Russia; 01.10.2018 - 31.03.2019*
6. Dhagat, P.
   *Oregon State University, USA; 01.04. - 30.06.2018*
7. Drozdziel, A.
   *University Lublin, Poland; 10.04. - 19.04.2018*
8. El-Said, A. S.
   *Mansoura University, Egypt; 12.01. - 20.01.; 25.06. - 01.07.2018*
9. French, R. H.
   *Case Western Reserve University, USA; 08.09. - 15.09.2018*
10. Huang, X.
    *Nanjing University, P. R. China; 25.08.2017 - 24.08.2018*
11. Iastremskyi, I.
    *Kyiv University, Ukraine; 19.07. - 24.08.2018*
12. Klause, R.
    *Indianapolis, USA; 14.05. - 12.08.2018*
13. Kononenko, D.
    *Kyiv University, Ukraine; 25.10. - 03.11.2018*
14. Kordyuk, A.
    *Institute for Metal Physics, Kyiv, Ukraine; 22.01. - 31.01.2018*
15. Liu, C.
    *Harbin Institute of Technology, P. R. China; 12.09.2017 - 11.09.2018*
16. Ma, L.
    *Shandong University, P. R. China; 28.09.2018 - 27.09.2019*
17. Méndez, A.
    *Nano4Energy SL, Spain; 03.04 .- 21.12.2018*
18. Mesko, M.
    *Bratislava University of Technology, Slovakia; 12.08. - 24.08.2018*
19. Mutlay, Z. G.
    *Ankara, Turkey; 01.07. - 31.08.2018*
20. Nadarajan, R.
    *University Pondicherry, India; 09.01. - 31.03.2018*
21. Pedroso, D.
    *Instituto Tecnologico de Aeronautica, Sao Jose dos Campos, Brazil; 01.08.2017 - 31.07.2018*

22. Pelekanos, N.
*University of Crete, Greece; 14.01. - 27.01.2018*

23. Pereira, P.
*Pontificia Universidade Católica do Rio de Janeiro, Brazil; 01.03.2018 - 31.05.2019*

24. Pylypovskyi, O.
*Kyiv University, Ukraine; 10.06. - 04.09.2018*

25. Pyszniak, K.
*University Lublin, Poland; 10.04. - 19.04.2018*

26. Sheka, D.
*Kyiv University, Ukraine; 04. - 26.02.; 01. - 23.07.; 05. - 27.08.; 25.10. - 03.11.2018*

27. Som, T.
*Institute of Physics, Bhubaneswar, India; 06.05. - 06.06.2018*

28. Tiessen, C.
*University of Ottawa, Canada; 15.05. - 27.07.2018*

29. Tsai, H.-S.
*National Tsing Hua University, Hsinchu, Taiwan; 15.03. - 31.12.2018*

30. Zhang, X.
*Harbin Institute of Technology, P. R. China; 15.03.2017 - 14.03.2018*

31. Zheng, C.
*Shanghai, P. R. China; 16.07. - 31.12.2018*

# Projects

The projects are listed by funding institution and project starting date. In addition, the institute has several bilateral service collaborations with industrial partners and research institutions. These activities are not included in the following overview.

## European Projects

1. 01/2015 – 12/2018 European Union EU
**FRIENDS$^2$ – Engineering of New Durable Solar Surfaces**
*Prof. S. Gemming* *Phone: 0351 260 2470* *s.gemming@hzdr.de*

2. 02/2016 – 01/2020 European Union EU
**IONS4SET – Single Electron Transistor**
*Dr. J. v. Borany* *Phone: 0351 260 3378* *j.v.borany@hzdr.de*

3. 01/2017 – 12/2020 European Union EU
**TRANSPIRE –Terahertz Radio Communication**
*Dr. A. Deac* *Phone: 0351 260 3709* *a.deac@hzdr.de*

4. 01/2017 – 12/2020 European Union EU
**npSCOPE – Nanoparticle Characterization**
*Dr. G. Hlawacek* *Phone: 0351 260 3409* *g.hlawacek@hzdr.de*

5. 05/2017 – 04/2021 European Union EU
**CALIPSOplus – Coordinated Access to Lightsources**
*Prof. M. Helm* *Phone: 0351 260 2260* *m.helm@hzdr.de*

6. 09/2017 – 02/2019 European Union EU
**Analytics – All-electrical analytic platform for digital fluidics**
*Dr. D. Makarov* *Phone: 0351 260 3273* *d.makarov@hzdr.de*

## Helmholtz Association Projects

1. 10/2012 – 12/2020 Helmholtz-Gemeinschaft HGF
**NANONET – International Helmholtz Research School on Nanoelectronics**
*Dr. A. Erbe* *Phone: 0351 260 2366* *a.erbe@hzdr.de*

2. 01/2013 – 12/2019 Helmholtz-Gemeinschaft HGF
**W3-Professorship TU Chemnitz**
*Prof. S. Gemming* *Phone: 0351 260 2470* *s.gemming@hzdr.de*

3. 01/2014 – 12/2018 Helmholtz-Gemeinschaft HGF
**Spintronics – Helmholtz Young Investigator Group**
*Dr. A.M. Deac* *Phone: 0351 260 3709* *a.deac@hzdr.de*

4. 11/2014 – 12/2019 Helmholtz-Gemeinschaft HGF
**Magnetism – HGF Postdoc Dr. K. Schultheiß**
*Prof. J. Fassbender* *Phone: 0351 260 3096* *j.fassbender@hzdr.de*

5. 05/2016 – 08/2019 Helmholtz-Gemeinschaft HGF
**THz Spectroscopy – HGF Postdoc Dr. A. Singh**
*Prof. M. Helm* *Phone: 0351 260 2260* *m.helm@hzdr.de*

6. 10/2017 – 08/2020 Helmholtz-Gemeinschaft HGF
**Helmholtz Exzellenznetzwerk – cfaed 2 + 3**
*Dr. A. Erbe* *Phone: 0351 260 2366* *a.erbe@hzdr.de*

7. 10/2017 – 02/2020 Helmholtz-Gemeinschaft HGF
**Helmholtz ERC Recognition Award**
*Dr. H. Schultheiß* *Phone: 0351 260 3243* *h.schultheiss@hzdr.de*

8. 11/2017 – 01/2019 Helmholtz-Gemeinschaft HGF
**Helmholtz Exzellenznetzwerk – DCM-MatDNA 2**
*Prof. S. Gemming* *Phone: 0351 260 2470* *s.gemming@hzdr.de*

9. 01/2018 – 09/2018 Helmholtz-Gemeinschaft HGF
**Coordination EU Project RADIATE**
*Prof. J. Fassbender* *Phone: 0351 260 3096* *j.fassbender@hzdr.de*

## German Science Foundation Projects

1. 01/2013 – 10/2019 Deutsche Forschungsgemeinschaft DFG
**Cluster of Excellence – Center for Advancing Electronics Dresden (cfaed)**
*Prof. M. Helm* *Phone: 0351 260 2260* *m.helm@hzdr.de*

2. 05/2014 – 03/2020 Deutsche Forschungsgemeinschaft DFG
**Emmy Noether Junior Research Group – Magnonics**
*Dr. H. Schultheiß* *Phone: 0351 260 3243* *h.schultheiss@hzdr.de*

3. 11/2014 – 10/2018 Deutsche Forschungsgemeinschaft DFG
**Thermal spin-transfer torques**
*Dr. J. Lindner* *Phone: 0351 260 3221* *j.lindner@hzdr.de*
*Dr. A. M. Deac* *Phone: 0351 260 3709* *a.deac@hzdr.de*

4. 11/2014 – 12/2018 Deutsche Forschungsgemeinschaft DFG
**All Optical Switching**
*Dr. H. Schultheiß* *Phone: 0351 260 3243* *h.schultheiss@hzdr.de*

5. 10/2015 – 09/2018 Deutsche Forschungsgemeinschaft DFG
**Ferromagnetic Silicon**
*Dr. S. Zhou* *Phone: 0351 260 2484* *s.zhou@hzdr.de*

6. 03/2017 – 08/2020 Deutsche Forschungsgemeinschaft DFG
**MUMAGI – Disorder induced magnetism**
*Dr. R. Bali* *Phone: 0351 260 2919* *r.bali@hzdr.de*

7. 07/2017 – 06/2020 Deutsche Forschungsgemeinschaft DFG
**HELEX2D – Interaction of highly charged ions with 2D materials**
*Dr. R. Wilhelm* *Phone: 0351 260 3378* *r.wilhelm@hzdr.de*

8. 08/2017 – 07/2020 Deutsche Forschungsgemeinschaft DFG
**FlexCom – Magnetic field sensitive flexible communication system**
*Dr. D. Makarov* *Phone: 0351 260 3273* *d.makarov@hzdr.de*

9. 09/2017 – 08/2020 Deutsche Forschungsgemeinschaft DFG
**Lane Formation**
*Dr. A. Erbe* *Phone: 0351 260 2366* *a.erbe@hzdr.de*

10. 11/2017 – 10/2020 Deutsche Forschungsgemeinschaft DFG
**ULTRACRITICAL – High-temperature superconductors**
*Dr. A. Pashkin* *Phone: 0351 260 3287* *o.pashkin@hzdr.de*

11. 04/2018 – 03/2021 Deutsche Forschungsgemeinschaft DFG
**Confined Microswimmers**
*Dr. A. Erbe* *Phone: 0351 260 2366* *a.erbe@hzdr.de*

12. 04/2018 – 03/2021 Deutsche Forschungsgemeinschaft DFG
**IMASTE – Graphene encapsulated quasi-2D materials**
*Dr. A. Krasheninnikov* *Phone: 0351 260 3148* *a.krasheninnikov@hzdr.de*

13. 06/2018 – 06/2018 Deutsche Forschungsgemeinschaft DFG
**Conference HeFIB 2018**
*Dr. G. Hlawacek Phone: 0351 260 3409 g.hlawacek@hzdr.de*

14. 10/2018 – 09/2020 Deutsche Forschungsgemeinschaft DFG
**Doping by ALD and FLA**
*Dr. L. Rebohle Phone: 0351 260 3368 l.rebohle@hzdr.de*

15. 10/2018 – 09/2020 Deutsche Forschungsgemeinschaft DFG
**Magnetic Landscapes – Spin Dynamics**
*Dr. A. Semisalova Phone: 0203 37 92474 anna.semisalova@uni-due.de*

## Federally and Saxony State Funded Projects

1. 01/2014 – 06/2018 Bundesministerium für Bildung und Forschung BMBF
**In-situ TEM**
*Prof. J. Fassbender Phone: 0351 260 3096 j.fassbender@hzdr.de*

2. 02/2016 – 12/2018 Sächsische Aufbaubank SAB
**PolCarr-Sens – Electrically Polarizable Materials**
*Dr. S. Hartmann Phone: 0351 260 2710 stefanie.hartmann@hzdr.de*

3. 01/2017 – 06/2018 Bundesministerium für Bildung und Forschung BMBF
**Elemental analytics with the Helium Ion Microscope**
*Dr. R. Heller Phone: 0351 260 3096 r.heller@hzdr.de*

4. 01/2017 – 03/2019 Bundesministerium für Bildung und Forschung BMBF
**German-Ukrainian Center for Large Scale Experiment**
*Dr. D. Makarov Phone: 0351 260 3273 d.makarov@hzdr.de*

5. 08/2017 – 11/2019 Sächsische Aufbaubank SAB
**PlatMOS – Atmospheric plasma treatment for corrosion suppression at organ pipes**
*Dr. W.Skorupa Phone: 0351 260 3612 w.skorupa@hzdr.de*

6. 09/2017 – 08/2019 Sächsische Aufbaubank SAB
**SiNergy – Si based battery electrodes**
*Dr. S. Prucnal Phone: 0351 260 2065 s.prucnal@hzdr.de*

7. 10/2017 – 03/2019 Bundesministerium für Bildung und Forschung BMBF
**Resistance-Tensormeter**
*Dr. T. Kosub Phone: 0351 260 2900 t.kosub@hzdr.de*

8. 11/2017 – 12/2019 Arbeitsgemeinschaft industrielle Forschung AiF
**Liquid metal ion source**
*Dr. L. Bischoff Phone: 0351 260 2866 l.bischoff@hzdr.de*

9. 01/2018 – 12/2019 DECHEMA e.V. DECHEMA
**High temperature oxidation resistance for nickel-based alloys by fluorine implantation**
*Dr. W.Skorupa Phone: 0351 260 3612 w.skorupa@hzdr.de*

10. 11/2018 – 10/2020 Bundesministerium für Bildung und Forschung BMBF
**Metal-germanium interface: Schottky barrier and ohmic contacts**
*Dr. S. Prucnal Phone: 0351 260 2065 s.prucnal@hzdr.de*

## Personnel Exchange Projects and Society Chairs

1. 06/2016 – 05/2019 Alexander-von-Humboldt-Stiftung AvH
**Humboldt fellowship Dr. Berencen**
*Dr. L. Rebohle* *Phone: 0351 260 3368* *l.rebohle@hzdr.de*

2. 05/2017 – 12/2018 Institute of Electrical and Electronics Engineers IEEE
**Magnetics Society German Chapter Chair**
*Dr. H. Schultheiß* *Phone: 0351 260 3243* *h.schultheiss@hzdr.de*

3. 06/2017 – 06/2020 Alexander-von-Humboldt-Stiftung AvH
**Humboldt fellowship Prof. Sheka**
*Dr. D. Makarov* *Phone: 0351 260 3273* *d.makarov@hzdr.de*

4. 04/2018 – 03/2020 Deutscher Akademischer Austauschdienst DAAD
**ULTIMAT – Superlattices of ultra-thin $In_xGa_{1-x}N$/GaN quantum wells**
*Dr. E. Dimakis* *Phone: 0351 260 2765* *e.dimakis@hzdr.de*

5. 06/2018 – 09/2017 Deutscher Akademischer Austauschdienst DAAD
**Visit Dr. Pylypovskyi**
*Dr. J. Lindner* *Phone: 0351 260 3221* *j.lindner@hzdr.de*

6. 09/2018 – 11/2018 Deutscher Akademischer Austauschdienst DAAD
**Visit Dr. Bohovicova**
*Dr. M. Krause* *Phone: 0351 260 3578* *matthias.krause@hzdr.de*

7. 09/2018 – 08/2019 Deutscher Akademischer Austauschdienst DAAD
**Leonhard Euler Grant: Curvature induced effects in nanowires**
*Dr. D. Makarov* *Phone: 0351 260 3273* *d.makarov@hzdr.de*

# Organization chart

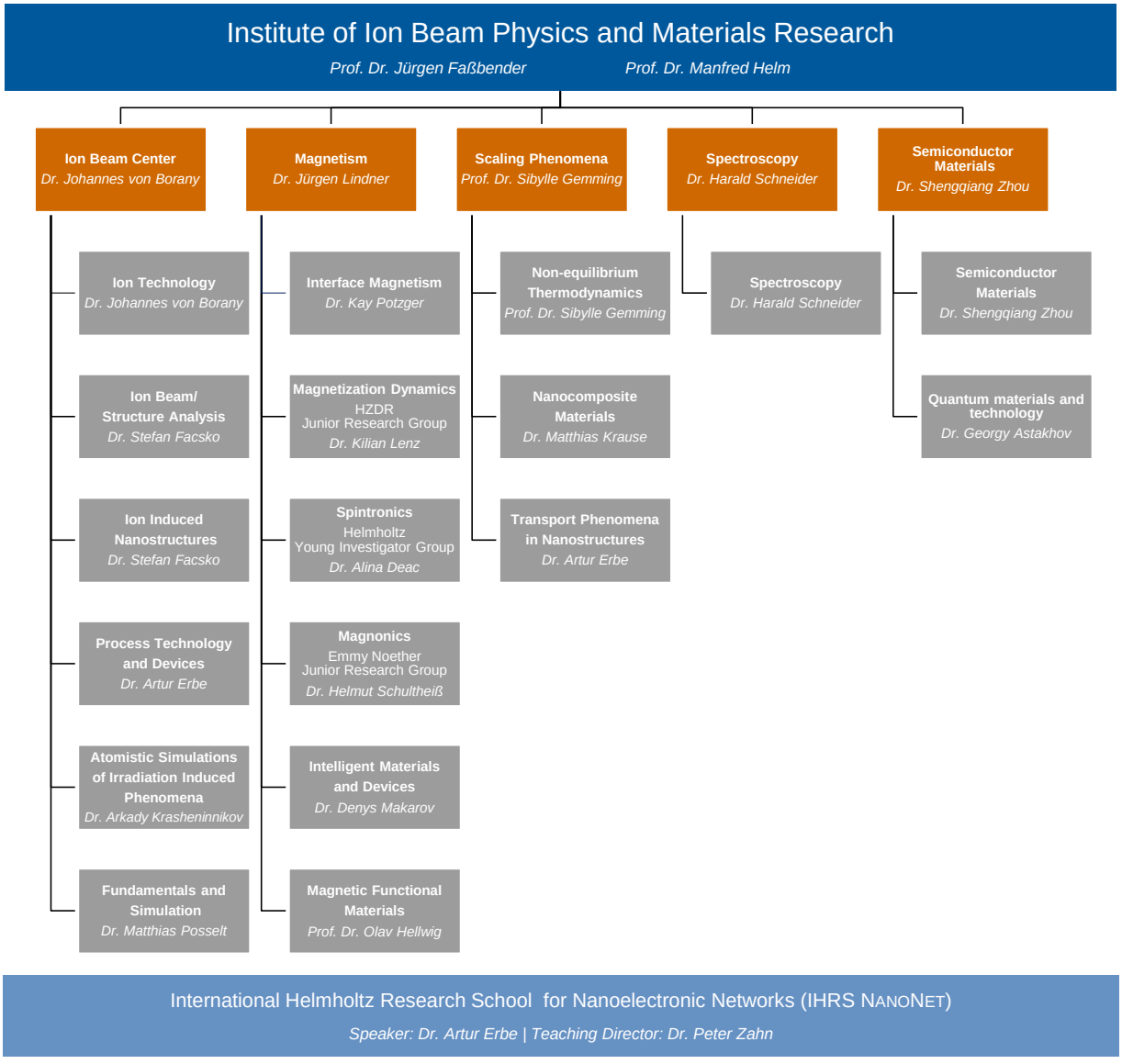

# List of personnel 2018

| DIRECTORS | OFFICE |
|---|---|
| Prof. Dr. M. Helm, Prof. Dr. J. Faßbender | S. Gebel, S. Kirch |

## SCIENTIFIC STAFF

### Permanent staff

Dr. C. Akhmadaliev
Dr. G. Astakhov
Dr. L. Bischoff
Dr. J. von Borany
Dr. E. Dimakis
Dr. A. Erbe
Dr. S. Facsko
Prof. Dr. S. Gemming
Dr. J. Grenzer
Dr. V. Heera
Dr. R. Heller
Dr. R. Hübner
Dr. A. Krasheninnikov
Dr. M. Krause
Dr. K. Lenz
Dr. J. Lindner
Dr. F. Munnik
Dr. A. Pashkin
Dr. M. Posselt
Dr. K. Potzger
Dr. S. Prucnal
Dr. L. Rebohle
Dr. H. Schneider
Dr. M. Voelskow
Dr. S. Winnerl
Dr. P. Zahn
Dr. S. Zhou

### Non-permanent

Dr. R. Bali
Dr. Y. Berencén (P)
D. Blaschke (P)
Dr. R. Böttger
Dr. A. Deac
Dr. A. Eichler-Volf
Dr. H.-J. Engelmann (P)
Dr. D. Erb
Dr. L. Fallarino (P)
Dr. C. Fowley
Dr. A. Froideval (P)
Dr. J. Ge (P)
Dr. M. Ghorbani Asl
Dr. M. Grobosch (P)
Dr. K.-H. Heinig (P)
Prof. Dr. O. Hellwig (P)
Dr. G. Hlawacek
Dr. R. Illing
Dr. J. Julin
Dr. A. Kákay (P)
R. Kaltofen (P)
Dr. N. Klingner (P)
T. Köhler (P)
Dr. T. Kosub
Dr. E. Kowalska
Dr. M. Lenz (P)
Dr. M. Liebsch
Dr. A. Lindner (P)
Dr. D. Makarov
Prof. Dr. W. Möller (P)
Dr. I. Mönch (P)
Dr. M. Neubert (P)
Dr. N. Nishida (P)
Dr. J. Osten (P)
Dr. W. Pilz (P)
Dr. A. Quade (P)
Dr. R. Rana
Dr. H. Schultheiß (P)
Dr. K. Schultheiß (P)
Dr. A. Semisalova
Dr. A. Singh (P)
Dr. W. Skorupa (P)
Dr. S. Stienen (P)
Dr. O. Volkov (P)
Dr. C. Wagner (P)
Dr. K. Wagner (P)
Dr. K. Wiesenhütter (P)
Dr. R. Wilhelm

(P) Projects

## TECHNICAL STAFF

### Permanent staff

Rb. Aniol
Rm. Aniol
E. Christalle
S. Eisenwinder
B. Gebauer
Dr. Y. Georgiev
A. Gerner
H. Gude
D. Hanf
J. Haufe
A. Henschke
H. Hilliges
S. Klare
J. Kreher
A. Kunz
H. Lange
U. Lucchesi
F. Ludewig
R. Mester
Dr. R. Narkovic
C. Neisser
F. Nierobisch
T. Putzke
A. Reichel
B. Scheumann
G. Schnabel
A. Schneider
A. Scholz
T. Schumann
I. Skorupa
M. Steinert
A. Thiel
K. Thiemig
J. Wagner
A. Weise
A. Weißig
J. Winkelmann
L. Zimmermann
J. Zscharschuch

### Non-permanent

A. Berens
L. Ehm
P. Freund
J. Heinze
U. Kentsch
K. Lang
L. Ramasubramanian (P)
T. Schönherr (P)
T. Voitsekhivska (P)

(P) Projects

## PhD STUDENTS

Y. Alsaadawi
H. Arora
A. W. Awan
N. Baghban Khojasteh
L. Balaghi
T. Bayrak
V. Begeza
M. Bejarano
J. Braun
G.S. Canon Bermudez
H. Cansever
P. Chava
S. Creutzburg
J. Duan
A. Echresh
J. Ehrler
I. Fotev
F. Fuchs
S. Ghaderzadeh
T. Hache
M. Hollenbach
T. Hula
D. Janke
S. Jazavandi-Ghamsari
T. Joseph
M. B. Khan
F. Kilibarda
S. Kretschmer
D. Lang
Zh. Li
Zi. Li
Lokamani
T. Prüfer
A. Schmeink
T. Schneider
A. Seidl
E. Serralta Hurtado
Z. Shang
S. Sorokin
M. Stöber
A. Strobel
T. Tauchnitz
A. Titova
M. Vallinayagam
T. Venanzi
C. Wang
M. Wang
X. Wang
Y. Wei
Y. Xie
C. Xu
X. Xu

## STUDENTS (Diploma / MSc / BSc)

Z. Fekri
M. Helbig
M. Hoppe
V. Kateel
L. Koch
V. Liersch
M. Neumann
A. Oelschlägel
A. Rayhan Rasel
W. Roscher
R. de Schultz
S. Shan
R. Sheldon
S. Shakeel
R. Thomas
M. Welsch

Wissenschaftlich-Technische Berichte
HZDR-097 | 2019 | ISSN 2191-8708

HELMHOLTZ ZENTRUM
DRESDEN ROSSENDORF

Institute of Ion Beam Physics and Materials Research
Bautzner Landstrasse 400 | 01328 Dresden | Germany
Phone +49 351 260-2345
Fax +49 351 260-3285
https://www.hzdr.de